University of Sheffield

Doctoral Thesis

Constraining neutrino interaction uncertainties for oscillation experiments

Author:
Callum Wilkinson

Supervisor:
Dr. Susan Cartwright

A thesis submitted in fulfilment of the requirements for the degree of Doctor of Philosophy in Physics

in the

Department of Physics and Astronomy

May 2015

The University Of Sheffield.

UNIVERSITY OF SHEFFIELD

Abstract

Faculty of Science
Department of Physics and Astronomy

Doctor of Philosophy in Physics

Constraining neutrino interaction uncertainties for oscillation experiments

by Callum Wilkinson

Neutrinos rarely interact, but sometimes they do. How much? And does it matter?

Charged-Current Quasi-Elastic (CCQE) neutrino-nucleus interactions are the main signal channel for T2K and other currently running neutrino oscillation experiments, but in recent years, with a number of experimental results, it has become clear that these interactions are not as well understood at few-GeV neutrino energies as was previously thought. This thesis focuses on the impact that this uncertainty will have on neutrino oscillation measurements.

Published CCQE and the closely related Neutral-Current Elastic (NCEL) cross section results from the MiniBooNE experiment are used to fit a 3+1 sterile neutrino model, and the uncertainty over fundamental parameters in the cross section model used is shown to badly bias the results. Conservative sterile neutrino limits which treat the cross section uncertainty correctly are used, and a general note of caution is sounded over sterile neutrino results which make tacit and unfounded assumptions about the neutrino cross section model.

New theoretical models of CCQE scattering which try to explain the experimental situation have become available, some of which have been implemented into NEUT, T2K's primary interaction generator. Two candidate models are used in a fit to all published CCQE data on nuclear targets to select a default model and constrain the parameters of that model in order to increase the sensitivity of T2K oscillation analyses. This CCQE parametrisation will be used for T2K oscillation analyses from the summer of 2015 onwards. The fit framework developed for this work has been integrated into the T2K oscillation analysis framework for future iterations. Additionally, the implementation of one such model, the Effective Spectral Function is described and compared with the available neutrino-nucleus scattering data.

Acknowledgements

I would struggle to make a comprehensive list of all those whose advice and support have helped guide the work in this thesis, or a comprehensive list of those whose camaraderie has made my experience over the last few years so enjoyable.

I owe a great deal to the advice and constant support of my supervisor, Dr. Susan Cartwright, who has allowed me to work on whatever interested me without letting me go too far wrong. She has shown remarkable fortitude when regularly confronted with draft chapters of this thesis over the last few months, and the finished document owes much to her editorial overview. I am also extremely grateful for the support of Prof. Lee Thompson, who has provided invaluable advice, and who ensures that every student at Sheffield takes up all possible opportunities available to them. I have also gained hugely from the additional supervision of Prof. Kevin McFarland at the University of Rochester who has taught me a huge amount (probably more than he knows), and whose tireless and infectious enthusiasm for the field of neutrino cross sections has been an inspiration to me.

There are many others who have offered important advice along the way, but I am particularly grateful to Dr. Ryan Terri, for offering invaluable advice and moral support (often via skype); Dr. Philip Rodrigues for patiently filling in (some of) the gaps in my knowledge and giving up half of his office at Rochester; and Dr. Jon Perkin, without whom I might still be trying to install ROOT.

It would have been a much less interesting time without the rest of the Sheffield group, Dr. Matthew Lawe, Leon Pickard, Mike Wallbank and Patrick Stowell, who have made travel to conferences a sometimes ridiculous but always enjoyable affair, and who all seem to share my unnatural love of Shin-chan. Thanks also to everyone at the University of Rochester for your hospitality and for making me feel so welcome, particularly to Connie Jones for going above and beyond the call of duty in helping me to settle in and giving me a place to stay on the first night. And thanks to everyone on T2K who made collaboration meetings a blast, there are too many of you to mention here.

I would also like to acknowledge the financial support of the Science and Technology Facilities Council.

Finally, I would like to thank my friends and family for supporting me through the years, and putting up with frequent absences in both body and spirit. Special thanks to Rachel for being a constant voice of reason and sanity.

Contents

List of Figures

List of Tables

Chapter 1

Introduction to neutrino physics

1.1 A brief history of neutrinos

The style of this section must be credited to Frank Close and his popular science book "Neutrino" [81], which provides a detailed account of the history of the neutrino, and the people involved.

1.1.1 First detection

The neutrino was first postulated in 1930 by Pauli [82] to explain the continuous energy spectrum observed in beta decay $n \to p + e^- + \bar{\nu}_e$, which had been a mystery since 1914 (when it had been observed by Chadwick). Although it was theorised that the existence of the neutrino could be proven by detecting inverse beta decay ($n + \bar{\nu}_e \to p + e^-$), the extremely low interaction probability meant that this was impractical at the time. The development of nuclear reactors in the late 1940's provided a strong enough source of antineutrinos to make their detection possible.

As well as inverse beta decay, Pontecorvo suggested that chlorine could be used as a target, where the signal would be argon nuclei, produced in the reaction $\nu_e + {}^{37}\mathrm{Cl} \to {}^{37}\mathrm{Ar} + e^-$ [83]. This idea was picked up by Ray Davis at Brookhaven National Laboratory (BNL), who set up a 4000 litre tank filled with carbon tetrachloride next to a test nuclear reactor at BNL, and saw nothing [84]. This experiment was the precursor to the long-running Homestake experiment which investigated solar neutrinos. Although unsuccessful, this experiment demonstrated that the antineutrinos produced by reactors are not the same as the neutrinos required for Pontecorvo's proposed detection channel. Reines and Cowan led the team who made the first successful detection of

neutrinos, dubbed "Project Poltergeist". They detected antineutrinos from a reactor through inverse beta decay at Savannah River in 1955 [85,86][1].

The muon had been discovered in 1937 [88], and later it was shown that muons decay to an electron and two other particles (as the electron had a continuous spectrum indicative of three-body decay). If muons can be thought of as heavy electrons, then the muon decay channel $\mu^- \to e^- + \gamma$ would be expected, and that it was not seen was something of a mystery[2]. Introducing lepton number conservation and therefore distinct muon and electron flavours of neutrinos could explain the observed muon decays $\mu^- \to e^- + \bar{\nu}_e + \nu_\mu$. In 1962 [90], the muon neutrino was discovered by looking at the charged-current interactions of neutrinos which had been produced by the charged pion decay $\pi^\pm \to \mu^\pm + {}^{(-)}\nu_\mu$. Far more muons than electrons were produced, indicating that the neutrino in this decay was associated exclusively with the muon flavour. If there was only one flavour of neutrino, it would be expected to couple equally to the muon and electron and thus produce equal numbers of each in the experiment.

The unexpected discovery of the tau lepton in the 1970s [91] implied the probable existence of a third neutrino by analogy with the electron and muon neutrinos. Indirect evidence for the existence of the tau neutrino came in 1989 from measurements of the Z^0 decay width at the Large Electron Positron collider (LEP) experiments at CERN [92–95] and the SLD detector at the Stanford Linear Collider [96]. By assuming that all of the invisible decay width of the Z^0 was due to decays to neutrinos (which were undetected by the LEP experiments), it is possible to infer the number of neutrino species which couple with the Z^0. A later analysis of all of the LEP experiments found the number of neutrino species which participate in the weak interaction, and which have $m_\nu \leq \frac{m_Z}{2}$, to be $N_\nu = 2.9840 \pm 0.0082$ [97]. Direct measurement of the tau neutrino came from the DONUT experiment at Fermilab in 2000 [98].

1.1.2 The solar neutrino problem

The chlorine detector Ray Davis had designed for detecting reactor antineutrinos was scaled up by two orders of magnitude and moved to the Homestake mine in South Dakota. The Homestake experiment was used to look for electron neutrinos produced

[1] A remarkable footnote from the history of "Project Poltergeist" is that Reines and Cowan first proposed, in 1951, to detonate a 20-kiloton nuclear bomb (approximately the same yield as the Hiroshima and Nagasaki bombs) ∼50m from their detector [87]. It was only after obtaining the bomb for this experiment that they realised a nuclear reactor would be a preferable source for their experiment. Although it now sounds absurd, Reines worked on the Manhattan project and later Los Alamos National Laboratory where he specialised in the effects of nuclear blasts, so had the relevant experience to make the bomb plan workable.

[2] Indeed, there are modern experiments (for example COMET [89]) which are still looking for lepton flavour violating muon decays.

by the sun as a means to verify the Standard Solar Model (SSM) developed by John Bahcall [99]. The predicted neutrino flux in the SSM comes from a variety of different processes, and has a complicated structure. It is shown as a function of neutrino energy in Figure 1.1.

The threshold for the reaction $\nu_e + {}^{37}\mathrm{Cl} \rightarrow {}^{37}\mathrm{Ar} + e^-$ is 814 keV, so it is clear from Figure 1.1 that the Homestake experiment was only sensitive to a small portion of the total solar neutrino flux. From the first paper in 1968 [100], a deficit of solar neutrinos was reported. The SSM was developed further, but over several decades experiment and theory failed to agree; this became known as the "solar neutrino problem". In the final Homestake dataset [101], the measured solar neutrino rate was approximately a third of that predicted by the SSM of the time [102].

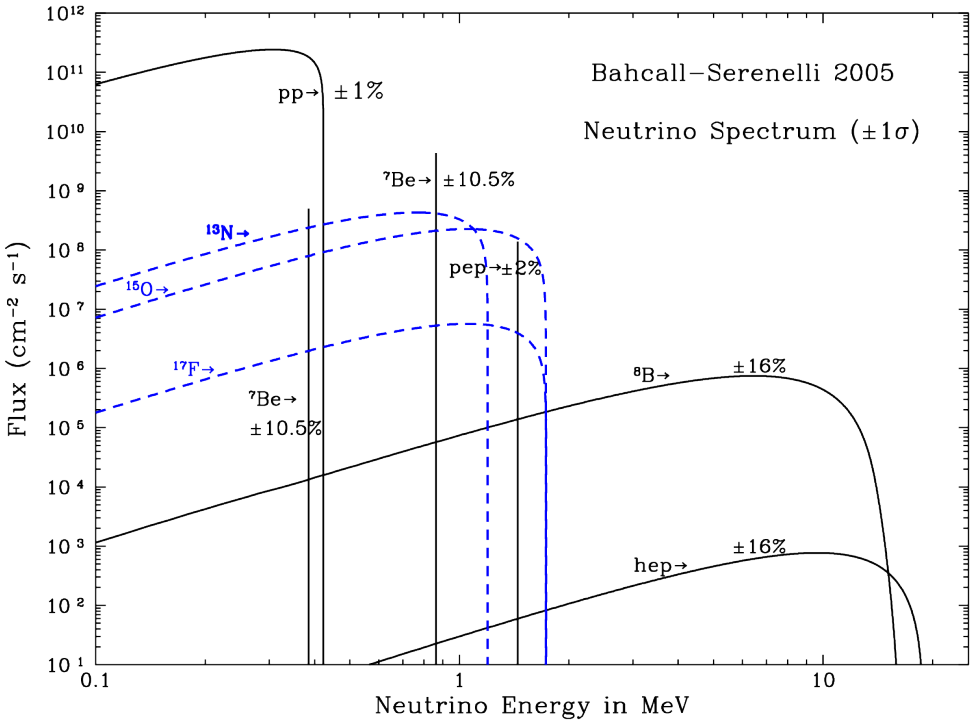

FIGURE 1.1: SSM (2005) spectrum as a function of neutrino energy [1]. Theoretical 1σ errors are shown next to each contribution to the flux. Solid lines come from the proton-proton fusion chain, and dashed lines come from the Carbon-Nitrogen-Oxygen chain. Details of later updates to the SSM can be found in Reference [2].

The Kamiokande water Cherenkov experiment observed high energy solar neutrinos on an event by event basis in the reaction $\nu_x + e^- \rightarrow \nu_x + e^-$. As the outgoing electron direction is strongly correlated with the incoming neutrino direction, Kamiokande confirmed that the neutrinos they were observing came from the direction of the sun, and also found a deficit in the expected rate [103]. Note that this reaction is sensitive to ν_μ and ν_τ neutrinos, but with a lower cross section, so the measured rate was less than

expected assuming a ν_e only neutrino flux from the sun. A deficit of solar neutrinos was also found in two gallium experiments, GALLEX (later GNO) and SAGE[3], which measured the solar neutrino flux with the reaction $\nu_e + {}^{71}\mathrm{Ga} \rightarrow {}^{71}\mathrm{Ge} + e^-$. The neutrino energy threshold for the gallium experiments was 233 keV, so they sampled more of the solar neutrino flux shown in Figure 1.1, including neutrinos produced in the proton-proton fusion process. Final results for GALLEX + GNO [104, 105] and SAGE [106] find a deficit of 50–60% in the total solar neutrino flux to which they were sensitive.

Although the idea of neutrino oscillation had been proposed as early as 1957 [107], the solar neutrino anomaly could have been due to poor predictions of the neutrino flux from the SSM[4] rather than due to unexpected neutrino behaviour. The atmospheric neutrino anomaly, observed by the Kamiokande [108] and IMB [109] experiments in the late 1980s, measured a deficit in the flux of muon neutrinos produced by cosmic rays interacting in the atmosphere. Conversely, the electron neutrino flux they measured was consistent with prediction. This became known as the "atmospheric neutrino anomaly". A later paper by Kamiokande showed there was a slight angular dependence to the deficit [110], which was confirmed by Super-Kamiokande [111]. Super-Kamiokande binned their data in terms of energy and distance (zenith angle) to show that the deficit they observed was consistent with $\nu_\mu \leftrightarrow \nu_\tau$ oscillations [112].

That neutrinos were also missing from atmospheric experiments lent support to explanations of the solar neutrino anomaly in terms of unexpected phenomena in the neutrino sector. But alternative explanations of the neutrino deficit, such as neutrino decay, would also have been plausible. The SNO experiment was a heavy water (D_2O) Cherenkov detector designed to resolve the solar neutrino problem. As well as the charged current reaction $\nu_e + d \rightarrow e^- + p + p$, SNO was sensitive to the neutral current channel $\nu_x + d \rightarrow \nu_x + p + n$, which is equally sensitive to all neutrino flavours. The threshold for the neutral current reaction is 2.2 MeV (so it is only sensitive to a small portion of the solar neutrino flux) and the signal is neutron capture on deuterium, which emits a 6.25 MeV gamma ray. By measuring a neutral current rate consistent with the solar flux prediction of the SSM [113], and a charged current rate with a deficit consistent with other solar neutrino experiments [114], SNO demonstrated that the electron neutrinos from the sun had oscillated into other flavours. It has been remarked that elastic scattering $\nu_x + e^- \rightarrow \nu_x + e^-$ is also sensitive to all active flavours (although the cross section is much higher for electron neutrinos), and high statistics data from Super-Kamiokande in this channel provided an independent check of the SNO result [115].

[3] The Soviet American Gallium Experiment (SAGE) was conceived before the fall of the Soviet Union, but began running afterwards. It is somewhat amusing that the acronym was not changed.

[4] In Neutrino [81], Frank Close claims that the money for the Homestake experiment was only approved by Maurice Goldhaber, the director of BNL, to prove that astrophysicists "did not know what they were talking about".

1.2 Neutrino oscillation formalism

In the three-neutrino mixing model, the neutrino flavour eigenstate ν_α, where $\alpha = e, \mu, \tau$, is a linear superposition of the mass eigenstates ν_j, where $j = 1, 2, 3$:

$$|\nu_\alpha\rangle = \sum_{j=1}^{3} U^*_{\alpha j} |\nu_j\rangle, \qquad |\nu_j\rangle = \sum_{\alpha=e,\mu,\tau} U_{\alpha j} |\nu_\alpha\rangle, \tag{1.1}$$

where $U_{\alpha i}$ represents elements of the Pontecorvo-Maki-Nakagawa-Sakata (PMNS) mixing matrix [116][5]. The PMNS matrix is given for Dirac neutrinos in Equation 1.2 and is decomposed into three axial rotations in Equation 1.3:

$$\begin{aligned} U &= \begin{pmatrix} U_{e1} & U_{e2} & U_{e3} \\ U_{\mu 1} & U_{\mu 2} & U_{\mu 3} \\ U_{\tau 1} & U_{\tau 2} & U_{\tau 3} \end{pmatrix} \\ &= \begin{pmatrix} c_{12}c_{13} & s_{12}c_{13} & s_{13}e^{i\delta} \\ -s_{12}c_{23} - c_{12}s_{23}s_{13}e^{i\delta} & c_{12}c_{23} - s_{12}s_{23}s_{13}e^{i\delta} & s_{23}c_{13} \\ s_{12}s_{23} - c_{12}s_{23}s_{13}e^{i\delta} & -c_{12}s_{23} - s_{12}c_{23}s_{13}e^{i\delta} & c_{23}c_{13} \end{pmatrix} \qquad (1.2) \\ &= \begin{pmatrix} 1 & 0 & 0 \\ 0 & c_{23} & s_{23} \\ 0 & -s_{23} & c_{23} \end{pmatrix} \begin{pmatrix} c_{13} & 0 & s_{13}e^{i\delta} \\ 0 & 1 & 0 \\ -s_{13}e^{i\delta} & 0 & c_{13} \end{pmatrix} \begin{pmatrix} c_{12} & s_{12} & 0 \\ -s_{12} & c_{12} & 0 \\ 0 & 0 & 1 \end{pmatrix}, \qquad (1.3) \end{aligned}$$

where $c_{ij} = \cos\vartheta_{ij}, s_{ij} = \sin\vartheta_{ij}$ and δ is a Dirac CP-violating phase. If neutrinos are Majorana particles, then U should be multiplied by diag $\left(e^{i\alpha_1/2}, e^{i\alpha_2/2}, 1\right)$ where α_1 and α_2 are Majorana phase factors. The Majorana phases do not affect neutrino oscillations so can be neglected in this discussion [2].

The $|\nu_j\rangle$ are eigenstates of the Hamiltonian, with eigenvalues $E_j = \sqrt{\vec{p}^2 + m_j^2}$. Their evolution is determined by the time-dependent Schrödinger equation:

$$|\nu_j(t)\rangle = e^{-iE_j t} |\nu_j\rangle. \tag{1.4}$$

The time evolution of a flavour state can be expressed as

$$|\nu_\alpha(t)\rangle = \sum_{\beta=e,\mu,\tau} \left(\sum_{j\,=\,1}^{3} U^*_{\alpha j} e^{-iE_j t} U_{\beta j} \right) |\nu_\beta\rangle, \tag{1.5}$$

[5] Pontecorvo first proposed neutrino oscillations (neutrino $\leftrightarrow$ antineutrino) in 1957 [107], but the fully developed theory describing oscillations between the three lepton flavours which is used today was developed by Maki, Nakagawa and Sakata [116].

from which it is clear that if U is not diagonal, a neutrino produced in flavour state α at time $t = 0$ has a nonzero probability of being observed in some other flavour state β at any other time t. Given the orthonormality of the mass eigenstates, the amplitude for the flavour change $\nu_\alpha \to \nu_\beta$ at time t is given by

$$\langle \nu_\beta | \nu_\alpha(t) \rangle = \sum_k \sum_j \langle \nu_j | U_{\beta j} U^*_{\alpha k} e^{-iE_k t} | \nu_k \rangle = \sum_k U^*_{\alpha k} U_{\beta k} e^{-iE_k t}. \tag{1.6}$$

The probability for a neutrino ν_α to oscillate into a neutrino ν_β, where $\alpha, \beta = e, \mu, \tau$ is therefore

$$\begin{aligned} P_{\nu_\alpha \to \nu_\beta}(t) &= |\langle \nu_\beta | \nu_\alpha \rangle|^2 \\ &= \sum_k \sum_j U^*_{\alpha k} U_{\beta k} U_{\alpha j} U^*_{\beta j} e^{-i(E_k - E_j)t}. \end{aligned} \tag{1.7}$$

Finally, in the highly relativistic limit for light neutrino masses, the probability can be rewritten as

$$P_{\nu_\alpha \to \nu_\beta}(L, E) = \sum_k \sum_j U^*_{\alpha k} U_{\beta k} U_{\alpha j} U^*_{\beta j} \exp\left(-i \frac{\Delta m^2_{kj} L}{2E} \right), \tag{1.8}$$

where $\Delta m^2_{kj} \equiv m^2_k - m^2_j$ is the mass-squared difference. The oscillation probability for antineutrinos, $P_{\bar{\nu}_\alpha \to \bar{\nu}_\beta}$, can be obtained by replacing U in equation 1.8 with its complex conjugate. Note that the study of neutrino oscillations is not sensitive to the absolute neutrino masses, only to the difference between the squares of the masses.

The oscillation probability can only be non-zero when $\alpha \neq \beta$ if neutrino masses are distinct ($\Delta m^2_{kj} \neq 0$), which implies that at least two of the neutrino masses m_i are non-zero; thus the discovery of neutrino oscillations marks a departure from the standard model (though some prefer to call it an enhancement of the standard model). The oscillation probability in the three-neutrino scheme is dependent on L, E, ϑ_{12}, ϑ_{13}, ϑ_{23}, Δm^2_{12}, Δm^2_{13}, Δm^2_{23}, and δ.

The Mikheyev-Smirnov-Wolfenstein (MSW) effect modifies the oscillation probabilities from those in a vacuum (Equation 1.8) when neutrinos are propagating through matter [117, 118]. Coherent forward scattering of electron neutrinos ($\nu_e + e^- \to \nu_e + e^-$) in normal matter adds an effective potential to the Hamiltonian, which changes the eigenvalues of the propagation eigenstates, and ultimately modifies the time evolution of neutrino flavour states. The size of the MSW effect depends on the electron density of matter, and whilst it is important for neutrinos produced in the sun, it can be neglected over the T2K baseline.

1.3 Current experimental status

A wealth of data supports the three-neutrino mixing model, and precision measurements of the oscillation parameters are being made by currently running experiments. There are two mass splittings of interest: $\Delta m^2_{21} \ll |\Delta m^2_{31}| \simeq |\Delta m^2_{32}|$. Atmospheric and beam experiments can determine the magnitude of Δm^2_{32} and ϑ_{23}. Solar and reactor measurements can determine the magnitude of Δm^2_{21} and ϑ_{12}, and the sign of Δm^2_{21} is known to be positive from solar neutrino experiments (because of the MSW matter effect). Finally, and most recently, beam and reactor experiments have determined the magnitude of ϑ_{13} and found it to be nonzero. A summary of the current limits on the mixing parameters is given in Table 1.1, and a summary of most neutrino oscillation experiments expressed in the $\Delta m^2 - \tan^2\vartheta$ plane is given in Figure 1.2.

Parameter	Best fit ($\pm 1\sigma$)
Δm^2_{21} [10^{-5} eV^2]	$7.54^{+0.26}_{-0.22}$
$\lvert\Delta m^2\rvert$ [10^{-3} eV^2]	2.43±0.06 (2.38±0.06)
$\sin^2\vartheta_{12}$	0.308±0.017
$\sin^2\vartheta_{23}$	$0.437^{+0.033}_{-0.023}$ ($0.455^{+0.039}_{-0.031}$)
$\sin^2\vartheta_{13}$	$0.0234^{+0.0020}_{-0.0019}$ ($0.0240^{+0.0019}_{-0.0022}$)

TABLE 1.1: Best fit three-neutrino oscillation mixing parameters with 1σ errors, shown for normal (inverted) hierarchy [2,75]. Note that the mass ordering is known for Δm^2_{21} and $\sin^2\vartheta_{12}$. $\Delta m^2 = m^2_3 - (m^2_2 + m^2_1)/2 \simeq \Delta m^2_{32} \simeq \Delta m^2_{31}$.

.

The presentation of Figure 1.2 is busy, but it nicely illustrates how various experiments contribute to our understanding of the oscillation parameters. The solar and reactor constraints on Δm^2_{21} and ϑ_{12} can be read off (using the Δm^2 values given in Table 1.1), with the strongest constraints from Super-Kamiokande [119], KamLAND [120] and SNO [121], which are also consistent with the results from the gallium [104–106] and Homestake [101] experiments. It is obvious that the solar results break the degeneracy seen in the KamLAND results and favour a positive value of Δm^2_{21}. Our understanding of Δm^2_{32} and ϑ_{23} comes from MINOS [122], T2K [123,124] and Super-Kamiokande [125], with values very close to maximal mixing ($\vartheta = 45°$, $\tan^2\vartheta = 1$). The much smaller angle ϑ_{13} allowed region is here shown as Daya Bay [126] only; additional strong constraints come from T2K [127,128] and RENO [129], which are not shown on Figure 1.2[6].

Outstanding questions for neutrino oscillation physics are: the sign of Δm^2_{32} (normal or inverted hierarchy); whether there is CP violation ($\delta \neq 0$) in neutrino oscillations[7];

[6] All of these measurements also contribute a strong constraint on Δm^2_{32} as $\Delta m^2_{32} \simeq \Delta m^2_{31}$, which could be demonstrated by projecting Figure 1.2 onto the Δm^2 axis.

[7] Combined fits to T2K and Daya Bay data show a weak preference for nonzero δ [75,128].

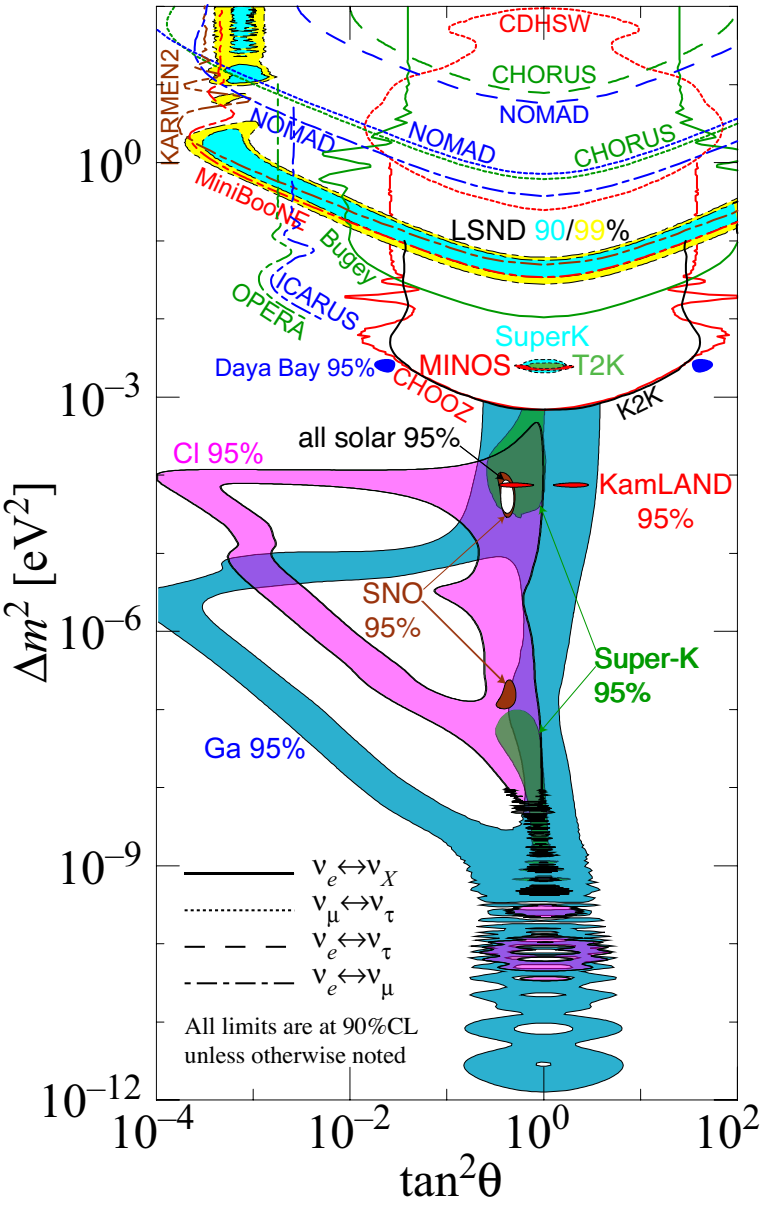

FIGURE 1.2: Regions of squared-mass splitting, Δm^2, and mixing angle favoured (coloured regions) or excluded (lines) by various named experiments for four types of neutrino oscillation. References to the data used in the plot and the plot itself can be found in Reference [3]. Note that vacuum oscillations are symmetric about $\tan^2\vartheta = 1$. Solutions with $\tan^2\vartheta < 1$ ($\tan^2\vartheta > 1$) correspond to positive (negative) values of Δm^2.

the quadrant of ϑ_{23}; and whether there are additional sterile neutrinos, which will be discussed further in Sections 1.4 and 1.5.

1.4 Extending the three-neutrino mixing framework

It has already been remarked that the number of active neutrino species has been strongly constrained by LEP data [97]. However, there are models which include additional, *sterile* neutrinos, which participate in neutrino mixing, but do not interact weakly. The addition of N sterile neutrinos requires an extension from the 3×3 PMNS matrix given in Equations 1.2 and 1.3 to a $(3 + N) \times (3 + N)$ matrix, though only the 3×3 part would be experimentally accessible. Equation 1.8 is still valid, but the number of species is extended with N sterile states $(\alpha, \beta = e, \mu, \tau, s_1, s_2, \ldots, s_N)$.

Although the additional sterile neutrinos could not be directly detected, the extension of the PMNS matrix would lead to several effects which could be detected in current neutrino experiments, and which could affect attempts to measure the experimentally accessible oscillation parameters of the 3×3 PMNS matrix. Oscillations between active states and sterile states (with larger masses) would result in discrepancies in $\nu_\alpha \to \nu_\alpha$ disappearance measurements, or enhancements in $\nu_\alpha \to \nu_\beta$ appearance measurements (where $\alpha, \beta = e, \mu, \tau$) over shorter baselines than could be explained in the three-neutrino mixing scheme. The experimentally accessible part of the PMNS matrix would also no longer be unitary, so the flux of active species would vary with distance and energy, which would show up as oscillations in neutral current (NC) interaction rates. There would also be more complex phases introduced to the PMNS matrix, so enhanced, or anomalous, patterns of CP violation might be seen.

It is common in the literature to refer to short baseline oscillations in the context of sterile neutrino searches [130]. More correctly, this refers to oscillations where the L/E is such that standard three flavour mixing can be neglected, so any oscillations are driven by the additional, predominantly sterile, mass state(s). In this approximation, $\Delta m^2_{21} = \Delta m^2_{32} = \Delta m^2_{31} = 0$.

Although light ($\mathcal{O}$1–100 eV) sterile neutrinos are of particular interest to this thesis, it is worth mentioning other sterile neutrino models where the additional sterile state is significantly heavier. Typically, sterile neutrino models above the $\mathcal{O}$1–100 eV scale do not participate in coherent neutrino oscillations with active neutrino flavours, but do decay to produce active neutrinos, so can be used to explain some anomalous mixing results. Massive neutrinos with right-handed chirality (which are necessarily sterile) which couple to each of the three active neutrino flavours are often included in theoretical models as a way of explaining why neutrino masses are so small via the *see-saw* mechanism [131]. However, the simplest see-saw mechanisms predict sterile neutrinos with masses on the GUT scale, which are difficult to probe experimentally [132]. The see-saw mechanism can also be modified to allow for sterile neutrinos on the keV scale, which make viable

dark matter candidates as relics from the big bang [133]. These keV scale neutrinos are predicted to decay to produce mono-energetic x-rays, for which there have been several searches using astronomical sources which are likely to have a high dark matter content [134–139], although no such signal has been found.

1.4.1 3+1 neutrino mixing

In the 3+1 case where there is a single additional sterile mass state, there is a single mass splitting in the short baseline approximation, here denoted as Δm^2_{42}. The appearance and disappearance probabilities simplify to the two-neutrino mixing equations given by Equation 1.9 and Equation 1.10:

$$P_{\overset{(-)}{\nu}_\alpha \to \overset{(-)}{\nu}_\beta} = \sin^2 2\vartheta_{\alpha\beta} \sin^2\left(\frac{\Delta m^2_{41} L}{4E}\right), \qquad (\alpha \neq \beta) \tag{1.9}$$

$$P_{\overset{(-)}{\nu}_\alpha \to \overset{(-)}{\nu}_\alpha} = 1 - \sin^2 2\vartheta_{\alpha\alpha} \sin^2\left(\frac{\Delta m^2_{41} L}{4E}\right), \tag{1.10}$$

for $\alpha, \beta = e, \mu, \tau, s$, with:

$$\sin^2 2\vartheta_{\alpha\beta} = 4|U_{\alpha 4}|^2 |U_{\beta 4}|^2, \tag{1.11}$$

$$\sin^2 2\vartheta_{\alpha\alpha} = 4|U_{\alpha 4}|^2 \left(1 - |U_{\alpha 4}|^2\right). \tag{1.12}$$

One important feature of these equations is the lack of a CP violating phase factor, so short baseline oscillations caused by an extra sterile neutrino in 3+1 models are the same in both the neutrino and antineutrino measurements. As will be discussed in Section 1.5, the tension between neutrino and antineutrino data has been one of the main problems facing 3+1 models.

These equations can also be applied when calculating the expected decrease in NC interaction probabilities by considering the probability of active neutrinos undergoing a flavour transition to a sterile state, or the probability of active to active survival decreasing as in Equation 1.13. Here the unitarity constraint $1 = |U_{e4}|^2 + |U_{\mu 4}|^2 + |U_{\tau 4}|^2 + |U_{s4}|^2$ [140] has been used. As the NC signal is sensitive to $|U_{e4}|^2 + |U_{\mu 4}|^2 + |U_{\tau 4}|^2$, NC disappearance experiments can place limits in the $\Delta m^2 - \sin^2 2\vartheta_{\mu s}$ plane. Similar limits would require an ensemble of charged current measurements.

$$\begin{aligned} P^{NC} &= 1 - \sin^2 2\vartheta_{\mu s} \sin^2\left(\frac{\Delta m^2_{42} L}{4E}\right) \\ &= 1 - 4|U_{\mu 4}|^2 \left(1 - |U_{e4}|^2 - |U_{\mu 4}|^2 - |U_{\tau 4}|^2\right) \sin^2\left(\frac{\Delta m^2_{42} L}{4E}\right) \end{aligned} \tag{1.13}$$

1.5 Evidence for light sterile neutrinos

Figure 1.2 shows an additional closed contour from LSND which does not fit into the three-neutrino mixing framework[8]. The LSND experiment looked for $\bar{\nu}_\mu \to \bar{\nu}_e$ oscillations where the neutrinos are produced from $\mu^+ \to e^+ + \nu_e + \bar{\nu}_\mu$ decaying at rest in the beam stop. The final LSND results show an excess of electron-like events, giving a 3.8σ excess which they interpreted as $\bar{\nu}_\mu \to \bar{\nu}_e$ oscillations mediated by $0.1 \leq \Delta m^2 \leq 10$ eV^2 [142]. As no such mass splitting exists in the three-neutrino mixing model, this is now interpreted as a hint of an additional sterile neutrino.

The LSND allowed region is restricted by data from KARMEN2 [4], which was a very similar decay at rest muon antineutrino oscillation experiment at the Rutherford Appleton Laboratory, as well as some other limits set on $\overset{(-)}{\nu}_\mu \to \overset{(-)}{\nu}_e$ mixing which can be seen in Figure 1.2. Because no other experiments could conclusively rule the LSND result out, the MiniBooNE experiment was built to directly test the anomaly. MiniBooNE had the same L/E as LSND, but both the baseline and the peak neutrino energy, $E_\nu = 0.8$ GeV, were an order of magnitude higher (to make the systematic errors different from those at LSND). MiniBooNE observed a 2.8σ excess at low energies in antineutrino mode, which is compatible with some of the LSND allowed region [6]. They also observed a 3.4σ excess in neutrino mode, but they found considerable tension for a 3+1 mixing model [6, 143]. The MiniBooNE neutrino and antineutrino results for a 3+1 model are shown in Figure 1.3, and are compared with the LSND allowed regions. It is clear that MiniBooNE neutrino and antineutrino mode data do not agree, and they also do not agree well with LSND. Unlike LSND, muon (anti)neutrinos are above theshold for CC interactions at MiniBooNE, and limits were also set for muon neutrino and antineutrino disappearance [61, 144].

Additional pieces to the sterile neutrino puzzle are the "Gallium Anomaly" and the "Reactor Antineutrino Anomaly"[9]. The former comes from the GALLEX [145] and SAGE [146, 147] solar neutrino experiments, which used radioactive ν_e sources to calibrate their detectors for low energy neutrinos. Both experiments found a deficit in the measured rate compared with theoretical predictions, which can be interpreted as electron neutrino disappearance in the context of a 3+1 sterile neutrino model. A combined analysis of the gallium data found that the Gallium Anomaly is significant at 3σ [148]. The Reactor Antineutrino Anomaly refers to an apparent deficit (94% of the predicted rate), significant at 3σ, in the electron antineutrino flux measured in many

[8] It should be noted that the first LSND result [141] to suggest short-baseline $\bar{\nu}_\mu \to \bar{\nu}_e$ oscillation predates most of the results which now constrain neutrino mixing.

[9] The sterile neutrino community likes to name things.

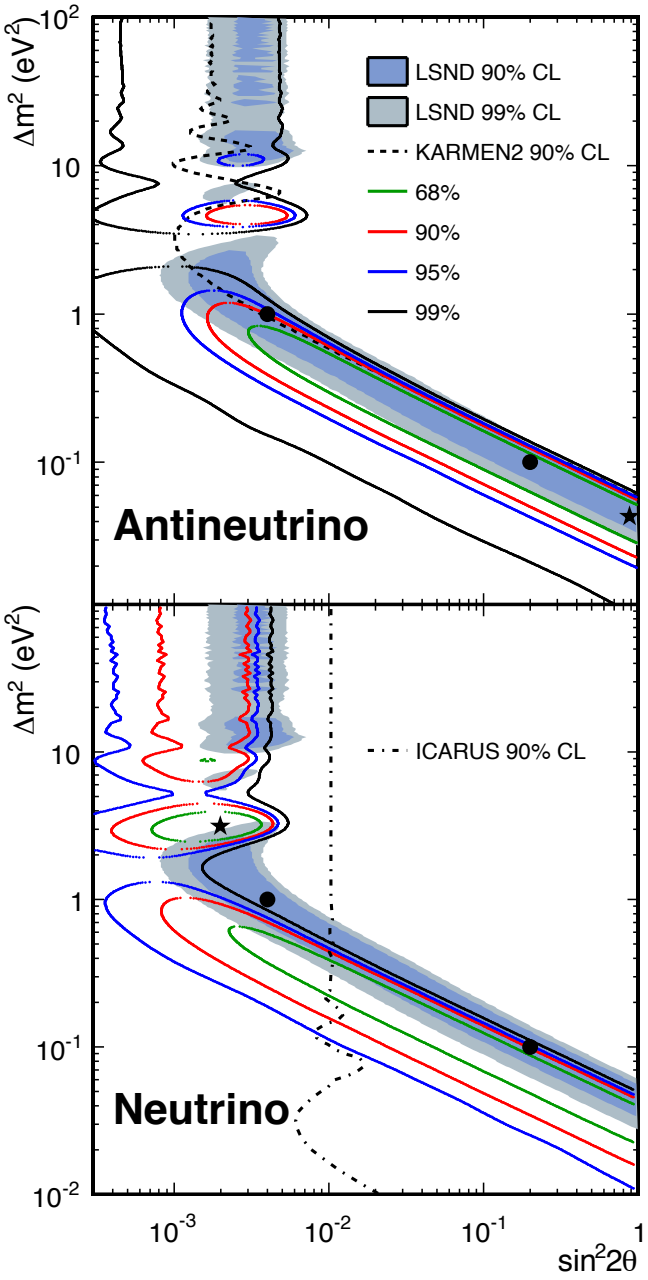

FIGURE 1.3: MiniBooNE allowed regions (68%, 90%, 95% and 99% regions are shown) for a 3+1 interpretation of their neutrino and antineutrino mode $E_\nu^{\mathrm{QE,\,RFG}} > 200$ MeV datasets. KARMEN2 [4] and ICARUS [5] appearance limits are also shown. Stars denote the MiniBooNE best fit values for neutrino and antineutrino modes. Black circles are LSND fit values for reference. This figure has been reproduced from Reference [6].

reactor neutrino experiments [149], based on a reanalysis of the neutrino flux prediction which increased the flux normalisation by ∼3% [150]. Recently, the significance of the anomaly has been questioned by a reanalysis of the reactor flux errors by different authors [151], whose calculation of the flux error is approximately twice that originally

reported. The predicted shape of the flux spectrum as a function of E_ν also differs between the two theoretical predictions.

Although there are a number of anomalous results which could be interpreted as evidence for the existence of sterile neutrinos, and individually each of these hints can be reasonably well described by a 3+1 sterile neutrino model, global fits find that there is a great deal of tension between the various anomalies [132, 152, 153]. Combined fits to the MiniBooNE and LSND antineutrino datasets found some tension (Figure 1.3), and best fit values from those datasets disagree with the MiniBooNE neutrino sample. Additional CP violating phases can be introduced by adding further sterile neutrino flavours (3+2, 3+3 models) to improve agreement between these appearance ($\overset{(-)}{\nu}_\mu \to \overset{(-)}{\nu}_e$) datasets. However, there is still considerable tension between the appearance and disappearance ($\overset{(-)}{\nu}_\mu \to \overset{(-)}{\nu}_\mu, \overset{(-)}{\nu}_e \to \overset{(-)}{\nu}_e$) datasets which cannot be resolved by adding any number of sterile neutrinos [152]. In particular, despite the reactor antineutrino anomaly, the strong limitations on $\bar{\nu}_e \to \bar{\nu}_e$ disappearance from reactors are in conflict with the indications of $\overset{(-)}{\nu}_\mu \to \overset{(-)}{\nu}_e$ appearance from accelerators. Despite the inconsistencies in the sterile neutrino data, the lingering doubt over the validity of the three-neutrino mixing model needs to be addressed in order to make precision measurements of the oscillation parameters. Otherwise the possible bias introduced by sterile neutrinos must be treated as a systematic error in future oscillation analyses.

A further interesting constraint on sterile neutrino models has been placed by MINOS using neutral current data [154] to constrain the fraction of $\nu_\mu \to \nu_s$ muon neutrino disappearance at the far detector. However, in the light of large ϑ_{13}, the constraint of no more than 40% of ν_μ disappearing at 90% confidence becomes rather weak. This is because the MINOS far detector is not designed to distinguish electron neutrino and neutral current events. Despite the weakness of the constraint, this is an interesting and general test of sterile neutrino oscillations, which inspired the MiniBooNE neutral current disappearance analysis presented in Chapter 4. If neutral current disappearance can be well constrained, then the effect of sterile neutrinos on three-neutrino mixing can be constrained in a model-independent way.

1.5.1 Cosmological constraints

Various measurements from cosmology are dependent on the number of effective neutrino species, N_{eff}, which played a role in the expansion of the early universe. Good reviews of the impact of N_{eff} on cosmological measurements is available in References [132, 155, 156], from which the discussion in this section is drawn unless otherwise cited. N_{eff} is

proportional to the number of thermalised neutrino species[10], and in the standard model, with only three generations of neutrino, $N_{\text{eff}} = 3.046$ (see, for example, Reference [132]). In most sterile neutrino models, the additional neutrino species are fully thermalised, so the additional sterile neutrino leads to $\Delta N_{\text{eff}} = 1$, so unexpectedly large values of N_{eff} from cosmological measurements could provide evidence of additional sterile neutrino species. Conversely, a tight constraint on N_{eff} from cosmology is generally treated as a constraint on sterile neutrino models. However, there are models with only three neutrinos which have a larger value of N_{eff}, and sterile neutrino models in which the neutrinos are not fully thermalised so N_{eff} does not scale with the number of neutrino species.

N_{eff} can be derived from several source of information: Big Bang Nucleosynthesis (BBN), the Cosmic Microwave Background (CMB) and Large Scale Structure (LSS) formation. The abundance of different stable isotopes of light elements produced when the temperature of the early universe was low enough to allow the formation of nuclei (BBN) is affected by the expansion rate of the early universe because the neutron-to-proton ratio is not constant (due to neutron decay). As the expansion of the early universe depends on N_{eff}, a constraint can be derived from the BBN abundances. CMB data is sensitive to the total relativistic energy density [156], and LSS formation is slowed down by the existence of additional massive particles [156], so both are affected by including additional relativistic neutrinos. The requirement that the neutrinos are relativistic implies that neutrinos on the keV scale or higher will not affect measurements of N_{eff} from the CMB or LSS as they will be non-relativistic [132] (note that BBN measurements do not have this added caveat). The strongest constraint on N_{eff} comes from recent Planck CMB data which finds $N_{\text{eff}} = 3.30 \pm 0.27$ [157], which is completely consistent with the standard value of $N_{\text{eff}} = 3.046$. Other datasets give a variety of values [132, 155, 156], but generally find that sterile models with more than 1 fully thermalised sterile neutrino model are strongly disfavoured.

An important additional constraint from cosmology, which is also of interest for the standard three-neutrino model is the constraint on the sum of the neutrino masses. The most recent Planck CMB data sets a limit of $\sum m_\nu \leq 0.23$ eV at 95% confidence [157], which also uses Baryon Acoustic Oscillation (BAO) information[11]. Note that the Planck limit assumes that there are three species of neutrino ($N_{\text{eff}} = 3.046$), but N_{eff} and $\sum m_\nu$ are correlated, and both depend (in different ways) on the cosmological model used. Planck also investigate both parameters simultanously with their CMB+BAO data, and

[10] Note that only left-handed neutrinos are thermalised because they are affected by the weak interaction.

[11] BAO are fluctuations in the density of the visible baryonic matter in the universe [157], and are not directly sensitive to the sum of the neutrino masses, but remove degeneracies between other parameters in the cosmological model used to extract the sum of neutrino masses from the CMB data [158].

find the marginalised single parameter constraints $N_{\text{eff}} < 3.91$ and the effective mass of any additional sterile neutrinos, $m^{\text{eff}}_{\nu,\,s}$, < 0.42 eV at 95% confidence [157]. The Planck result is marginally compatible with a single additional sterile neutrino with a mass of $\sim$0.5 eV, but such a sterile neutrino does not fit well with the short baseline oscillation anomalies observed in accelerator and reactor experiments, which typically require a larger mass splitting. Different limits on $\sum m_\nu$, N_{eff} and $m^{\text{eff}}_{\nu,\,s}$ can be obtained by combining different cosmological datasets [158–160], but it is clear that cosmological data disfavours the existence of additional sterile neutrinos on the eV scale. The constraint on $\sum m_\nu$ also provides a constraint on the ordering of sterile neutrino models, as the active states cannot be heavier than most sterile neutrinos without disagreeing strongly with this constraint[12].

It should be stressed that cosmological constraints on N_{eff} and $m^{\text{eff}}_{\nu,\,s}$ only apply if additional sterile neutrino species were fully thermalised in the early universe, so many theoretical models are unaffected by these constraints. Additionally, it is worth noting that cosmological constraints are highly model dependent, it is observed in Reference [161] that cosmological constraints are discussed as a way to restrict the models used to explain anomalies from terrestrial neutrino oscillation experiments. However, if the latter find strong evidence for additional sterile neutrinos which conflict with cosmological measurements, the cosmological models should be adapted to account for them.

1.6 Structure of this thesis

The current status of neutrino oscillation physics has been sketched out in this introduction. In recent years, focus has started to shift from the discovery of new phenomena to the precision measurement of neutrino mixing parameters. There are still important questions which need to be answered. The neutrino mass hierarchy and whether there is CP violation in the neutrino sector have yet to be determined, but a worldwide strategy on how to make these measurements appears to be converging. Upcoming experiments such as JUNO, DUNE, Hyper-K [162] and PINGU [163] promise to pin down these outstanding questions and further improve the precision measurements of neutrino oscillation parameters being made by currently running experiments such as T2K, NOνA [164], IceCube [165], Super-Kamiokande and MINOS+.

[12] Short baseline oscillation experiments are, of course, only sensitive to Δm^2, not the mass ordering of the sterile and active neutrino mass states.

Neutrino oscillation experiments measure the charged-current and neutral-current event rates in their detectors, which can generically be expressed as

$$R(\vec{\mathbf{x}}) = \Phi(E_\nu) \times \sigma(E_\nu, \vec{\mathbf{x}}) \times \epsilon(\vec{\mathbf{x}}) \times P(\nu_A \to \nu_B), \tag{1.14}$$

where $R(\vec{\mathbf{x}})$ is the event rate as a function of the reconstructed kinematic variables $\vec{\mathbf{x}}$, $\Phi_\nu(E_\nu)$ is the neutrino flux as a function of the neutrino energy E_ν, σ is the neutrino cross section and ϵ is the detector efficiency. It is obvious from this equation that in order to measure the neutrino oscillation probability $P(\nu_A \to \nu_B)$, the unoscillated flux must be well understood, the neutrino cross section must be known, and the detector efficiency must be understood. Any assumptions in the neutrino oscillation model must also be well tested. If any of these components is not well modelled, the final oscillation measurement may be biased. Large uncertainties on any of these components will limit the sensitivity of an experiment.

This dissertation investigates two possible limiting factors for the precision of neutrino oscillation measurements. The main focus is on cross section systematics, which are a large and difficult to reduce uncertainty, particularly for Charged-Current Quasi-Elastic (CCQE) interactions, which is the main signal channel at T2K and other accelerator experiments. Short baseline oscillations, mediated by sterile neutrinos, could seriously bias neutrino oscillation measurements which assume the three-neutrino mixing framework. Constraining sterile oscillations is further complicated by the current uncertainties in cross section measurements (as is obvious from Equation 1.14).

The structure of this thesis is as follows:

- In Chapter 2, a theoretical introduction to neutrino cross sections is given, and the current status of cross section measurements is reviewed.
- In Chapter 3, an overview of the T2K experiment is given. Brief overviews of two other experiments, MiniBooNE and MINERvA are also given as data from both experiments are used extensively in later chapters.
- In Chapter 4, published MiniBooNE data is used to constrain the 3+1 sterile neutrino model.
- Chapter 5 decribes a fit to published CCQE data which is used to produce cross section systematics for T2K analyses.
- Chapter 6, details the implementation and validation of the Effective Spectral Function model for CCQE scattering into NEUT, T2K's primary neutrino interaction generator.

- In Chapter 7, the work of the preceeding analysis chapters is put into context with a detailed description of the general T2K oscillation analysis strategy, with particular emphasis on the importance of cross section model constraints.
- Finally, Chapter 8 contains some concluding remarks.

Chapter 2

Neutrino scattering

This chapter provides a background to neutrino scattering, which is essential to put future chapters in context. In Section 2.1, all of the ingredients of a neutrino interaction model are described. In Section 2.2, the formalism for neutrino scattering cross sections is discussed, with particular attention paid to Charged-Current Quasi-Elastic (CCQE) and Neutral-Current Elastic (NCEL) scattering, which are the interaction models of most interest to this thesis. Section 2.3 provides a review of available cross section measurements. Finally, Section 2.4 discusses new theoretical models for CCQE interactions which have recently been developed to try and explain discrepancies in the experimental data.

2.1 Neutrino interaction model

A complete neutrino-nucleus interaction model involves a number of different ingredients: a nuclear model, describing the initial state of nucleons within the nucleus; a cross section model, describing the interaction of the neutrino with some component of the nucleus; and a model to relate the products of the initial interaction to the experimentally observable particles emerging from the nucleus, which will be referred to as a Final State Interaction (FSI) model throughout this work. Note that the terminology for the final component can vary: sometimes "FSI" is used to refer to nuclear corrections to the initial interaction, and FSI as defined here are then referred to as subsequent interactions.

The work presented in this dissertation uses and develops the interaction models in two Monte Carlo (MC) neutrino interaction generators: NEUT [166], the official generator of the Super-Kamiokande and T2K collaborations; and GENIE [167], which is widely used by the neutrino scattering and oscillation communities. In this section, special consideration is given to the neutrino interaction models used in these two generators.

2.1.1 Nuclear model

Early neutrino experiments used hydrogen or deuterium targets to measure neutrino-nucleon interaction rates. Modern experiments typically use heavier and cheaper target materials such as carbon and oxygen to increase statistics and reduce safety concerns. As the nucleus is a complicated environment, a nuclear model is required to describe the initial state of the nucleons within the nucleus. These nuclear models are generically referred to as spectral function models.

The impulse approximation, where the neutrino interaction is with a single nucleon, is also currently assumed by many neutrino MC generators. Models which go beyond the impulse approximation and which are currently available in MC generators will be discussed in more detail in Section 2.4.

A simple and commonly used spectral function model which uses the impulse approximation is the Relativistic Fermi Gas (RFG) model, where nucleons within the nucleus are treated as non-interacting fermions and all possible momentum states are filled up to the Fermi momentum, p_{F}. The probability $P_{RFG}(|\vec{p}|, E)$ of finding a nucleon with three-momentum $\vec{p}$ and energy E is described by

$$P_{RFG}(|\vec{p}|, E) = \frac{6\pi^2 A}{p_{\mathrm{F}}^2}\Theta(p_{\mathrm{F}} - |\vec{p}|)\delta(\Delta E), \tag{2.1}$$

where A is the number of nucleons within the nucleus, $\Delta E = E_p - E_b + E$ with E_p being the energy of the proton and E_b the binding energy, which is constant for each nucleus. Note that as all momentum states are filled, outgoing nucleons with a momentum less than the Fermi momentum are Pauli blocked. Values for p_{F} and E_b are obtained through fits to electron scattering data [168].

2.1.2 Cross section model

At the few-GeV energies which are of interest to accelerator neutrino experiments, the main neutrino–nucleus interaction processes can be divided into a number of categories. A recent review of generator and theoretical model predictions is given in [169], which gives an interesting insight into how diverse the predictions can be.

For interactions which can be treated as two-body scattering between a neutrino and a nucleon, the Feynman diagram shown in Figure 2.1 applies, where k and k' denote the incoming and outgoing leptons, and p and p' denote the incoming and outgoing nucleon respectively. The variables which feature in neutrino cross section calculations, and which are measured by experimentalists, are: the energy transfer, $\omega = E_\nu - E_{l'}$; the

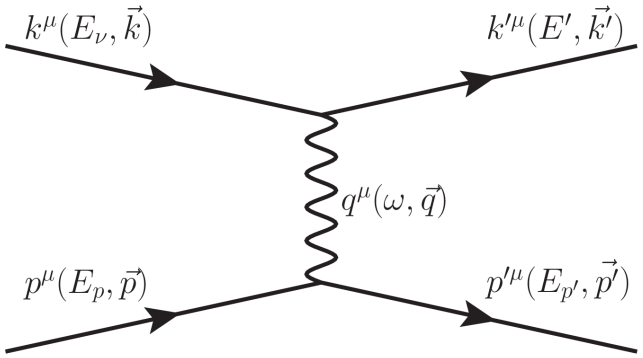

FIGURE 2.1: Feynman diagram for two-body scattering between a neutrino and a nucleon. The four-vector naming convention is as follows: the incoming neutrino, k^μ; the outgoing lepton, k'^μ; the initial state nucleon, p^μ; and the final state nucleon, p'^μ.

four-momentum transferred, $Q^2 = -q^2$, where $q = k - k'$; and the angle between the outgoing lepton and the incoming neutrino, which can be calculated with the equation $\cos\theta = \frac{\vec{k}\cdot\vec{k'}}{|\vec{k}||\vec{k'}|}$. The four-vector labelling convention used in Figure 2.1 is used throughout this chapter.

2.1.2.1 CCQE and NCEL scattering

In these interactions, the neutrino scatters off a nucleon within the nucleus, rather than a constituent quark of the nucleon. In CCQE interactions, the incoming and outgoing particles are different (so it is not an elastic interaction):

$$\nu_l + n \to l^- + p \qquad \bar{\nu}_l + p \to l^+ + n \tag{2.2}$$

In NCEL interactions, there is no change of particle type, and both neutrinos and antineutrinos can interact with protons and neutrons:

$$\begin{aligned} \nu_l + n &\to \nu_l + n & \bar{\nu}_l + n &\to \bar{\nu}_l + n \\ \nu_l + p &\to \nu_l + p & \bar{\nu}_l + p &\to \bar{\nu}_l + p \end{aligned} \tag{2.3}$$

Note that $\overline{\nu}_\mu$ and $\overline{\nu}_\tau$ CCQE interactions have a non-zero threshold energy because the invariant mass of the final state is greater than that of the initial state, whereas NCEL have no reaction threshold for free nucleons. Interactions on bound nucleons can be Pauli blocked, so in the RFG model there is a non-zero reaction threshold for all processes.

These are the dominant charged and neutral current reactions in the few-GeV region so are of particular importance to this thesis and will be discussed in much more detail in Section 2.2.

2.1.2.2 Resonance production

Inelastic neutrino interactions with the nucleon as a whole produce a baryon resonance, which then decays to produce mesons and hadrons. Both GENIE and NEUT use the Rein-Sehgal model [170], which considers 18 resonances with invariant mass $W \leq 2$ GeV, and also considers multi-pion production[1].

The dominant CC and NC resonant processes listed in Equations 2.4 and 2.5 respectively come from the production of the lowest lying $\Delta(1232)$ resonances. These resonances quickly decay, predominantly into final states containing a pion and a nucleon [2].

$$\begin{aligned} \nu_l + p &\rightarrow l^- + \Delta^{++} & \nu_l + n &\rightarrow l^- + \Delta^+ \\ \bar{\nu}_l + p &\rightarrow l^+ + \Delta^0 & \bar{\nu}_l + n &\rightarrow l^+ + \Delta^- \end{aligned} \tag{2.4}$$

$$\begin{aligned} \nu_l + p &\rightarrow \nu_l + \Delta^+ & \nu_l + n &\rightarrow \nu_l + \Delta^0 \\ \bar{\nu}_l + p &\rightarrow \bar{\nu}_l + \Delta^+ & \bar{\nu}_l + n &\rightarrow \bar{\nu}_l + \Delta^0 \end{aligned} \tag{2.5}$$

Although pions are the only mesons considered in the Rein-Sehgal model, the formalism is modified in NEUT to include photon, kaon and eta[2] resonant production [166].

2.1.2.3 Coherent scattering

These are interactions where the neutrino scatters from the nucleus as a whole, and the nucleus is left in its ground state after the interaction. Both NC and CC coherent interactions are possible. Neutrino interaction generators (including GENIE and NEUT) typically simulate coherent scattering with the Rein-Sehgal coherent model [41, 42].

$$\begin{aligned} \nu_l + A &\rightarrow \nu_l + A + \pi^0 & \bar{\nu}_l + A &\rightarrow \bar{\nu}_l + A + \pi^0 \\ \nu_l + A &\rightarrow l^- + A + \pi^+ & \bar{\nu}_l + A &\rightarrow l^+ + A + \pi^- \end{aligned} \tag{2.6}$$

2.1.2.4 Deep Inelastic Scattering (DIS)

In deep inelastic scattering, the neutrino interacts with a constituent quark within the nucleon, N, thus breaking apart the nucleon and generally producing a jet of hadrons. Both NC and CC interactions can occur. Whilst DIS events are easy to visualise, and DIS models are relatively well validated by the greater availability of high energy (as opposed

[1] GENIE only uses the 16 resonances which are deemed to be unambiguous by the Particle Data Group [2].

[2] Note that only η production is considered, η' production is not simulated in NEUT.

to few-GeV) neutrino data, the modelling of these events can be particularly difficult for experiments at intermediate energies. The transition between resonant production and DIS events is at the limit of validity for cross section models of both interaction types, and there is the possibility for overlap between the models. DIS reactions are generically described by Equation 2.7, where X represents the hadronic system (of multiple particles).

$$\begin{aligned} \nu_l + N &\rightarrow \nu_l + X & \bar{\nu}_l + N &\rightarrow \bar{\nu}_l + X \\ \nu_l + N &\rightarrow l^- + X & \bar{\nu}_l + N &\rightarrow l^+ + X \end{aligned} \tag{2.7}$$

2.1.3 Final State Interactions (FSI)

Particles produced in the nuclear environment have a nonzero probability of interacting with the nuclear medium, and indeed with other particles produced by the same initial interaction. Modelling these processes is extremely difficult, and only a flavour of the problem will be given here.

Most neutrino interaction generators use a cascade model [169], where each particle coming out of the vertex is treated independently and is moved through the nucleus in discrete steps. The interaction probability is determined at each step based on the local nuclear density until the final particles exit the nuclear medium. Interactions between the interaction products are neglected because of the complexity of solving many-body problems. The notable exception is GiBUU [171], which uses coupled transport equations to propagate all interaction products out of the nuclear medium. The computational cost of this sort of approach is predictably severe, and therefore GiBUU is restricted to generator level studies, but it provides a valuable benchmark as the cutting edge in understanding FSI effects.

Cascade models are used by both NEUT [166] and GENIE [167, 172] although there are some differences between the implementations. Both use a Woods-Saxon distribution [173] to model the nuclear density and simulate the reinteractions of pions and nucleons, which are treated differently[3]. Note that outgoing leptons are not affected by FSI, as they do not participate in strong interactions. The interactions considered for both pions and nucleons are elastic and inelastic scattering, charge exchange, absorption and pion production (although NEUT only considers a subset of these), the probabilities for which are tuned to data [174]. At each step in the cascade, the probability of any interaction occurring is calculated based on the density of the nucleus and the energy of the hadron, and a random number is generated to determine if an interaction

[3] NEUT also considers kaon and eta reinteractions, using a similar procedure as for pions [166].

occurred. If an interaction occurred, the type of interaction is selected based on their relative probability, the interaction is simulated, and the outgoing particles (including daughter particles) from this secondary interaction are entered into the cascade from the secondary vertex[4]. If no interaction occurred, the particle is moved by another step. The process is repeated until all particles in the cascade exit the nucleus.

It is known that particle interaction cross sections are suppressed during the hadronisation process [175]. This *formation zone* is approximated as a free step without interactions at the start of the cascade (the initial position of hadrons produced in the initial interaction is not at the neutrino interaction point). Both GENIE and NEUT employ a formation zone where the initial step size is based on results from the SKAT experiment [21]. NEUT currently only uses a formation zone for hadrons produced in deep inelastic scattering, whereas GENIE uses the formation zone for all channels.

The possibility for charge exchange and pion reabsorption, as well as additional pion production, make measurements of pion production cross sections on heavy nuclear targets extremely difficult as only the final state particles can be measured. Any attempts to relate the final states observed to the underlying cross sections are necessarily model dependent. FSI are possibly the most challenging aspect of neutrino interaction modelling.

2.2 Neutrino scattering cross section

The neutrino scattering cross section can generically be written, for a CC process, as $\nu_l + A \to l^- + X$ where the neutrino has four-momentum $k = (E_\nu, \vec{k})$, the outgoing lepton has four-momentum $k' = (E_l, \vec{k'})$, and the initial and final state nucleon four-momenta are $p = (E_p, \vec{p})$ and $p' = (E_{p'}, \vec{p'})$ respectively [176]:

$$\sigma = \int d^3p \int dE \int d^3k' \; P(\vec{p}, E_b) \frac{G_{\mathrm{F}}^2 \cos^2 \vartheta_C}{8\pi^2 E_\nu E_\mu E_{p'} E_p} L_{\mu\nu} H^{\mu\nu} \delta(\omega - M_{p'} - E_b - E_{p'}), \quad (2.8)$$

where G_{F} is the Fermi constant and ϑ_{C} is the Cabibbo angle. $P(\vec{p}, E_b)$ is a spectral function describing the probability of the initial state nucleon having momentum $\vec{p}$ and binding energy E_b. Note that spectral functions may depend on different variables (for example, the RFG spectral function given in Equation 2.1). The cross sections for NC processes $\nu_l + A \to \nu_l + X$ are given by a similar expression to Equation 2.8, with the factor $\cos^2 \vartheta_C$ omitted. The details of the leptonic and hadronic tensors $L_{\mu\nu}$ and $H^{\mu\nu}$ depend on the process in question: for details see Reference [176].

[4] GENIE has two cascade models, one where outgoing particles are re-entered into the cascade, and another where only particles from the primary vertex participate in the cascade, and are only permitted one re-interaction [172].

2.2.1 Charged-Current Quasi-Elastic (CCQE) differential cross section

The CCQE neutrino–nucleon differential cross section for free nucleons as a function of the four-momentum transfer squared, Q^2, can be expressed using the Llewellyn-Smith formula [177]:

$$\frac{d\sigma}{dQ^2}\begin{pmatrix}\nu_l + n \to l^- + p \\ \bar{\nu}_l + p \to l^+ + n\end{pmatrix} = \frac{M^2 G_{\mathrm{F}}^2 \cos^2\vartheta_C}{8\pi E_\nu^2}\left[A(Q^2) \pm B(Q^2)\frac{(s-u)}{M^2} + C(Q^2)\frac{(s-u)^2}{M^4}\right], \tag{2.9}$$

where M is the mass of the nucleon, G_{F} is Fermi's constant, ϑ_C is the Cabibbo angle, E_ν is the incoming neutrino energy, and s and u are the Mandelstam variables.

The functions $A(Q^2)$, $B(Q^2)$ and $C(Q^2)$ are given in terms of the vector ($F_V^{1,\,2}$), axial (F_A) and pseudoscalar (F_P) nucleon form factors:

$$\begin{aligned} A(Q^2) = \frac{(m_l^2 + Q^2)}{M^2}\Bigg[&(1+\tau)F_A^2 - (1-\tau)(F_V^1)^2 \\ &+ \tau(1-\tau)(\xi F_V^1)^2 + 4\tau(F_V^1 \xi F_V^2) \\ &- \frac{m_l^2}{4M^2}\left((F_V^1 + \xi F_V^2)^2 + (F_A + 2F_P)^2 - 4(1+\tau)F_P^2\right)\Bigg], \end{aligned} \tag{2.10}$$

$$B(Q^2) = \frac{Q^2}{M^2}F_A(F_V^1 + \xi F_V^2), \tag{2.11}$$

$$C(Q^2) = \frac{1}{4}\left(F_A^2 + (F_V^1)^2 + \tau(\xi F_V^2)^2\right). \tag{2.12}$$

where $\tau = \frac{Q^2}{4M^2}$, $\xi = (\mu_p - \mu_n) - 1$, m_l is the outgoing lepton mass and μ_p, μ_n are the proton and neutron magnetic moments.

Note that $B(Q^2)$ (Equation 2.11) contains the interference between the axial and vector currents, and that it is this term which is responsible for the Q^2 dependent difference between the $\nu_l + n \to l^- + p$ and $\bar{\nu}_l + p \to l^+ + n$ cross sections. At $Q^2 = 0$, there is no difference between the CCQE cross sections for neutrinos and antineutrinos.

Although this formalism is instructive, modern experiments on heavy nuclear targets use the RFG model to describe the initial state of the nucleons within the nucleus. For the full CCQE cross section calculation in this framework, see References [78, 178][5]. For more complex spectral functions, it is not possible to express the cross section in terms of such simple functions, but Equation 2.8 is still valid.

[5] An interesting historical aside is that one of the authors of the RFG model for CCQE, Ernest Moniz, is the 13th and current United States Secretary of Energy.

2.2.2 Nucleon form factors

Nucleons are not point particles, but are composed of a sea of quarks and gluons, so a method for describing their spatial extent is necessary. Dipole form factors assume an exponential charge distribution for the nucleon, $\rho(r) = \rho_0 \exp(-Mr)$, and are the Fourier transform of that distribution. However, this approximation only works for low Q^2 when the recoil of the nucleon can be neglected; when the probe has a higher momentum, the nucleon recoil is also described by the form factors and this simple interpretation breaks down [179].

2.2.2.1 Vector form factors

Because vector current is conserved, the vector form factors $F_V^{1,\,2}$ can be related to the electromagnetic form factors measured in electron–nucleon elastic scattering experiments [180]:

$$\begin{aligned} F_V^1(Q^2) &= \frac{G_E^V(Q^2) + \tau G_M^V(Q^2)}{1+\tau} \\ \xi F_V^2(Q^2) &= \frac{G_M^V(Q^2) - G_E^V(Q^2)}{1+\tau} \end{aligned} \tag{2.13}$$

where G_E^V and G_M^V are a linear combination of the proton and neutrino electric and magnetic form factors:

$$\begin{aligned} G_E^V(Q^2) &= G_E^p(Q^2) - G_E^n(Q^2) \\ G_M^V(Q^2) &= G_M^p(Q^2) - G_M^n(Q^2). \end{aligned} \tag{2.14}$$

These form factors are expressed in terms of dipoles, with values at $Q^2 = 0$ of:

$$G_E^p(0) = 1, \tag{2.15}$$

$$G_E^n(0) = 0, \tag{2.16}$$

$$G_M^p(0) = \mu_p, \tag{2.17}$$

$$G_M^n(0) = \mu_n, \tag{2.18}$$

The final expressions for the vector form factors are:

$$F_V^1(Q^2) = \frac{1 + \tau(\mu_p - \mu_n)}{(1+\tau)\left(1 + \frac{Q^2}{M_V^2}\right)^2},$$
$$F_V^2(Q^2) = \frac{\mu_p - \mu_n - 1}{(1+\tau)\left(1 + \frac{Q^2}{M_V^2}\right)^2}. \tag{2.19}$$

where $M_V^2 = 0.71$ GeV^2 is an empirical parameter extracted from electron scattering data [181, 182].

Although this dipole approximation works well for $Q^2 \leq 2.0$ GeV^2, high statistics electron scattering measurements have shown some deviations at higher Q^2. These discrepancies are parametrised by a number of fitting groups [179, 183, 184]. The BBA03 [180], BBBA05 [183] and BBBA07 [185] form factors (an initialism of the authors Bodek, Budd, Bradford and Arrington and the year of the release), are used widely in the neutrino community. These form factors have been used in the work described in this thesis.

2.2.2.2 Axial form factor

Conventionally, the axial form factor has been parametrised with a dipole form factor by analogy with the vector form factors, so is usually expressed as

$$F_A(Q^2) = \frac{g_A}{\left(1 + \frac{Q^2}{M_A^2}\right)^2}, \tag{2.20}$$

where M_A is the axial mass and g_A is the axial coupling constant. The latter is measured by β decay measurements [2] to be $g_A = -1.272 \pm 0.002$, leaving the former as the only parameter left relatively unconstrained in the Llewellyn-Smith CCQE cross section model [177]. The axial mass is well measured by fits to the Q^2 shape of ν_μ–H_2 and ν_μ–D_2 bubble chamber measurements as well as pion electroproduction data. A recent fit to these datasets found $M_A = 1.014 \pm 0.014$ GeV [185]. The value of M_A has recently become the subject of much discussion in the neutrino cross section community due to discrepancies found between heavy target neutrino scattering data in the few-GeV region and the bubble chamber measurements on light targets, which will be discussed in Sections 2.3 and 2.4.

Although the axial form factor is not as well studied as the vector form factors, fits have been performed to the complete dataset of bubble chamber results and a correction to the dipole approximation to fit high Q^2 data has been produced [185]. Unlike the non-dipole corrections to the vector form factors, the non-dipole correction to the axial form factor

has not been widely adopted in the neutrino community. It is also interesting to note that some early bubble chamber experiments experimented with drastically different forms for the axial form factor [25, 36].

2.2.2.3 Pseudoscalar form factor

The pseudoscalar form factor describes the single pion exchange (pion pole) contribution to the cross section. It is related to the axial form factor using the partial conservation of axial current hypothesis, that the axial current is conserved in the limit $m_\pi \to 0$. The pseudoscalar form factor is expressed [186]:

$$F_P(Q^2) = \frac{2M^2}{Q^2 + m_\pi^2} F_A(Q^2). \tag{2.21}$$

2.2.3 Neutral-Current Elastic (NCEL) differential cross section

This section follows References [76, 187]. The same Llewellyn-Smith formalism used for CCQE scattering from free nucleons can be applied to NCEL scattering, using different form factors. Equations 2.9, 2.10, 2.11 and 2.12 still apply, although the pseudoscalar form factor can now be neglected from $B(Q^2)$ because it only appears with a $\frac{m_l^2}{M^2}$ term, and Equation 2.9 is divided by $\cos^2\vartheta_C$. The vector form factors appropriate for NCEL are given by

$$\begin{aligned}
F^1_{V,\,Z}(Q^2) &= \left(\frac{1}{2} - \sin^2\vartheta_W\right)\tau_3 F^1_V(Q^2) - \sin^2\vartheta_W \left[\frac{1+\tau(\mu_p+\mu_n)}{(1+\tau)\left(1+\frac{Q^2}{M_V^2}\right)^2}\right] - \frac{F^1_s(Q^2)}{2}, \\
F^2_{V,\,Z}(Q^2) &= \left(\frac{1}{2} - \sin^2\vartheta_W\right)\tau_3 F^2_V(Q^2) - \sin^2\vartheta_W \left[\frac{\mu_p+\mu_n-1}{(1+\tau)\left(1+\frac{Q^2}{M_V^2}\right)^2}\right] - \frac{F^2_s(Q^2)}{2},
\end{aligned} \tag{2.22}$$

where $F^1_s(Q^2)$ and $F^2_s(Q^2)$ are contributions from strange quarks. Strong constraints on these contributions have been set by parity violating electron scattering experiments [188], which are consistent with 0, so these form factors are omitted from most analyses of NCEL neutrino–scattering data [35, 77].

The axial form factor has an additional term for NCEL which is generally assumed to have a dipole form [189]:

$$F_A(Q^2) = \frac{g_A \tau_3}{2\left(1 + \frac{Q^2}{M_A^2}\right)^2} - \frac{\Delta s}{2\left(1 + \frac{Q^2}{M_A^2}\right)^2} \tag{2.23}$$

where M_{A} is the same axial mass as for CCQE and Δs is the strange quark contribution to the spin of the nucleon, and can be constrained by neutrino-nucleon scattering experiments [77, 190, 191].

2.3 Status of cross section measurements

The available data on CC-inclusive cross section measurements are shown in Figure 2.2 as a function of incoming neutrino energy, E_ν, for ν_μ and $\bar{\nu}_\mu$ scattering. At high energies, where DIS interactions dominate the cross section, there is a linear dependence between the neutrino energy and the cross section. At lower energies, where CCQE and resonant interactions make large contributions (as a rough guide, $E_\nu \leq 10$ GeV), this dependence is broken. Other datasets are available with specific final states, as well as differential cross section measurements; for an up to date summary, see Reference [2]. Additional CC-inclusive measurements exist [22, 192], but are not published as a function of E_ν to avoid dependence on the nuclear model used by the experiment. Increasingly, modern experiments with heavy nuclear targets prefer to give flux-averaged cross section results, differential in some model-independent reconstructed variable[6], rather than differential cross sections as a function of E_ν. They also provide their neutrino flux prediction so that their results can be tested with various models. As a result, it is difficult to put all modern cross section measurements on the same figure as older bubble chamber datasets, or indeed with other modern cross section measurements.

There is no comparable plot showing the CC-inclusive cross section for other neutrino flavours because of the difficulty in producing beams of these other flavours with accelerators. That said, T2K has recently made two measurements of the ν_e CC-inclusive cross section [193, 194] and will make a $\bar{\nu}_e$ measurement in the future. There is also no comparable NC-inclusive plot for any flavour because the data are much more sparse, and there are obvious difficulties with energy reconstruction when the outgoing lepton is unmeasured.

[6] Of course, this is not true of all experiments as is clear from Figure 2.2, and most modern experiments produce at least a single data point in E_ν, produced by averaging over the energy distribution of their neutrino flux.

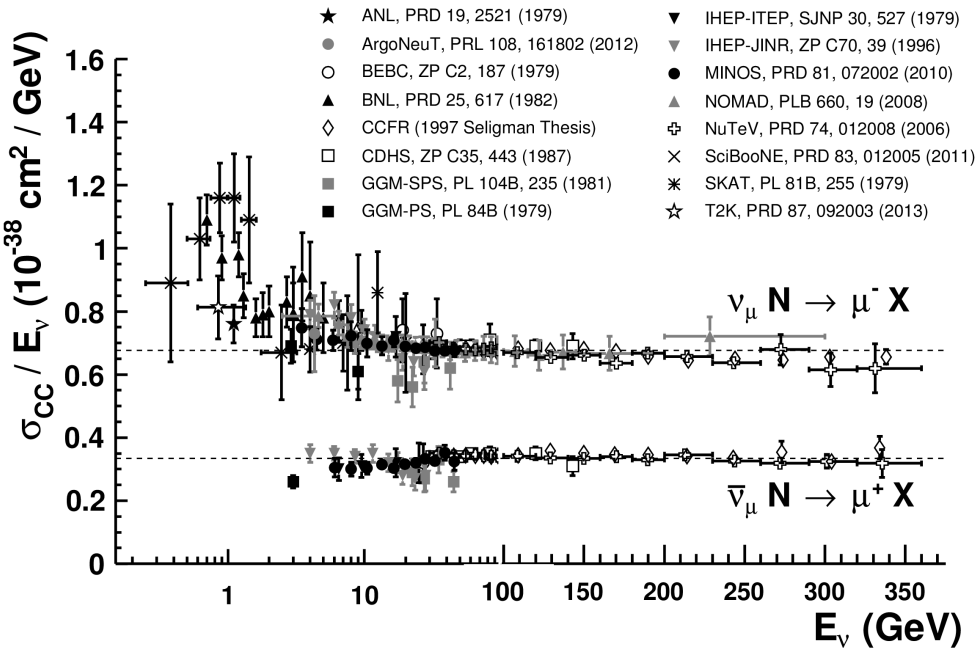

FIGURE 2.2: All available data on ν_μ and $\bar{\nu}_\mu$ CC-inclusive cross sections reproduced from Reference [2]. The data is shown divided by the neutrino energy, as a function of neutrino energy. Note that the x-axis scale changes from logarithmic to linear at 100 GeV. The data are from References [7–22].

All data available as a function of E_ν for ν_μ and $\bar{\nu}_\mu$ CCQE scattering are summarised in Figure 2.3. The NUANCE predictions shown are representative of MC generators which use the Smith-Moniz RFG (for nuclear targets) and Llewellyn-Smith (for free nucleons) cross section models with a value of M_A constrained by bubble chamber and pion electroproduction data. There is reasonably good agreement between high energy data on all targets, and low energy data collected on hydrogen and deuterium targets, but it is clear that MiniBooNE does not fit the rest of the data, particularly for the neutrino measurement [34, 195, 196].

This disagreement is known as the MiniBooNE large axial mass anomaly because the axial mass is the only parameter in the RFG CCQE model without strong constraints from electron scattering experiments, and to find agreement with their data, MiniBooNE had to inflate the axial mass considerably, finding $M_A = 1.35 \pm 0.17$ GeV. Although the effect is named after MiniBooNE, there are a number of other experiments using heavy nuclear targets which also required large axial mass values to fit their data (K2K [197], MINOS [198], T2K [199, 200]), but which did not produce a cross section as a function of E_ν so are not included on Figure 2.3[7]. It should be noted that the MiniBooNE

[7] Both T2K CCQE measurements did produce cross sections as a function of E_ν with a limited number of bins, but have not been included in Figure 2.3.

antineutrino mode CCQE analysis also found a higher axial mass when fitting the double-differential distribution [35] with the RFG model, which is not obvious from Figure 2.3.

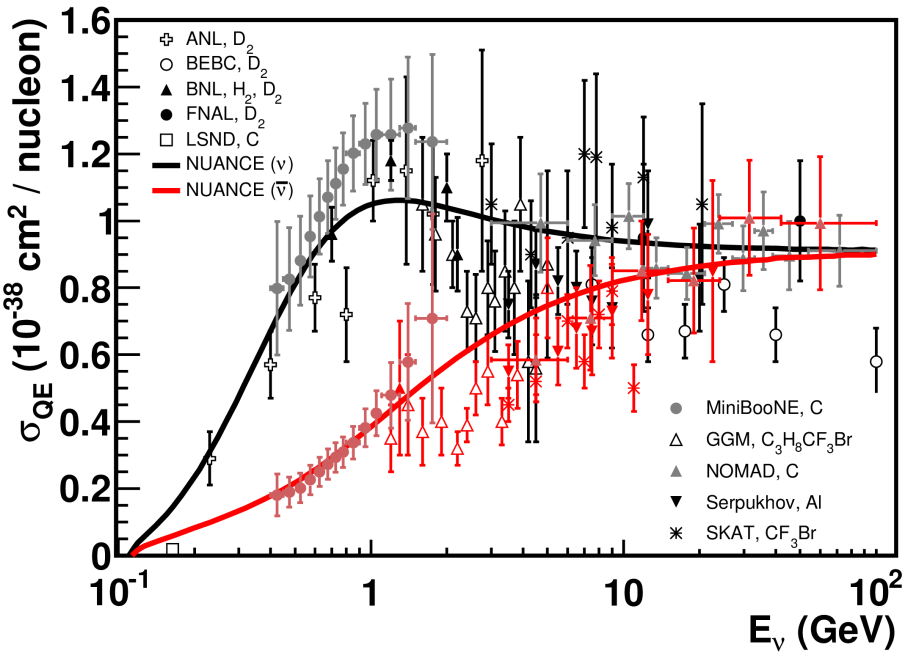

FIGURE 2.3: All available data on ν_μ and $\bar{\nu}_\mu$ CCQE cross sections reproduced from Reference [2]. The data are taken from References [23–35]. The data is shown as a function of neutrino energy. Black points represent ν_μ data, red points represent $\bar{\nu}_\mu$ data.

The large axial mass anomaly and its impact on oscillation experiments is the main focus of this dissertation. In Chapter 4, the impact that a large cross section uncertainty has on short baseline oscillation results is discussed in the context of a fit to MiniBooNE data. A lot of recent theoretical work has gone into developing new CCQE cross section models which can account for the discrepancy between free nucleon and heavy target results with nuclear effects. A brief overview of these models will be given in Section 2.4. The implementation of some of these models into NEUT, T2K's primary generator, and the use of these models to constrain cross section systematics in the T2K oscillation analyses is one of the principal topics of this thesis, and will be discussed in more detail in Chapter 5.

As for CC-inclusive measurements, the data on ν_e CCQE scattering is limited, although some differential distributions have been published recently by MINERνA [201]. NCEL measurements are also limited, but differential cross sections have been published by BNL E734 [190] and MiniBooNE [77, 191]. There are also a series of historical measurements of the ratio between NCEL and CCQE, which are summarised in [202]. Note that the MiniBooNE NCEL measurements also prefer an increased value of M_A.

The experimental situation with resonant pion production is similar to that of CCQE and NCEL. There is an axial mass parameter, $M_{\mathrm{A}}^{\mathrm{RES}}$, which is well constrained by bubble chamber measurements of single pion production [203] to be $M_{\mathrm{A}}^{\mathrm{RES}} = 1.12 \pm 0.03$ GeV, but which does not agree with data taken on heavy nuclear targets [204–208]. Comparisons of heavy nuclear target data with model predictions can be found in References [209–211]. Single pion production measurements are far more sensitive to FSI effects than CCQE, which makes development of new theoretical models to account for these discrepancies much more challenging as FSI effects can generally only be included with a full MC simulation.

An additional and longstanding problem for modelling single pion production has been the discrepancy between the Argonne (ANL) [36] and Brookhaven (BNL) [37] cross section measurements for the dominant single pion production channel $\nu_\mu + p \rightarrow \mu^- + p + \pi^+$ using deuterium and hydrogen as a target. It can be seen from Figure 2.4a that these measurements disagree by 20–30% at ∼1 GeV, the region of interest for modern neutrino oscillation experiments, where there are no other measurements. Although the data had been found to be consistent given the flux normalisation uncertainties quoted by both experiments [211–213], the discrepancy led to increased uncertainties in the T2K cross section model[8]. A simple reanalysis of the ANL and BNL data which removed the flux uncertainty by taking ratios with the well understood (on deuterium) CCQE channel found good agreement between ANL and BNL data [40]. The extracted cross sections from this analysis are shown in Figure 2.4b.

Bubble chamber measurements for the other charged-current single production channels $\nu_\mu + n \rightarrow \mu^- + n + \pi^+$ and $\nu_\mu + n \rightarrow \mu^- + p + \pi^0$ are also available, and these are important for current oscillation analysis experiments. For a review of the data available, see References [2, 202]. Additionally, limited statistics cross section data is available for antineutrino charged-current pion production and some neutral-current channels (for both ν_μ and $\bar{\nu}_\mu$), and some measurements of multi-pion production cross sections are available from the same references. Pion production cross section measurements are exclusively made using $^{(}\overline{\nu}_\mu^{)}$ beams, so there are no measurements available for other neutrino flavours.

A summary of coherent pion production as a function of E_ν is given in Figure 2.5 for both ν_μ and $\bar{\nu}_\mu$. The GENIE and NEUT predictions show significant differences[9], and

[8] The effect that the reanalysis had on the T2K systematic uncertainties is discussed in Chapter 7.

[9] Although NEUT and GENIE use the same Rein-Sehgal coherent cross section model [41, 42], it strongly depends on pion-nucleon scattering cross sections $\sigma(\pi A \rightarrow \pi A)$, which have large uncertainties at low energy. NEUT uses the pion-nucleon scattering cross sections given in the first Rein-Sehgal coherent model paper [41], whereas GENIE use an updated set of pion-nucleon scattering inputs (though the details of the experimental data used have not been made clear). For a broader discussion of the tunable parameters in the Rein-Sehgal coherent model and the generator differences, see Reference [214].

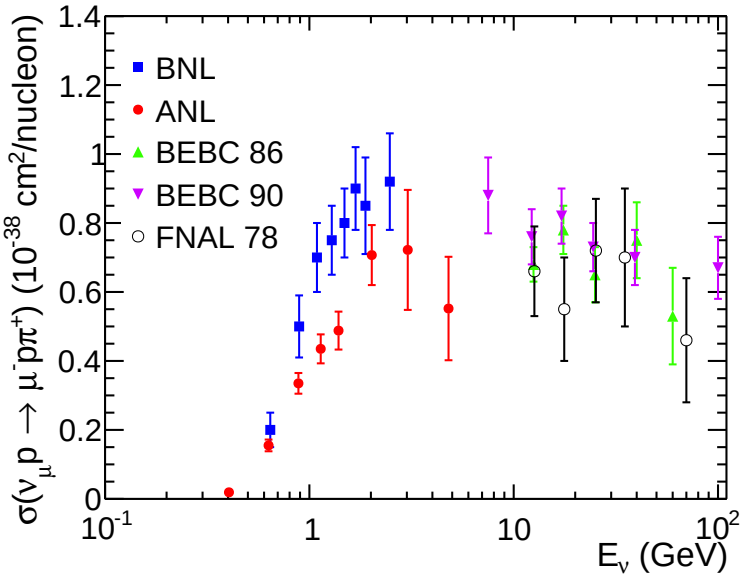

(A) Published

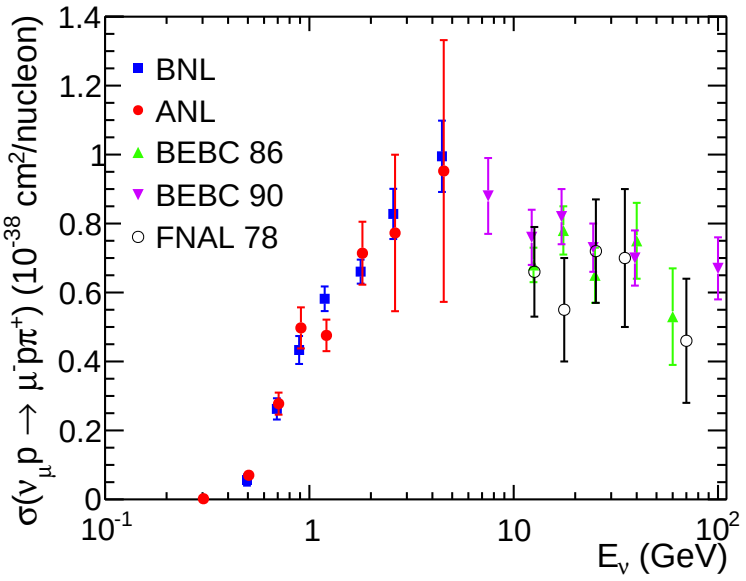

(B) Reanalysis

FIGURE 2.4: The published and extracted ANL [36] and BNL [37] data are compared with other measurements of $\nu_\mu + p \to \mu^- + p + \pi^+$ on hydrogen or deuterium targets [24, 38,39]. Note that the ANL and BNL data have no invariant mass cut, whereas the other datasets have an invariant mass cut of $W \leq 2\,\text{GeV}$. This figure has been reproduced from Reference [40].

some of the experimental results are in tension with each other. The tension is particularly apparent for neutrinos at low energies, where the K2K and SciBooNE upper limits disagree with MINERνA data. The latest coherent pion production results from MINERνA also show that there are significant discrepancies between data and generator predictions for the pion energy and angle with respect to the incoming neutrino beam [43]. There are a number of measurements of neutral-current coherent scattering, as well as additional measurements of NC and CC coherent scattering given as ratios with other channels; for a summary, see References [2, 202]. A lot of theoretical and generator work is ongoing to improve the model of coherent scattering in light of data; some of the models considered are listed in References [2, 202].

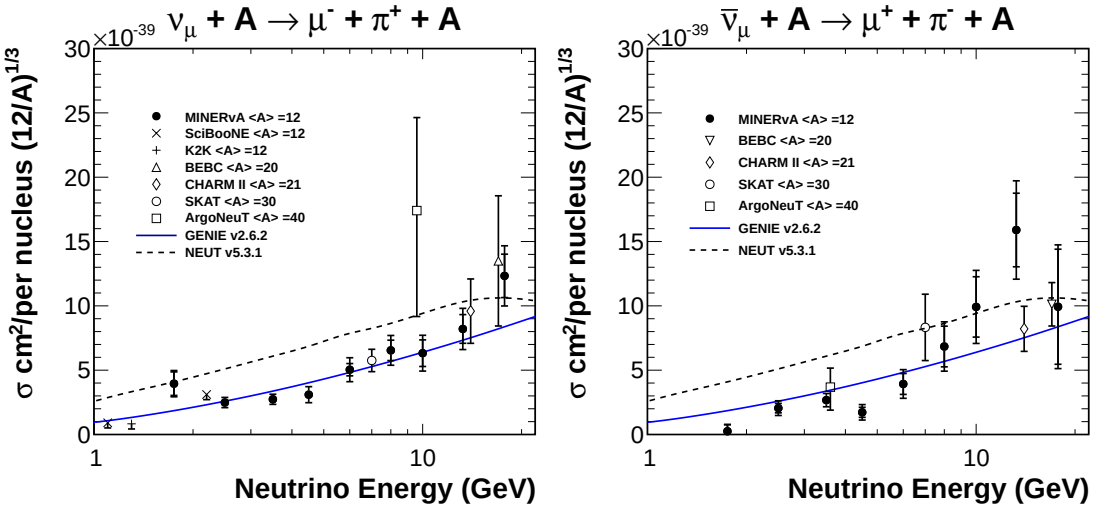

(A) Neutrino (B) Antineutino

FIGURE 2.5: Charged-current coherent pion production cross section data on a variety of targets, scaled to match carbon target data using the predicted $A^{\frac{1}{3}}$ dependence [41, 42]. Both figures have been reproduced from Reference [43] where the MINERνA data points are presented, the other data is taken from References [44–50]. Note that the SciBooNE [44] and K2K [45] measurements are upper limits given to 90% confidence.

2.4 CCQE cross section model development

This section aims to give a broad overview of the new theoretical models for CCQE neutrino–nucleus scattering which are of particular interest as they may explain the large axial mass anomaly. Some of these models have been implemented in NEUT, and are used in fits to CCQE data in Chapter 5, where details of the NEUT implementation have also been given. Comparisons are drawn with the RFG model described in Section 2.1.1, which has been the standard nuclear model used by experimentalists for decades. This overview is certainly not exhaustive, and is focused on the models which are currently implemented in neutrino interaction generators. Exhaustive descriptions and model

comparisons are available in recent review articles [53,202,215], from which much of this discussion is drawn.

2.4.1 Nuclear models

The Local Fermi Gas (LFG) is an improvement on the RFG model, where the Fermi momentum is modified based on the local proton or neutron density of the nucleus [53]:

$$p_{\mathrm{F}}^{p,n}(r) = \left[3\pi^2 \rho_{p,n}(r)\right]^{\frac{1}{2}}, \tag{2.24}$$

where $\rho_{p,n}$ is the local density of protons or neutrons, and r is the distance from the centre of the nucleus. As for the RFG model, the probability of finding a nucleon in a particular initial state using the LFG model is governed by Equation 2.1, after making the substitution $p_{\mathrm{F}} \to p_{\mathrm{F}}^{p,n}(r)$.

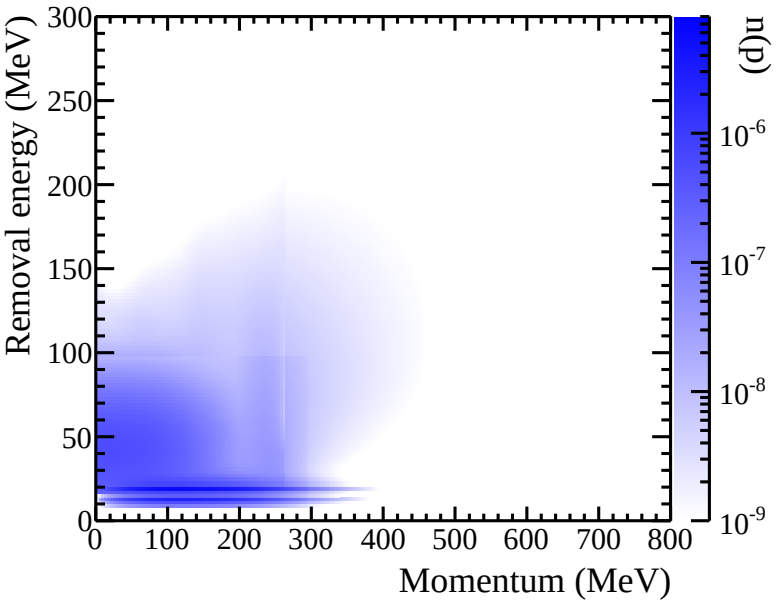

FIGURE 2.6: The probability distribution for initial state protons within an oxygen nucleus for Benhar's Spectral Function model [51]. The SF is normalised such that the integral of this distributions is 1.

Although a Spectral Function (SF) is a generic term for any description of the nucleons within the nucleus, it is often used to imply a more sophisticated model than the RFG or LFG which cannot be written in a compact form. Here SF will refer to the SF model from Omar Benhar and collaborators [51], which provides a more realistic description of the momentum and energy distributions of initial nucleons within a nucleus than the Fermi gas models. The Benhar SF is shown in Figure 2.6 and includes two terms: a mean field term, which is a description of single nucleons within the nucleus, for

which a shell-like structure is seen as bands at certain values of the removal energy in Figure 2.6, and a short range correlation term which describes particles in quasi-deuteron states within the nucleus. The correlation term accounts for ∼20% of the total cross section, and leads to a very diffuse SF extending to large values of initial state nucleon momentum and removal energy. Note that the impulse approximation is still assumed for the Benhar SF: the neutrino interacts with one nucleon only, even though short range correlations between nucleons are included (these correlations affect the energy and momentum distribution for the nucleon involved in the interaction). Similar SF models exist from other authors [216, 217], but the Benhar SF is available in a number of neutrino interaction generators [166, 167, 218] so is of particular interest in this thesis. In Figure 2.7, the SF is projected onto the momentum axis and compared with the momentum distribution of the RFG model.

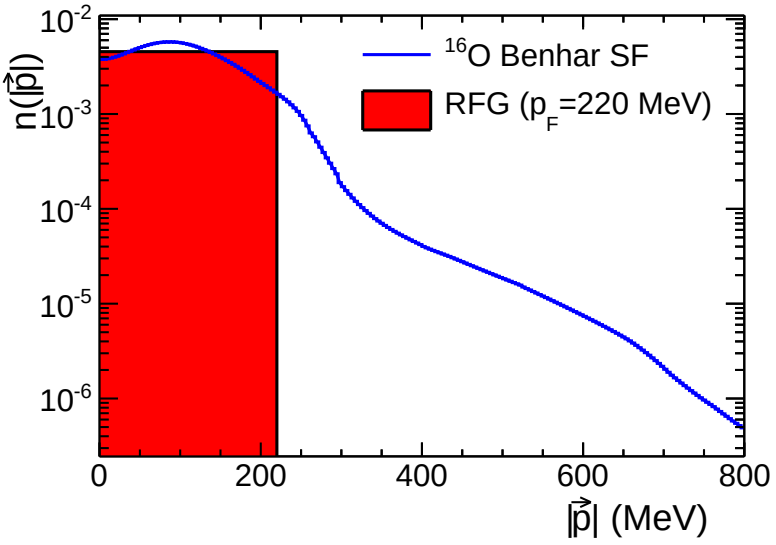

FIGURE 2.7: Projection of the SF shown in Figure 2.6 onto the momentum axis and comparison with the RFG model.

The initial state of the nucleus is also modelled by the Effective Spectral Function (ESF) model [71, 80], which modifies the initial state nucleon momentum distribution to model the outgoing lepton kinematics through comparisons with electron scattering data. Electron scattering, the ESF model and its implementation in NEUT are discussed in detail in Chapter 6.

More complex models which go beyond the simple picture of non-interacting fermions are available [219–222]. However, with the exception of the GiBUU model [219], these are not currently implemented in neutrino interaction generators. In these models, a mean field potential due to the presence of other nucleons within the nucleus is calculated, which will generally depend on the position and momentum of the struck nucleon.

2.4.2 Nuclear modifications

Although the alternative nuclear models discussed in Section 2.4.1 are more sophisticated than the RFG model, they generally do not significantly change the total cross section as a function of neutrino energy, although they do significantly change the shape of differential cross sections in various kinematic variables [215]. Therefore, they fail to describe the much larger cross sections measured by experiments with heavy nuclear targets. It has been noted that theorists and experimentalists are working with different definitions of what CCQE is, and that in some sense this may be the cause of the discrepancy [215]. Experimentalists typically define CCQE interactions as interactions with no mesons in the final state (sometimes referred to as CC-0π interactions), which is more inclusive than the CCQE interaction defined in Equation 2.2 and used by theorists.

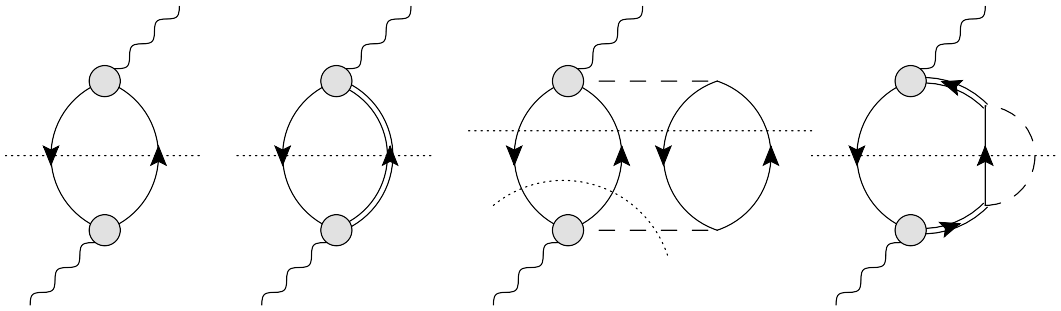

(A) 1p–1h (B) Δ resonance (C) 2p–2h or π production (D) 1p–1h–1π

FIGURE 2.8: W-boson self-energy diagrams used to produce the Nieves model predictions for different interaction channels. Solid lines represent particles or holes; double lines represent Δ resonances; dashed lines represent mesons; and wavy lines represent the incoming and outgoing W-boson. The dotted represents a line for applying a Cutkosky cut: intersected lines are put on mass shell, and represent a possible final state (calculating W self-energy is therefore a convenient way to sum many possible diagrams). The grey circles can be any possible vertex, the possibilities for which are shown in Figure 2.9. This figure has been reproduced from Figure 5 of Reference [52].

The Nieves [223] and Martini [224] models look at a large number of possible W-boson self-energy diagrams in nuclear matter and consider diagrams where the interaction is with more than one nucleon to produce a CCQE-*like* cross section. Tree level $\nu_l + n \rightarrow l^- + p$ interactions are referred to as one-particle, one-hole (1p–1h), or sometimes as *true* CCQE; higher order two-particle, two-hole (2p–2h) corrections are included in the Nieves and Martini models, and the class of models are often referred to as are referred to as n-particle, n-hole (npnh) models. Note that they both use the LFG as the underlying nuclear model. First and second order diagrams are shown in Figure 2.8 to illustrate the processes considered in the Nieves model[10]. At each of the vertices marked with a grey

[10]Both Nieves and Martini models include some third order (3p3h) diagrams following the π-less Δ-decay contribution discussed in [225], which forms part of the npnh contribution.

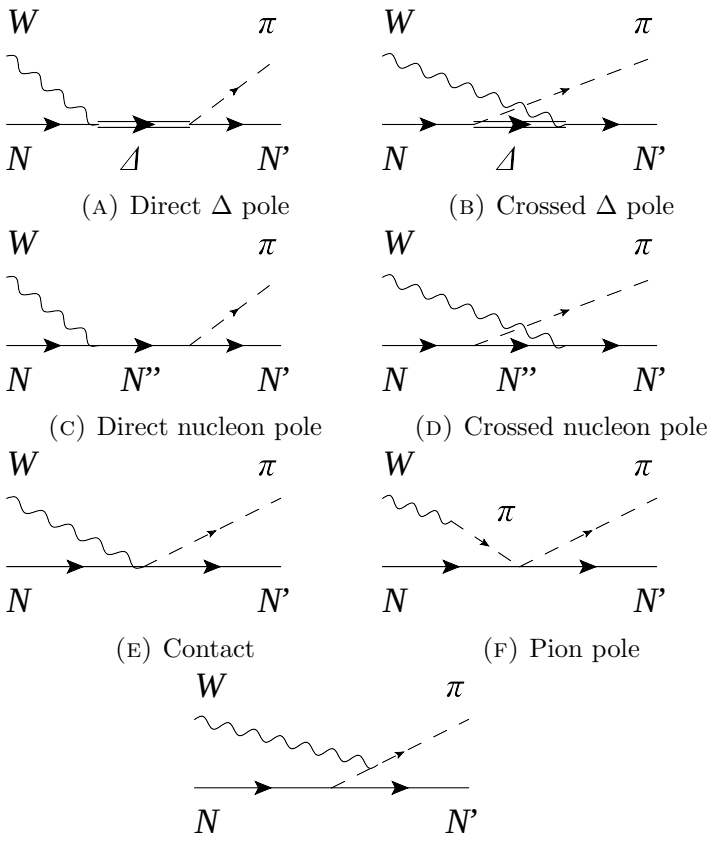

(A) Direct Δ pole (B) Crossed Δ pole

(C) Direct nucleon pole (D) Crossed nucleon pole

(E) Contact (F) Pion pole

(G) Pion in flight

FIGURE 2.9: Possible vertices considered in the W self-energy diagrams shown in Figure 2.8. This figure has been reproduced from Figure 6 of Reference [52].

circle, each of the seven diagrams shown in Figure 2.9 can be included, and the total cross section prediction involves the summation of all possible diagrams.

Additionally, the Random Phase Approximation (RPA) is a nuclear screening effect that modifies the propagator for interactions in nuclear matter [223, 224], and needs to be included in the Martini and Nieves model calculations to find good agreement with data. RPA calculations consider effective interaction terms between particle–hole excitations within the nucleus which change the electroweak coupling in nuclear matter due to strongly interacting nucleons [226]. RPA is illustrated in Figure 2.10, where V indicates the effective interaction; the sum is substituted into the 1p–1h response shown in Figure 2.8a, which modifies the cross section for CCQE in an LFG (it is also included in other diagrams shown in Figure 2.8). RPA has a small effect on the overall cross section as a function of neutrino energy, and has a significant effect on the differential cross section as a function of Q^2 for CCQE interactions.

In the language of the Martini and Nieves models, the 1p–1h interaction is the CCQE interaction considered by theorists, whereas the CC-0π interactions measured by experimentalists actually include 1p–1h (with RPA corrections applied) *and* 2p–2h interactions,

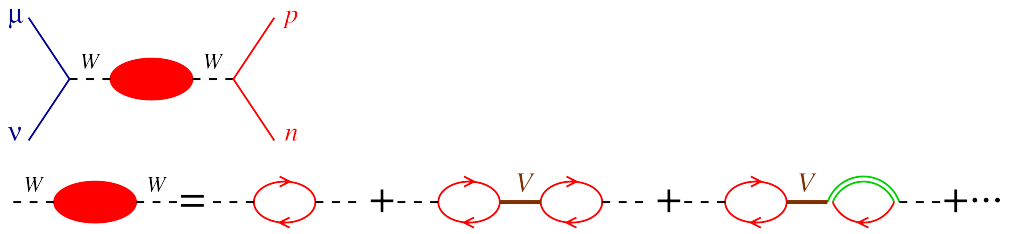

FIGURE 2.10: RPA modification to CCQE scattering. The effective interactions between particle–hole and Δ–hole excitations are denoted V (Δ is denoted as a double green line). This figure has been reproduced from Figure 6 of Reference [53].

plus higher order terms which are mostly neglected in the calculations. By including the 2p–2h component, the Martini and Nieves models add additional strength to the CCQE-*like* cross section which produces good agreement with MiniBooNE neutrino [227, 228] and antineutrino [229, 230] CCQE data without requiring an ad hoc inflation of the axial mass. Note that such agreement seems to be impossible for models which do not have an np-nh component [53].

The Nieves model [223] was limited to $E_\nu \lesssim 1.2\,\text{GeV}$ because only the lowest delta resonance was included in the calculation (see Figure 2.9). In a later paper [54], the observation was made that as the neutrino energy increases the cross section is relatively stable as a function of energy and three-momentum ($|\vec{q}|$) transfer. The cross section for the Nieves multi-nucleon–neutrino model for 3 GeV neutrinos and antineutrino interactions on a carbon target is shown as a function of energy and momentum transfer in Figure 2.11. The top peak comes from the Δ component, the bottom non-Δ peak fills in the dip region [54]. By imposing a cut on the three momentum transfer, the model can be extended up to $E_\nu \leq 10\,\text{GeV}$ for low momentum transfer events, which is acceptable for many experiments where mostly forward going (low four-momentum transfer) events are measured. The nominal three-momentum cutoff is $|\vec{q}| \leq 1.2\,\text{GeV}$, but the authors of the model note that variations of $\pm$ 0.1 GeV can change the model cross section by up to 10% due to the large amount of phase space included or omitted in the calculation. With this high energy extension, the Nieves model should in principle be valid for experiments at higher energies (see Figure 2.3).

Finally, an effective np–nh model called the Transverse Enhancement Model (TEM) is available and is motivated by electron scattering data. This is described in detail in Chapter 6, so is not covered here. It is unclear how reliable an electron scattering based multi-nucleon–neutrino interaction can be because it is unclear what the multi-nucleon enhancement to the axial response should be. For the TEM the axial response is not enhanced, and the enhancement to the axial response cannot be extracted from electron scattering data. There is an interesting discussion in Reference [215] on the difference between the enhancement of the axial response in the Martini and Nieves models. In

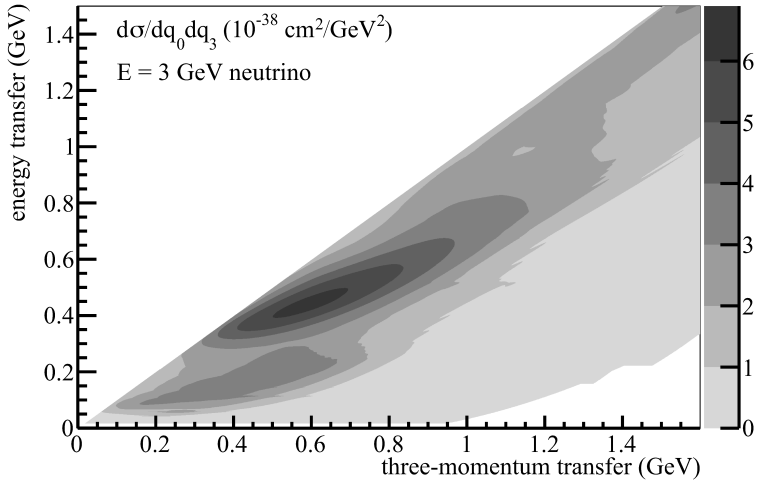

(A) Neutrinos

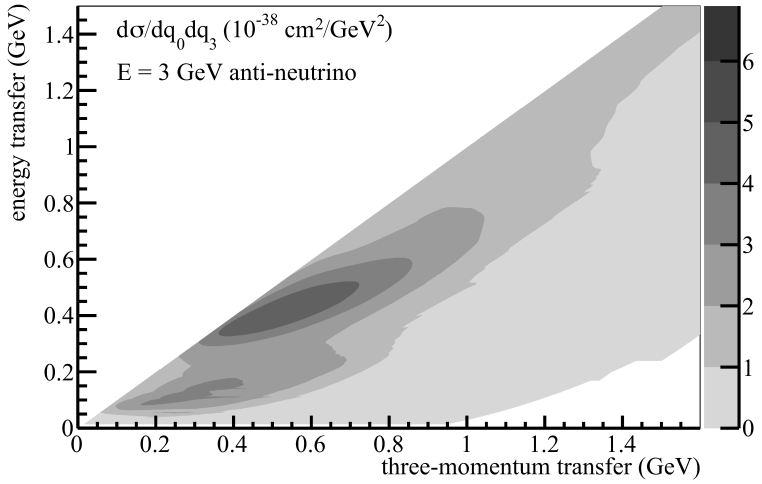

(B) Antineutrinos

FIGURE 2.11: Figures reproduced from Figure 2 of Reference [54], which show the Nieves multi-nucleon–neutrino cross section as a function of momentum and energy transfer. This example is for 3 GeV (anti)neutrinos on a carbon target.

the Nieves model, the axial response is not enhanced, whereas in the Martini model, the enhancement to the magnetic and axial response is assumed to be identical. This difference may account for the large difference in total cross section predicted by the two models.

Chapter 3

Experimental Setup

Usually, T2K theses have a chapter describing the T2K experiment. This thesis is no different in this regard: an overview of the T2K experiment is given in Section 3.1. Additionally, published data from two other experiments, MINERνA and MiniBooNE, are an integral part of the analysis work presented in Chapters 4, 5 and 6, so brief descriptions of both of these experiments are given in Sections 3.2 (MINERνA) and 3.3 (MiniBooNE).

3.1 The T2K experiment

The T2K (Tokai to Kamioka) experiment is a long-baseline neutrino oscillation experiment designed to make high precision measurements of various neutrino mixing parameters using a high intensity off-axis muon neutrino beam.

The experimental setup is shown in Figure 3.1. A high purity ν_μ beam is produced at the Japan Proton Accelerator Research Complex (J-PARC) on the east coast of Japan. There is a near detector complex located 280 m downstream of the target, which is designed to measure the unoscillated beam intensity, purity and direction to high precision. The flavour composition of the beam is then measured 295 km downstream of the production point at the far detector, Super-Kamiokande (SK), which measures oscillations in the flux. Both SK and the off-axis near detector are designed to be at an angle of 2.5° with respect to a direct line between each detector and the target. This technique produces a narrow-band beam, which allows greater precision oscillation measurements to be made. The peak neutrino energy at the off-axis angle is 0.6 GeV, which was selected such that the far detector is at the first oscillation maximum.

This section gives an overview of the design of the detectors that make up the T2K experiment. A more thorough description of the T2K experiment can be found in Reference [55]. A detailed description of the T2K oscillation analysis strategy is given in Chapter 7.

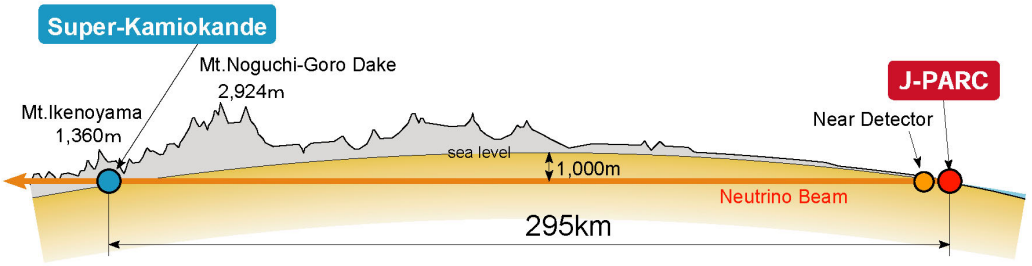

FIGURE 3.1: Location of T2K near and far detectors relative to neutrino production at J-PARC. This figure has been reproduced from Figure 1 of Reference [55].

3.1.1 T2K neutrino beam

The T2K neutrino beam [57] is produced at J-PARC by colliding 30 GeV protons with a graphite target. Magnetic horns focus hadrons produced with the desired charge (and defocus wrong-sign hadrons), which then decay in flight to produce a predominantly muon neutrino beam. An overview of the J-PARC site is shown in Figure 3.2.

The J-PARC accelerator, which accelerates the protons, is described in Section 3.1.1.1. Both the primary neutrino beamline, where the protons are directed for T2K, and the secondary beamline, where the protons strike the target and the secondary beam is focused, are described in Section 3.1.1.2. T2K is an off-axis experiment, meaning that the beam is not directed directly towards the far detector, rather 2.5° off-axis, the motivation for which is discussed in Section 3.1.1.3.

3.1.1.1 J-PARC accelerator

Three accelerators are used to produce the 30 GeV proton beam. First, a linear accelerator accelerates H^- ions up to kinetic energies of 400 MeV. Charge stripping foil then removes the electrons from the protons before the second stage, a rapid-cycling synchrotron (RCS), which accelerates the beam up to 3 GeV kinetic energy. Finally, the main ring (MR) synchrotron accelerates the beam up to 30 GeV. Only ∼5% of bunches from the RCS are supplied to the MR; the rest are supplied to other facilities and beamlines on the J-PARC site. The MR can be extracted in two ways, slow and fast

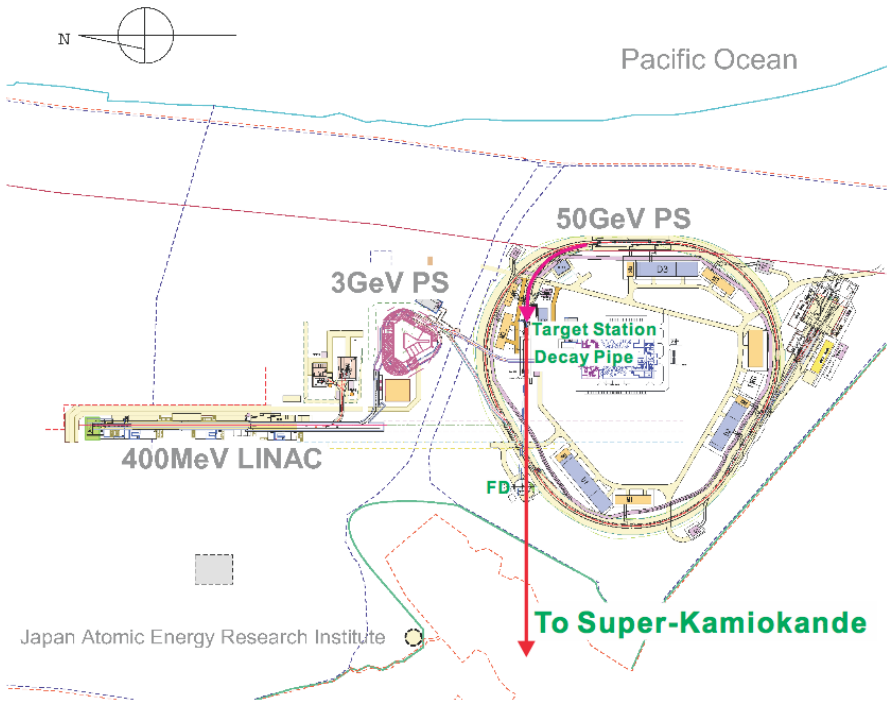

FIGURE 3.2: Overview of the J-PARC accelerator complex. This figure has been reproduced from Reference [56].

extraction, but only the latter is used by T2K. In fast extraction mode, all 8 bunches in the MR are delivered in a single spill to the neutrino beamline.

3.1.1.2 T2K beamline

The T2K neutrino beamline is shown in Figure 3.3. The primary beamline, consisting of the preparation, arc and final focusing sections, is primarily used to bend the beam towards Kamioka and slightly downwards. Various beam monitors are used to ensure a stable beam and to minimise beam loss. These are described in References [55, 57].

The secondary beamline consists of the target station (TS), decay volume, beam dump and muon monitor, as shown in Figure 3.4. The entire TS is located within a helium gas filled vessel. Protons enter the TS from the left of Figure 3.4, passing through a titanium alloy window which separates the vacuum of the primary beamline from the helium of the TS. An upstream collimator (the baffle) protects the magnetic horns from stray protons. Then the optical transition radiation monitor [231] is used, along with information from monitors in the final focusing section of the primary beamline, to guide the beam onto the target.

The target itself is a 91.4 cm long (1.9 interaction lengths), 2.6 cm diameter and 1.8 g/cm^3 graphite rod located within the first magnetic horn. The target is encased in titanium and cooled by helium gas.

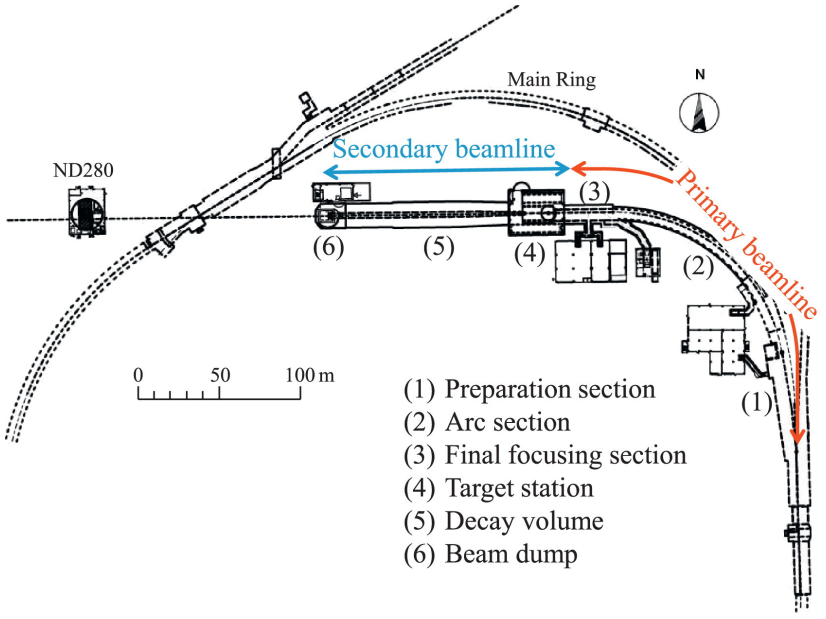

FIGURE 3.3: Overview of the T2K neutrino beamline. This figure has been reproduced from Figure 2 of Reference [55].

Each of the three magnetic horns is pulsed with 250–300 kA to produce a toroidal magnetic field in time with the proton beam arrival on the target. This results in the collection and focusing of positively (negatively) charged secondary particles to enhance the neutrino (antineutrino) flux [232]. Wrong sign secondaries are defocused by the horns, so running the horns with different polarities enhances either the neutrino or the antineutrino component of the beam.

The focused secondary beam is then allowed to decay in a ∼96 m long decay volume, which has a cross section of 1.4 m wide × 1.7 m high (3.0 m wide × 5.0 m high) at the upstream (downstream) end. At the downstream end of the decay volume is a 75 t graphite beam dump measuring 3.174 m long × 1.94 m wide × 4.69 m high, with an additional 2.4 m thick series of iron plates at the downstream end. The beam dump stops all hadrons and most muons below 5.0 GeV.

A muon monitor [233] is located downstream of the beam dump to measure the remaining muons in order to monitor the neutrino beam direction to a precision of 0.25 mrad on a bunch by bunch basis, and to monitor the neutrino beam intensity.

3.1.1.3 Off-axis approach

The off-axis approach exploits the kinematics of the two body pion decay used to produce the majority of neutrinos in accelerator experiments $\pi^{\pm} \rightarrow \mu^{\pm} + \overset{(-)}{\nu}_{\mu}$. Neglecting the neutrino mass, the neutrino energy in the pion centre of mass frame, E_{ν}^{CM}, can be

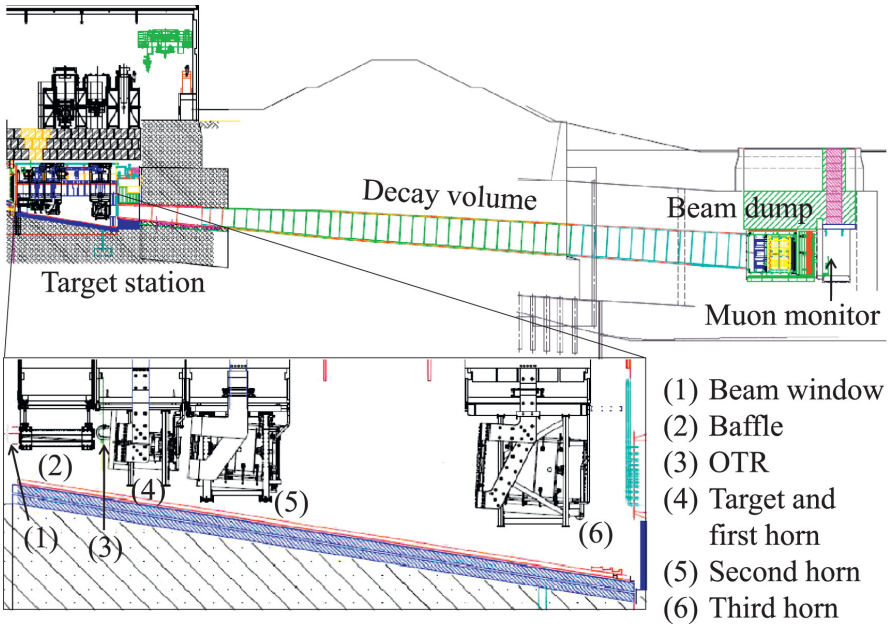

FIGURE 3.4: The secondary beamline viewed from the side, protons travel from left to right in this view. The inset shows the target station in more detail. The beam passes through a collimator (the baffle) and the OTR monitor which guides it onto the target. The resulting secondary particles (π and K) are focused by the magnetic horns and allowed to decay in the decay volume to produce the neutrino beam. Remaining hadrons and lower energy muons are absorbed by the beam dump. Penetrating muons are measured by the muon monitor to monitor the beam direction and intensity on a bunch by bunch basis. This figure has been reproduced from Figure 6 of Reference [55].

expressed as [234]

$$E_\nu^{\mathrm{CM}} = \frac{m_\pi^2 - m_\mu^2}{2m_\pi} = 29.8 \text{ MeV}, \tag{3.1}$$

where m_π and m_μ are the pion and muon masses. Therefore there is a maximum transverse component to the neutrino momentum with respect to the beam axis. From this it can be inferred that the maximum neutrino energy decreases with off-axis angle, and that an off-axis beam has a much narrower peak in energy, as can be seen in Figure 3.5. It is clear that small changes in the off-axis angle affect the energy spectrum, so the beam direction must be tightly controlled for this approach to be useful in an oscillation experiment.

3.1.2 Near detector complex

The near detector complex is located on the J-PARC site, 280 m downstream of the target, in a cylindrical pit which is 37 m deep, 17.5 m in diameter, and has no overburden. The near detector complex is shown in Figure 3.6. The INGRID detector is designed to measure the neutrino beam profile and beam direction. As has already been remarked, this is important because small deviations in the beam direction cause relatively large

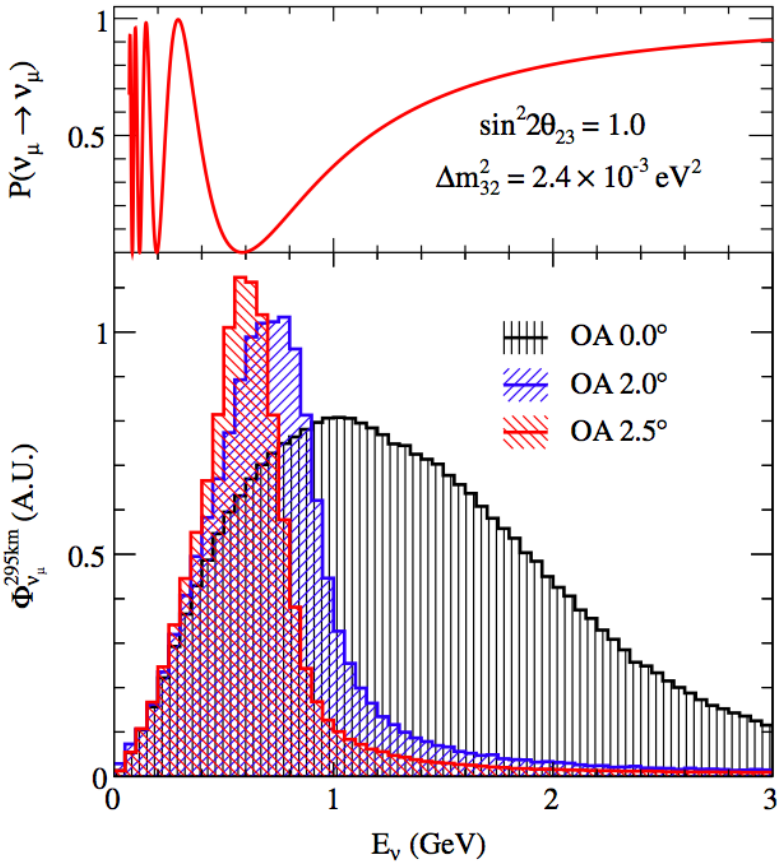

FIGURE 3.5: The bottom plot shows the neutrino flux as a function of energy for different off-axis angles. The top plot shows the muon neutrino survival probability for a baseline of 295 km [57], equal to the T2K baseline. The neutrino flux peaks at 0.6 GeV for an off-axis angle of 2.5°, which corresponds to the first oscillation maximum for T2K. This figure has been reproduced from Figure 1 of Reference [57].

changes in the peak neutrino energy of the off-axis beam. The off-axis ND280 detector is designed to characterise the components and energy composition of the beam, as well as constrain cross section systematics which are used at SK for oscillation fits[1]. Additionally, the ND280 is the first detector which can make cross section measurements with a narrow-band beam.

3.1.2.1 On-axis near detector (INGRID)

The Interactive Neutrino GRID (INGRID) [235] detector monitors the neutrino beam direction and intensity. Sufficient statistics are collected to provide daily measurements at nominal beam intensities. The beam centre is measured to a precision of 10 cm, corresponding to 0.4 mrad, which is combined with measurements on the beamline to precisely determine the ND280 and SK off-axis angle.

[1]There is a detailed discussion of the ND280 flux and cross section constraints in Chapter 7.

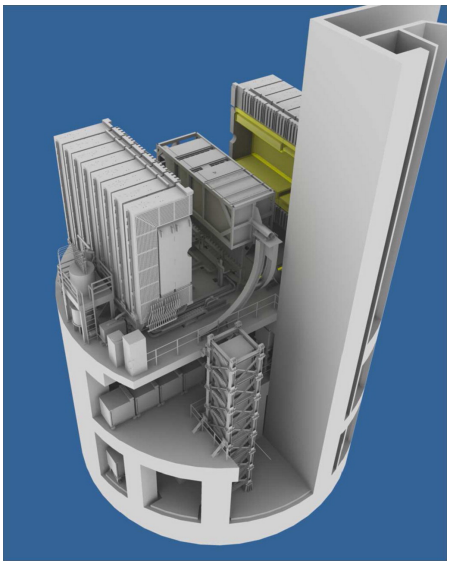

FIGURE 3.6: The three storey near detector complex. The upper level contains the off-axis detector and magnet (here the magnet has been opened). The horizontal INGRID modules are located on the middle level, and the vertical INGRID modules span the bottom two levels. This figure has been reproduced from Figure 9 of Reference [55].

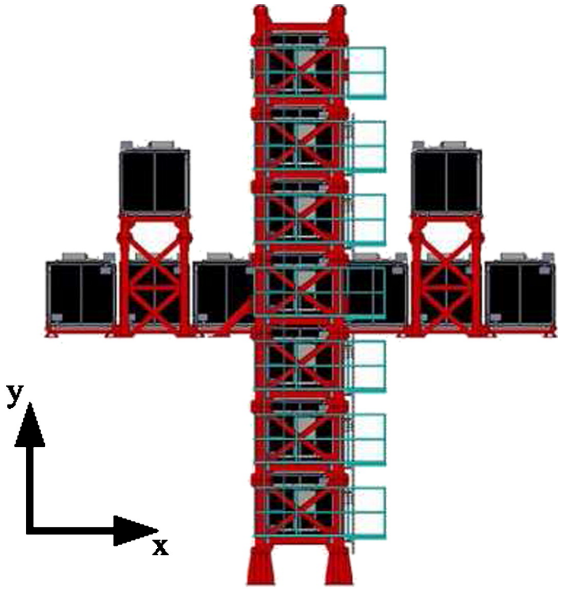

FIGURE 3.7: The on-axis INGRID detector. The neutrino beam direction is into the page. This figure has been reproduced from Figure 11 of Reference [55].

INGRID consists of 16 modules, as shown in Figure 3.7, with 14 modules arranged in a cross perpendicular to the beamline[2], and two modules centred on the beam centre, defined as 0° with respect to the proton beamline. Additionally, there are 2 modules positioned off-axis and outside the main cross, which measure the axial symmetry of the beam. Each module is composed of alternating layers of iron and scintillator, read out by wavelength shifting (WLS) fibres. The target mass of iron in each module is 7.1 t.

[2]Note that the horizontal and vertical lines in the cross are separated, so there are two modules at the centre of the cross where the two lines overlap.

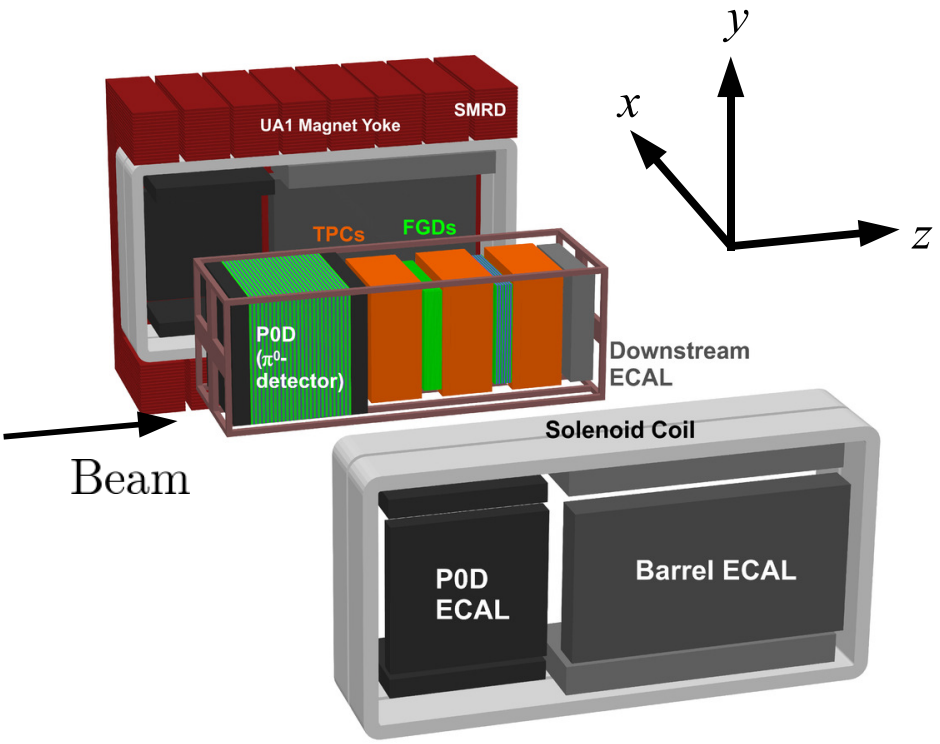

FIGURE 3.8: An exploded view of the off-axis near detector. This figure has been reproduced from Figure 16 of Reference [55].

An additional module, called the Proton Module, lies at the centre of the cross, between the horizontal and vertical lines of the cross. The Proton Module is composed entirely of scintillator planes, and is surrounded by veto planes. Its main purpose is to measure protons (and muons) produced in charged-current quasi-elastic scattering so the on-axis beam can be used to help constrain the neutrino interaction model used in neutrino event generators [200].

3.1.2.2 Off-axis near detector (ND280)

The ND280 lies slightly downstream of INGRID and is set at an off-axis angle of 2.5°. The primary aim of the ND280 is to measure the energy spectrum of the off-axis ν_μ flux before oscillation, and to measure the intrinsic ν_e component of the beam, which is crucial for the ν_e appearance measurement. As well as constraining the flux prediction, the ND280 constrains the cross section systematics, as described in Chapter 7.

To fulfill all of the requirements for the near detector, the ND280 consists of a series of subdetectors, and like any complex detector, has its fair share of associated jargon and acronyms[3]. An exploded view of the ND280 is shown in Figure 3.8. The central basket

[3]Presumably this is to confuse first year graduate students.

region is 6.5 m (long) × 2.6 m (wide) × 2.5 m (high), and contains a π^0 detector (the PØD) and the tracker region, comprising three time projection chambers (TPCs), and two fine-grained detectors (FGDs), as well as the downstream electromagnetic calorimeter (DsECal). The basket is surrounded by electromagnetic calorimeters (ECals), which are attached to the magnet return yoke in which the ND280 is contained. There is also a side-range muon detector (SMRD), instrumented in the air gaps in the return yoke. The external dimensions of the magnet return yoke are 7.8 m (long) × 5.6 m (wide) × 6.1 m (high).

The UA1 magnet The refurbished UA1 [236] and NOMAD [237] magnet was donated by CERN. Four water-cooled aluminium coils which sit inside the magnet return yoke provide a magnetic field of 0.2 T perpendicular to the neutrino beam direction, allowing for charge separation and measurements of the momentum of charged particles within the ND280. The return yoke separates into two clams, which can be moved apart to allow access to the basket. Each clam consists of low carbon steel plates separated by air gaps. The total mass of the magnet and the return yoke is 850 t, which accounts for most of the mass of the ND280.

Side Muon Range Detector (SMRD) The SMRD [238] consists of 440 scintillator paddles instrumented with WLS fibres, which fit into the air gaps of the magnet return yoke. The primary purpose from which the detector gets its name is to detect and measure the momentum of muons exiting the basket at high angles relative to the beam, which may be missed by the TPCs. It is also used to veto events which occur outside the detector, in the walls of the near detector pit, or in the magnet yoke. Finally, it also serves as a trigger for cosmic ray muons, which are used to calibrate the other ND280 detectors.

π^0 detector (PØD) The PØD [239] is the most upstream subdetector within the ND280. It has three distinct regions: upstream and downstream electromagnetic calorimeters, consisting of alternating layers of scintillator bars instrumented with WLS fibres and lead, and a water target region in the centre which consists of alternating layers of scintillator, brass and high density polyethylene water bags.

The PØD is primarily designed to measure NC1π^0 interactions on water, an important background at SK. By comparing the event rate with the water bags filled, and with them drained, it is possible to extract a measurement on water. The electromagnetic calorimeter regions surrounding the water target region allow particles entering the PØD to be vetoed. The PØD occupies approximately a third of the basket, with dimensions

2.1 m (long) × 2.2 m (wide) × 2.4 m (high) and has a total target mass with (without) water of 16.1 t (13.3 t).

Fine-Grained Detectors (FGDs) The FGDs [240] are composed of layers of scintillator bars read out by WLS fibres and provide the main target mass for interactions in the tracker region. Each FGD measures 2.300 m wide × 2.400 m high × 0.365 m long and weighs 1.1 t. Each bar has a cross section of 9.61 mm × 9.61 mm, and they are arranged in alternating layers of 192 bars in the x and y directions (as defined on Figure 3.8). This design allows for high resolution tracking around the interaction vertex, and particle identification is possible using energy loss in the scintillator. FGD1 is more upstream and is composed of 30 layers scintillator bars. The more downstream FGD2 has a total of 14 layers of scintillator bars, arranged in pairs of XY layers between which there are six 2.5 cm thick layers of water. Comparing the interaction rates between FGD1 and FGD2 allows the cross sections on water and carbon to be determined separately. This design is similar to the PØD, but the FGD design has the advantage that water and carbon measurements can be made simultaneously, without the need to drain or fill the water layers. The performance of the FGDs was tested in the M11 testbeam at TRIUMF, and are discussed in detail in Reference [240].

Time Projection Chambers (TPCs) The three TPCs [241] are labelled 1 to 3 from upstream to downstream, and surround the FGDs in the tracker region. Each TPC has outer dimensions of approximately 2.3 m wide × 2.4 m high × 1.0 m long, and is filled with a predominantly argon gas mixture. Charged particles passing through a TPC produce ionisation electrons which drift away from the central cathode toward one of the readout planes. The pattern and arrival time of electrons measured on the readout pads allows the 3D path of the charged particles to be reconstructed.

The TPCs perform three main functions. They record the number and tracks of charged particles in the tracker. As the entire basket is within the magnetic field, the curvature of the tracks measured by the TPCs is used to measure the momentum of charged particles. Finally, the amount of ionisation left by each track can be combined with the momentum information for particle identification. In particular, the TPCs provide excellent discrimination between electrons and muons, which is used to measure the electron neutrino contamination in the beam.

A useful figure of merit for the TPCs is the deposited energy resolution, which is measured to be 7.8±0.2% for minimum ionising particles. Full performance information for the TPCs can be found in Reference [241].

Electromagnetic calorimeters (ECals) The ECals are a UK responsibility, and during my long term attachment living in Japan, I shared responsibility with other UK students for the day to day calibration and maintenence tasks necessary to run the ECals. Because of my involvement with this subdetector, more technical details are given in this section than for other subdetectors.

The ND280 ECal [242] is the collective name for a number of sampling electromagnetic calorimeters which surround the detectors in the tracker (PØD, TPCs and FGDs). It is composed of 13 independent modules, as can be seen in Figure 3.8. There are 6 Barrel–ECal modules which surround the four sides of the tracker region (TPCs and FGDs) and 6 PØD–ECal modules which surround the four sides of the PØD. Both Barrel–ECal and PØD–ECal are aligned parallel to the beam axis, and are secured to the magnet flux return, requiring the top and bottom planes to be split into two separate modules to allow the magnet to be opened. There is also a downstream ECal (Ds–ECal), secured within the basket, downstream of TPC3. All of the ND280 ECal modules are composed of layers of scintillator bars interleaved with lead sheets; however, their design differs considerably. The scintillator bars all have a 4.0 cm × 1.0 cm cross section with a WLS fibre running through the middle, and a 0.25 mm thick layer of TiO_2 on the surface of the bars to reflect the light and isolate bars.

The Ds–ECal module has 34 layers of scintillator bars with 1.75 mm of lead between each layer (for a total of 10.6 radiation lengths). Layers alternate in the x–axis and y–axis as defined in Figure 3.8 to allow three dimensional reconstruction of electromagnetic showers and particles passing through the detector. Each scintillator bar is read out at both ends. The Ds–ECal was placed in the CERN T9 testbeam to test the performance of the calorimeters. The measured energy resolution for 0.5 GeV (1.0 GeV) electromagnetic showers was ∼14% (∼10%). The timing resolution has been calculated in situ to be ∼1 ns. For full performance information, see Reference [242].

The Barrel–ECal modules each have 31 layers of scintillator bars with 1.75 mm of lead between each layer (for a total of 9.7 radiation lengths). Alternate layers are orientated along the z–axis, and rotated 90° (whether this is the x–axis or y–axis varies by module, as can be seen from Figure 3.8), again for the reconstruction of three-dimensional tracks and showers. Bars running parallel to the z–axis are read out at both ends, but due to space limitations within the magnet, bars running along the x–axis or y–axis are only read out at one end, and are mirrored at the other end to increase light collection and to allow limited reconstruction of the hit position along the bar axis.

The PØD–ECal modules have 6 layers of scintillator bars with 4.0 mm of lead between each layer (for a total of 3.6 radiation lengths). The bars all run in the z–axis direction for simple reconstruction, and are read out at one end only. The PØD–ECal is intended

to detect charged particles exiting or entering the PØD, and to detect showers which are not fully contained by the PØD.

ECal light injection system The light injection (LI) calibration system for the ECals [242] is a University of Sheffield responsibility, and I have been involved in commissioning the system, and running the light injection in normal beam operation. The LI system receives information from the main T2K DAQ through a series of control cards, which interpret the instructions and the trigger timing information from the DAQ clock module. The control cards send instructions to junction boxes located inside the ECals, which each illuminate two LED strips. The LED strips and junction boxes are instrumented in a 1 cm cavity between the scintillator bars and the bulkhead through which the WLS fibres pass before being read out by the Multi-Pixel Photon Counters (MPPCs), as illustrated in Figure 3.9. A lens is attached to the LEDs to reduce the divergence of the light produced, which ensures a more uniform response for bars located further away from the LEDs.

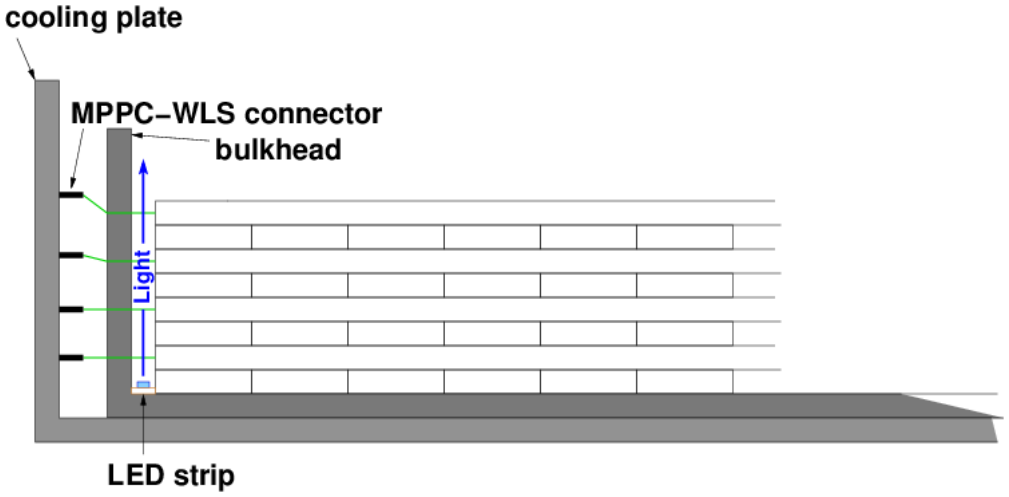

FIGURE 3.9: Instrumentation of the ND280 ECal light injection system [58].

By illuminating all of the fibres in the ECal at a known time (with $\simeq$1 ns precision), the LI system provides an easy way to calibrate for electronic timing offsets which would otherwise smear the time distribution of hits recorded as a particle deposits charge in the detector, and make track and shower reconstruction more difficult. The LI complements the existing timing calibration method (described in Reference [242]), which uses cosmic muon tracks to correct for timing offsets by comparing hit times in neighbouring bars, by offering vastly increased statistics which essentially allows the LI to detect changes in the relative hit times between bars as often as the LI is flashed (once per minute in the regular beam sequence).

I have written a package to use LI events to produce timing calibration constants in a format suitable to be uploaded into the calibration database. Currently the LI is simply used as a cross-check of the existing timing calibration methods using cosmic muons, but in future this package will be used to integrate the LI into the production T2K calibration.

3.1.3 Far detector (SK)

Super-Kamiokande (SK) [243] serves as the far detector of the T2K experiment. It is a large water Cherenkov detector, located 295 km west of J-PARC, 1 km under the centre of Mt. Ikenoyama. SK has been operating since 1996, long before the T2K experiment, with a broad physics programme, which has included neutrino oscillation measurements for solar, atmospheric and accelerator produced neutrinos (as described in Section 1.3), as well as searches for proton decay [244–247], dark matter [248], supernova relic neutrinos [249, 250] and magnetic monopoles [251]. Using SK as the T2K far detector does not prevent its continued work in these areas, as the bunch structure of the T2K beam only takes up a fraction of the total SK running time.

Charged particles produced by neutrino interactions[4] emit Cherenkov radiation in a cone as they travel through water, and it is this light which SK uses to determine the particle momentum and particle type. Note that Cherenkov light is only produced by charged particles with sufficient energy to travel faster than the speed of light in the medium through which they are passing; typically, nucleons are below threshold so are unseen by SK. The SK detector consists of two optically separated volumes as shown in Figure 3.10, the inner (ID) and outer (OD) detectors. The ID is a cylinder 33.8 m in diameter and 36.2 m high containing approximately 32 kt of ultra-pure water. The Cherenkov light is detected by 11,129 inward facing 50 cm diameter photomultiplier tubes (PMTs) on the walls of the ID (approximately 40% PMT cathode coverage). The ID inner walls are lined with black plastic to reduce photon scattering, which helps with particle identification. The OD surrounds the entire ID with a ∼2 m layer of water, and is primarily used to veto particles entering from outside the detector. The OD is much more sparsely instrumented than the ID with 1885 20 cm PMTs, and its walls are covered in a reflective material to increase light collection efficiency.

Muons and electrons can be differentiated at SK by the ring-shaped patterns produced by the Cherenkov light cones (the rings are sections of the cone at a given time). Muons have a relatively large mass and do not rescatter as they pass through the water in the detector, producing a “sharp” ring, as seen in Figure 3.11a. Electrons scatter much more

[4] Other particles may be detected by the charged secondaries they produce. In particular, photons are detectable because they shower electromagnetically.

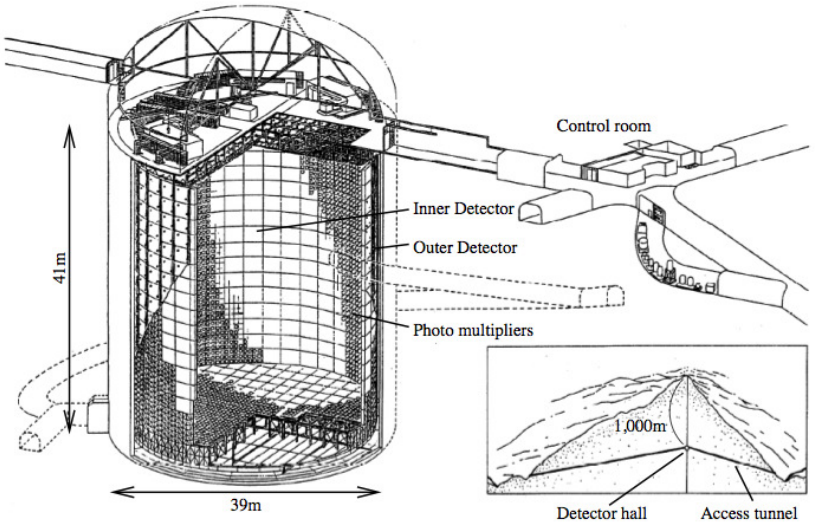

FIGURE 3.10: Schematic of the Super-Kamiokande detector. This figure has been reproduced from Figure 30 of References [55].

readily and generally induce electromagnetic showers at SK energies which produces a "fuzzy" ring, a sum of multiple Cherenkov light cones, as shown in Figure 3.11b. SK reconstruction uses the "fuzziness" of rings to identify particles, and collected charge to reconstruct the particle momentum. By identifying the charged leptons produced by neutrino interactions, SK can determine the neutrino flavour composition of the T2K beam. This information can be combined with the flavour composition produced at the target, and measured at the ND280, to make neutrino oscillation measurements.

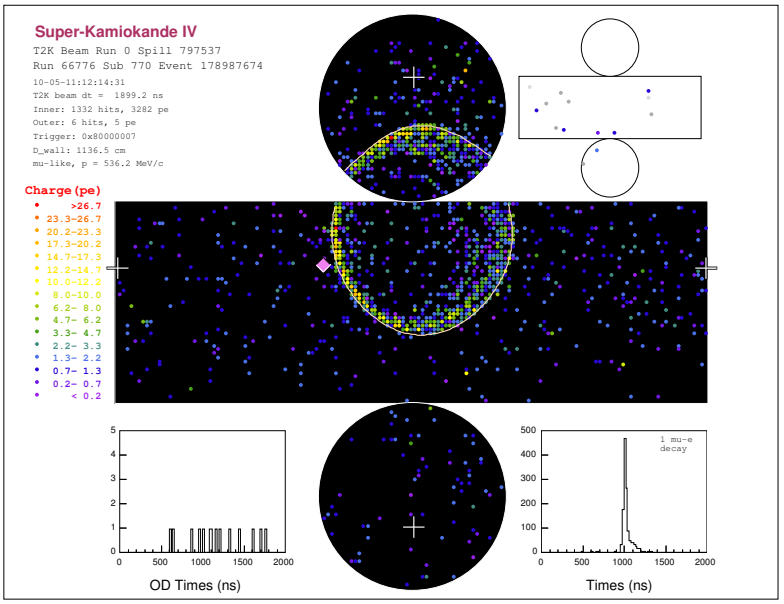

(A) Muon-like event

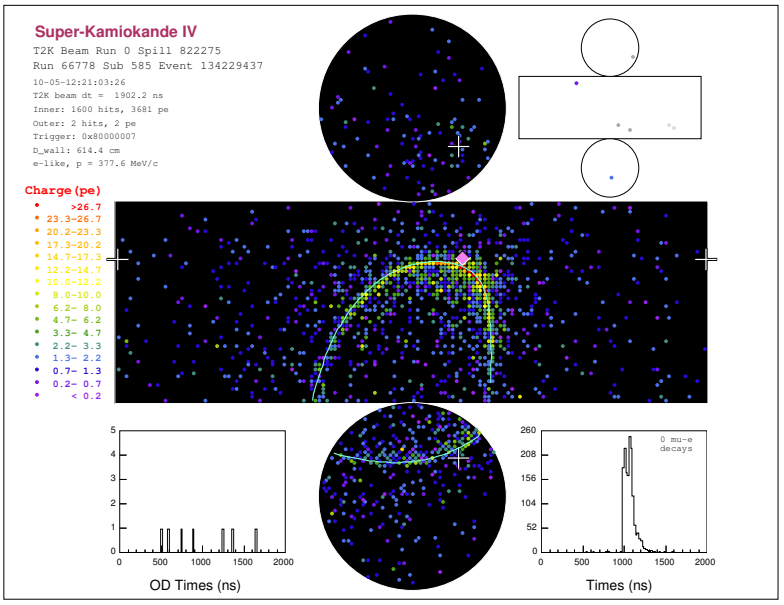

(B) Electron-like event

FIGURE 3.11: Example events in Super-Kamiokande for 3.11a a muon-like event, and 3.11b a electron-like event. The reconstructed ring for each case is shown as a white line. The walls of the cyclindrical inner detector are unrolled onto a plane in the central images. The inset figures in the top right corners are the same for the outer detector. Each point represents a PMT, where the colour indicates the amount of charge collected. This figure has been reproduced from Figure 32 of Reference [55].

3.2 The MINERνA experiment

The MINERνA experiment (Main INjector ExpeRiment ν–A) [59] is designed to make high precision measurements of neutrino-nucleus scattering cross sections on a variety of nuclear targets using the Neutrinos at the Main Injection (NuMI) beam [252] at

Fermilab. The on–axis NuMI beam is described briefly in Section 3.2.1, and the key features of the MINERνA detector are descibed in Section 3.2.2.

3.2.1 NuMI beam

The beam is similar in principle to the T2K beam, and is described in Reference [252]. The primary 120 GeV proton beam is delivered by the Fermilab Main Injector and strikes a graphite target. An upstream baffle is used to protect the target station from stray protons. The secondary beam of pions and kaons is refocused using two magnetic horns, which focus right sign particles and defocus the wrong sign mesons, allowing two modes of operation (primarily neutrino or antineutrino modes). The target position relative to the first horn can be changed to modify the energies of secondary particles focused by the horns, and therefore the neutrino flux spectrum produced [59]. The results discussed in this thesis all used the low–energy configuration, where the target was located as close as possible to the first horn, resulting in a peak neutrino flux of 3 GeV. Higher energy configurations are produced by moving the target further upstream of the horns.

The secondary beam is directed down a 675 m long steel decay pipe, where the mesons are allowed to decay to produce a predominantly muon neutrino or antineutrino beam. Hadron monitors are located at the end of the decay pipe to characterise the beam, with an absorber located immediately downstream to remove remaining hadrons from the beam.

There are 240 m of rock between the end of the decay pipe and the MINERνA detector to remove muons, leaving only a neutrino beam. Muon monitors are placed at intervals in the upstream end of the rock to further characterise the beam. The NuMI beam is directed through the Earth, towards the MINOS (Main Injector Neutrino Oscillation Search) far detector, located in Soudan, Minnesota.

3.2.2 MINERνA detector

The MINERνA detector is shown in Figure 3.12. The steel shield and scintillator veto wall absorb low energy hadrons and tag muons produced by interactions upstream of the detector. The MINOS near detector [253] (simply referred to as MINOS from now on) is located downstream of the main MINERνA detector, and is used as a muon spectrometer. As the MINOS detector is magnetised, it provides charge separation and momentum measurements which are not possible in the unmagnetised MINERνA detector. MINERνA analyses which rely on MINOS to tag muons have a low angular acceptance as they only sample events with very forward going muons.

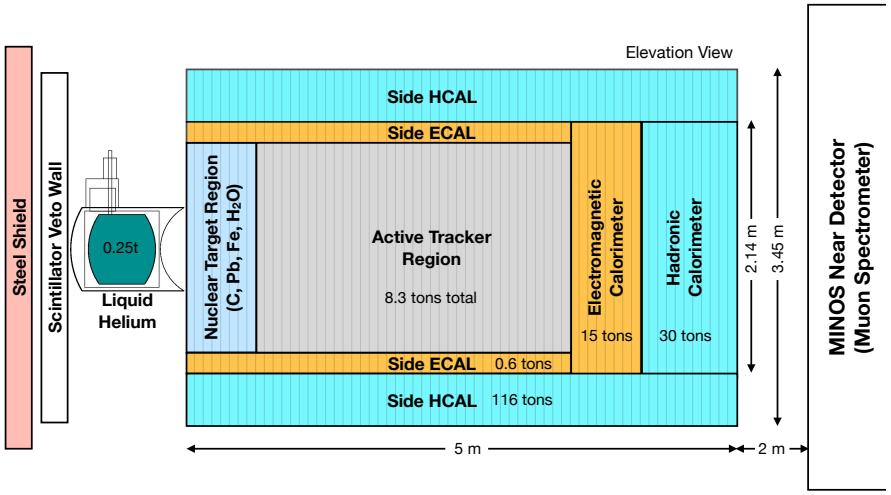

FIGURE 3.12: The MINERνA detector shown from the side. This figure has been reproduced from Figure 1 of Reference [59].

The main part of the MINERνA detector is separated into inner and outer detector regions. The inner detector is composed of four distinct regions: the nuclear targets region, the tracker region, an electromagnetic calorimeter, and a hadronic calorimeter. Each region is divided into modules which consist mostly of hexagonal scintillator planes, each made of 127 triangular scintillator bars, arranged in three different orientations (60° rotations between each plane). A single module is shown in Figure 3.13.

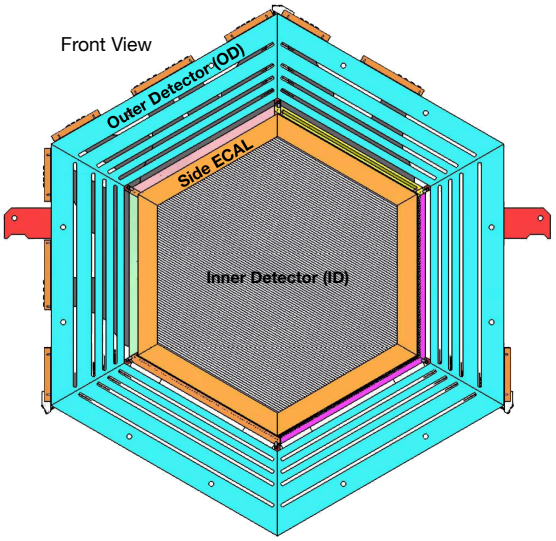

FIGURE 3.13: View of a single MINERνA module viewed from the front (transverse relative to the beam direction). This figure has been reproduced from Figure 1 of Reference [59].

The fully active tracker region is the target for the analyses discussed in this thesis. The target material is therefore the scintillator itself, composed of long-chain hydrocarbons, which can be treated as a CH target. There are 62 modules in the tracker region,

each composed of two scintillator layers. A 15 cm border of 0.2 mm thick lead on the downstream end of each module provides electromagetic calorimetry for particles exiting the side of the tracking region. Because the tracker region is fully active, activity around the vertex can be investigated.

The nuclear targets region is a combination of fully active tracking modules and passive planes composed of different nuclear targets. The various nuclear targets are carbon, lead, iron and water. Although the nuclear target region is an important part of MINERνA's cross section programme, it is not relevant for the analyses referred to in this thesis, so will not be discussed further. For more details, see Reference [59].

The downstream electromagnetic calorimeter is composed of 10 modules, each with two scintillator planes and a 0.2 mm thick lead plate on the downstream end. There are 20 modules in the downstream hadronic calorimeter, each with a single scintillator plane and a 2.54 cm thick hexagonal steel plane. The outer detector consists of a steel frame supporting structure with embedded scintillator planes, as can be seen in Figure 3.13, which turns the support structure into a hadronic calorimeter. The combination of the downstream and side electromagnetic and hadronic calorimeters allows for containment of most particles produced by vertices within the central tracking, or nuclear targets region, and allows for particle identification and momentum measurements.

3.3 The MiniBooNE experiment

The MiniBooNE experiment [60] was designed to test the LSND $\bar{\nu}_\mu \to \bar{\nu}_e$ oscillation signal [142], as described in Section 1.5. MiniBooNE uses the Booster Neutrino Beam (BNB) at Fermilab, which has a peak energy of approximately 700 MeV. In the LSND experiment, the distance neutrinos travelled from the source to the detector, L, was 30 m, and the neutrino energies, E, were in the range 30–60 MeV, giving an $L/E \simeq 1$ km/GeV. MiniBooNE also has an $L/E \simeq 1$ km/GeV, but with neutrinos on a higher energy scale, so that the backgrounds are largely different from those at LSND.

The BNB at Fermilab [254] uses 8 GeV protons from the Fermilab booster. The same booster feeds the Main Injector used by the MINERνA experiment. The protons strike a beryllium target inside a single magnetic horn, which focuses the beam of secondary mesons of a given charge (selected by changing the polarity of the horn). The secondary beam is directed down a 50 m long decay pipe, where most mesons decay in flight. There is a 3.8 m thick steel and concrete beam dump at the end of the decay tunnel to absorb undecayed hadrons. Muons are absorbed by 474 m of earth between the beam dump and the MiniBooNE detector hall.

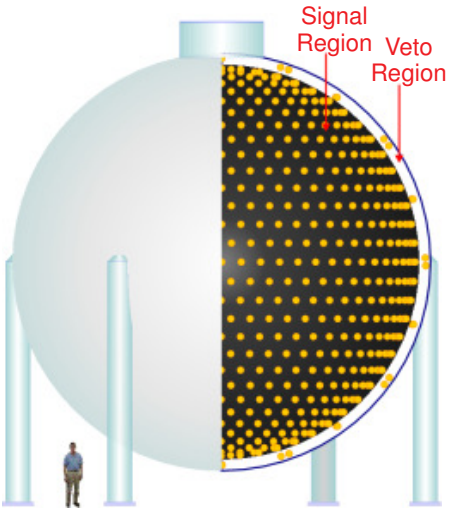

FIGURE 3.14: A diagram of the MiniBooNE detector tank. This figure has been reproduced from Figure 1 of Reference [60].

The MiniBooNE detector is a 6.1 m radius spherical tank filled with 818 t of undoped mineral oil [60], shown in Figure 3.14. Mineral oil is a long-chain hydrocarbon, but can be considered to be a CH_2 target [34]. The tank is divided into signal (inner) and veto (outer) regions by an optical barrier at a radius of 5.7 m. MiniBooNE is a Cherenkov detector, although mineral oil also produces some scintillation light, which improves light yields. The optical properties of mineral oil are discussed in Reference [255]. The signal region is instrumented with 1280 8 inch PMTs which corresponds to a total photocathode coverage of 11.3%. The veto region is instrumented with 240 8 inch PMTs. Approximately 88% of the PMTs used by MiniBooNE were recycled from the LSND experiment.

Chapter 4

Using MiniBooNE cross section results to constrain 3+1 sterile neutrino models

This chapter describes a fit to MiniBooNE neutral current elastic and charged current quasielastic cross section results to produce limits on muon to sterile neutrino mixing. The results have been included in two publications. Reference [256] includes the fit to the neutral current sample and most of the the details of the analysis. Reference [257] presents the results of the joint neutral and charged current analysis.

4.1 Introduction

The primary aim of this analysis is to use the published MiniBooNE Neutral Current Elastic (NCEL) cross section results [77] to produce limits on muon to sterile neutrino mixing (limits in the Δm^2 - $\sin^2 2\vartheta_{\mu s}$ plane) for a 3+1 sterile neutrino model with a mass splitting $0.1 \leq \Delta m^2 \leq 10.0$ eV^2. For details on 3+1 sterile neutrino models, refer to Section 1.4.1. The analysis is improved by using the published MiniBooNE Charged Current Quasi-Elastic (CCQE) cross section results [34] as an additional constraint. Although using cross section measurements in the context of sterile neutrinos is unusual, limits have previously been produced from ν_e-carbon cross section measurements [258] by comparing the published results with theoretical cross section predictions. This analysis uses the GENIE interaction generator [167] and the Smith-Moniz Relativistic Fermi Gas (RFG) model [178] to make event rate predictions with simple Monte Carlo simulations on the MiniBooNE detector medium, CH_2. The cross section model employed in

this analysis closely follows the MiniBooNE cross section model [76,78], and is described in detail in Section 4.2.1.

Although the RFG model is currently widely used, and is the default nuclear model for many neutrino generators [166,167,259], it cannot explain the modern heavy target data, and so the the axial mass parameter M_{A} is inflated to cover various other contributions[1]. This *effective* axial mass parameter is here denoted $M_{\mathrm{A}}^{\mathrm{eff}}$ to highlight this throughout this chapter. Although it has been argued that large $M_{\mathrm{A}}^{\mathrm{eff}}$ values fit the experimental data reasonably well [191], there is no current consensus on how to correctly model nuclear effects. Additionally, it has been shown that the choice of cross section model affects the results of sterile neutrino analyses [260]. Despite the shortcomings of the RFG model, it is the appropriate choice of cross section model for this analysis because it is the model most widely used in the current generation of neutrino experiments including MiniBooNE, and therefore is commonly used to produce sterile neutrino limits [61,144, 261].

In general, it is not possible to take $M_{\mathrm{A}}^{\mathrm{eff}}$ measured by an experiment and apply it to another experiment, as the additional contributions parametrised by this enhancement depend on the type of target, the type of detector, and the energy distribution of the neutrino beam. For this reason, it is necessary for neutrino experiments to use their own *in situ* cross section measurement of $M_{\mathrm{A}}^{\mathrm{eff}}$ in sterile analyses as there is no agreed upon global best fit value. Because each experiment must rely on its own $M_{\mathrm{A}}^{\mathrm{eff}}$ measurement, experiments that produce sterile neutrino limits run the risk of fitting to the same dataset twice if the cross section parameters are not varied in the fit. Current sterile limits have been produced which rely on a pre-measured value of $M_{\mathrm{A}}^{\mathrm{eff}}$ [61,144], which is only valid if all of the fitted cross section parameters are independent of all of the sterile neutrino parameters. MiniBooNE state that their cross section and sterile parameters are uncorrelated for the ν_μ-disappearance measurement using their CCQE dataset [261], but this may not be the case for other datasets.

In this analysis, we mimic this 'sequential' fitting by fitting first the $M_{\mathrm{A}}^{\mathrm{eff}}$, and then to the sterile neutrino model, as well as fitting to all parameters concurrently in a 'simultaneous' fit. If the cross section and sterile neutrino model parameters used in the fita are completely uncorrelated, then the sequential fitting method is valid, and will produce identical results to the simultaneous fitting method. If the fitted cross section and sterile neutrino parameters are correlated, then a sequential type fit risks masking, or partially masking, a sterile neutrino signal, or any statistical fluctuations that mimic a signal, resulting in stronger than justified limits on sterile mixing parameters. It has been pointed out in [196] that underestimated cross sections might hide an oscillation

[1] These issues are discussed in Section 2.3.

signal: similarly, overestimating the cross section could produce a false oscillation signal. It has been noted in the literature [196] that the shortcomings of the RFG model have led to experiments making ad hoc modifications to describe their data, using effective axial masses to indicate this. A further example available in GENIE is the ability to use different effective axial masses for NCEL and CCQE scattering, $M_{\mathrm{A}}^{\mathrm{NC}}$ and $M_{\mathrm{A}}^{\mathrm{CC}}$. To allow for, and investigate, the effect of this in the joint NCEL and CCQE analysis, the fits have been repeated with two separate, and one common $M_{\mathrm{A}}^{\mathrm{eff}}$ parameter. This further highlights the difficulty of performing a sterile neutrino analysis with an inadequate cross section model.

Section 4.2 gives details about how the predicted distributions were produced for any value of the cross section or sterile models for both NCEL and CCQE samples. The fit details and results for the NCEL-only analysis are given in Section 4.3. The fit details and results for the joint NCEL and CCQE analysis are given in Section 4.4. Finally, some conclusions are drawn in Section 4.5.

4.2 Analysis method

4.2.1 Cross section model

The MiniBooNE cross section results are given in terms of reconstructed kinematic variables so that theorists can use them to test different models. To test oscillation hypotheses using these results a cross section model is required to relate the energy of the incoming neutrinos to the measured kinematic variables – oscillation results are dependent on the choice of cross section model. This analysis uses an RFG cross section model to simulate events on CH_2 (the MiniBooNE target material) with the GENIE interaction generator [167]. Although MiniBooNE and this analysis use different interaction generators with different cross section parameters, the cross section model parameters used in this analysis have been chosen to minimise this difference, with the aim of reproducing the MiniBooNE model as closely as possible.

MiniBooNE use NUANCE v3 as their neutrino interaction generator [259]; in the current work, GENIE 2.6.2 [167] was used. In NUANCE, the Llewellyn-Smith formalism [177] is used to describe neutral current scattering off free protons, and the Smith-Moniz RFG model [178] is used to describe both neutral current and charged current scattering off bound nucleons (CCQE interactions are all from bound neutrons). In GENIE, the

Bodek-Ritchie [262] RFG model[2] is used for CCQE, whereas NCEL interactions are modelled in the same way, but with the form factors described in Reference [190]. Although BBA03 [180] vector form factors could have been used in this analysis, BBBA05 [183] are the default in GENIE, reflecting a wider usage of the newer form factors, so the GENIE defaults were retained in this analysis. The MiniBooNE cross section model had a value[3] of $\Delta s = 0.0$; they make a measurement of this parameter in [77] of $\Delta s = 0.08 \pm 0.26$ which they point out is in agreement with the value measured by the BNL E734 experiment [190], which is the GENIE default value used in this analysis. A summary of the cross section models used by MiniBooNE and in this analysis are given in Table 4.1, further details for the MiniBooNE model can be found in [76, 78] from which the summary here has been drawn. $M_{\mathrm{A}}^{\mathrm{eff}}$ has not been included in Table 4.1 because the value is obtained through a fit in both of the analyses presented in this chapter, details of which are given in Sections 4.3.2 and 4.4.3.

	NUANCE	GENIE
Binding energy for ^{12}C	34.0 MeV	34.0 MeV
Fermi momentum in ^{12}C	220.0 MeV	221.0 MeV
Vector mass, M_{V}	850 MeV	850 MeV
Vector form factors	BBA03 [180]	BBBA05 [183]
Pauli blocking, κ	1.0220	1.0
Δs	0.0	-0.15

TABLE 4.1: Summary of cross section parameters used in the MiniBooNE analysis (NUANCE) and this analysis (GENIE).

While most cross section measurements are made using shape-only fits [202], including the normalisation uncertainty is important for the sterile neutrino fit performed in this analysis, so it would have been inconsistent to omit the normalisation uncertainty from the cross section fits performed here. As such, care must be taken when making comparisons between the results found here and published results.

4.2.2 Experimental details

The signal definition and experimental details relevant for this analysis are given in Table 4.2, and along with the flux prediction [254], are all of the details required to predict the true event rate in MiniBooNE for any given sterile hypothesis.

[2]The Bodek-Ritchie model is a slight enhancement to the Smith-Moniz RFG model. It includes a small tail of higher momentum nucleons in the initial state to model short range correlations between nucleons [262].

[3]The parameter Δs is the strange quark contribution to the spin of the nucleon. For a discussion of how it enters the NCEL cross section, see Section 2.2.3.

Property	MiniBooNE NCEL	MiniBooNE CCQE
Baseline L (m)	541	541
Peak neutrino energy (GeV)	0.788	0.788
Energy range (GeV)	$0 \leq E_\nu \leq 10$	$E_\nu \leq 3$
Signal events	$\nu_{\mu,e} + n, p \rightarrow \nu_{\mu,e} + n, p$	$\nu_\mu + n \rightarrow \mu^- + p$
POT	6.46×10^{20}	5.58×10^{20}
Integrated flux, Φ_ν (ν cm^{-2} POT^{-1})	5.22227×10^{-10}	5.16×10^{-10}
Target material	CH_2	CH_2

TABLE 4.2: Summary of the important experimental details for the two samples used in this analysis. Further details describing the NCEL sample can be found in [76, 77], and for the CCQE sample in [34, 78].

The MiniBooNE NCEL results are given as event rates in bins of T_{reco}, the sum of the reconstructed kinetic energies of final state nucleons, for which the full covariance matrix has been provided [77]. They are also available as a flux-averaged single-differential cross section in Q^2_{QE} bins, $\frac{d\sigma}{dQ^2_{\text{QE}}}$, but only bin errors are given: the covariance matrix is not included in the public release. It was found that attempting this analysis using the $\frac{d\sigma}{dQ^2_{\text{QE}}}$ results led to problems in the fit because correlations between the bins were not taken into account. The MiniBooNE estimations of the beam-related and beam-unrelated backgrounds are available with the T_{reco} results, and were used in this analysis (details are in Section 4.2.3.1). It is important to note that the effect of sterile neutrinos on the beam-related backgrounds was not taken into account in this analysis as there were insufficient details available to do so.

The CCQE results are given in several different ways: as a flux-averaged single-differential cross section in Q^2_{QE} bins, $\frac{d\sigma}{dQ^2_{\text{QE}}}$; as a flux-unfolded cross section as a function of neutrino energy, $\sigma\left[E_\nu^{\text{QE, RFG}}\right]$; and as a flux-averaged double-differential cross section as a function of the muon kinetic energy and scattering angle, $\frac{d^2\sigma}{dT_\mu d\cos\theta_\mu}$ [34]. The flux-unfolded cross section is dependent on the MiniBooNE cross section model, so was not appropriate for this analysis. Although the double-differential cross section contains more information than the single-differential cross section, the latter is more consistent with the presentation of the NCEL results, so was used in this analysis. The latter was also used to extract the value of $M_{\text{A}}^{\text{eff}}$ in the MiniBooNE analysis [34], and has been used in several published cross section fits [196, 263]. The covariance matrix was not made available for any of the published CCQE results, only bin errors were provided. The CCQE $\frac{d\sigma}{dQ^2_{\text{QE}}}$ results are given with backgrounds subtracted or signal fractioned out. It has been assumed that the beam-related backgrounds are correctly removed, and the effect of sterile neutrino oscillations on these backgrounds has been neglected.

4.2.3 Generating samples

To perform this analysis, it was necessary to vary the cross section and sterile model parameters simultaneously in a fit, in a computationally feasible way.

GENIE allows reweighting of cross section parameters, so a single sample produced at a fixed $M_{\mathrm{A}}^{\mathrm{eff}}$ can be used with the reweighting tools to investigate a range of $M_{\mathrm{A}}^{\mathrm{eff}}$ values. Event weights are produced for each incremental change in the cross section parameters being varied. By binning the weighted events into the desired kinematic variables, a plot of expected event rate per bin against the cross section parameter can be produced, which can then be interpolated to give a predicted event rate in each bin for any value of the cross section parameter in the range specified. For further details on event reweighting, refer to the GENIE documentation [167] (also the information on the GENIE webpages).

MiniBooNE provide detailed flux information [254], so it is trivial to produce the expected MiniBooNE flux under any sterile hypothesis by applying the equations in Section 1.4.1. Producing a predicted event rate in terms of kinematic variables from a predicted flux requires a migration matrix, where events are split into $(E_\nu, Q^2_{\mathrm{QE}})$ bins for the CCQE sample, and (E_ν, T_{true}) bins for the NCEL sample. By producing a sample with a flat flux distribution, it is possible to produce an expected event rate for any sterile hypothesis using the following method, where i denotes E_ν bins, and j denotes the kinematic variable binning:

1. Bin signal events into $(E_\nu, Q^2_{\mathrm{QE}})$ or (E_ν, T_{true}) bins to produce a two-dimensional histogram of signal events, S.
2. Bin all simulated events into E_ν bins to produce a histogram of all events R.
3. Produce a plot of the total cross section on the target molecule (CH_2) in E_ν bins, giving σ_i^{total} for all i.
4. Produce a modified flux histogram for the sterile hypothesis, Φ.
5. Find a scaling factor, ϵ_i for each energy bin i such that $R_i \times \epsilon_i = \sigma_i^{total}$.
6. Apply ϵ_i to S_i for all j.
7. Calculate $\Phi_i \times S_i$ for all j.
8. Project S onto the axis j, this is the expected event rate in terms of the kinematic variable.

Steps 1-6 are precalculated before fitting, which leaves S as a matrix of cross section values for each $(E_\nu, Q^2_{\mathrm{QE}})$ or (E_ν, T_{true}) bin. Figure 4.1 shows an example matrix, showing the cross section values in (E_ν, T_{true}) bins for the NCEL sample with $M_{\mathrm{A}}^{\mathrm{eff}} = 1.24$ GeV. Steps 7 and 8 are performed for each iteration of the fit, thus producing a predicted event rate in terms of the true values of the kinematic variables for each sterile hypothesis without having to produce a new sample at each iteration. A very large sample of 100 million neutrino interactions were produced with a flat flux with E_ν in the range $0 - 10$ GeV. Although computationally rather expensive, this was necessary to neglect the statistical error in the simulated samples.

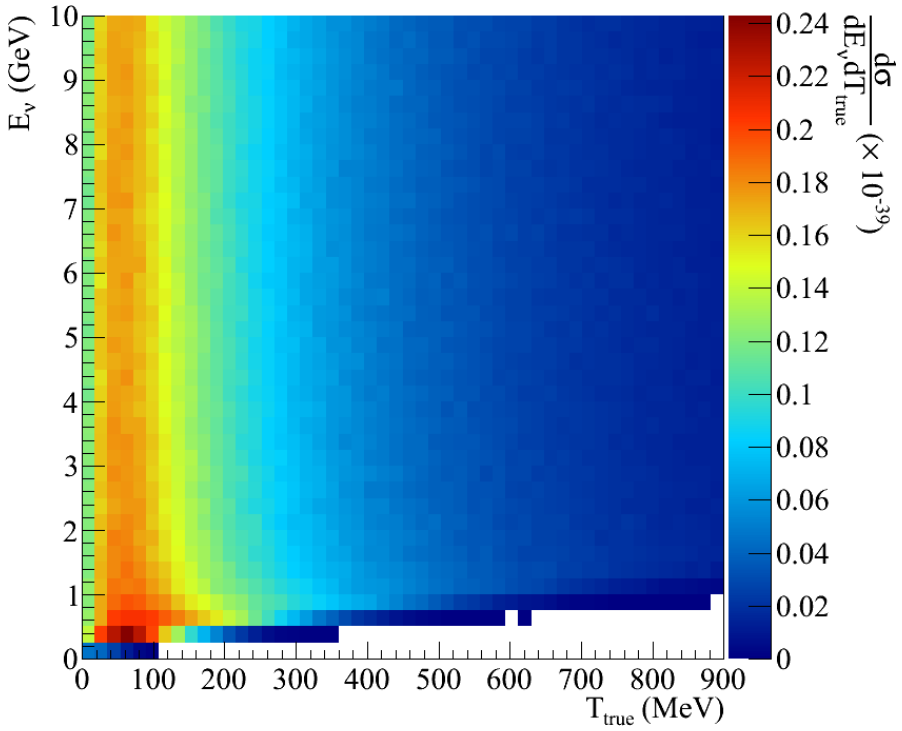

FIGURE 4.1: Shows an example migration matrix of cross section values for the NCEL prediction in (E_ν, T_{true}) bins for $M_{\mathrm{A}}^{\mathrm{eff}} = 1.24$ GeV.

It is trivial to combine the two methods described above to allow both the cross section and sterile model parameters to be varied in the fit: S becomes a three-dimensional matrix of cross section values, where the additional dimension is $M_{\mathrm{A}}^{\mathrm{eff}}$. At each iteration of the fit, the array of $M_{\mathrm{A}}^{\mathrm{eff}}$ values for each (E_ν, T_{true}) bin is used to form a spline, which can then be interpolated for any $M_{\mathrm{A}}^{\mathrm{eff}}$ value to give the cross section prediction in that (E_ν, T_{true}) bin. The two-dimensional matrix produced can then be dealt with as described in steps 7 and 8 above. Figure 4.2 shows the splines formed with the $M_{\mathrm{A}}^{\mathrm{eff}}$ values for various (E_ν, T_{true}) bins of the NCEL matrix.

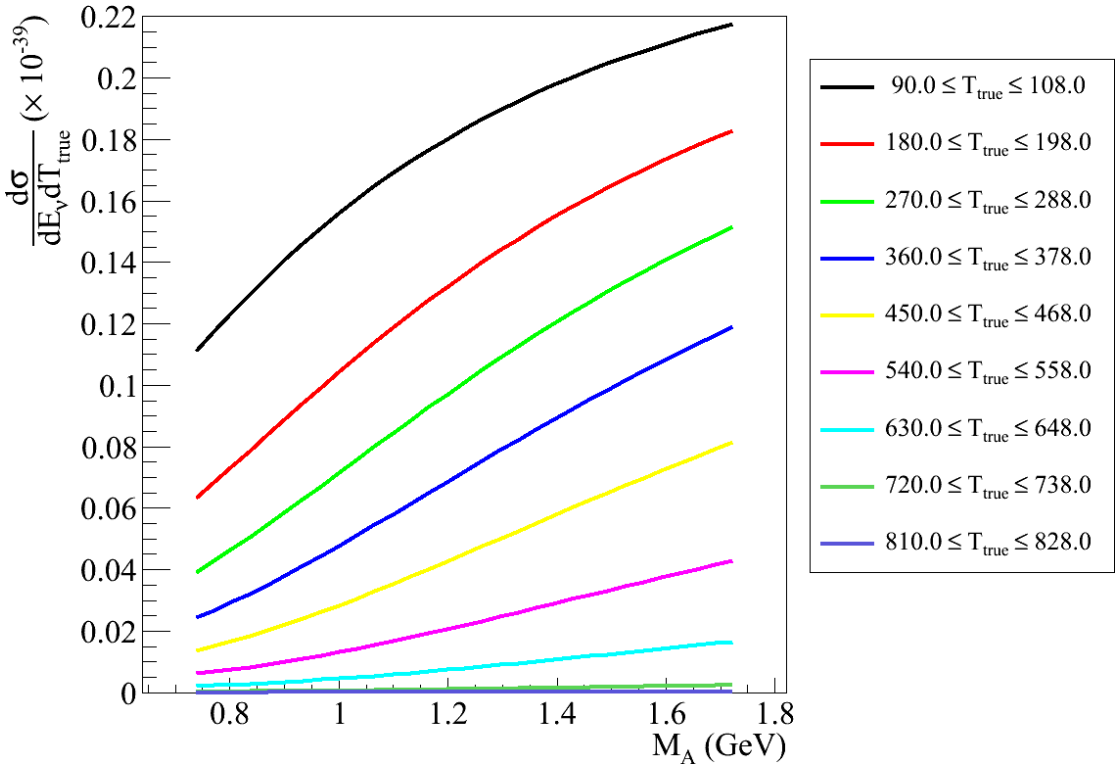

FIGURE 4.2: Example splines used to interpolate the M_A^{eff} values for various (E_ν, T_{true}) bins of the NCEL prediction. For each example shown, $1.00 \leq E_\nu \leq 1.25$ GeV.

4.2.3.1 NCEL comparison

The method outlined above gives a predicted event rate in terms of the *true* nucleon kinetic energy, T_{true}, whereas the NCEL results are given in terms of the *reconstructed* nucleon kinetic energy, T_{reco}, without removing the energy smearing and detector inefficiencies. To produce an expected event rate in T_{reco}, it is necessary to transform the T_{true} results (produced with the above method) using a response matrix, which simulates the detector inefficiencies and energy smearing. Appendix B of Reference [76] gives all of the necessary details to use the information released with Reference [77] to produce a response matrix.

The GENIE simulation used in this analysis simulates all potential signal events identified in [76] apart from the irreducible backgrounds. A combined response matrix for the simulated signal events is calculated as described, and used to transform the predicted T_{true} event rate into T_{reco} at each iteration of the fit. The T_{reco} event rate distributions from irreducible backgrounds and the beam-unrelated backgrounds are added to produce a final T_{reco} distribution which can be compared with the published MiniBooNE results. It should be stressed that the beam-unrelated, and more importantly, the irreducible beam-related background event rates are both MiniBooNE calculations included in the

data release, which therefore use the MiniBooNE cross section model, not the GENIE model used for the signal events in this analysis.

4.2.3.2 CCQE comparison

Turning the predicted event rate produced following the above method into $\frac{d\sigma}{dQ^2_{\mathrm{QE}}}$ is trivial as the two are related by Equation 4.1 [76, 78]:

$$\frac{d\sigma_i}{dQ^2_{\mathrm{QE}}} = \frac{\epsilon_i}{\Delta Q^2_i N_N N_{POT} \Phi_\nu}, \tag{4.1}$$

where the index i denotes the Q^2_{QE} bin, ϵ_i gives the predicted event rate in each bin, N_N is the total number of nucleons, N_{POT} is the number of protons on target corresponding to the sample used in the analysis, Φ_ν is the total integrated flux, and ΔQ^2_i is the width of the ith Q^2_{QE} bin.

4.2.3.3 Example plots

Figures 4.3 and 4.4 illustrate the effect that changing the single free cross section parameter and the value of Δm^2, respectively, have on the predicted NCEL and CCQE distributions, given set values of the other mixing parameters. These provide a visual confirmation that the analysis method and cross section model used in this analysis give sensible predictions. Both sets of plots show the comparisons with normalisation and shape-only; MiniBooNE data points taken from Reference [34, 77] are shown on the plots with normalisation included. The errors on the NCEL data points are the diagonal elements from the covariance matrix given in the data release.

It can be seen from 4.3a and 4.3c that an increasing $M_{\mathrm{A}}^{\mathrm{eff}}$ value only has a large effect on the shape of the predicted distributions at low T_{reco} and Q^2_{QE} bins respectively, though the overall normalisation increases with increasing $M_{\mathrm{A}}^{\mathrm{eff}}$ for both samples. It is also clear from Figure 4.3 that the CCQE sample favours a larger $M_{\mathrm{A}}^{\mathrm{eff}}$ in the model used in this analysis.

Because there are more variable sterile parameters, it is difficult to illustrate the effect that sterile parameters can have on the distribution. Figure 4.4 shows the effect that different values of Δm^2 have on the predicted distributions; the other parameters have been fixed for simplicity. $U_{\mu 4} = 0.4$ was chosen because it is around the limit placed by an analysis of atmospheric neutrinos for all values of Δm^2 [264, 265]; the other independent parameters, $U_{e4} = U_{\tau 4} = 0.2$, have been chosen as equal for simplicity and to keep the U_{s4} component large, as would be expected. These example sterile

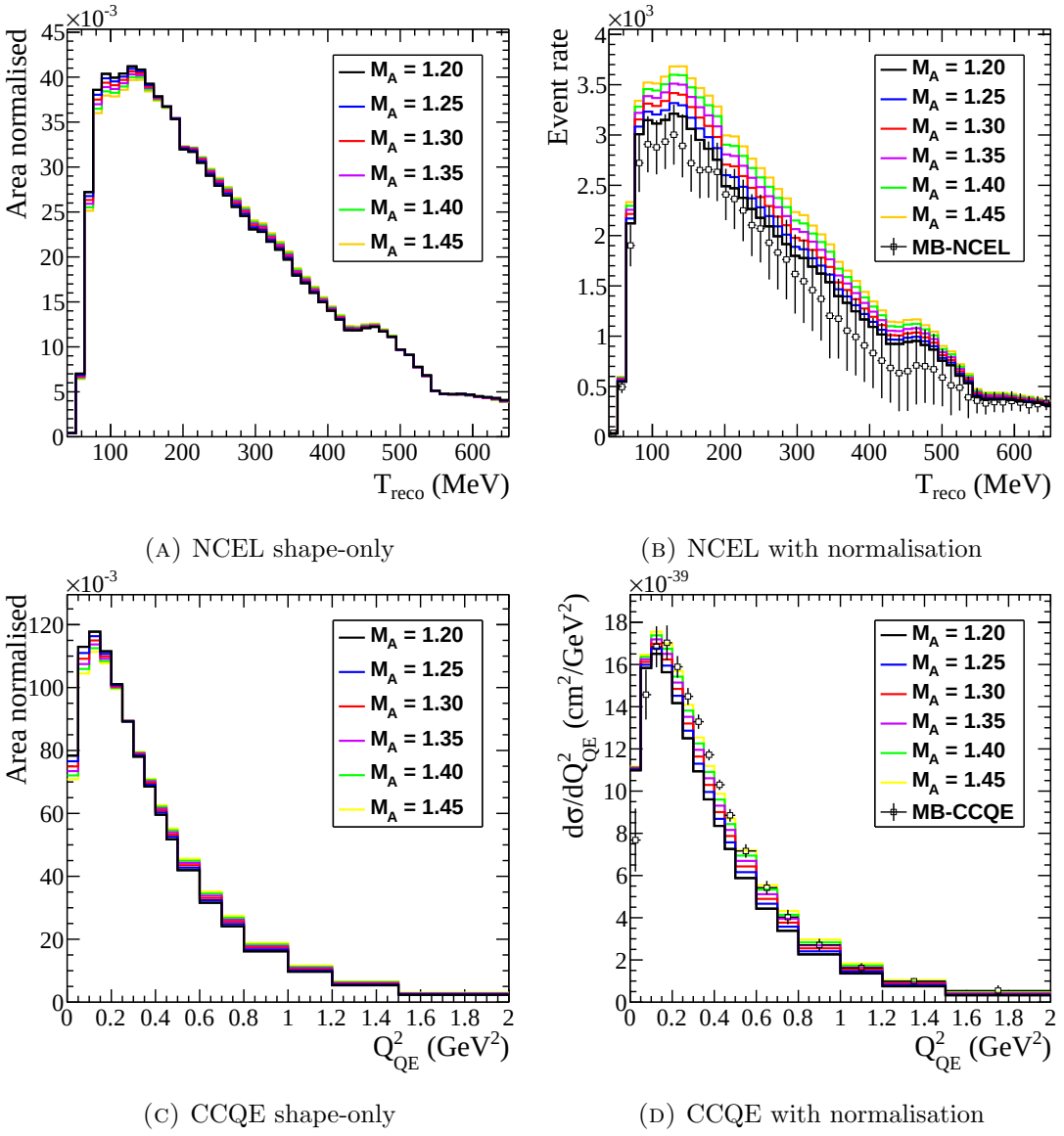

(A) NCEL shape-only

(B) NCEL with normalisation

(C) CCQE shape-only

(D) CCQE with normalisation

FIGURE 4.3: Shows the effect of varying M_A^{eff} on the predicted cross section measured for both NCEL and CCQE samples. Both shape-only (area normalised to unity), and normalised plots are shown. 'MB' is used as an abbreviation for 'MiniBooNE' in the figure legends.

parameters correspond to $\sin^2 2\vartheta_{\mu s} \approx 0.49$. The CCQE sample is easier to understand as it only depends on Δm^2 and $U_{\mu 4}$, and it is clear from Figure 4.4d why adding the CCQE sample can provide a strong constraint on $U_{\mu 4}$.

The NCEL sample is harder to visualise because it is affected by all of the sterile parameters, so the relationship of any one parameter to the T_{reco} distribution is less straightforward. If $U_{e4} = U_{\tau 4} = 0$, the effect of $U_{\mu 4}$ and Δm^2 is similar to the effect in the CCQE sample, but as U_{e4} or $U_{\tau 4}$ increases, the effect on the overall normalisation decreases. Because the sterile oscillations decrease the event rate more in the low T_{reco} bins, as seen in Figure 4.4b, this causes a subtle shift in the shape across the entire distribution as

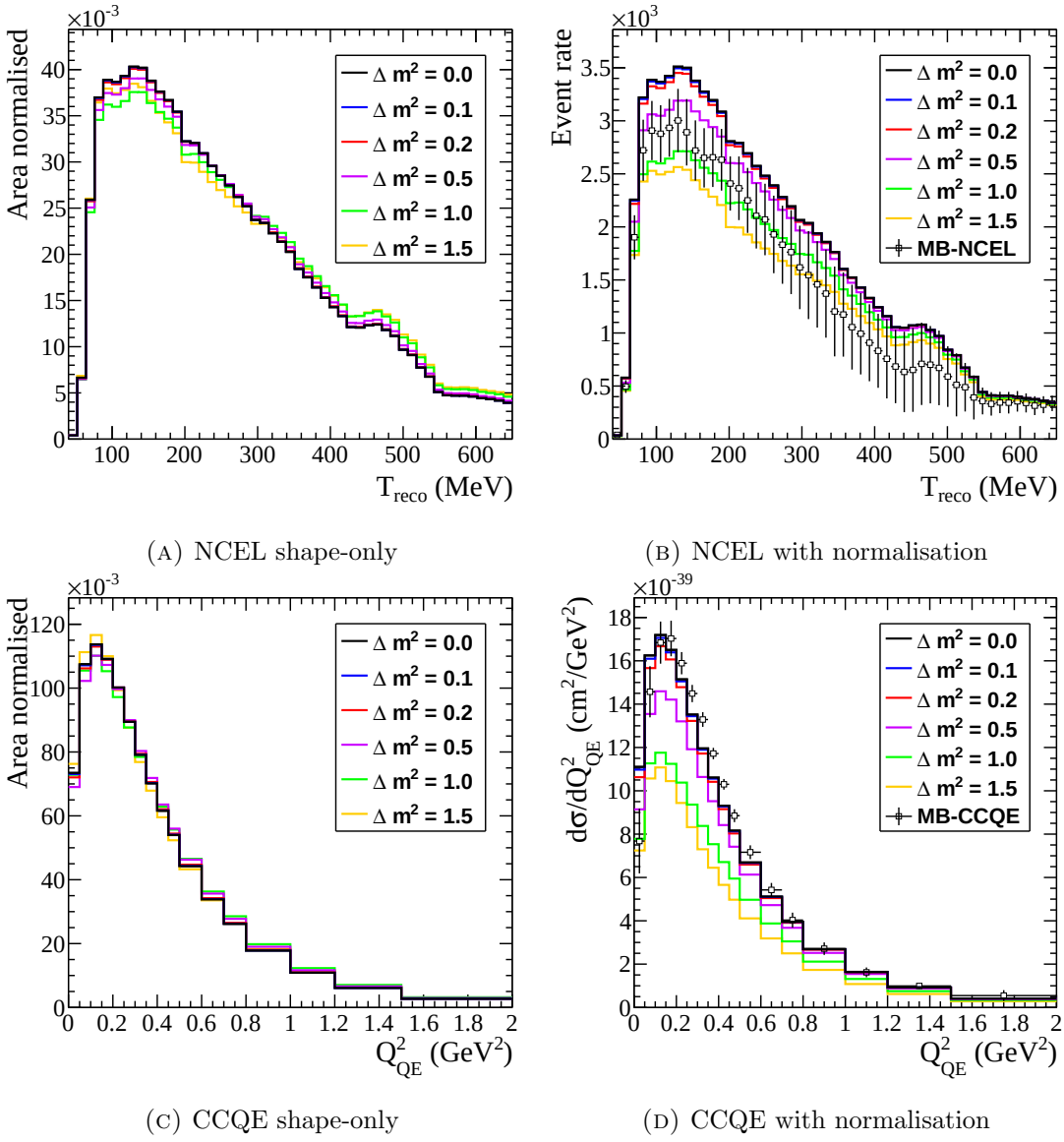

(A) NCEL shape-only

(B) NCEL with normalisation

(C) CCQE shape-only

(D) CCQE with normalisation

FIGURE 4.4: Shows the effect of varying the sterile parameter Δm^2 on the predicted cross section measured for the NCEL and CCQE samples, where the other sterile parameters have been fixed: $U_{\mu 4} = 0.4$, $U_{e4} = U_{\tau 4} = 0.2$. Both shape-only (area normalised to unity), and normalised plots are shown. 'MB' is used as an abbreviation for 'MiniBooNE' in the figure legends.

can be seen in Figure 4.4a. The effect on shape is complicated by the ν_e contamination in the beam, which causes differences in the way U_{e4} and $U_{\tau 4}$ affect the shape (because the shape of the ν_e flux is not the same as the ν_μ flux [254]). However, the effect that the ν_e contamination has on the shape is minimal as the contamination is only 0.52% of the total flux [254] (the ν_μ which forms the rest of the signal for the NCEL analysis is 93.6% of the total flux for reference). As an aside, it would be interesting to conduct a NC sterile search in a beam with more ν_e contamination to investigate the effect this has on the shape.

4.3 NCEL-only fit

4.3.1 Fitting procedure

The best fit points are obtained by minimising the $\chi^2(\vec{\mathbf{x}})$ statistics defined in Equation 4.2 and Equation 4.3, where $\vec{\mathbf{x}}$ are the parameters which are minimised in the fit. The minimisations were performed using the MINIMIZE algorithm (MIGRAD algorithm, reverting to the SIMPLEX algorithm if there is no convergence) in the MINUIT minimiser [266] within the ROOT framework [267]. The IMPROVE algorithm was used several times (alternating with calls to MINIMIZE) to ensure that the minimum in each case was global rather than local.

$$\chi^2(\vec{\mathbf{x}}) = \sum_{i=1}^{52}\sum_{j=1}^{52}\left(\nu_i^{DATA} - \nu_i^{MC}(\vec{\mathbf{x}})\right) V_{ij}^{-1} \left(\nu_j^{DATA} - \nu_j^{MC}(\vec{\mathbf{x}})\right) \tag{4.2}$$

Equation 4.2 is used in the simultaneous fit, where the free parameters $\vec{\mathbf{x}}$ are Δm^2, U_{e4}, $U_{\mu 4}$, $\sin^2 2\vartheta_{\mu s}$ and $M_{\mathrm{A}}^{\mathrm{eff}}$. It is also used in $M_{\mathrm{A}}^{\mathrm{eff}}$ only fit, where all of the sterile parameters are set to zero. V_{ij} is the 52×52 bin covariance matrix between T_{reco} bins, ν^{DATA} is the vector of values measured by MiniBooNE, and $\nu^{MC}(\vec{\mathbf{x}})$ is the vector of values predicted at each iteration of the fit.

$$\chi^2(\vec{\mathbf{x}}) = \sum_{i=1}^{52}\sum_{j=1}^{52}\left(\nu_i^{DATA} - \nu_i^{MC}(\vec{\mathbf{x}})\right) V_{ij}^{-1} \left(\nu_j^{DATA} - \nu_j^{MC}(\vec{\mathbf{x}})\right) + \left(\frac{\Delta \vec{M}_{\mathrm{A}}^{\mathrm{eff}}}{\sigma_{M_{\mathrm{A}}^{\mathrm{eff}}}}\right)^2 \tag{4.3}$$

Equation 4.3 is used in the sequential fit, where there is an additional penalty term which uses the one sigma error on $M_{\mathrm{A}}^{\mathrm{eff}}$, $\sigma_{M_{\mathrm{A}}^{\mathrm{eff}}}$, obtained in the $M_{\mathrm{A}}^{\mathrm{eff}}$ only fit, and $\Delta M_{\mathrm{A}}^{\mathrm{eff}}$ is the difference between the best fit value from the $M_{\mathrm{A}}^{\mathrm{eff}}$ only fit and the current value of $M_{\mathrm{A}}^{\mathrm{eff}}$.

4.3.2 $M_{\mathrm{A}}^{\mathrm{eff}}$ fit

The fit to $M_{\mathrm{A}}^{\mathrm{eff}}$ serves two purposes in this analysis. Firstly, as all of the sterile parameters are set to zero, it gives the χ^2 value of the null hypothesis. Secondly, it is used as an *in situ* cross section measurement to provide a penalty term on the value of $M_{\mathrm{A}}^{\mathrm{eff}}$ in the sequential fit. The error on $M_{\mathrm{A}}^{\mathrm{eff}}$ is calculated by moving the $M_{\mathrm{A}}^{\mathrm{eff}}$ value away from the best fit incrementally until $\Delta\chi^2 = 1$ [2].

Table 4.3 shows the best fit value of $M_{\mathrm{A}}^{\mathrm{eff}}$ found in this analysis, along with the calculated error. For comparison, the published MiniBooNE result [77] is included. The value found this analysis is lower than the published MiniBooNE result, which is probably due to

	χ^2	M_A^{eff} (GeV)	DOF
This analysis	32.1	1.24 ± 0.08	50
MiniBooNE [77]	26.9	1.39 ± 0.11	50

TABLE 4.3: Shows the best fit values for the M_A^{eff} only fit to the NCEL sample, along with the published MiniBooNE value for comparison.

differences in the generators. The increased Pauli blocking in the MiniBooNE cross section model and the different values of Δs between the generators have both been shown to have an effect on the calculated M_A^{eff} value [76, 77]. Also, the change between BBA03 and BBBA05 vector form factors cannot be neglected, which may also explain the slight difference observed.

4.3.3 Best fit results

Table 4.4 gives the best fit values for both the sequential and simultaneous fits. It is interesting that the best fit values are very different between sequential and simultaneous fits, indicating that there are correlations between the cross section and sterile model parameters. This highlights how the sequential fit method could mask a sterile signal: a low value of M_A^{eff} could compensate for disappearance in the signal due to sterile oscillations, masking the disappearance in the subsequent fit to the sterile parameters. It is also interesting that M_A^{eff} tends to a significantly higher value in the simultaneous fit, much higher than is expected.

	Sequential	Simultaneous
χ^2	27.717	23.684
Δm^2 (eV^2)	5.904	2.588
U_{e4}	0.570	0.474
$U_{\mu 4}$	0.707	0.745
$\sin^2 2\vartheta_{\mu s}$	0.349	0.490
M_A^{eff} (GeV)	1.307	1.714
DOF	47	46

TABLE 4.4: Best fit values for the NCEL-only fits.

The lowest values found during the parameter scans were used as initial values when calculating the best fit points. This reduced the computation time, and ensured that the fits did not become trapped in local minima as sometimes happened when fits were performed using randomly generated starting values for all parameters.

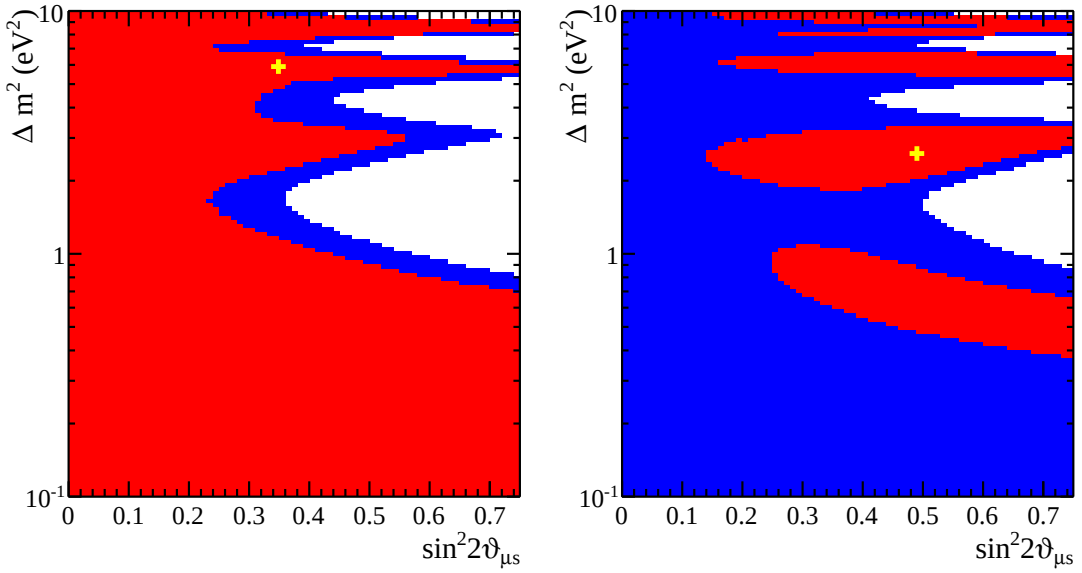

(A) NCEL sequential fit (B) NCEL simultaneous fit

FIGURE 4.5: Shows the exclusion plots produced by both the sequential and simultaneous fit techniques for the MiniBooNE NCEL dataset. The 90% region is shown in red, the 99% region is shown in blue, and the best fit point is indicated with a yellow cross.

4.3.4 Parameter scans

It can be seen from the equations in Section 1.4.1 that the value of $\sin^2 2\vartheta_{\mu s}$ depends on $U_{\mu 4}$ and U_{s4}, or equivalently on U_{e4}, $U_{\mu 4}$ and $U_{\tau 4}$ given the unitarity constraint $1 = |U_{e4}|^2 + |U_{\mu 4}|^2 + |U_{\tau 4}|^2 + |U_{s4}|^2$ [140]. The parameter U_{s4} cannot be measured directly as the NCEL measurement is not made in a pure ν_μ beam, so the latter combination must be used. This leaves a 4 dimensional sterile parameter space to scan, which would be very expensive computationally. Instead, the $\Delta m^2 - \sin^2 2\vartheta_{\mu s}$ plane is scanned, and the other sterile parameters are allowed to vary to minimise the χ^2 but whilst also obeying the unitarity constraint and the constraint imposed by fixing $\sin^2 2\vartheta_{\mu s}$. The unitarity constraint is enforced by including a severe penalty term in the χ^2, forcing the fitter into the physically allowed region.

χ^2 values for 9000 points in the $\Delta m^2 - \sin^2 \vartheta_{\mu s}$ plane were calculated, with 120 Δm^2 points distributed logarithmically in the region $0.1 \leq \Delta m^2 \leq 10$ eV^2 and 75 $\sin^2 \vartheta_{\mu s}$ points in the region $0.005 \leq \sin^2 \vartheta_{\mu s} \leq 0.745$ with spacing $\delta \sin^2 \vartheta_{\mu s} = 0.01$. The confidence regions are calculated using the constant $\Delta\chi^2$ method, $\chi^2_{allowed} \leq \chi^2_{min} + \Delta\chi^2$, where the best fit value χ^2_{min} is given in Table 4.4, and $\Delta\chi^2$ is calculated for 2 degrees of freedom: 4.61 for 90% confidence level; 9.21 for 99% confidence level [2].

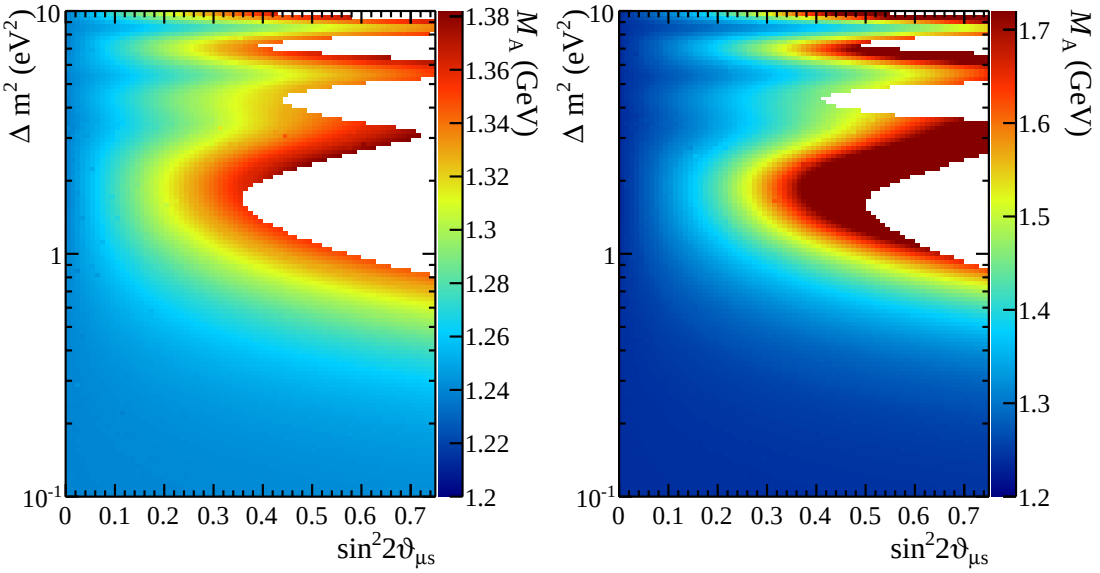

(A) NCEL sequential fit (B) NCEL simultaneous fit

FIGURE 4.6: Shows how the best fit value for M_A^{eff} varies with the sterile parameters across the 99% region.

The allowed regions for the sequential fit are shown in Figure 4.5a, and for the simultaneous fit in Figure 4.5b. The variation in the best fit values for M_A^{eff} across the 99% allowed regions is shown in Figure 4.6a for the sequential fit, and in Figure 4.6b for the simultaneous fit. Although the best fit value of the simultaneous fit is high, this is not the case for much of the allowed region.

4.3.5 Discussion

The M_A^{eff} only fit, shown in Section 4.3.2, gave a value, $M_A^{\text{eff}} = 1.24 \pm 0.08$ GeV, which is somewhat lower than the published MiniBooNE result of $M_A^{\text{eff}} = 1.39 \pm 0.11$ GeV; the differences between the two values can be understood in terms of the differences between the cross section models, and the different generators used. In particular, it was shown in Reference [76] that $M_A^{\text{eff}} = 1.24$ GeV with $\kappa = 0$ is consistent at 1σ with the MiniBooNE fit result of $M_A^{\text{eff}} = 1.39$ GeV and $\kappa = 1.022$. This is a useful sanity check for the method used to produce event rate predictions for this analysis.

Two fits to a 3+1 sterile neutrino model were performed: the sequential fit, which mimics previous MiniBooNE ν_μ-disappearance analyses [61,144,261] by implicitly assuming that the cross section and sterile neutrino model parameters are uncorrelated, and the simultaneous fit, where all parameters are fitted concurrently, making no assumption about the correlations between models. Given the current uncertainty surrounding neutrino cross section predictions, discussed in Section 4.1, it is not possible to use constraints on

$M_{\mathrm{A}}^{\mathrm{eff}}$ from other experiments as the effective axial mass is so dependent on experimental details. Until this uncertainty is resolved, the only consistent way to produce short baseline sterile neutrino limits is to perform a sequential or simultaneous fit as described here[4]. We find that the sequential and simultaneous fits produce different best fit values and contours, as can be seen in Figures 4.5b and 4.5a. This shows that for the NCEL dataset, it is wrong to assume that the sterile and cross section model parameters are uncorrelated. As such, it should be stressed that the sequential fit shown here is not valid.

It is, however, interesting to compare the contours produced by sequential and simultaneous fits. The sequential fit produced stronger limits in the $\Delta m^2 - \sin^2 2\vartheta_{\mu s}$ plane as would be expected if the sterile and cross section model parameters are correlated but not treated as such in the fit. Limits produced by sequential fits should be therefore be treated with caution unless it is shown that there are no correlations between models. Otherwise, the cross section parameters may be pulled so as to partially mask a signal, or a statistical fluctuation that mimics a signal. Of course, if we entertain a healthy scepticism about the existence of light sterile neutrinos, in this instance it is most likely that the effect is caused by deficiencies in the cross section model which no $M_{\mathrm{A}}^{\mathrm{eff}}$ value can account for, but which the sterile parameters can mimic. This is also a serious problem for sterile analyses because a false positive is more embarrassing than a false negative.

The 90% and 99% confidence regions produced by the simultaneous fit are shown in Figure 4.5b. These are the main result of this analysis and are the first short baseline oscillation results in the $\Delta m^2 - 2\sin^2\vartheta_{\mu s}$ plane. The 99% limits produced by this analysis are not particularly strong as a result of the freedom between the sterile mixing parameters U_{e4}, $U_{\mu 4}$ and $U_{\tau 4}$: a large change in one value can be countered by large changes in the others to diminish the effect on the signal. This analysis does find that the 3+1 model is favoured over no oscillations to greater than 90% confidence, which is an intriguing result. However the best fit point tends towards a value of $M_{\mathrm{A}}^{\mathrm{eff}}$ which is considerably higher than is found by other experiments [202], though it can be seen in Figure 4.6 that $M_{\mathrm{A}}^{\mathrm{eff}}$ is not as high for much of the allowed regions. The mass splitting of $\Delta m^2 = 2.588\ \mathrm{eV}^2$ at the best fit point is in conflict with global best fit values for 3+1 mixing models [132, 152, 153].

The comparison with other published sterile neutrino limits shown in Figure 4.7 highlights the disagreement with other datasets. Note that limits on $\sin^2 2\vartheta_{\mu\mu}$ have been treated as if they are limits on $\sin^2 2\vartheta_{\mu s}$ in Figure 4.7; this is justified because $\sin^2 2\vartheta_{\mu s} \leq \sin^2 2\vartheta_{\mu\mu}$. The MINOS NC limit [64, 65, 268] is only a strong constraint for a small range

[4] This is not the case if there is a near detector where oscillations can be neglected.

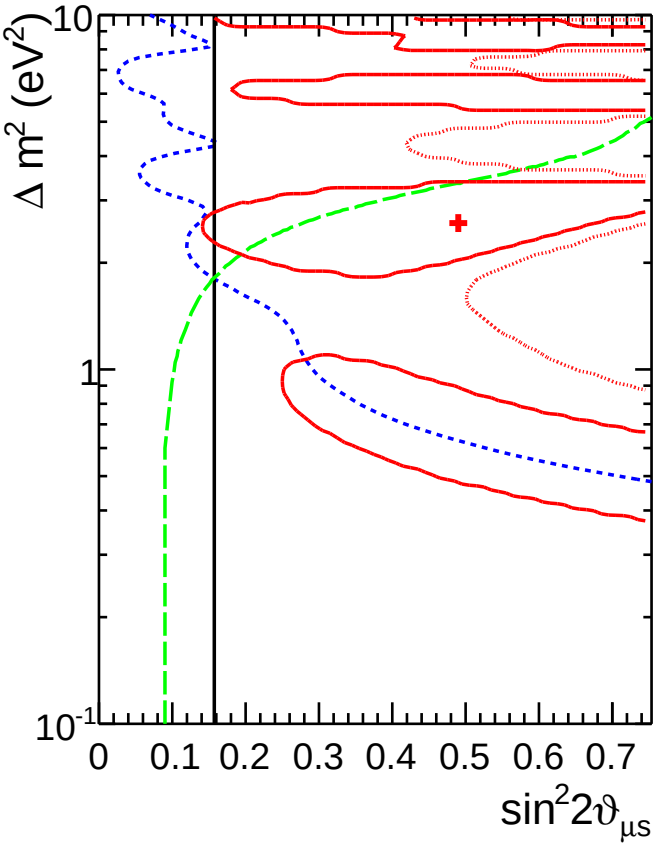

FIGURE 4.7: The 90% (99%) confidence region from the simultaneous fit to the MiniBooNE NCEL dataset is shown by the solid (dotted) red line), with the best fit point indicated by the red cross. Also shown are 90% confidence limits from other experiments: MiniBooNE-SciBooNE ν_μ-disappearance limits using the spectral fit method [61] (short dashed blue line); limits from the analysis of SK atmospheric data [62, 63] (black solid line); limits extracted in [64] from the MINOS NC-disappearance analysis [65] (long dashed green line). The authors of [64] consider oscillations in the MINOS near detector to set limits over a wider range of Δm^2 values using a two-parameters least-squares analysis, the limit given here is approximate as it is taken from the plot in the paper (Figure 6). For all open contours, the region to the right is excluded.

of Δm^2 because possible oscillations at the near detector weaken the limit, but their 90% limit excludes the best fit point we find in this analysis and some of our 90% allowed region. The MiniBooNE-SciBooNE limit depends implicitly on the value of $M_{\mathrm{A}}^{\mathrm{eff}}$ measured by the experiment, but MiniBooNE assert in [261] that the value of $M_{\mathrm{A}}^{\mathrm{eff}}$ is uncorrelated with the sterile model parameters. This is the most interesting comparison, as the difference between the NCEL and CCQE sterile analyses may point to a problem with the cross section model. The atmospheric constraint alone rules out much of the 90% preferred region in this analysis.

There are strong bounds on U_{e4} from reactor experiments (for a summary of reactor constraints, see References [152, 153]), which are not accounted for in this analysis. However, changes to U_{e4} can be almost fully compensated for by changes in $U_{\tau 4}$. The

only difference arises from the effect U_{e4} has on the small amount of ν_e contamination in the beam (less than 0.52% of the total flux [254]). Therefore including reactor constraints in the fit performed here would only have a minimal effect on the χ^2 value found at each fitted point, though the value for $U_{\tau 4}$ would increase and the value for U_{e4} would decrease. Strong constraints on both $U_{\tau 4}$ and U_{e4} would, however, affect the contours found in this analysis, which should be kept in mind if these results are used in a global fit.

4.4 Joint fit to NCEL and CCQE samples

4.4.1 Motivation

Although the NCEL-only sample can restrict the allowed sterile parameter space, it allows a lot of freedom between the matrix elements U_{e4}, $U_{\mu 4}$ and $U_{\tau 4}$. It has already been remarked that a large change in any one of these parameters can be partially compensated for by large changes in the others, so certain combinations of these parameters produce a lot of mixing between active species, but without a large overall disappearance in the NCEL signal. Strong limits on all three parameters are available from other experiments, so adding an additional constraint on one of them increases the power of the NCEL fit to constrain the $\Delta m^2 - \sin^2 2\vartheta_{\mu s}$ plane. Given that the MiniBooNE beam is predominantly ν_μ, an additional constraint on $U_{\mu 4}$ would be the most effective way to reduce the allowed parameter space with only one additional constraint. As previous limits on $U_{\mu 4}$ have been produced by MiniBooNE [261] using a CCQE event sample to look for $\nu_\mu \to \nu_\mu$ disappearance, including a MiniBooNE CCQE sample is the natural choice for an extension to the MiniBooNE NCEL analysis presented in Section 4.3. The single-differential MiniBooNE CCQE cross section measurement [34] is used as it allows for a consistent treatment with the NCEL results[5]. The structure of the joint CCQE-NCEL analysis is very similar to the NCEL-only sample, with the CCQE sample included in the fit as described in Section 4.2.

It should be noted that an $\sigma^{\mathrm{NCEL}}/\sigma^{\mathrm{CCQE}}$ ratio, differential in Q^2_{QE}, was made available in Reference [77], which would properly account for the correlations between the NCEL and CCQE samples. However, the covariance matrix is not part of the public data release; only central values and bin variances are available. As previously discussed, the NCEL bins are strongly correlated, so neglecting bin to bin correlations would have caused problems for the fit. No other information regarding correlations between the NCEL and CCQE samples has been released publicly, so they have been treated as uncorrelated in

[5] Note that a stronger constraint could be obtained with the double-differential results if one were interested in producing constraints using a MiniBooNE CCQE sample alone.

the joint analysis presented in this section. As the selection methods are very different for the NCEL and CCQE measurements [76,78], correlations in the detector systematics may be safe to neglect. However, the flux uncertainty will be strongly correlated between the samples, both in terms of the shape and overall normalisation uncertainty. An attempt was made to perform shape-only fits to the CCQE dataset to mitigate the effect of the common flux normalisation uncertainty, but this was found to cause difficulties, with the fits tending to very large overall normalisation factors.

Adding a CCQE sample introduces another complication to the cross section model used in the fit: whether to use one or two effective axial mass values, either a separate $M_{\mathrm{A}}^{\mathrm{NC}}$ and $M_{\mathrm{A}}^{\mathrm{CC}}$ for each sample, or a common $M_{\mathrm{A}}^{\mathrm{eff}}$. Although there is no theoretical reason to suggest different M_{A} values for NCEL and CCQE, the nuclear effects covered by an inflated $M_{\mathrm{A}}^{\mathrm{eff}}$ value may not be the same for NCEL and CCQE interactions. In practice, different $M_{\mathrm{A}}^{\mathrm{eff}}$ values are used by current experiments [76,78] to improve agreement with experimental data. To investigate this issue, both sequential and simultaneous fits have been performed for each possibility in this analysis.

4.4.2 Fitting procedure

The fitting procedure is similar as for the NCEL-only case, with χ^2 statistics defined in Equation 4.4, Equation 4.5, Equation 4.6 and Equation 4.7, where ξ is the CCQE normalisation factor and σ_ξ is the published one sigma uncertainty on the overall normalisation, 10.7% [34]. The indices i and j run over the 51 T_{reco} bins of the NCEL sample, and the index k runs over the 17 $\frac{d\sigma}{dQ^2_{\mathrm{QE}}}$ bins of the CCQE sample.

$$\chi^2(\vec{\mathbf{x}}) = \sum_{k=1}^{17} \left(\frac{\nu_k^{DATA} - \xi^{-1}\nu_k^{MC}(\vec{\mathbf{x}})}{\sigma_k} \right)^2 + \left(\frac{\xi - 1}{\sigma_\xi} \right)^2 \tag{4.4}$$

Equation 4.4 is used to fit the CCQE sample: this is used in the fit to $M_{\mathrm{A}}^{\mathrm{CC}}$, where the only free parameters $\vec{\mathbf{x}}$ are ξ and $M_{\mathrm{A}}^{\mathrm{CC}}$.

$$\begin{aligned}\chi^2(\vec{\mathbf{x}}) = &\left[\sum_{i=1}^{52}\sum_{j=1}^{52} \left(\nu_i^{DATA} - \nu_i^{MC}(\vec{\mathbf{x}})\right) V_{ij}^{-1} \left(\nu_j^{DATA} - \nu_j^{MC}(\vec{\mathbf{x}})\right) \right] \rightarrow \chi^2_{\mathrm{NCEL}}(\vec{\mathbf{x}}) \\ &+ \left[\sum_{k=1}^{17} \left(\frac{\nu_k^{DATA} - \xi\nu_k^{MC}(\vec{\mathbf{x}})}{\sigma_k} \right)^2 + \left(\frac{\xi - 1}{\sigma_\xi} \right)^2 \right] \rightarrow \chi^2_{\mathrm{CCQE}}(\vec{\mathbf{x}})\end{aligned} \tag{4.5}$$

Equation 4.5 is used in the simultaneous fits, where the free parameters $\vec{\mathbf{x}}$ are Δm^2, U_{e4}, $U_{\mu 4}$, $\sin^2 2\vartheta_{\mu s}$ and either $M_{\mathrm{A}}^{\mathrm{eff}}$ or $M_{\mathrm{A}}^{\mathrm{NC}}$ and $M_{\mathrm{A}}^{\mathrm{CC}}$ depending on the fit. It is also used in the fit to a single $M_{\mathrm{A}}^{\mathrm{eff}}$ value, where the free parameters $\vec{\mathbf{x}}$ are ξ and $M_{\mathrm{A}}^{\mathrm{CC}}$.

$$\begin{aligned}\chi^2(\vec{\mathbf{x}}) = &\left[\sum_{i=1}^{52}\sum_{j=1}^{52}\left(\nu_i^{DATA}-\nu_i^{MC}(\vec{\mathbf{x}})\right)V_{ij}^{-1}\left(\nu_j^{DATA}-\nu_j^{MC}(\vec{\mathbf{x}})\right)\right]\rightarrow\chi^2_{\mathrm{NCEL}}(\vec{\mathbf{x}})\\ &+\left[\sum_{k=1}^{17}\left(\frac{\nu_k^{DATA}-\xi\nu_k^{MC}(\vec{\mathbf{x}})}{\sigma_k}\right)^2+\left(\frac{\xi-1}{\sigma_\xi}\right)^2\right]\rightarrow\chi^2_{\mathrm{CCQE}}(\vec{\mathbf{x}})\\ &+\left[\left(\frac{\Delta M_{\mathrm{A}}^{\mathrm{eff}}}{\sigma_{M_{\mathrm{A}}^{\mathrm{eff}}}}\right)^2\right]\rightarrow\chi^2_{M_{\mathrm{A}}^{\mathrm{eff}}}\end{aligned}\tag{4.6}$$

Equation 4.6 is used in the sequential fits with one common $M_{\mathrm{A}}^{\mathrm{eff}}$ value, where $\sigma_{M_{\mathrm{A}}^{\mathrm{eff}}}$ is the one sigma error calculated in the $M_{\mathrm{A}}^{\mathrm{eff}}$ only fit and $\Delta M_{\mathrm{A}}^{\mathrm{eff}}$ is the difference between the current $M_{\mathrm{A}}^{\mathrm{eff}}$ value and the best fit from the$M_{\mathrm{A}}^{\mathrm{eff}}$ only fit.

$$\begin{aligned}\chi^2(\vec{\mathbf{x}}) = &\left[\sum_{i=1}^{52}\sum_{j=1}^{52}\left(\nu_i^{DATA}-\nu_i^{MC}(\vec{\mathbf{x}})\right)V_{ij}^{-1}\left(\nu_j^{DATA}-\nu_j^{MC}(\vec{\mathbf{x}})\right)\right]\rightarrow\chi^2_{\mathrm{NCEL}}(\vec{\mathbf{x}})\\ &+\left[\sum_{k=1}^{17}\left(\frac{\nu_k^{DATA}-\xi\nu_k^{MC}(\vec{\mathbf{x}})}{\sigma_k}\right)^2+\left(\frac{\xi-1}{\sigma_\xi}\right)^2\right]\rightarrow\chi^2_{\mathrm{CCQE}}(\vec{\mathbf{x}})\\ &+\left[\left(\frac{\Delta M_{\mathrm{A}}^{\mathrm{NC}}}{\sigma_{M_{\mathrm{A}}^{\mathrm{NC}}}}\right)^2\right]\rightarrow\chi^2_{M_{\mathrm{A}}^{\mathrm{NC}}}\\ &+\left[\left(\frac{\Delta M_{\mathrm{A}}^{\mathrm{CC}}}{\sigma_{M_{\mathrm{A}}^{\mathrm{CC}}}}\right)^2\right]\rightarrow\chi^2_{M_{\mathrm{A}}^{\mathrm{CC}}}\end{aligned}\tag{4.7}$$

Equation 4.7 is used in the sequential fits with separate $M_{\mathrm{A}}^{\mathrm{NC}}$ and $M_{\mathrm{A}}^{\mathrm{CC}}$ values, where $\sigma_{M_{\mathrm{A}}^{\mathrm{NC}}}$ and $\sigma_{M_{\mathrm{A}}^{\mathrm{CC}}}$ are the one sigma errors calculated in the $M_{\mathrm{A}}^{\mathrm{NC}}$ and $M_{\mathrm{A}}^{\mathrm{CC}}$ only fits, and $\Delta M_{\mathrm{A}}^{\mathrm{NC}}$ and $\Delta M_{\mathrm{A}}^{\mathrm{CC}}$ are the difference between the current $M_{\mathrm{A}}^{\mathrm{NC}}$ and $M_{\mathrm{A}}^{\mathrm{CC}}$ values and the best fit values found in the $M_{\mathrm{A}}^{\mathrm{NC}}$ and $M_{\mathrm{A}}^{\mathrm{CC}}$ only fits.

4.4.3 $M_{\mathrm{A}}^{\mathrm{eff}}$ fits

As in the NCEL-only case, the $M_{\mathrm{A}}^{\mathrm{eff}}$ only fits are intended to replicate the *in situ* cross section measurements made by experiments before producing sterile neutrino limits. As all of the sterile parameters are set to 0, it also gives the χ^2 value of the no mixing hypothesis. The calculated values are summarised in Table 4.5, along with the published

MiniBooNE values. The error on M_A^{eff} is found in each case by moving M_A^{eff} away from the best fit value incrementally until $\Delta\chi^2 = 1$. The value of M_A^{NC} was previously calculated in Section 4.3.2.

	Fit	χ^2	M_A^{eff} (GeV)	DOF
This analysis	NCEL	32.1	1.24 ± 0.08	50
	CCQE	20.2	1.46 ± 0.05	16
	Combined	57.0	1.40 ± 0.04	57
MiniBooNE	NCEL [77]	26.9	1.39 ± 0.11	50
	CCQE [34]	-	1.35 ± 0.17	16

TABLE 4.5: Shows the best fit parameter values for each of the M_A^{eff} fits performed in the joint CCQE and NCEL analysis, and the published MiniBooNE values for comparison.

The published value of M_A^{CC} is found using a shape-only fit and also fits an enhanced Pauli blocking factor [34], whereas the one calculated in this analysis includes the overall normalisation factor. The published result included bin to bin correlations in the fit which were not made publicly available. The value found in this analysis is consistent with the published result, and is consistent with other fits to the MiniBooNE CCQE dataset [195]. The smaller error is due to the lack of correlations available for the CCQE dataset.

4.4.4 Best fit results

As described in Section 4.3.3 for the NCEL-only fit, the best fit values were calculated using the minimum found during the parameter scan as an initial value. This was done to help guide the fitter to the minimum as the function being minimised is very complicated, and guiding the fit initially to the best fit point found in the grid search reduced the computation time, and ensured that the fits did not become trapped in a local minimum as sometimes happened when a fit was performed using randomly generated starting values for all parameters. The best fit results for all of the different fits are given in Table 4.6.

The difference in the best fit parameter values between simultaneous and sequential fits is similar to that seen in the NCEL-only fit (Table 4.4). Table 4.6 shows that the simultaneous fits have a lower χ^2 value at the best fit point as expected. The M_A^{eff} value(s) tend to much higher values when unconstrained, which is compensated for by larger best fit values for the sterile mixing parameters U_{e4}, $U_{\mu 4}$ and $\sin^2 2\vartheta_{\mu s}$. It is clear that treating the cross section and sterile parameters as uncorrelated is not justified in this case.

Fit Description	Sequential		Simultaneous	
	M_A^{NC} and M_A^{CC}	M_A^{eff}	M_A^{NC} and M_A^{CC}	M_A^{eff}
χ^2 /DOF	47.3/47	46.8/47	44.1/45	44.6/46
Δm^2 (eV^2)	0.32	0.38	2.75	2.74
U_{e4}	5.10×10^{-2}	4.84×10^{-7}	3.86×10^{-2}	2.71×10^{-7}
$U_{\mu4}$	0.50	0.46	0.33	0.34
$\sin^2 2\vartheta_{\mu s}$	0.74	0.74	0.38	0.40
M_A^{NC} (GeV)	1.26	-	1.52	-
M_A^{CC} (GeV)	1.43	-	1.62	-
M_A^{eff} (GeV)	-	1.38	-	1.62
CCQE Norm	1.10	1.16	1.24	1.26

TABLE 4.6: Gives the best fit values for all of the sequential fits performed. Each fit uses the relevant M_A^{eff} values and errors calculated in Table 4.5.

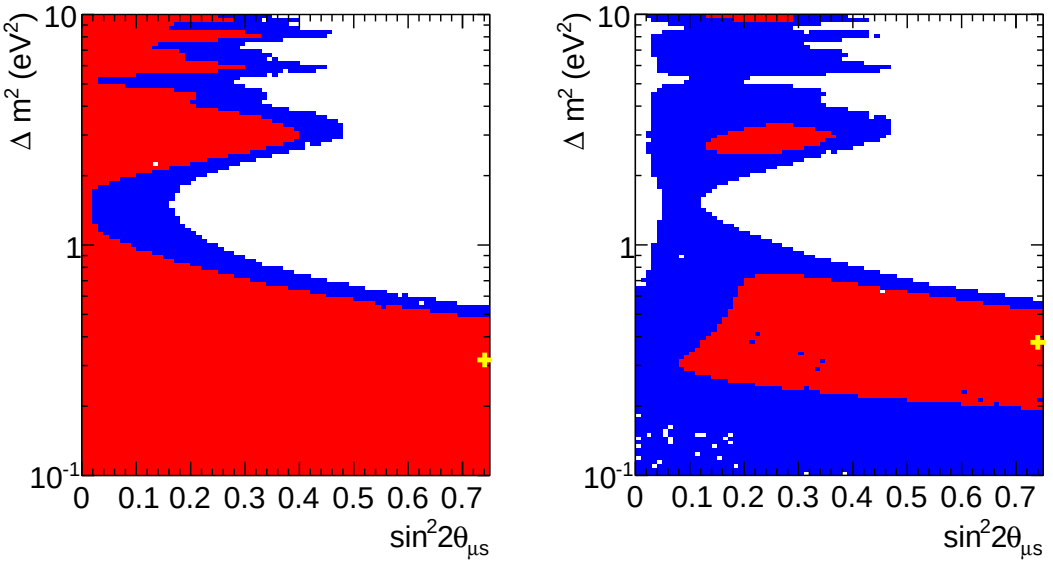

(A) Joint sequential fit, M_A^{NC} and M_A^{CC} (B) Joint sequential fit, common M_A^{eff}

FIGURE 4.8: Shows the exclusion plots produced by both the sequential fits to both datasets, with either one common M_A^{eff} or two effective values, M_A^{NC} and M_A^{CC}. The 90% region is shown in red, the 99% region is shown in blue, and the best fit point is indicated with a cross.

4.4.5 Parameter scans

The parameter scans were carried out as described for the NCEL-only fit in Section 4.3.4, with χ^2 statistics given in Section 4.4.2.

Figure 4.8 gives the 90% and 99% confidence regions in the $\Delta m^2 - \sin^2 2\vartheta_{\mu s}$ plane for the sequential fits to both NCEL and CCQE datasets. It is clear that adding the

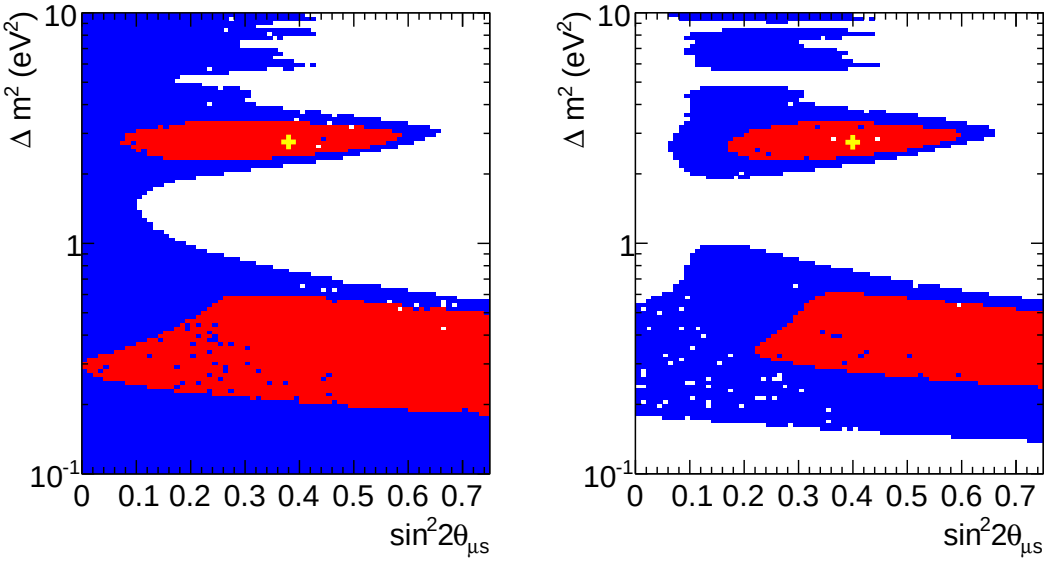

(A) Joint simultaneous fit, M_A^{NC} and M_A^{CC} (B) Joint simultaneous fit, common M_A^{eff}

FIGURE 4.9: Shows the exclusion plots produced by both the simultaneous fits to both datasets, with either one common M_A^{eff} or two effective values, M_A^{NC} and M_A^{CC}. The 90% region is shown in red, the 99% region is shown in blue, and the best fit point is indicated with a cross.

CCQE sample gives stronger limits than for the NCEL-only case (Figure 4.5). However, using one M_A^{eff} value common to both NCEL and CCQE (Figure 4.8b) increases the sterile mixing compared with the NCEL-only sequential fit (Figure 4.5a) or the fit to both NCEL and CCQE with two M_A^{eff} values (Figure 4.8a). This is because the CCQE sample drives M_A^{eff} to a higher value than NCEL prefers, and thus increased mixing is preferred to also fit the NCEL data. This highlights the difficulty of using an external constraint on M_A^{eff} for sterile neutrino measurements when the underlying cross section is not well understood. Different measurements at the same experiment do not agree.

Figure 4.9 gives the 90% and 99% confidence regions in the $\Delta m^2 - \sin^2 2\vartheta_{\mu s}$ plane for the simultaneous fits to both NCEL and CCQE datasets. It has already been shown that performing a simultaneous fit for the NCEL-only sample led to closed 90% contours (see Figure 4.5b), and the addition of the CCQE dataset has limited the allowed parameter space significantly. As with the sequential case, fitting the NCEL and CCQE samples to one value of M_A^{eff} leads to a shift to higher values of $\sin^2 2\vartheta_{\mu s}$.

Figure 4.10 shows the variation of the best fit value for M_A^{eff} across the 99% allowed regions in the $\Delta m^2 - \sin^2 2\vartheta_{\mu s}$ plane for both simultaneous and sequential fits with a single M_A^{eff} parameter.

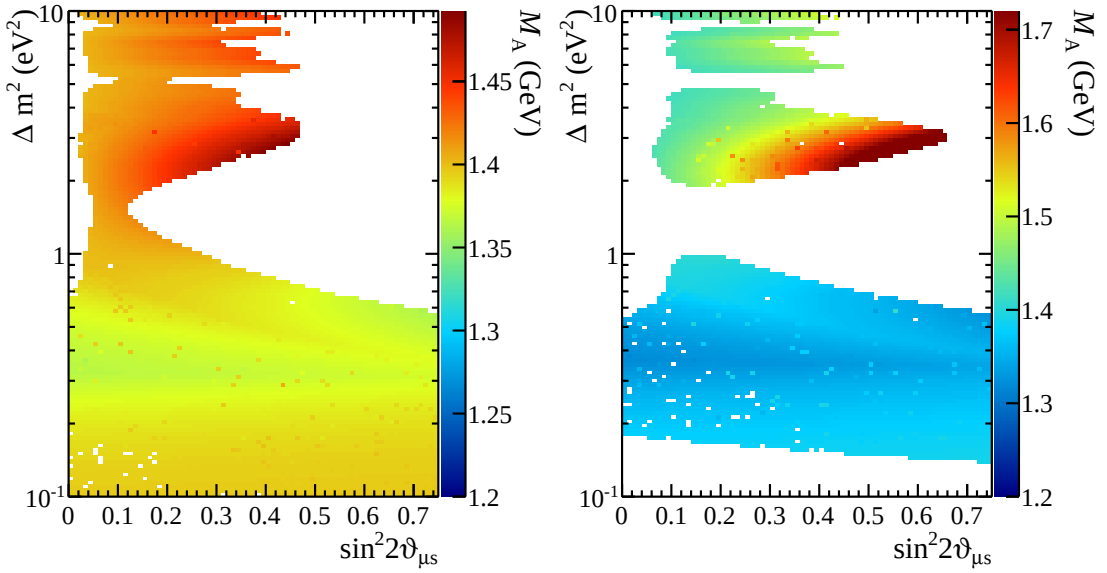

(A) Joint sequential fit

(B) Joint simultaneous fit

FIGURE 4.10: Shows how the best fit value of M_A^{eff} changes across the 99% allowed regions for sequential and simultanous fits to both the NCEL and CCQE datasets with a common M_A^{eff} value.

4.4.6 Discussion

The CCQE sample appears to dominate the M_A^{eff} value from the combined fit. This is to be expected given the greater effect that changes in M_A^{eff} has on the CCQE shape, as shown in Figure 4.3, and the greater normalisation uncertainty in the NCEL sample compared with the CCQE sample, 18.1% [77] and 10.7% [34] respectively. However, the result may be biased by the lack of correlations for the CCQE sample. The best fit values for M_A^{eff} for both NCEL and CCQE are consistent with the values published by MiniBooNE, as can be seen in Table 4.5.

As for the NCEL-only fit, two types of fit to a 3+1 sterile model were performed. The sequential fit mimics previous analyses by fitting first to the cross section model and then to the sterile neutrino model, and the simultaneous fit floats the parameters from both cross section and sterile neutrino models simultaneously. As in the NCEL-only case, the joint fit to NCEL and CCQE produced different results for the sequential and simultaneous type fits, implying that the sterile and cross section moel parameters are not independent. Of course, this means that the sequential fit results should not be trusted. It can be seen by comparing Figures 4.8 and 4.9 with Figure 4.5 that both sequential and simultaneous joint fit results show confidence limits which are stronger than for the NCEL-only fit, due to the additional constraint on $U_{\mu 4}$ from the CCQE dataset.

The choice of one or two effective M_A^{eff} values has a considerable impact on the results, as shown by comparing Figures 4.8a and 4.8b (sequential) or Figures 4.9a and 4.9b (simultaneous). It is clear that such ad hoc modifications to the RFG model affect the sterile limits produced. As most cross section models use different M_A^{eff} values for different processes, it is reasonable to conclude that the fit to M_A^{NC} and M_A^{CC} more closely matches the usual practice for producing sterile neutrino results. However, it further highlights the problems with sterile neutrino limits which rely on a cross section model in which we do not have much confidence [195, 196, 202].

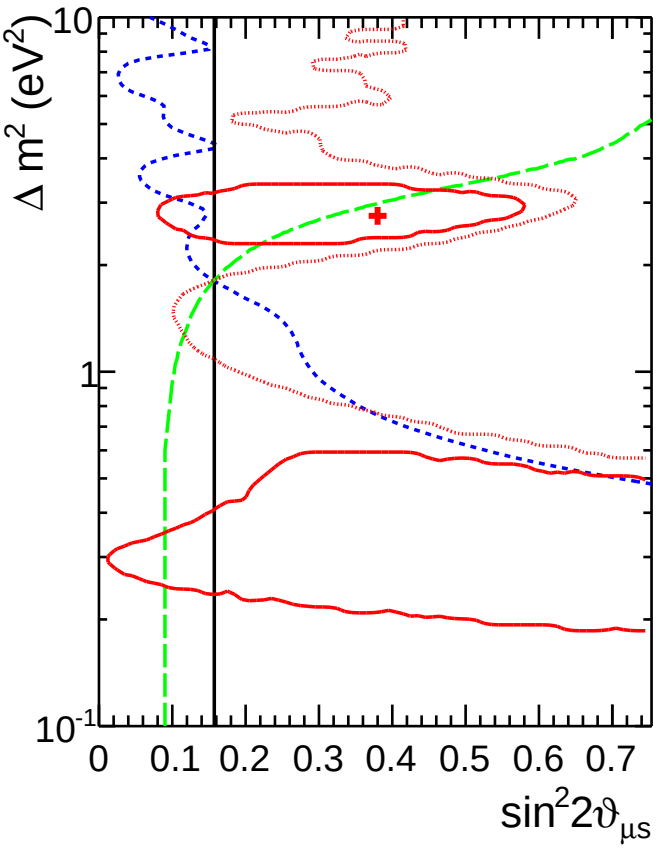

FIGURE 4.11: The 90% (99%) confidence region from the simultaneous fit to both the MiniBooNE NCEL and CCQE datasets is shown by the solid (dotted) red line, with the best fit point indicated by the red cross. Note that the results shown here are with separate values of M_A^{eff} for each channel. Also shown are 90% confidence limits from other experiments: MiniBooNE-SciBooNE ν_μ-disappearance limits using the spectral fit method [61] (short dashed blue line); limits from the analysis of SK atmospheric data [62, 63] (black solid line); limits extracted in [64] from the MINOS NC-disappearance analysis [65] (long dashed green line). The authors of [64] consider oscillations in the MINOS near detector to set limits over a wider range of Δm^2 values using a two-parameters least-squares analysis, the limit given here is approximate as it is taken from the plot in the paper (Figure 6). For all open contours, the region to the right is excluded.

It is clear that the simultaneous rather than the sequential fit should be preferred, and that having two M_A^{eff} values produces more conservative limits on sterile neutrino mixing

than a single common $M_{\mathrm{A}}^{\mathrm{eff}}$ value for NCEL and CCQE. The 90% and 99% limits from the corresponding joint fit are compared with existing sterile neutrino limits in Figure 4.11. It is clear, as in the NCEL-only case shown in Figure 4.7, that the limits from this analysis contradict other limits available. It is important to stress that these are the first limits from a short baseline experiment in the $\Delta m^2 - \sin^2 2\vartheta_{\mu s}$ plane, and that such strong disagreement is also seen by other experiments which test the 3+1 sterile model in a different way. The other experiments included in Figure 4.11 were discussed in Section 4.3.5.

4.5 Conclusions

This analysis has produced the first ever limits on 3+1 sterile neutrino mixing in the $\Delta m^2 - \sin^2 2\vartheta_{\mu s}$ plane using MiniBooNE NCEL and CCQE data. The assumption that $M_{\mathrm{A}}^{\mathrm{eff}}$ is uncorrelated with sterile mixing parameters was tested by performing sequential fits, where $M_{\mathrm{A}}^{\mathrm{eff}}$ was fitted to the dataset before the sterile model. If the cross section and sterile neutrino models are uncorrelated, this procedure would produce the same results as a simultaneous fit, where all model parameters are varied at the same time without prior constraints. However, this analysis finds that the sequential and simultaneous fits tend to very different best fit values, and produce very different limits, for fits to the NCEL dataset only, and the joint CCQE and NCEL dataset. It is therefore important to stress that only the simultaneous fit is statistically justified in the MiniBooNE NCEL and CCQE case. Although the shortcomings of the sequential fit may be expected, the method reflects how sterile neutrino fits are currently being performed [61, 144, 261]. As $M_{\mathrm{A}}^{\mathrm{eff}}$ is an effective parameter which varies by experiment and signal channel, each experiment must constrain $M_{\mathrm{A}}^{\mathrm{eff}}$ as well as the sterile model. This result demonstrates that it is extremely difficult to produce sterile neutrino mixing limits when there are severe inadequacies in the cross section model, as has been discussed elsewhere [260]. It is no longer sufficient for short baseline experiments to produce sterile neutrino limits under a tacit assumption that the cross section model will not affect the results. It is also difficult for global fits to sterile neutrino experiments to account for the different cross section models used, which may bias global fit results.

The results produced in the NCEL-only analysis are described in Section 4.3 and shown in the $\Delta m^2 - \sin^2 2\vartheta_{\mu s}$ plane in Figure 4.7. The limits are conservative because of the treatment of $M_{\mathrm{A}}^{\mathrm{eff}}$ in the simultaneous fit, and the correlations are properly taken into account as the covariance matrix is included in the public data release [77]. Much stronger limits in the same plane are produced by adding an additional CCQE sample and performing a joint fit to CCQE and NCEL as described in Section 4.4, and shown

in Figure 4.11. It should be kept in mind that possible correlations between the NCEL and CCQE samples were not accounted for, and only bin variances were available for the CCQE sample, the covariance matrix was not part of the public data release [34]. Ad hoc modifications to the RFG models have been discussed here and elsewhere [196,202], and the effect of using one or two effective axial mass values has been investigated as part of the joint fit analysis. The sterile limits produced using a single $M_{\mathrm{A}}^{\mathrm{eff}}$ value favour more mixing than those produced using two effective axial mass values, $M_{\mathrm{A}}^{\mathrm{NC}}$ and $M_{\mathrm{A}}^{\mathrm{CC}}$, which further highlights the need for extreme caution when interpreting sterile neutrino limits using the RFG model. The fit with two effective axial mass values is more conservative, so has been favoured as the final result of this analysis.

The limits produced in both analyses are clearly at odds with other external data when interpreted in the context of a 3+1 sterile neutrino model, and conflict with the values favoured by global best fits [132, 152, 153]. It should be noted that there is a great deal of tension in the 3+1 model already (discussed in Section 1.5), so finding tension is no great surprise. The tension between neutral current disappearance and existing ν_μ-disappearance limits shown in Figures 4.7 and 4.11 may be an interesting new way to constrain more exotic sterile neutrino models in global fits. That said, we note that the 99% confidence limits placed by this analysis are not very strong, and accurately assessing and interpreting tension from a plot of 90% confidence limits is very difficult.

Although the 90% contours are interesting, it is prudent to sound a further note of caution. There are two possible issues for this and other sterile analyses which may cause these differences. First, it is possible that the NCEL and CCQE datasets are insufficient to constrain both the cross section and sterile neutrino model parameters, particularly when each must constrain an $M_{\mathrm{A}}^{\mathrm{eff}}$ value. Second, it is possible that the differences between this analysis and ν_μ-disappearance analyses are caused by the inadequacies of the RFG model. Here we followed the assertion made in [191] that an inflated $M_{\mathrm{A}}^{\mathrm{eff}}$ is a reasonable, though ad hoc, way to model the additional multi-nucleon effects. If this is not the case, the differences between multi-nucleon contributions will affect the sterile neutrino fit, and this effect may not be the same for NCEL and CCQE selections, which could explain the different preferred values for the sterile parameters found through sterile fits to these datasets.

Chapter 5

Charged-Current Quasi-Elastic (CCQE) external data fits

This chapter describes a fit of the NEUT Charged-Current Quasi-Elastic (CCQE) cross section model to external CCQE data, which has been documented in two internal T2K technical notes [269, 270]. Some of the work described in this chapter was presented in Reference [271]. The primary purpose of the work is to constrain CCQE cross section systematics for T2K oscillation analyses. It is a major update to work done in 2012 [272, 273] which produced CCQE cross section systematics for T2K oscillation analyses from 2012 to February 2015 [73,123,124,128]. The previous work fitted only $M_{\mathrm{A}}^{\mathrm{eff}}$ and a CCQE normalisation parameter to MiniBooNE neutrino mode data, and found an inflated value for the axial mass[1], $M_{\mathrm{A}}^{\mathrm{eff}} = 1.64 \pm 0.03$ GeV, in keeping with other analyses which rely on RFG models with no additional nuclear effects [34, 195]. The issue of the large axial mass measured by MiniBooNE and other experiments was discussed in Section 2.3.

Since the 2012 CCQE fits, three new CCQE datasets (described in detail in Section 5.2.1) have been made available by MINERνA and MiniBooNE. There has also been a great deal of recent theoretical work into CCQE cross sections, which has led to the development of many new models as described in Section 2.4. T2K's Neutrino Interaction Working Group (NIWG) has implemented a number of these models into NEUT to make a more realistic CCQE model available for use in T2K analyses.

The fits described in this chapter use all available CCQE data to select a default model from those now available in NEUT, and to produce uncertainties for the parameters of that model to be used as inputs to T2K oscillation analyses, and for T2K cross section analyses. The fit framework developed for this work has been designed to be easily

[1]The prior constraint on $M_{\mathrm{A}}^{\mathrm{eff}}$ passed to the oscillation analysis groups was actually the difference between the best fit, and the NEUT nominal value for $M_{\mathrm{A}}^{\mathrm{eff}}$ of 1.21 GeV.

extensible and is now being developed into a generic external data fitting tool for use by the NIWG group to constrain model parameters for various interaction channels. Documentation is available with the source code to help analysers in future iterations of the NIWG external data fits.

The different model ingredients implemented in NEUT are described in Section 5.1, and two distinct candidate CCQE models are identified. To avoid the reader getting lost in the detail, it is instructive to outline the motivations for each step of the fits in some detail here:

1. Section 5.2 describes the fit method, and the datasets used in the fit.
2. Section 5.3.2 presents fits to both candidate models for all datasets. A naive interpretation of the χ^2 values returned from the fits suggests reasonable agreement for both models. The lack of a MiniBooNE correlation matrix causes issues with this interpretation of results, so a more sophisticated goodness of fit statistic is required to choose a default model.
3. In Sections 5.3.3 and 5.3.4, the Parameter Goodness of Fit (PGoF) test is introduced, and used as the answer to the problems with the naive χ^2 results. One candidate model shows much less tension between different datasets, so is selected as the preferred model at this point.
4. In Section 5.3.5 an ad hoc normalisation parameter is included in the fit. No significant pull from the nominal is observed, so CCQE normalisation is fixed at the nominal model prediction.
5. Section 5.3.6 outlines the problems for parameter error estimation with incomplete MiniBooNE data. A rescaling procedure is defined based on PGoF test designed to cover the difference between the different datasets used in the fit.

Finally, the main results of the fit are summarised in Section 5.4, and conclusions from the analysis are presented in Section 5.5.

5.1 CCQE model development in NEUT

Section 2.4 introduced new theoretical models which aim to overcome the deficiencies of the RFG model, and consequent large axial masses required to describe heavy target data, by including additional nuclear effects. This section will briefly outline the important details of the NEUT implementations of these models, and highlight any caveats

that should be borne in mind when fitting with them. The implementation of these models is documented in hundreds of pages of internal T2K technical notes, which are referenced here, but may not be publicly available.

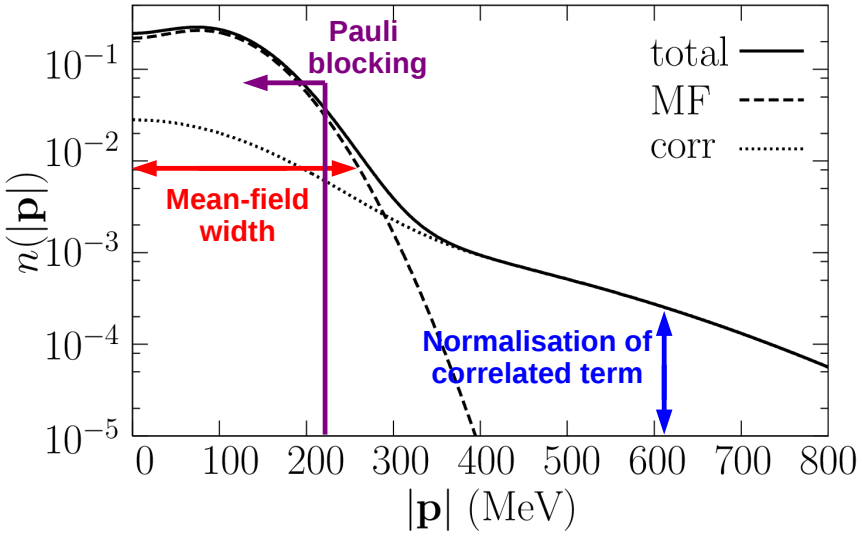

FIGURE 5.1: The effect of modifying the SF variable parameters in NEUT on the SF initial state momentum distribution. The figure has been adapted from Reference [66].

The NEUT implementation of the Spectral Function (SF) model from Omar Benhar and collaborators [51] is described in Reference [274]. The model information is all encoded in the initial state nucleon distribution shown in Figure 2.6. Pauli blocking is implemented as a hard cut-off: final state nucleons with three-momenta less than the Fermi momentum $p_{\mathrm{F}}^{\mathrm{SF}}$ are forbidden. There are two terms in the SF model: a short range correlation term, which extends to higher initial state nucleon momenta, and a mean field term, which contributes the main peak at lower momenta. These terms can be seen in Figure 5.1, where the two-dimensional SF in terms of the removal energy and initial state nucleon momentum has been projected on to the momentum axis. There are three ways to modify the SF, which are reweightable parameters in NEUT, and are illustrated in Figure 5.1. The default values for these parameters are given in Table 5.2. The mean field width and normalisation of the correlation term are constrained by electron–scattering data [274], and have little effect on the datasets used in this chapter, so are neglected in the fits. Pauli blocking is modified by changing the Fermi momentum in the fits. It should be noted that in the RFG model, the Fermi momentum defines the Pauli blocking, but *also* modifies the width of the initial state nucleon distribution. As a result, changing $p_{\mathrm{F}}^{\mathrm{RFG}}$ affects a wide range of Q^2, whereas changing $p_{\mathrm{F}}^{\mathrm{SF}}$ only affects very low Q^2 events.

The multi-nucleon–neutrino model from Nieves *et al.* [54, 223] has been implemented in NEUT as described in [52, 273]. These models are alternatively referred to as Meson Exchange Current (MEC) models, and will be referred to as MEC models from now on.

The cross section as a function of neutrino energy and the outgoing lepton kinematics was made available by the authors of the model, and is implemented as a series of lookup tables for various nuclear targets and neutrino species. The tables provided had hadronic variables integrated out, so a generic model [275] for simulating the initial and final hadronic states was used for generating NEUT events[2]. The discrepancy between the leptonic and hadronic simulation makes the current NEUT implementation of the Nieves model inadequate for comparisons with experimental measurements of the final state hadrons from CCQE events. For this reason, only leptonic measurements are used in this analysis, but it should be noted that hadronic measurements are becoming available (for example, see Reference [276]). As the Nieves model is very complex, the current NEUT implementation does not allow fundamental model parameters to be changed. Two variable parameters are currently available in NEUT: a simple scaling parameter which changes the overall normalisation of MEC events, and a parameter which varies the $|\vec{q}|$ cut-off used for MEC events (for details on this cut-off, see Section 2.4) from the default value of $|\vec{q}| = 1.2$ GeV.

The Random Phase Approximation (RPA) [223] is implemented into NEUT as an E_ν and Q^2 dependent modification to the CCQE cross section as described in Reference [277]. Figure 5.2 shows the ratio of the CCQE cross section with RPA included over the CCQE cross section; these two-dimensional tables of the ratio were supplied by the authors of Reference [223] and are used to apply the RPA correction in NEUT. Note that the RPA calculation implemented in NEUT is based on a Local Fermi Gas (LFG) model of the nucleus [223]. However, the authors of the calculation have noted [54] that it can be applied, with reasonable precision, to a global Fermi gas (no LFG is available in NEUT). Note that this RPA model cannot be used self-consistently with the SF model, and currently no RPA calculation appropriate for the SF model is available. There are two different RPA calculations available from the same authors, relativistic and non-relativistic, which affect the quenching of the RPA at high Q^2 ($Q^2 \geq 0.5$ GeV^2). The ratio of non-relativistic over relativistic RPA is shown in Figure 5.3, where it is clear that the difference is a function of Q^2 and affects the size of the RPA enhancement at higher Q^2 values. Both models are investigated in this analysis as there is no theoretical guidance on which model is preferred. The NEUT event reweighting code contains a parameter to reweight between the two available models. Note that the 'stray' points in Figures 5.2 and 5.3 are artefacts from the authors of the RPA model, who provided the data used to produce these figures. The cause of these artefacts is unknown, but as these points lie outside the kinematically allowed region of (E_ν, Q^2) space, they do not

[2]This model simply enforces energy and momentum conservation, treats initial nucleons as uncorrelated and drawn from a local Fermi gas model, and shares momentum equally between final state nucleons [52, 275].

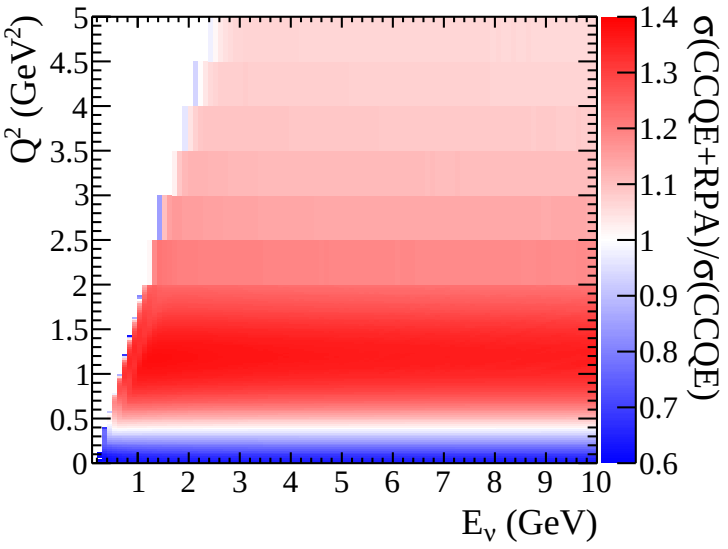

(A) ν_μ – ^{12}C

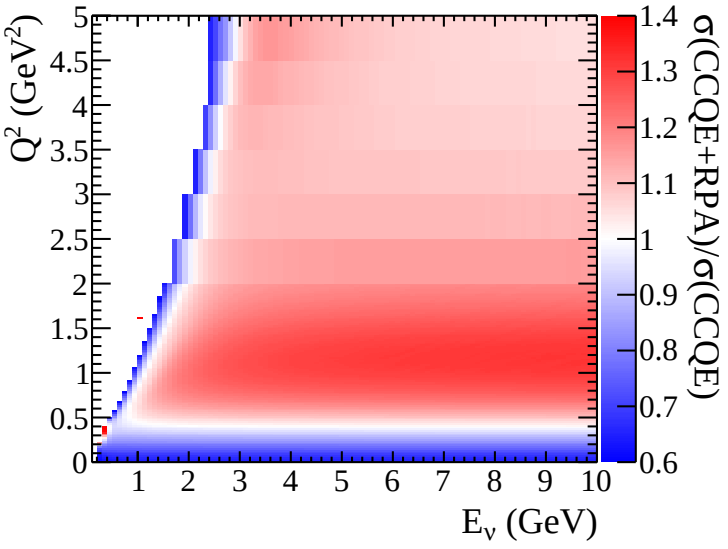

(B) $\bar{\nu}_\mu$ – ^{12}C

FIGURE 5.2: The ratio of the CCQE cross section including the non-relativistic RPA model to the CCQE cross section without RPA, shown for both muon neutrino and muon antineutrino interactions with carbon. These E_ν and Q^2 dependent tables are used in NEUT to apply the RPA model. For these plots, the axial mass $M_\mathrm{A} = 1.00$ GeV is used.

affect the RPA reweighting in the NEUT code as no event outside this region can be generated, so will have no affect on the analysis presented here.

Of these models, two distinct candidate CCQE models are available in NEUT, which are both fitted in this work with the intention of choosing the model which most consistently described all external data as the default NEUT model for T2K analyses:

1. RFG+RPA+MEC

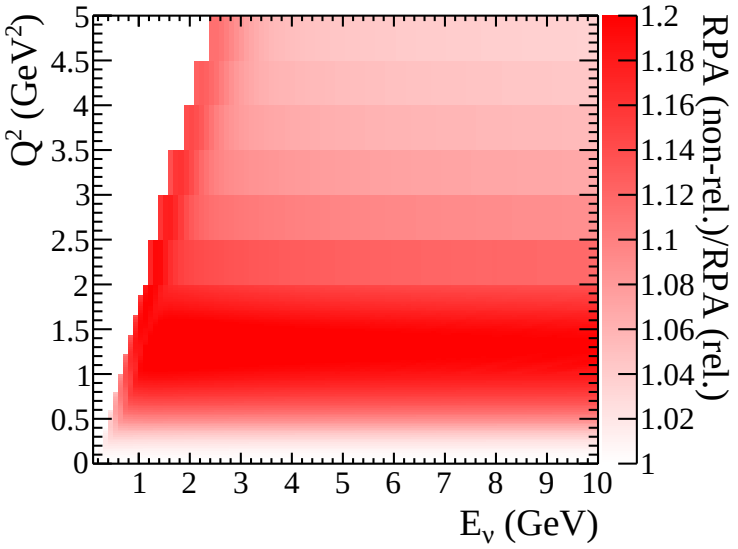

(A) ν_μ – ^{12}C

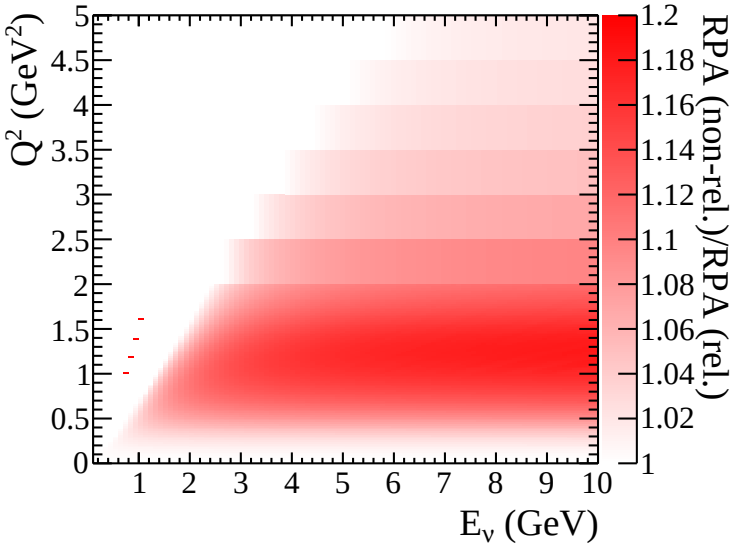

(B) $\bar{\nu}_\mu$ – ^{12}C

FIGURE 5.3: The ratio of the non-relativistic RPA correction to the relativistic RPA correction, shown for both muon neutrino and muon antineutrino interactions with carbon. These E_ν and Q^2 dependent tables are used to reweight NEUT events from one RPA model to the other.

2. SF+MEC

Note that there is no systematic to cover the difference between the two models. They are distinct nuclear models, so allowing a fitter to find some halfway house between them would have no physical meaning. Each model has different variable parameters implemented in T2KReWeight, which are described fully in Reference [270]. The default values for all variable model parameters are listed in Tables 5.1 and 5.2 for the RFG+RPA+MEC and SF+MEC models respectively. For both models, the BBBA05 vector form factors are used [183], and the axial form factor is treated as a dipole.

Model parameter	NEUT default value
$M_{\mathrm{A}}^{\mathrm{QE}}$	1.01 GeV
Fermi momentum, $p_{\mathrm{F}}^{\mathrm{RFG}}$	217 MeV (^{12}C)
Binding energy, E_b	25 MeV (^{12}C)
RPA	Nieves relativistic model [223]
MEC normalisation	100% Nieves model [54, 223]
$\lvert\vec{q}\rvert$ cut for MEC events	1.2 GeV
Axial form factor	Dipole
Vector form factors	BBBA05 [183]

TABLE 5.1: Nominal model parameters for the RFG+RPA+MEC model. The default value for the axial mass assumed in NEUT is $M_{\mathrm{A}}^{\mathrm{eff}} = 1.21\,\mathrm{GeV}$, but a value in line with the deuterium constraints has been considered the nominal value throughout this work. Note that the values for $p_{\mathrm{F}}^{\mathrm{RFG}}$ and E_b vary with nuclear target, and are given for carbon here.

Model parameter	NEUT default value
$M_{\mathrm{A}}^{\mathrm{QE}}$	1.01 GeV
Fermi momentum, $p_{\mathrm{F}}^{\mathrm{SF}}$	209 MeV
Mean field width	200 MeV (Benhar SF nominal [51])
Normalisation of the correlated term	Benhar SF nominal [51] where correlated tail accounts for ∼20% of the total CCQE cross section
MEC normalisation	100% Nieves model [54, 223]
$\lvert\vec{q}\rvert$ cut for MEC events	1.2 GeV
Axial form factor	Dipole
Vector form factors	BBBA05 [183]

TABLE 5.2: Nominal model parameters for the SF+MEC model. The default value for the axial mass assumed in NEUT is $M_{\mathrm{A}}^{\mathrm{eff}} = 1.21\,\mathrm{GeV}$, but a value in line with the deuterium constraints has been considered the nominal value throughout this work.

In the SF+MEC fits, four free parameters are considered: the Fermi momentum ($p_{\mathrm{F}}^{\mathrm{SF}}$), the MEC normalisation, the axial mass, and the CCQE normalisation. It was found that the mean field width and the normalisation of the correlated term did not have a significant effect on the datasets used in the fits, so these were fixed at the best fit values from electron scattering data [51]. In the RFG+RPA+MEC fits, five free parameters are considered: the Fermi momentum ($p_{\mathrm{F}}^{\mathrm{RFG}}$), the MEC normalisation, the axial mass, the CCQE normalisation and the RPA model (non-relativistic or relativistic). The binding energy is fixed at the best fit value from electron scattering data [168] because of concerns over the validity of the reweighting strategy in the T2K reweighting code. For both models, the three-momentum transfer cut used in the MEC model, $|\vec{q}|$, has been kept at the nominal value for the fits described in this chapter, but was investigated as a later addition to the analysis, and fit results with this parameter included are available

in Appendix A.

Additionally, the Effective Spectral Function has been implemented in NEUT as described in Chapter 6, and is included for comparison with the other nominal models in Section 5.2.4. However, this model was implemented too late to be a candidate model for the T2K oscillation analysis, and is not considered further in the fitting work described in this chapter (although some fits were performed with this model, as will be described in Chapter 6).

It should be noted that there are deficiencies in both models as currently implemented in NEUT. The RFG+RPA+MEC model is very like the full Nieves model: both the RPA, and MEC calculations are from Nieves *et al.* [223]. However, these components are calculated with a Local Fermi Gas, where the Fermi momentum depends on the local nuclear density, whereas the RFG model in NEUT currently is a global Fermi Gas model, where the Fermi momentum is fixed. Also, it should be noted that currently there is no ability within NEUT to reweight the value of M_{A} used in the Nieves model prediction, making the results slightly inconsistent in this regard. As previously remarked upon, the SF+MEC model has no RPA correction applied, which is physically inconsistent as the MEC enhancement is used (both corrections are due to complications in heavy nuclear targets). Currently no appropriate RPA calculation is available, so this inconsistency is unavoidable.

5.2 Fit strategy

5.2.1 CCQE datasets

Four datasets are used in the CCQE fits presented in this thesis. These datasets are the MiniBooNE neutrino [34] (2010) and antineutrino results [35] (2013), and the MINERνA neutrino [278] (2013) and antineutrino [279] (2013) results. All experimental details and information about these results given in this section are taken from these references unless otherwise stated. The MiniBooNE and MINERνA experiments are described in Sections 3.3 and 3.2.2 respectively.

Note that single-differential cross section results are given in terms of Q^2_{QE}, the four-momentum transfer derived from lepton kinematics under the quasi-elastic hypothesis, which is calculated using the equations

$$E_{\nu}^{\mathrm{QE,\,RFG}} = \frac{2M_i' E_{\mu} - (M_i'^2 + m_{\mu}^2 - M_f^2)}{2(M_i' - E_{\mu} + \sqrt{E_{\mu}^2 - m_{\mu}^2}\cos\theta_{\mu})}, \tag{5.1}$$

$$Q^2_{\mathrm{QE}} = -m^2_\mu + 2E_\nu^{\mathrm{QE,\,RFG}}(E_\mu - \sqrt{E^2_\mu - m^2_\mu}\cos\theta_\mu), \tag{5.2}$$

where E_μ is the muon energy, m_μ is the muon mass, M_i and M_f are the initial and final nucleon masses respectively, and $M_i' = M_i - V$ where V is the binding energy of carbon assumed in the analysis. For both MiniBooNE datasets and the MINERνA neutrino dataset, $V = 34\,\mathrm{MeV}$; for the MINERνA antineutrino dataset, $V = 30\,\mathrm{MeV}$.

In the MiniBooNE analysis, Q^2_{QE} is calculated from unfolded T_μ and $\cos\theta_\mu$ distributions. The MINERνA analysis unfolds the Q^2_{QE} distribution calculated with the reconstructed p_μ and $\cos\theta_\mu$ values. The errors on the Q^2_{QE} distributions for both experiments include the uncertainties relating to the muon reconstruction, so should cover the difference in the method used to produce the Q^2_{QE} cross section results. The main results of this analysis use MiniBooNE double-differential results only, so there is no possiblity of tension from differences between the methods used to produce Q^2_{QE} distributions.

5.2.1.1 MiniBooNE neutrino

The MiniBooNE CCQE data [34] has been released as a double-differential cross section as a function of $(T_\mu, \cos\theta_\mu)$, shown in Figure 5.4a, where T_μ is the kinetic energy of the outgoing muon, and θ_μ is the angle between the incoming neutrino and outgoing muon. It has also been released as a single-differential cross section as a function of Q^2_{QE} (defined in Equation 5.2), shown in Figure 5.4b. Results were also given in terms of $E_\nu^{\mathrm{QE,\,RFG}}$, where the neutrino energy is reconstructed from the final state kinematics of the event using Equation 5.1, and corrected to the true neutrino energy assuming the relativistic Fermi Gas model (RFG), though this result is not considered further in this analysis because of its explicit dependence on the RFG model. All CCQE data released by the MiniBooNE collaboration are central values and the diagonal elements of the shape-only covariance matrix for each bin. Correlations between bins were not released. Additionally, the overall flux normalisation uncertainty was given as 10.7% for neutrino running.

CCQE cross section data for MiniBooNE is released as both CCQE-corrected, and CCQE-like measurements. The CCQE-like sample is obtained by selecting events in which a muon was detected with no pions, but no requirement was made on the proton. The CCQE-corrected measurement was produced by subtracting background events (where the primary interaction was not CCQE) based on the NUANCE prediction. The dominant background is CC1π^+, and a dedicated sample was used by MiniBooNE to tune the NUANCE prediction, which was used in the background subtraction. It should be noted that the NUANCE CC1π^+ simulation included π-less Δ-decay. The published signal purity for the neutrino dataset is 77%.

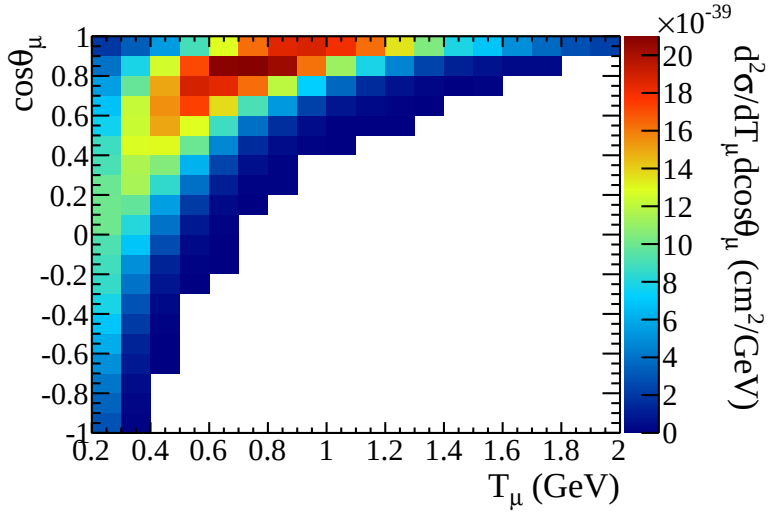

(A) $(T_\mu, \cos\theta_\mu)$

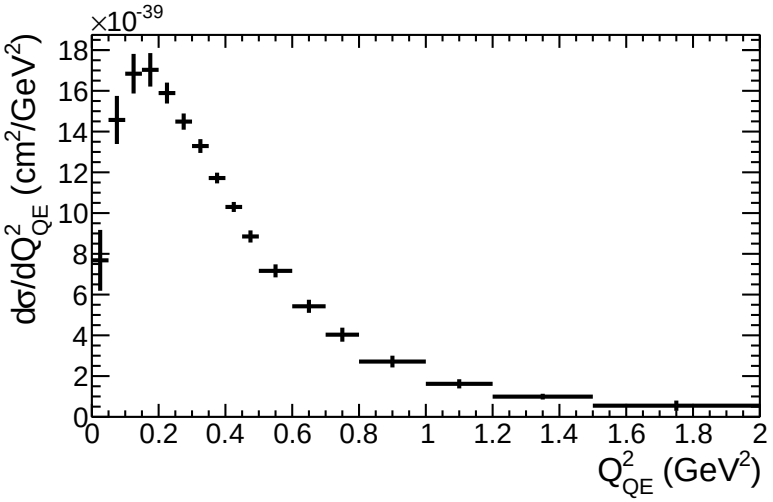

(B) Q^2_{QE}

FIGURE 5.4: MiniBooNE CCQE-corrected data for neutrino running. Note that the error bars shown on the Q^2_{QE} dataset are shape-only uncertainties.

CCQE-like results are more model independent than CCQE-corrected results (as they do not rely on their experiment's own MC correction strategy). However, they are more difficult to use correctly because it may be difficult to mimic the selection properly without using a simulation of the MiniBooNE detector. CCQE-like results are not used in this analysis to avoid this complication, and because it makes the analysis less reliant on NEUT's modelling of the FSI effects which enter into the CCQE-like sample. A downside of using the CCQE-corrected data is the explicit subtraction of π-less Δ-decay events in the MiniBooNE analysis. These events are included in the Nieves multi-nucleon–neutrino prediction, which is treated as signal in this analysis. Unfortunately, there is no obvious way to account for this effect, so this issue is not considered further.

5.2.1.2 MiniBooNE antineutrino

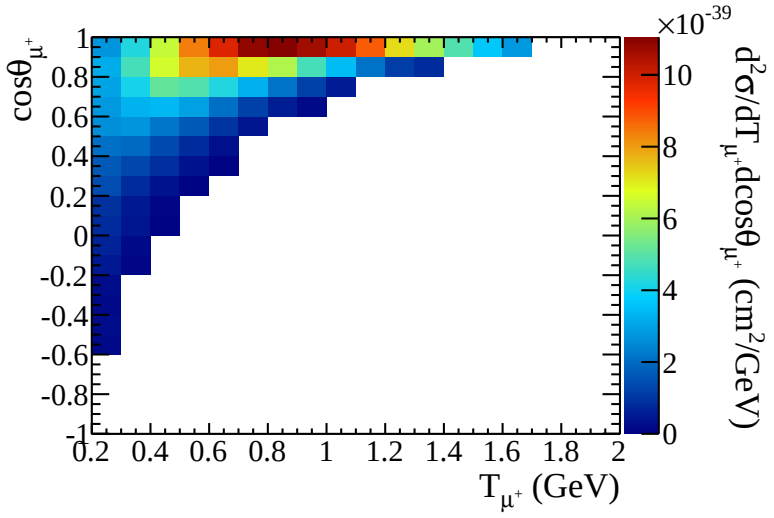

(A) $(T_\mu, \cos\theta_\mu)$

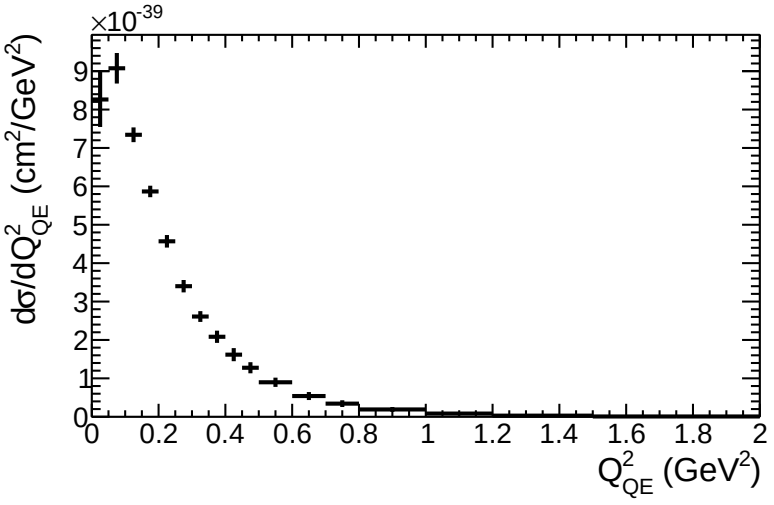

(B) Q^2_{QE}

FIGURE 5.5: MiniBooNE CCQE-corrected dataset for antineutrino running. Note that the error bars on the Q^2_{QE} dataset are shape-only uncertainties.

As for the neutrino CCQE result, the MiniBooNE antineutrino data [35] has been released as a double-differential cross section as a function of $(T_\mu, \cos\theta_\mu)$, shown in Figure 5.5a, and as a single-differential cross section as a function of Q^2_{QE}, shown in Figure 5.5b. A result is also given in terms of $E_\nu^{\mathrm{QE,\,RFG}}$, but as before, this data has not been considered further in this analysis because of the RFG model dependence. As with the neutrino dataset, the data released by the MiniBooNE collaboration are central values and the diagonal elements of the shape-only covariance matrix for each bin. Correlations between bins were not released. Additionally, the overall flux normalisation uncertainty was given as 13.0% for antineutrino running.

Both CCQE-like and CCQE-corrected results are given; the CCQE-corrected results are used in this analysis. The correction strategy for the antineutrino dataset is more complicated because of the relatively high ν_μ contamination in the $\bar{\nu}_\mu$ beam, which is the largest background in the antineutrino CCQE sample as MiniBooNE is an unmagnetised detector. There is also a large CC1π^- background, the analogue of the contamination in the neutrino dataset. Two properties are used to measure the ν_μ background: 8% of ν_μ-induced CC interactions produce no decay electron due to muon-nucleus capture; and as most π^- mesons are absorbed, the ν_μ-induced CC1π^+ events can be identified independently of $\bar{\nu}_\mu$-induced CCπ^-. Unfortunately, this property means that a CC1π^- sample cannot be used to tune the NUANCE model, so the neutrino mode CC1π^+ has to be used. Other backgrounds are subtracted using the NUANCE interaction model after some tuning and corrections. As a result of the two large backgrounds in the antineutrino sample, the purity of the CCQE-like sample is 61%.

5.2.1.3 MINERνA

The CCQE datasets from MINERνA [278, 279] are released as CCQE-corrected single-differential flux-averaged cross section as a function of Q^2_{QE}, where the flux has been averaged over the region $1.5 \leq E_\nu \leq 10\,\text{GeV}$. There is an additional requirement that $1.5 \leq E_\nu^{\text{QE, RFG}} \leq 10\,\text{GeV}$, using $E_\nu^{\text{QE, RFG}}$ as defined in Equation 5.1. Both neutrino and antineutrino results are available as both shape and absolutely normalised distributions. Correlation matrices have been released for both the shape-only and absolutely normalised neutrino and antineutrino datasets. In this work, the absolutely normalised distributions have been used in the fit.

The correction strategy for the MINERνA data is to fit the relative normalisations of simulated background distributions to the data in terms of the recoil energy, energy deposited outside a vertex region (the recoil region), and then subtract the predicted background from the CCQE-like sample. The published purity for the neutrino dataset ranges from 65% at low Q^2_{QE} to 40% at high Q^2_{QE} (with an overall purity of 49%). The purity for the antineutrino dataset is given as 77%. The purity is lower for the neutrino analysis because events with a proton from the initial interaction are more complicated to reconstruct than those with a neutron. The antineutrino analysis has an additional cut requiring no additional (other than the muon) tracks from the vertex, and allows only one isolated energy shower, whereas the neutrino mode analysis allows two [278, 279].

The distributions published in the MINERνA CCQE papers [278, 279] have been corrected to account for unsampled regions of the muon phase space, using an RFG model in GENIE with an axial mass of 0.99 GeV. In the current MINERνA CCQE analyses,

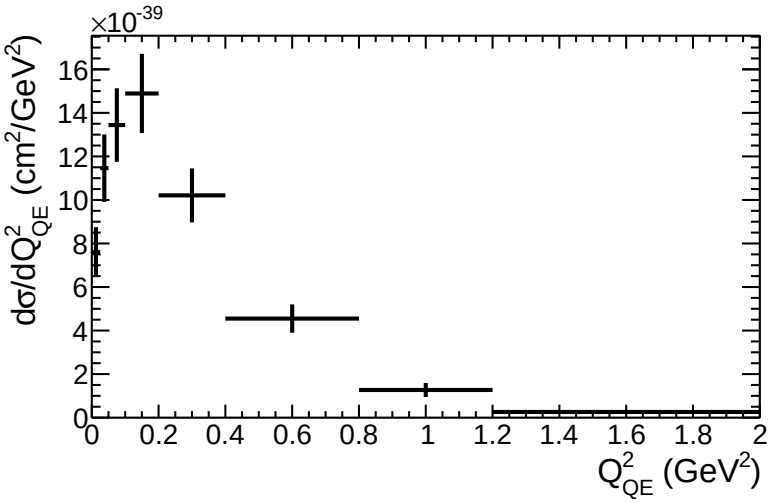

(A) Neutrino

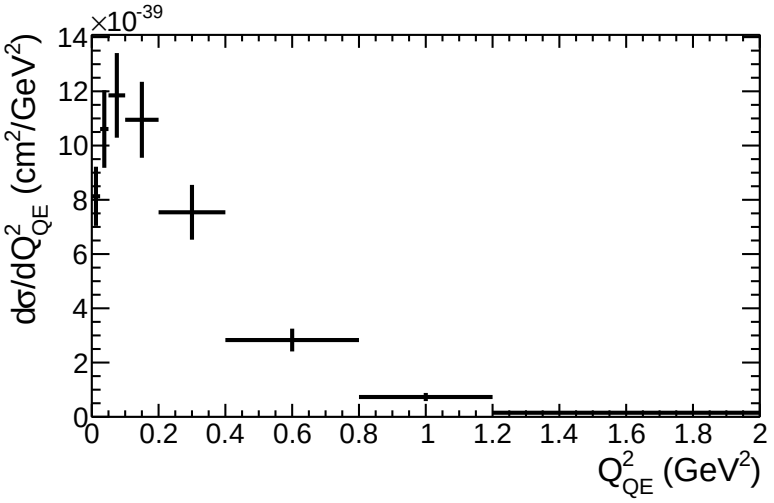

(B) Antineutrino

FIGURE 5.6: MINERνA CCQE dataset for neutrino and antineutrino running with the restricted phase space $\theta_\mu \leq 20°$. Note that the error bars shown are the diagonals from the covariance matrix, which includes both shape and normalisation errors.

the efficiency for selecting events with $\theta_\mu > 20°$ is very low because the MINOS near detector, which is just downstream of MINERνA, is used to tag muons. This introduces a small model dependence on the results because of the reliance on an RFG model for the correction. The MINERνA collaboration subsequently released a distribution where the cross section is measured for CCQE events with $\theta_\mu \leq 20°$. As this dataset is less model-dependent, it has been used in the fits.

The absolutely normalised neutrino and antineutrino datasets used in the fits are shown in Figure 5.6. MINERνA also made cross-correlations between the neutrino and antineutrino datasets available in a data release after the publication of their CCQE papers. The cross-correlations are available for both the $\theta_\mu \leq 20°$ and full phase space samples. Although they were only released as correlation matrices including both shape and

normalisation errors, it is possible to extract shape-only correlation matrices [78]. The matrix with shape and normalisation errors included was used in all fits discussed here[3], and is shown in Figure 5.7.

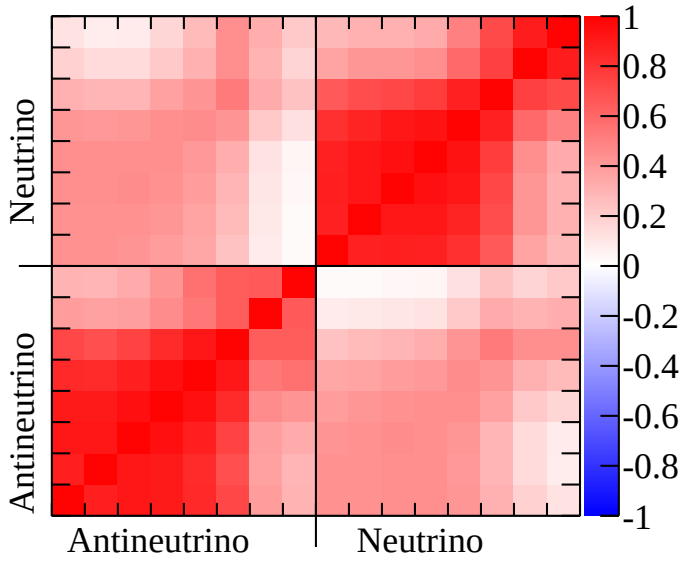

FIGURE 5.7: Cross-correlation matrix for the MINERνA neutrino and antineutrino samples with a cut of $\theta_\mu \leq 20°$. The 8 neutrino and 8 antineutrino bins shown here correspond to the 8 Q^2_{QE} bins from the MINERνA datasets. Note that this matrix includes both shape and normalisation uncertainties.

5.2.2 Monte Carlo prediction

For each of the four experiments included in the fit, NEUT samples were produced using the nominal model predictions and the published flux for each sample. The flux-averaged cross section predictions were produced using the following method:

1. For each event, apply experiment-specific cuts, and if the event passes, calculate the relevant reconstructed quantity and fill the 1D or 2D histogram.
2. Calculate the event rate by integrating the MC event rate histogram (flux $\times$ cross section).
3. Integrate the published flux histogram to get the average flux.
4. Scale the filled histogram by the event rate / average flux to get the flux-averaged cross section/nucleon.

[3]Shape-only fits were carried out as a cross-check of the main results of this chapter, and the results are given in Appendix B.

5. Scale by the number of target nucleons / number of neutrons (protons) for neutrino (antineutrino) running.

6. Divide the content of each bin by the bin width.

For each dataset, 1 million simulated NEUT events are used to produce the cross section predictions. Only the CCQE and MEC interaction modes are simulated to increase signal statistics.

5.2.3 Definition of the χ^2 statistic

The χ^2 statistic is given by:

$$\begin{aligned}\chi^2(\vec{\mathbf{x}}) = &\left[\sum_{k=0}^{N}\left(\frac{\nu_k^{DATA} - \lambda_\nu^{-1}\nu_k^{MC}(\vec{\mathbf{x}})}{\sigma_k}\right)^2 + \left(\frac{\lambda_\nu - 1}{\varepsilon_\nu}\right)^2\right] \rightarrow \text{MiniBooNE } \nu \\ &+ \left[\sum_{l=0}^{M}\left(\frac{\nu_l^{DATA} - \lambda_{\bar{\nu}}^{-1}\nu_l^{MC}(\vec{\mathbf{x}})}{\sigma_l}\right)^2 + \left(\frac{\lambda_{\bar{\nu}} - 1}{\varepsilon_{\bar{\nu}}}\right)^2\right] \rightarrow \text{MiniBooNE } \bar{\nu} \\ &+ \left[\sum_{i=0}^{16}\sum_{j=0}^{16}\left(\nu_i^{DATA} - \nu_i^{MC}(\vec{\mathbf{x}})\right) V_{ij}^{-1}\left(\nu_j^{DATA} - \nu_j^{MC}(\vec{\mathbf{x}})\right)\right] \rightarrow \text{MINER}\nu\text{A} \quad (5.3)\end{aligned}$$

where $\vec{\mathbf{x}}$ are the model parameters varied in the fit, V_{ij} is the cross-covariance matrix provided by MINERνA, and λ_ν and $\lambda_{\bar{\nu}}$ are the normalisation parameters for MiniBooNE neutrino and antineutrino respectively, with the published normalisation uncertainties of ε_ν (10.7%) and $\varepsilon_{\bar{\nu}}$ (13.0%).

Fits to individual datasets only include the relevant terms from the χ^2 definition in Equation 5.3, and fits to single MINERνA datasets neglect cross-correlations (the sum is over the relevant 8 bins).

5.2.4 Nominal NEUT predictions

The default predictions for various models are shown in Figures 5.8, 5.9 and 5.10 for the MINERνA $\theta_\mu \leq 20°$, MiniBooNE single-differential and MiniBooNE double-differential samples respectively. The SF+MEC and RFG+RPA+MEC models (abbreviated to RPA+MEC in the legend) are shown with the default parameter sets described in Tables 5.2 and 5.1 respectively. The RFG model with the relevant parameters from Table 5.1 and Effective SF models[4] are also shown for comparison. The MEC enhancement

[4]See Chapter 6 for details of the Effective SF model.

is also shown: this is only a component of the models used, separated for reference and not a complete model in its own right.

To produce a meaningful nominal χ^2 for the MiniBooNE datasets, it is necessary to fit the MiniBooNE normalisation parameters. The single and double-differential plots shown in 5.9 and 5.10 are scaled according to the relevant MiniBooNE normalisation parameter at the best fit point. The best fit values of the pull parameters $\lambda_{\nu}^{\mathrm{MB}}$ and $\lambda_{\bar{\nu}}^{\mathrm{MB}}$ are given in Table 5.3. Additionally, the nominal predictions for the MiniBooNE double-differential datasets, without the scaling factor applied, are shown in Figure 5.11. The distributions without the normalisation factor applied are easier to interpret by eye.

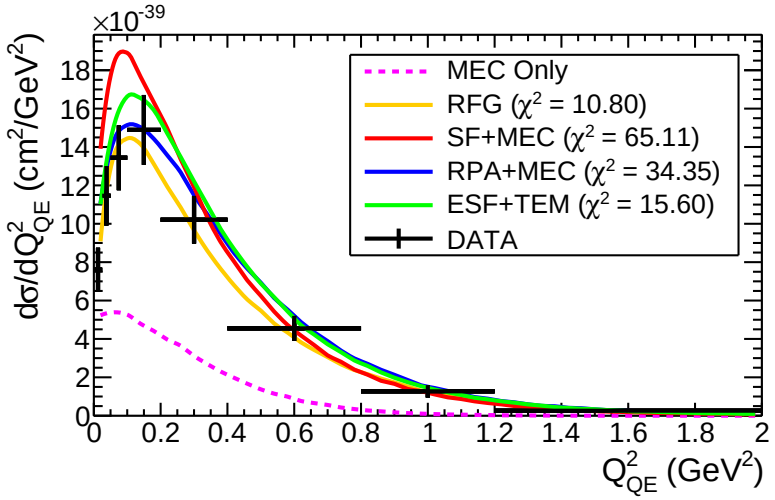

(A) Neutrino

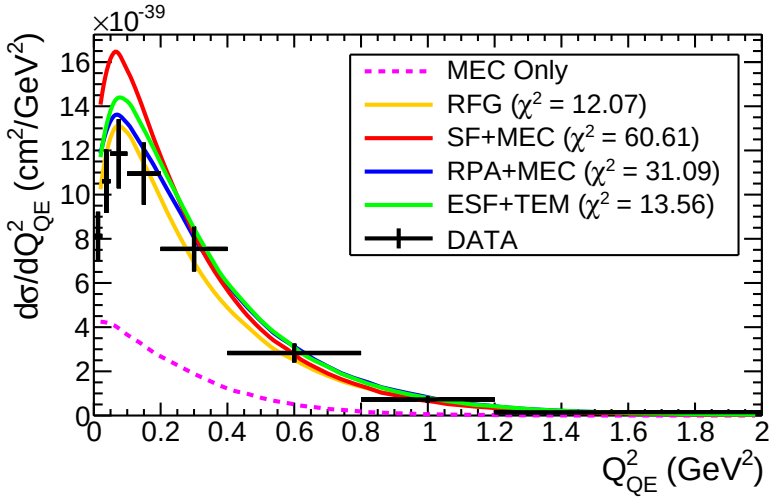

(B) Antineutrino

FIGURE 5.8: Nominal model predictions for the MINERνA $\theta_{\mu} \leq 20°$ datasets with $M_{\mathrm{A}} = 1.01\,\mathrm{GeV}$, and all other model parameters at their default values.

Note that the double-differential cross section plots shown in Figures 5.10 and 5.11 have been rebinned. In the distributions released by MiniBooNE, and used in the fits, there are 20 $\cos\theta_{\mu}$ bins, uniformly distributed between -1 and 1. For ease of presentation,

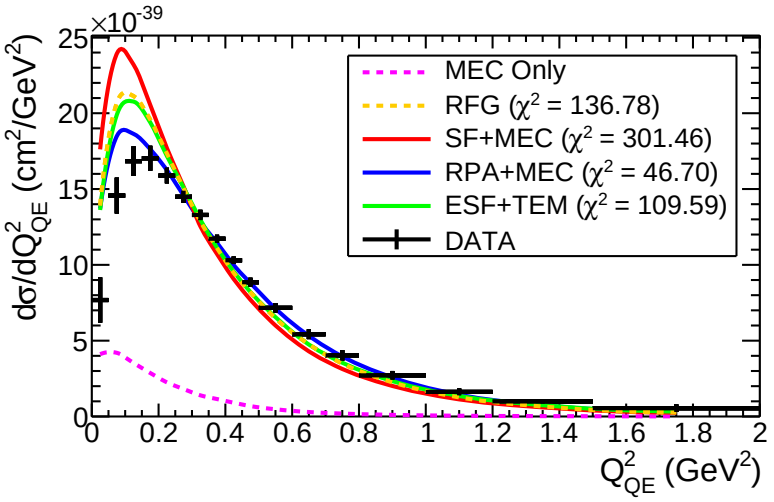

(A) Neutrino

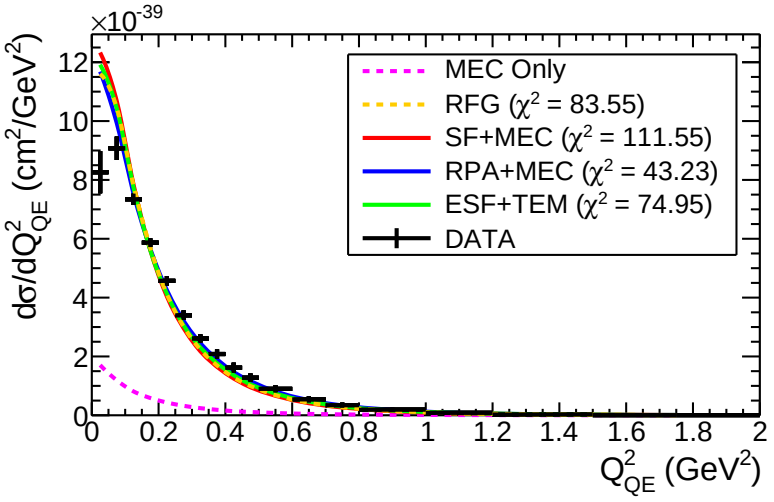

(B) Antineutrino

FIGURE 5.9: Nominal model predictions for the MiniBooNE single-differential datasets with $M_A = 1.01\,\text{GeV}$, and all other model parameters at their default values. Note that for each model, the relevant MiniBooNE normalisation parameter has been allowed to vary to minimise the χ^2 value. This is necessary to obtain meaningful χ^2 results for each default model.

these have been rebinned, and results are shown in 8 $\cos\theta_\mu$ slices of varying sizes, where merged bins have been averaged and their errors combined in quadrature. This representation of the MiniBooNE datasets has been used consistently in this chapter (and supporting appendices).

Fit type		$\lambda_{\nu}^{\mathrm{MB}}$	$\lambda_{\bar{\nu}}^{\mathrm{MB}}$
Neutrino 1D	RFG	0.732±0.007	—
	SF+MEC	0.741±0.007	—
	RPA+MEC	0.760±0.007	—
	ESF+TEM	0.804±0.008	—
Antineutrino 1D	RFG	—	0.805±0.011
	SF+MEC	—	0.826±0.011
	RPA+MEC	—	0.774±0.010
	ESF+TEM	—	0.803±0.011
Neutrino 2D	RFG	0.725±0.011	—
	SF+MEC	0.756±0.011	—
	RPA+MEC	0.760±0.011	—
	ESF+TEM	0.827±0.012	—
Antineutrino 2D	RFG	—	0.808±0.015
	SF+MEC	—	0.838±0.015
	RPA+MEC	—	0.802±0.015
	ESF+TEM	—	0.833±0.015

TABLE 5.3: Table of best fit MiniBooNE normalisation parameter values for the nominal model comparisons shown in Figures 5.9 and 5.10.

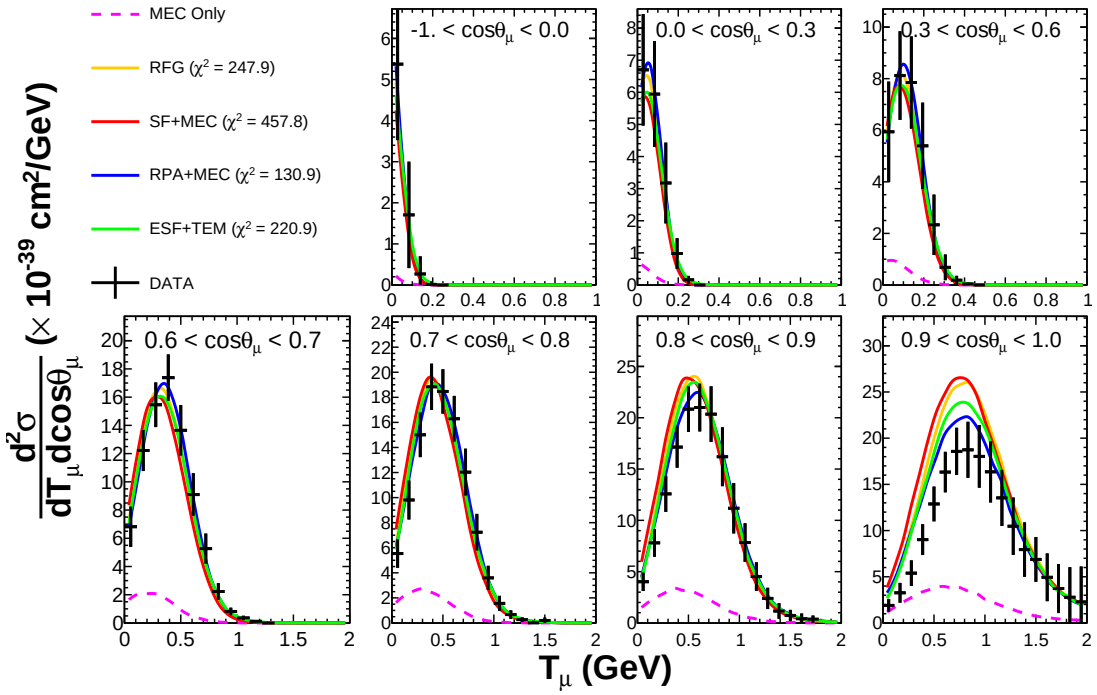

(A) Neutrino

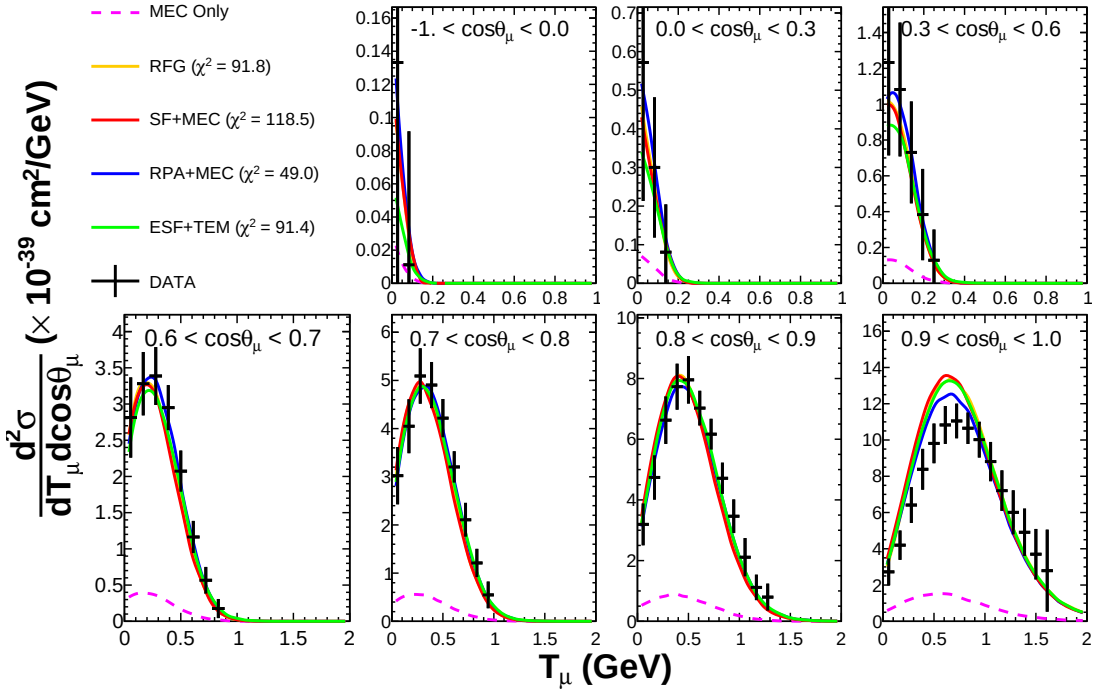

(B) Antineutrino

FIGURE 5.10: Nominal model predictions for the MiniBooNE double-differential datasets with $M_A = 1.01\,\text{GeV}$, and all other model parameters at their default values. Note that for each model, the relevant MiniBooNE normalisation parameter has been allowed to vary to minimise the χ^2 value. This is necessary to obtain meaningful χ^2 results for each default model.

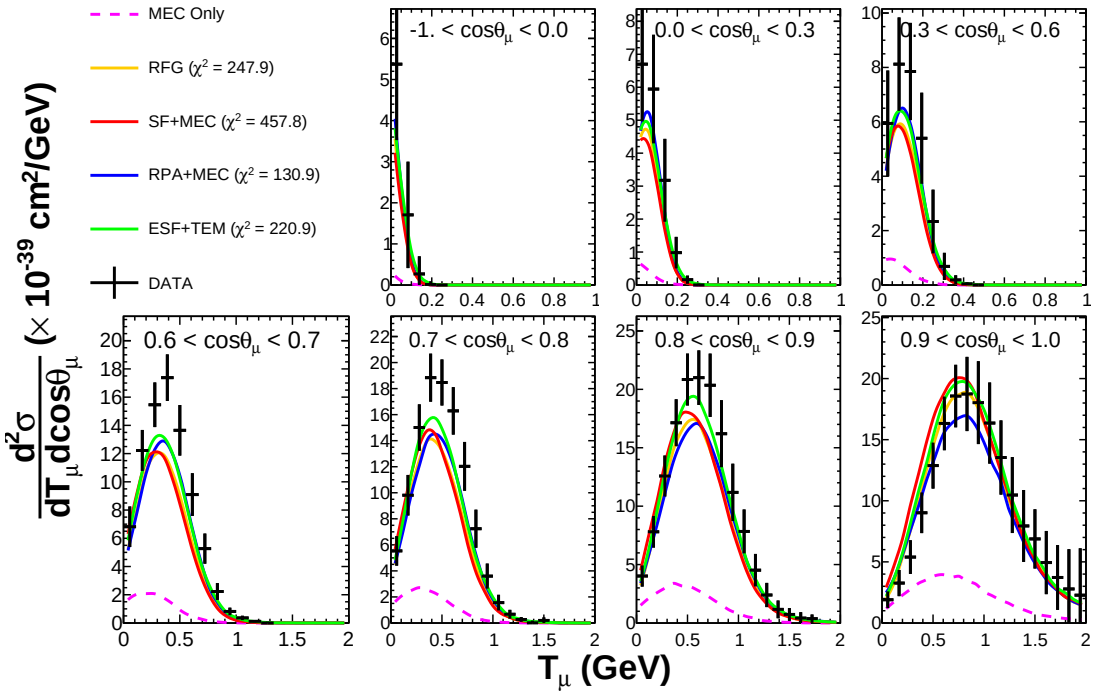

(A) Neutrino

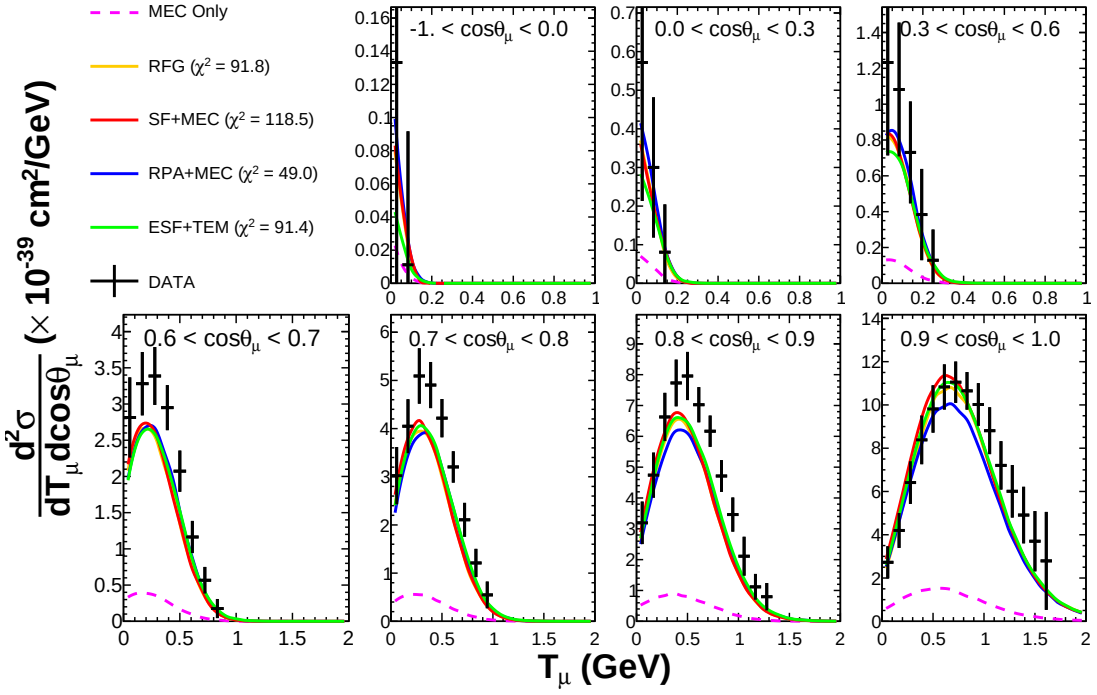

(B) Antineutrino

FIGURE 5.11: Nominal model predictions for the MiniBooNE double-differential datasets with $M_A = 1.01\,\text{GeV}$, and all other model parameters at their default values. Note that for each model, the relevant MiniBooNE normalisation parameter has been allowed to vary to minimise the χ^2 value, but the scaling factor has not been applied in this figure.

5.2.5 Kinematics of the MiniBooNE double-differential dataset

The MiniBooNE double-differential datasets avoid model dependences by using the model-independent variables T_μ (muon kinetic energy) and $\cos\theta_\mu$ (where θ_μ is the angle between the outgoing muon and incoming neutrino), but it can be difficult to visualise the effect that modifications to the model parameters described in Section 5.1 have on these distributions. It is interesting to look at how this binning relates to basic kinematic quantities of the interaction, in particular, the four-momentum transfer squared, Q^2, the energy transfer, ω, and the three-momentum transfer, $|\vec{q}|$. Figures 5.12 and 5.13 show the relationship between these quantities and the variables T_μ and $\cos\theta_\mu$ for the nominal RFG and MEC models respectively (as implemented in NEUT). The values plotted were obtained by averaging the kinematic variable in question for all of the entries in each bin using a sample of five million NEUT events generated with true CCQE (RFG) and MEC interaction modes enabled.

For the RFG model shown in Figure 5.12, it is clear that very forward events with low energy muons have the lowest Q^2 value, and higher angle events or events with higher muon energies increase the Q^2, although the relationship between the two is not linear (the same observation can be made for ω and $|\vec{q}|$). It is also interesting to note that the fringes of phase-space occupied by the MiniBooNE neutrino and antineutrino data is around the upper limit of Q^2_{QE} measured in the single-differential distributions. There is also a very high Q^2 region of phase space occupied by the RFG model for which there is no measurement, although there are very few events in this region. This unmeasured 'fringe' is larger for the antineutrino dataset than for the neutrino dataset.

The MEC model shown in Figure 5.13 shows a similar behaviour in Q^2 and $|\vec{q}|$ as for the RFG case. It is also interesting to note that the MEC model does not occupy all of the phase space occupied by the MiniBooNE neutrino data, due to the cut-off at $|\vec{q}| = 1.2$ GeV used in NEUT. This will cause a discontinuity in the NEUT prediction, but is unlikely to affect the fit because the MEC cross section is very low in this region. The ω distribution for MEC appears to have the opposite behaviour to the RFG model, where the higher values are in the very forward regions of $T_\mu - \cos\theta_\mu$ space, and the lowest values are at the fringes of the occupied phase space. The ω distribution in each $T_\mu - \cos\theta_\mu$ bin is more smeared for MEC events than RFG events, which accounts for the slow change in the mean ω value across $T_\mu - \cos\theta_\mu$ space, as shown in Figure 5.13. This smearing is due to the multiple components of the MEC model, with a Δ component at higher ω, and a non-Δ component at lower ω, as can be see in Figure 2.11. The fall in the mean ω value observed at the fringes of $T_\mu - \cos\theta_\mu$ space is due to the higher average $|\vec{q}|$ in this region, necessary to produce the outgoing lepton kinematics, which

reduces the dominance of the Δ component in the MEC cross section (which can also be observed in Figure 2.11).

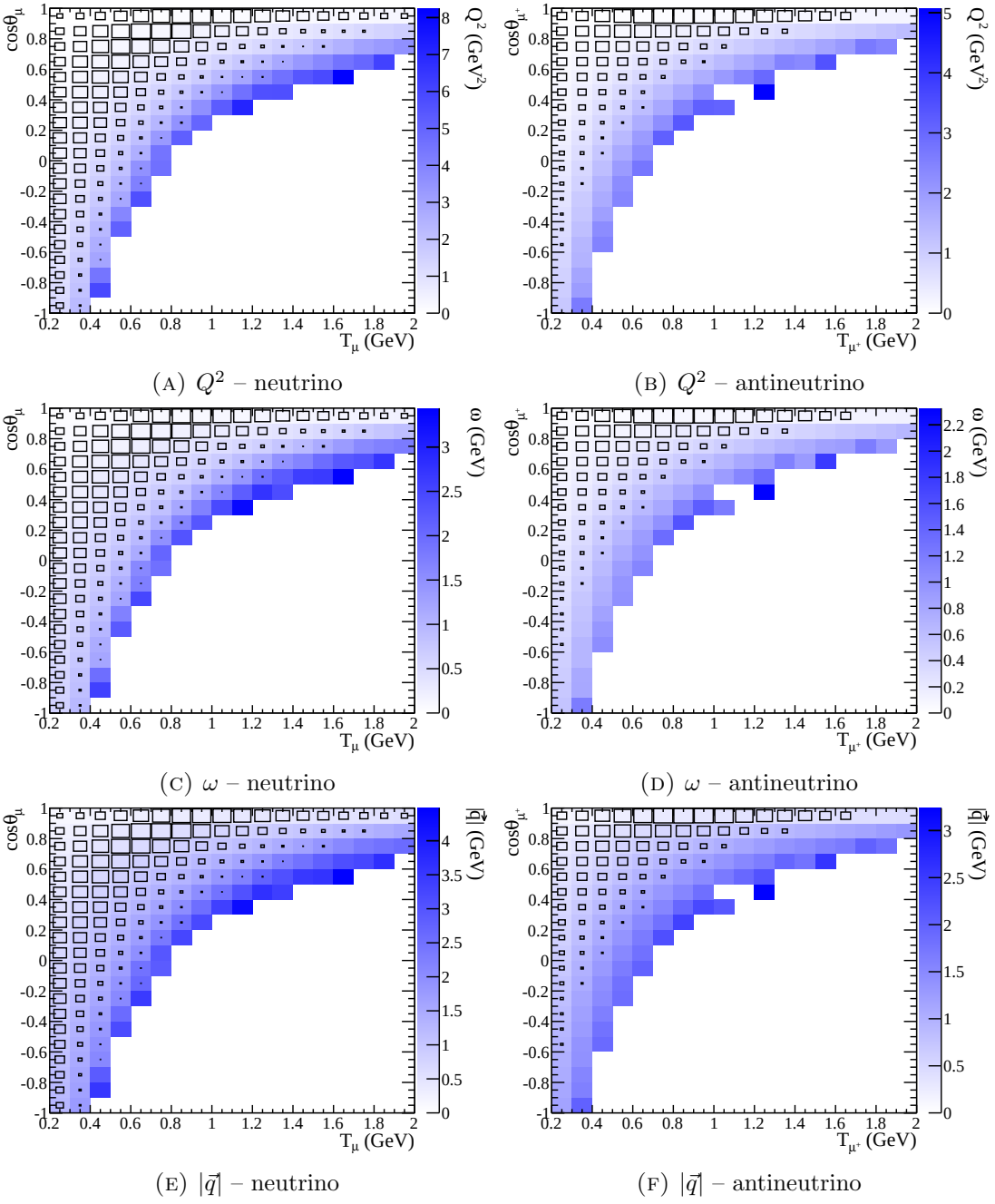

(A) Q^2 – neutrino

(B) Q^2 – antineutrino

(C) ω – neutrino

(D) ω – antineutrino

(E) $|\vec{q}|$ – neutrino

(F) $|\vec{q}|$ – antineutrino

FIGURE 5.12: The average Q^2, ω and $|\vec{q}|$ in each bin of the MiniBooNE neutrino and antineutrino double-differential datasets are shown, as predicted by the nominal RFG model. The MiniBooNE data is overlaid as boxes, where the size of the box indicates the relative strength of the cross section in that bin.

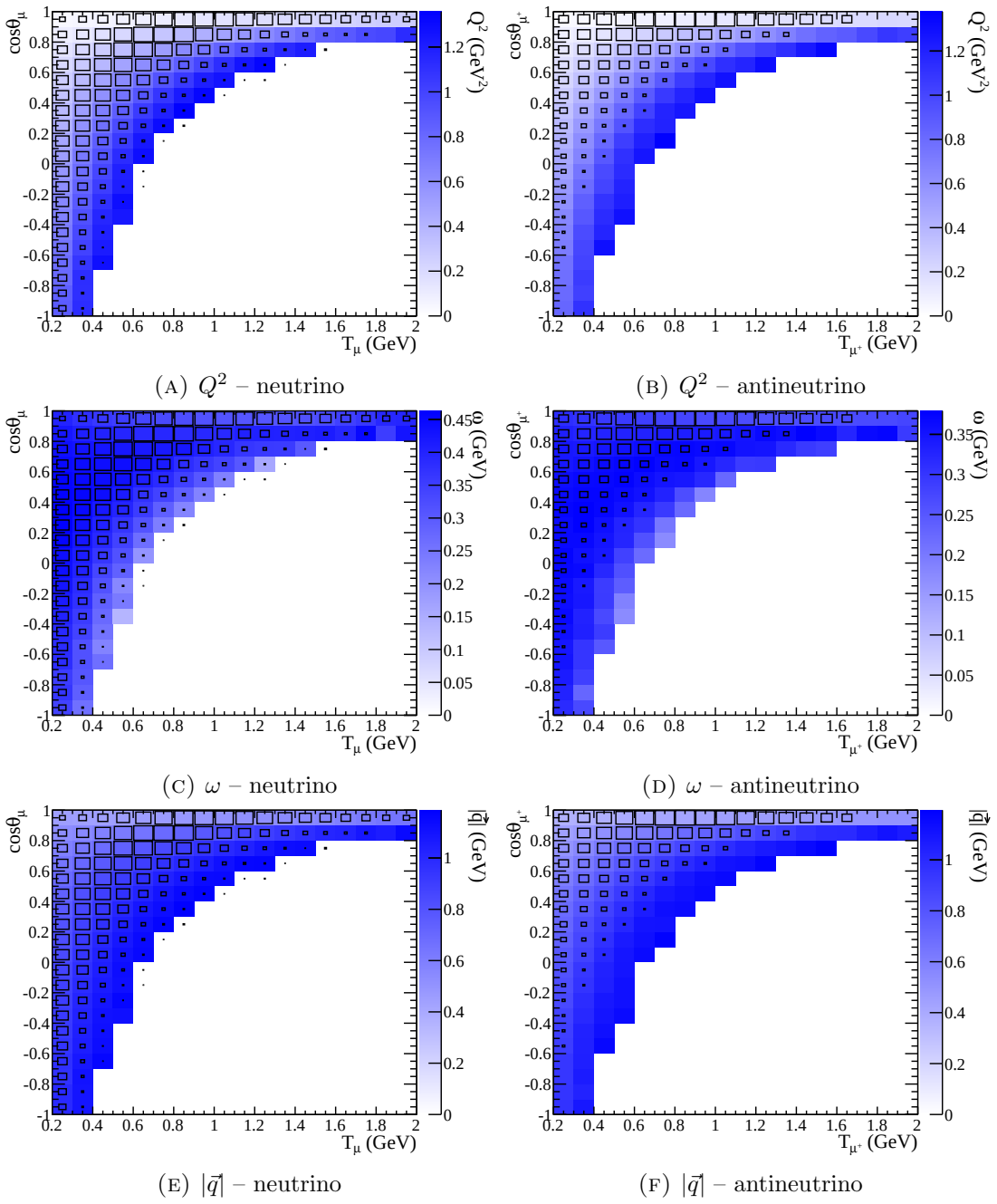

(A) Q^2 – neutrino

(B) Q^2 – antineutrino

(C) ω – neutrino

(D) ω – antineutrino

(E) $|\vec{q}|$ – neutrino

(F) $|\vec{q}|$ – antineutrino

FIGURE 5.13: The average Q^2, ω and $|\vec{q}|$ in each bin of the MiniBooNE neutrino and antineutrino double-differential datasets are shown, as predicted by the nominal MEC model. The MiniBooNE data is overlaid as boxes, where the size of the box indicates the relative strength of the cross section in that bin.

5.3 Fit results

5.3.1 Fake data studies

Fake datasets are produced by the fitting package using the following method:

1. Run one iteration of the fitting code to produce MC distributions for all datasets with a given set of parameters.

2. Use the MC distributions from step 1 as the central values of the data.

3. Modify the MiniBooNE errors bin by bin, $\sigma_F = \sigma_P \times \frac{N_F}{N_P}$, where σ and N are the error and bin contents, and the subscripts F and P denote fake and published respectively.

4. Modify the MINERνA covariance matrix, $M_{ij} = \left(\sigma_P \times \frac{N_F}{N_P}\right)_i \mathrm{Corr}(i,j) \left(\sigma_P \times \frac{N_F}{N_P}\right)_j$, where $\mathrm{Corr}(i,j)$ is the published correlation between bins.

These fake datasets can be used to validate the fitter, check for biases and estimate the size of the parameter errors which will be produced by the fit. For an Asimov fake dataset [280], where the errors are not thrown, the output parameter set from the fit to a fake data set is expected to exactly equal the input parameter set used to produce that data. The parameter errors produced by fitting to an Asimov fake dataset are approximately equal to the size of errors expected in the fit to real data (if the model used in the fit is a reasonable description of real data), which removes the need to make a series of fake datasets where the errors are thrown each time.

Asimov fake datasets were produced using the nominal parameter set $M_{\mathrm{A}} = 1.01$ GeV, MEC = 100% Nieves and $p_{\mathrm{F}} = 217$ MeV, for each of the three models SF+MEC and RFG+RPA+MEC with non-relativistic or relativistic RPA models. Combined fits using these Asimov datasets for the four samples, MiniBooNE double-differential neutrino and antineutrino and MINERνA $\theta \leq 20^\circ$ neutrino and antineutrino, were performed and the results are collected in Table 5.4. Note that the MiniBooNE normalisation parameters were not varied from nominal when producing the fake datasets. The expected errors

Fit type	χ^2/DOF	M_{A} (GeV)	MEC (%)	p_{F} (MeV)	$\lambda_\nu^{\mathrm{MB}}$	$\lambda_{\bar{\nu}}^{\mathrm{MB}}$
Rel. RPA	0.00/228	1.01±0.03	100±18	217±3	1.00±0.05	1.00±0.04
Non-rel. RPA	0.00/228	1.01±0.03	100±18	217±3	1.00±0.05	1.00±0.04
SF+MEC	0.00/228	1.01±0.03	100±21	217±10	1.00±0.05	1.00±0.04

TABLE 5.4: The parameter errors produced by fitting the Asimov datasets for the three models SF+MEC and RFG+RPA+MEC with non-relativistic or relativistic RPA in combined fits with the four datasets MiniBooNE double-differential neutrino and antineutrino and MINERνA $\theta \leq 20^\circ$ neutrino and antineutrino. The Asimov datasets were produced with the nominal parameter set $M_{\mathrm{A}} = 1.01$ GeV, MEC = 100% Nieves and $p_{\mathrm{F}} = 217$ MeV. MiniBooNE normalisation parameters were kept at the nominal value.

found in Table 5.4 are perfectly consistent between the relativistic and non-relativistic RPA models. The expected errors for the SF+MEC model are different, which can be understood because the $p_{\mathrm{F}}^{\mathrm{SF}}$ parameter is localised at low Q^2, and so a strong correlation

with the MEC normalisation is expected, which results in larger errors on both parameters. It is reassuring that all three of the fits find the correct minimum, and this is a very basic validation of the fitter developed for this work.

5.3.2 Combined Fit

Results for the combined fits to all four published datasets are given for the RFG+RPA+MEC and SF+MEC models in Table 5.5. The best fit distributions are compared with MINERνA data in Figure 5.14, and MiniBooNE data in Figure 5.15. Relativistic RPA is shown in the figures, as this was the better fit of the two RPA models available. In the legends of these figures, each entry is given two χ^2 values, the contribution from that dataset to the minimum χ^2 in the combined fit, and the total minimum χ^2 from the combined fit in parentheses. Note that in Figure 5.14, the contributions from MINERνA are calculated for the individual datasets, ignoring cross-correlations, making these numbers slightly misleading. Explicitly, $\chi^2_{\text{MN total}} \neq \chi^2_{\text{MN }\nu} + \chi^2_{\text{MN }\bar{\nu}}$ due to cross-correlations, so the values shown in the figure should be treated with caution.

Fit type	χ^2/DOF	M_{A} (GeV)	MEC (%)	p_{F} (MeV)	$\lambda_{\nu}^{\text{MB}}$	$\lambda_{\bar{\nu}}^{\text{MB}}$
Rel. RPA	97.84/228	1.15±0.03	27±12	223±5	0.79±0.03	0.78±0.03
Non-rel. RPA	117.87/228	1.07±0.03	34±12	225±5	0.80±0.04	0.75±0.03
SF+MEC	97.46/228	1.33±0.02	0 (at limit)	234±4	0.81±0.02	0.86±0.02

TABLE 5.5: Best fit parameter values for the fits to all datasets simultaneously for the RFG+RPA+MEC and SF+MEC fits.

It is clear from Figures 5.14 and 5.15 that MiniBooNE is not completely dominating the fits, as might be expected given the large number of bins in each of the MiniBooNE datasets. Indeed, these fits exploit the fact that, without correlations, $\chi^2_{\text{MB}} \approx \chi^2_{\text{MN}}$. It is also clear that neither model fits all of the datasets perfectly at the best fit point, which is not reflected by the reduced χ^2 values of 97.46/228 and 97.84/228 for the SF+MEC and RFG+RPA+MEC models, respectively. As MiniBooNE lacks bin correlations, the χ^2_{MB} contributions are not as large as would be expected for the number of bins contributed. This may explain why so many theoretical models are able to find good agreement with the MiniBooNE CCQE data.

In all fits performed as part of this work, it was observed that the RFG+RPA+MEC (SF+MEC) fits consistently favoured large pulls on the MiniBooNE normalisation values for both neutrino and antineutrino datasets indicating that the MC underestimated the published data by 20–30% (10–20%)[5]. The MINERνA normalisation uncertainties

[5]That theoretical predictions underestimate MiniBooNE data by 10–20% has been observed elsewhere [195, 227, 229].

cannot be determined accurately as the normalisation uncertainty is included in the published covariance matrix. However, the output distributions show that the MC normalisation is approximately equal to the data normalisation.

The parameter errors from the combined fit results shown in Table 5.5 can be compared with the errors produced in the fake data study shown in Table 5.4. The SF+MEC errors differ because the MEC normalisation parameter is at a limit in the real data fit, so there is no correlation between MEC normalisation and p_{F} which results in a smaller p_{F} error. The RFG+RPA+MEC errors are consistent between the two RPA models in both the real data and fake data fits, but the error on MEC is significantly smaller in the real data fit than the fake data study. The strong suppression of MEC normalisation in the real data fits suggests that there is a shape problem, which probably causes the reduced error in the real data fit. The increase in the p_{F} error seen in the real data fits is likely compensating for the reduction in the MEC error.

Because of the large pulls on the MiniBooNE normalisation parameters, shape-only fits were also performed, as described in Appendix B. It was found that the best fit parameters were largely unchanged by this change in the χ^2 definition. The results from fits to individual datasets, and to various combinations of datasets are shown in Appendix C.

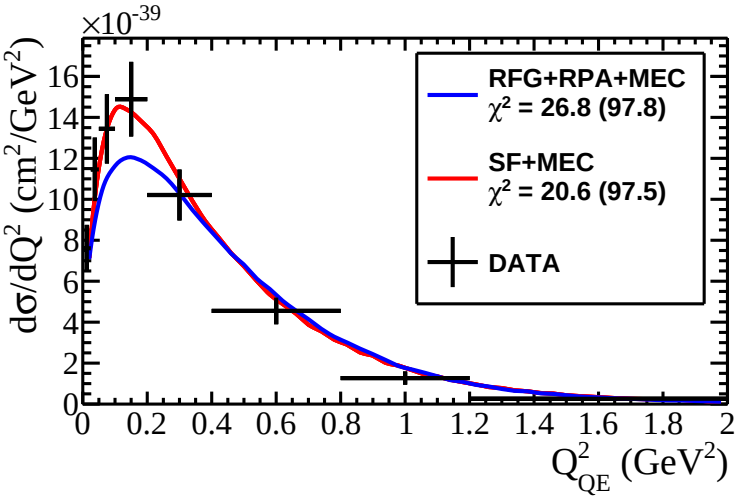

(A) Neutrino

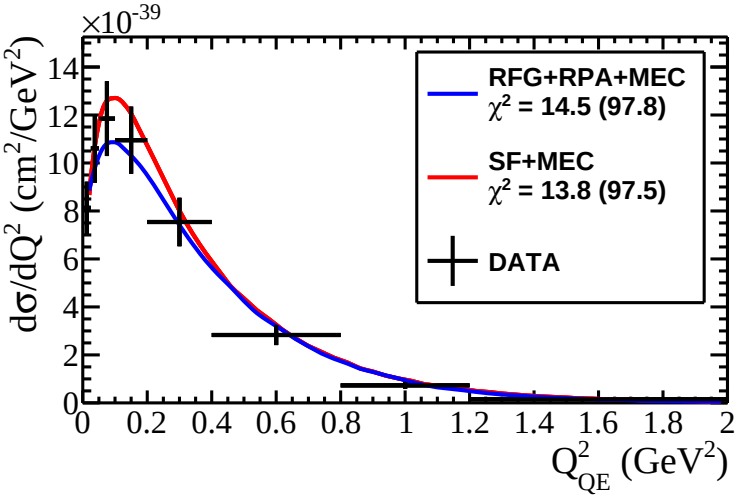

(B) Antineutrino

FIGURE 5.14: Comparison of the best fit from the combined fits detailed in Table 5.5 with the MINERνA datasets used in the fit. The χ^2 values in the legend are the contribution from each dataset at the best fit point, and the total minimum χ^2 for the combined fit.

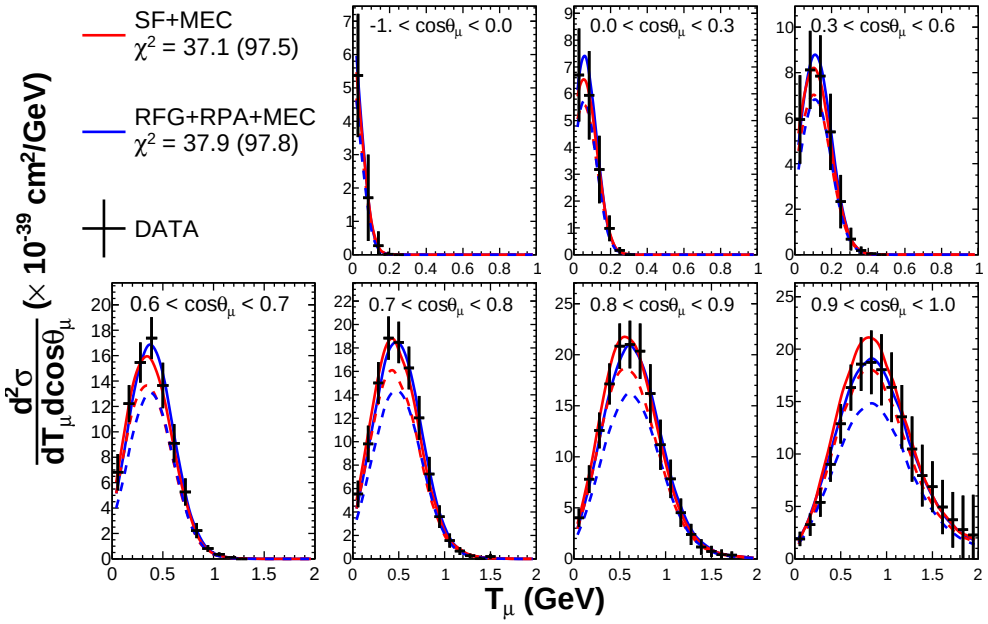

(A) Neutrino

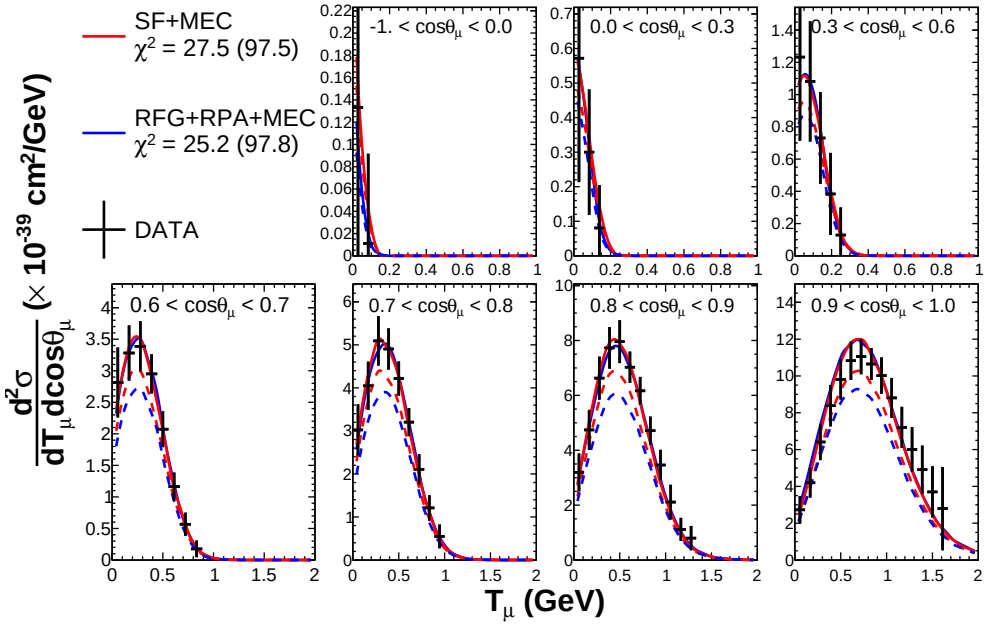

(B) Antineutrino

FIGURE 5.15: Comparison of the best fit from the combined fits detailed in Table 5.5 with the MiniBooNE double-differential datasets used in the fit. The χ^2 values in the legend are the contribution from each dataset at the best fit point, and the total minimum χ^2 for the combined fit. Note that some of the $\cos\theta_\mu$ slices have been combined for presentational purposes. The solid lines include the MiniBooNE normalisation terms, the dashed lines do not, to indicate the large pulls on these parameters.

5.3.3 Parameter Goodness-of-Fit (PGoF) test

Standard goodness-of-fit tests, such as the Pearson χ^2 test used here, test the agreement between prediction and data, but some issues can arise with their use in global fits, as discussed in Reference [281]. The basic problem is that much of the data will have limited or no power to constrain any one parameter, but may agree well with the prediction, so will add little to the χ^2, but contribute another degree of freedom. Thus the minimum χ^2 found may be deceptively good, despite the best fit parameter set not agreeing well with those parts of the dataset that have the most power to constrain key parameters. It is also possible that a dataset with a large number of datapoints (such as MiniBooNE) which does agree well with a model may hide disagreements with other datasets included in a global fit for which fewer datapoints are available (such as MINERνA); again, the key problem is a dilution of the χ^2.

This problem is worsened in the case of datasets for which correlations between datapoints have not been included, when it is expected for χ^2/DOF to be much less than 1, such as is the case for MiniBooNE. So looking at the Pearson χ^2 test statistic is not very illuminating when fitting to both MiniBooNE and MINERνA datasets.

The PGoF is a more rigorous test proposed in Reference [281] for fitting to global datasets, and has been used extensively in sterile neutrino literature [152, 153], where there are often contradictory results coming from different experiments, and the fitters are fitting to many different experiments which are sensitive to different parameters. The PGoF test statistic is given by

$$\chi^2_{\mathrm{PGoF}}(\vec{\mathbf{x}}) = \chi^2_{tot}(\vec{\mathbf{x}}) - \sum_{r=1}^{D} \chi^2_{r,\,min}(\vec{\mathbf{x}}), \tag{5.4}$$

where $\vec{\mathbf{x}}$ are the parameters floated in the fits, D is the number of datasets, χ^2_{tot} is the minimum χ^2 in a fit to all D subsets of the data, and $\chi^2_{r,\,min}$ is the minimum χ^2 obtained in a fit to the rth subset of the data. The PGoF test statistic forms a χ^2 distribution with the number of degrees of freedom

$$P_{\mathrm{PGoF}} = \sum_{r=1}^{D} P_r - P_{tot},$$

where P_r and P_{tot} are the number of degrees of freedom for each fit.

The aim of the PGoF is to test the compatibility of the different datasets in the framework of the model. Put simply, it tests whether the best fit to subsets of the data pulls the fit parameters far from the best fit values found when fitting to all of the data. If different subsets favour very different values, then the subsets are not compatible in

the framework of the model, although individually each may be able to find parameter combinations which produce a good fit.

A further advantage of the PGoF test for a global dataset where a full correlation matrix is not available for some of the data is that the number of degrees of freedom comes from the number of parameters varied in the fits, not from the number of bins that dataset contributes, which partially mitigates the $\chi^2/\text{DOF} \ll 1$ issue. The PGoF test still assumes that the datasets follow a χ^2 distribution, but allows for a lower effective number of degrees of freedom.

A detailed investigation showed that the PGoF test statistic does not follow a χ^2 distribution when some correlations are neglected [282]. However, it has proven extremely useful at highlighting the causes of tension in the combined dataset despite this, and in the absence of MiniBooNE covariance matrices, approximate solutions are necessary.

5.3.4 PGoF results

Using the PGoF test defined in previous section, it is possible to test the compatibility between different subsets of the data. Tables 5.7, 5.8, and 5.9 show a breakdown of the four datasets used in the the combined fits for the non-relativistic RFG+RPA+MEC, relativistic RFG+RPA+MEC and SF+MEC models respectively. The Standard Goodness of Fit (SGoF) for each row is determined using Pearson's χ^2_{min} test, where χ^2_{min} is found by minimising the function given in Equation 5.3, including only terms for the relevant datasets. The PGoF test is found by subtracting χ^2_{min} for each of the constituent datasets from the minimum of the combined dataset. For clarity, the formulae for calculating the PGoF test statistic χ^2_{PGoF} are given explicitly in Table 5.6. The χ^2_{min} value for each dataset is again determined by minimising the function given in Equation 5.3 with only the relevant terms included.

	χ^2_{PGoF}
All	$\chi^2_{\text{ALL}} - \chi^2_{\text{MB}\,\nu} - \chi^2_{\text{MB}\,\bar{\nu}} - \chi^2_{\text{MN}\,\nu+\bar{\nu}}$
MINERνA	$\chi^2_{\text{MN}\,\nu+\bar{\nu}} - \chi^2_{\text{MN}\,\nu} - \chi^2_{\text{MN}\,\bar{\nu}}$
MiniBooNE	$\chi^2_{\text{MB}\,\nu+\bar{\nu}} - \chi^2_{\text{MB}\,\nu} - \chi^2_{\text{MB}\,\bar{\nu}}$
ν	$\chi^2_{\text{MB}\,\nu+\text{MN}\,\nu} - \chi^2_{\text{MB}\,\nu} - \chi^2_{\text{MN}\,\nu}$
$\bar{\nu}$	$\chi^2_{\text{MB}\,\bar{\nu}+\text{MN}\,\bar{\nu}} - \chi^2_{\text{MB}\,\bar{\nu}} - \chi^2_{\text{MN}\,\bar{\nu}}$
MINERνA vs MiniBooNE	$\chi^2_{\text{ALL}} - \chi^2_{\text{MB}\,\nu+\text{MB}\,\bar{\nu}} - \chi^2_{\text{MN}\,\nu+\bar{\nu}}$
ν vs $\bar{\nu}$	$\chi^2_{\text{ALL}} - \chi^2_{\text{MB}\,\nu+\text{MN}\,\nu} - \chi^2_{\text{MN}\,\bar{\nu}+\text{MB}\,\bar{\nu}}$

TABLE 5.6: Explicit formulae for calculating the χ^2_{PGoF} test statistics for each of the subsets of the data investigated. MiniBooNE and MINERνA are denoted with MB and MN respectively. Each χ^2 value listed in this table denotes the χ^2 at the minimum.

In each fit, M_A, MEC normalisation, p_F, and any MiniBooNE normalisation terms are allowed to float. The best fit χ^2 and parameter values are shown in Appendix C.1 for all of the fits used to produce the PGoF results shown in this section.

	χ^2_{min}/DOF	SGoF (%)	χ^2_{PGoF}/DOF	PGoF (%)
All	117.9/228	100.00	25.3/6	0.03
MINERνA	30.3/13	0.42	0.4/3	93.09
MiniBooNE	65.7/212	100.00	3.4/3	33.09
ν	69.1/142	100.00	12.7/3	0.53
$\bar{\nu}$	46.1/83	99.97	10.4/3	1.55
MINERνA vs MiniBooNE	117.9/228	100.00	21.9/3	0.01
ν vs $\bar{\nu}$	117.9/228	100.00	2.6/3	45.12

TABLE 5.7: PGoF results for various subsets of the data for the RFG+RPA+MEC model with the RPA shape parameter fixed at the non-relativistic limit.

One subtlety must be kept in mind when analysing the results in Tables 5.7, 5.8, and 5.9: the PGoF test is only appropriate for statistically independent datasets. This makes the interpretation difficult for MINERνA, where cross-correlations are provided and used in the fits. Whenever a subset of data includes both MINERνA ν and $\bar{\nu}$ datasets, the fits include cross-correlations, but if only one dataset is included, they do not (and indeed, cannot). This means that two of the rows in each table give slightly unreliable results: 'MINERνA', and 'ν vs $\bar{\nu}$'. In each case, the χ^2 function for the combined dataset includes cross-correlations, and the χ^2 functions for the subdivided dataset does not. The issue is most obvious in Table 5.8, where the 'ν vs $\bar{\nu}$' row gives a negative PGoF χ^2. These values are still useful as a comparison between models and to give a rough idea of compatibility between datasets, but the exact values must be treated with caution.

	χ^2_{min}/DOF	SGoF (%)	χ^2_{PGoF}/DOF	PGoF (%)
All	97.8/228	100.00	17.9/6	0.66
MINERνA	23.4/13	3.74	1.0/3	79.03
MiniBooNE	58.6/212	100.00	2.0/3	57.69
ν	62.6/142	100.00	16.1/3	0.11
$\bar{\nu}$	38.5/83	100.00	6.1/3	10.75
MINERνA vs MiniBooNE	97.8/228	100.00	15.9/3	0.12
ν vs $\bar{\nu}$	97.8/228	100.00	-3.3/3	100.00

TABLE 5.8: PGoF results for various subsets of the data for the RFG+RPA+MEC model with the RPA shape parameter fixed at the relativistic limit.

The PGoF test will give misleading results when parameters are at a limit (results will show more compatibility than they should). As the RPA shape parameter is very

strongly bounded, it was not allowed to vary in any PGoF test. Instead it was fixed at the non-relativistic limit for all fits used in Table 5.7, and at the relativistic limit for all fits used in Table 5.8.

	χ^2_{min}/DOF	SGoF (%)	χ^2_{PGoF}/DOF	PGoF (%)
All	97.5/228	100.00	41.1/6	0.00
MINERνA	12.6/13	47.75	1.0/3	79.49
MiniBooNE	50.2/212	100.00	6.5/3	8.92
ν	54.8/142	100.00	25.1/3	0.00
$\bar{\nu}$	34.1/83	100.00	8.5/3	3.61
MINERνA vs MiniBooNE	97.5/228	100.00	34.6/3	0.00
ν vs $\bar{\nu}$	97.5/228	100.00	8.5/3	3.59

TABLE 5.9: PGoF results for various subsets of the data for the SF+MEC model.

The PGoF test highlights the incompatibility of the various datasets within the framework of the SF+MEC and both RFG+RPA+MEC models, despite the apparent goodness of fit when only considering χ^2_{min}/DOF. It is clear from Table 5.9 that the SF+MEC model does not fit the various datasets consistently: the poor PGoF statistics indicate that the datasets favour very different parameter values when fitted separately. This is particularly true for any fits involving the MiniBooNE neutrino dataset, though there is no *a priori* reason to exclude this dataset and thus improve the fit results.

The PGoF tests for RFG+RPA+MEC using both relativistic and non-relativistic RPA, shown in Tables 5.8 and 5.7, show much better compatibility between experiments than SF+MEC. There is still a considerable amount of tension, but the PGoF is a stringent test, so the values obtained are not surprising. In particular, the good agreement between neutrino and antineutrino is reassuring as it is intended for T2K to use the same systematics for both neutrino and antineutrino running. Much of the disagreement comes from differences between MINERνA and MiniBooNE. Because of the relatively poor consistency between datasets for the SF+MEC model compared with RFG+RPA+MEC, the latter model has been chosen as the T2K default. This is an important result of the work in this chapter.

The RPA shape reweighting parameter was at the relativistic limit when allowed to float in the combined fit to all datasets, and the χ^2_{min} obtained in that fit is lower than the value obtained in a fit using the non-relativistic model. Although this already suggests that the relativistic RPA model may be preferable to the non-relativistic RPA model, the PGoF test provides an additional, more compelling reason. The difference in the PGoF results between using non-relativistic and relativistic RPA in the RFG+RPA+MEC model, shown in Tables 5.7 and 5.8, are not as pronounced as the differences between

the SF+MEC and either RFG+RPA+MEC model. But the relativistic RPA model shows better overall compatibility between the datasets, and much better agreement between the neutrino and antineutrino datasets (although the caveat about dividing the MINERνA samples applies). For this reason, the relativistic RFG+RPA+MEC model has been selected as the default T2K model for future oscillation analyses.

5.3.5 CCQE normalisation

The previous NIWG fits of the CCQE cross section [272, 273], used since 2012 for T2K oscillation analyses, included an overall normalisation uncertainty of the CCQE cross section. The CCQE normalisation error was taken to be the MiniBooNE neutrino normalisation error of 10.7%, which was necessary as it was the only dataset available at the time. An advantage of having more datasets is that it is possible to resolve the ambiguity between normalisation uncertainty on any single measurement, and on the normalisation of the model itself. Because the CCQE model normalisation error can only properly be constrained by fitting to all datasets simultaneously, it has been fixed up to this point to ensure meaningful PGoF results (where fits to individual datasets are necessary). Note that CCQE normalisation only affects true CCQE events, not MEC events (which are a different NEUT interaction mode). Note also that an energy independent normalisation parameter on the CCQE model is not physically motivated, but it is a convenient parameter to use, and has previously been included in T2K analyses.

Table 5.10 shows the best fit parameters when a fit is performed to the relativistic RFG+RPA+MEC model with the inclusion of the CCQE normalisation parameter. This fit is performed in the same way as the fit to RFG+RPA+MEC shown in Section 5.3.2. Two main conclusions can be drawn from Table 5.10: firstly, when the

Fit type	χ^2/DOF	M_A (GeV)	MEC (%)	p_F (MeV)	CCQE (%)
Fixed CCQE	97.84/228	1.15±0.03	27±12	223±5	N/A
Free CCQE	97.62/227	1.16±0.03	29±12	223±5	96±8

TABLE 5.10: Results from fits to all datasets with the relativistic RFG+RPA+MEC model, with and without allowing the normalisation of the CCQE model to float.

CCQE normalisation is free in the fit, the best fit value is very close to the nominal; secondly, floating the CCQE normalisation parameter does not change the best fit values for the other parameters significantly. Figure 5.16 shows the correlation matrices with and without inclusion of the CCQE normalisation parameter in the fits. The MiniBooNE normalisation parameters are included in the matrix because they are likely to be strongly correlated with the CCQE normalisation, although it should be stressed that

these are properties of the fit, rather than interesting output from it. It is clear that the correlations are not significantly changed by the inclusion of the CCQE normalisation parameter.

A shape-only CCQE fit was also performed, as described in Appendix B, which found no significant change to the best fit parameters, compared with the fit with fixed CCQE normalisation, described in Section 5.3.2. This agrees well with the conclusion of the fit presented in this section, where the CCQE normalisation has been allowed to vary. Discrepancies between the best fit parameter values favoured by the two would indicate a tension in the fit arising from the normalisation errors provided by the experiments. It is reassuring that no such tension is seen.

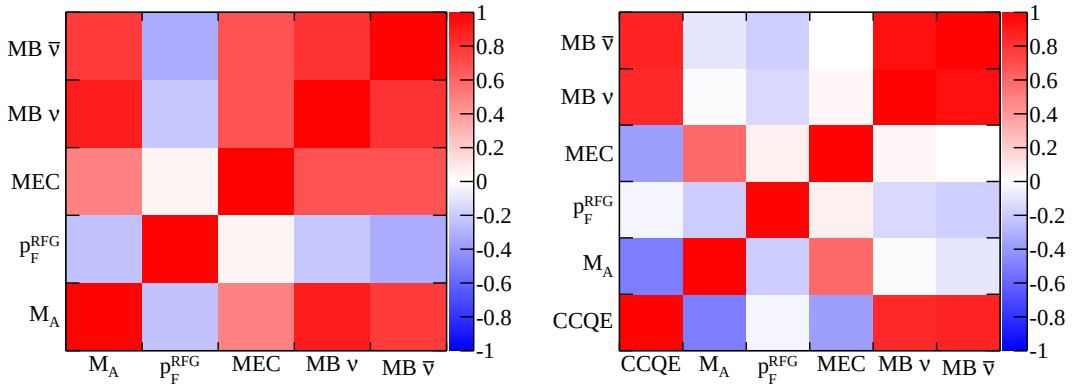

(A) Fixed CCQE normalisation (B) Free CCQE normalisation

FIGURE 5.16: The correlation matrix between parameters with both fixed and free CCQE normalisation

Because the CCQE normalisation is not significantly pulled away from 1 when it is allowed to float in the fit, it is possible to have confidence in the nominal normalisation of the CCQE model, and so CCQE normalisation is no longer a recommended NIWG parameter for T2K oscillation or cross section analyses.

5.3.6 Rescaling parameter errors

Assuming Gaussian statistics, 1σ errors on a fit parameter are defined by the parameter value for which $\chi^2 = \chi^2_{min} + 1$. MINUIT uses this assumption when calculating the errors at the minimum, which were included with the best fit values for the combined fit in Table 5.5. However, as well as motivating the use of the PGoF test, the lack of bin correlations from MiniBooNE also means that Gaussian statistics no longer work as expected when estimating parameter errors.

There is a large body of literature looking at how this problem affected fits to parton density distributions, where fitters attempted to perform global fits to a large number of datasets, many of which did not provide bin correlations [283–285]. A summary of the work of one PDF fitting group is given in Reference [283] and was used as a guide here. Their solution for producing reasonable parameter error estimates is to inflate the value of the $\Delta\chi^2$ used to define the 1σ parameter errors, although no generic solution is offered for defining that value. In the case of the PDF fits in [283], the $\Delta\chi^2$ used was very large, $\sim$100, although it should be kept in mind that many more datasets are used in that fit than in the current work.

The PGoF gives a value for the incompatibility between the datasets: how much the χ^2 increases between the best fit points of each experiment and the best fit point for the combined dataset. The PGoF value can therefore be used as a measure of how much the errors have to be inflated to cover the difference between the best fit parameter values from the combined fit and the best fit values of individual datasets, this is shown explicitly in Equation 5.5:

$$\Delta\chi^2 = \sqrt{\chi^2_{\text{PGoF}}/\text{DOF}_{\text{PGoF}}} \tag{5.5}$$

Note that this PGoF rescaling procedure does not modify the correlations between parameters, it simply rescales the error on each parameter.

There is some ambiguity over which PGoF statistic to use, the 'All' or 'MINERνA vs MiniBooNE' row of Table 5.8, with χ^2_{PGoF}/DOF values of 17.9/6 and 15.9/3 respectively. The more conservative value is from the 'MINERνA vs MiniBooNE' (because the greatest differences are between experiments, not between neutrino and antineutrino running), so this is used. To be explicit, we multiply the parameter errors from MINUIT by $\sqrt{15.9/3} \approx 2.3$ based on this statistic. It should also be noted that this rescaling procedure more than covers the difference between neutrino and antineutrino datasets.

5.4 Inputs to other T2K analyses

Before concluding, it is worth summarising the main results of the CCQE fits presented in this chapter which will be used as an input to T2K oscillation analyses, and as a systematic error for T2K cross section analyses.

- The RFG+RPA+MEC model should be used, the SF+MEC model is disfavoured by the fits.
- There is no systematic covering the difference between the base nuclear models.

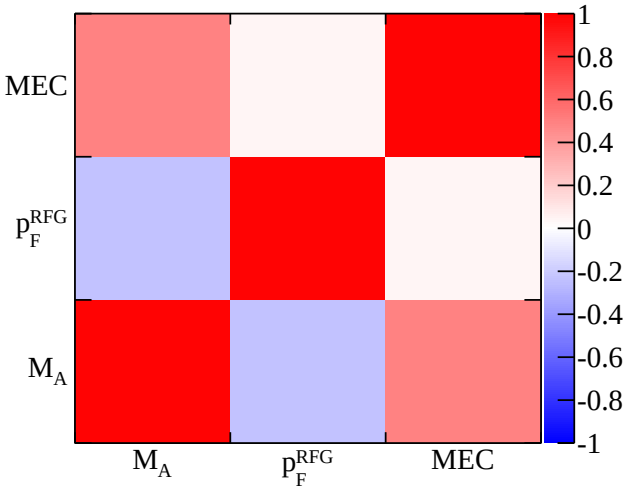

FIGURE 5.17: Correlation matrix for the CCQE parameters for the RFG+RPA+MEC model.

- The RPA shape parameter should be set at the relativistic limit. It is a very strongly bounded parameter so care must be taken in any analyses which want to free it.
- CCQE normalisation should be fixed at 1, and no error has been assigned to this parameter.
- The best fit values and errors for the other CCQE parameters, M_A, p_F^{RFG} and MEC normalisation, are summarised in Table 5.11, and are correlated according to the matrix shown in Figure 5.17.

Fit type	χ^2/DOF	M_A (GeV)	MEC (%)	p_F (MeV)
Unscaled	97.84/228	1.15±0.03	27±12	223±5
PGoF scaling		1.15±0.06	27±27	223±11

TABLE 5.11: The final errors for the CCQE parameters. Note that the scaled errors should be used by T2K analyses which use these results.

5.5 Summary

This chapter describes a fit to two sophisticated models for CCQE-like interactions to all of the available cross section data on heavy nuclear targets. This analysis is a major update to the T2K neutrino interaction model, and will be used in T2K oscillation and cross section analyses from the summer of 2015 onwards. This is the first time that these new models have been used in a fit to all of the available CCQE heavy target data and

will be the first time that these new models have been used consistently by an oscillation experiment.

The relativistic RFG+RPA+MEC model has been recommended as the default T2K CCQE cross section model based on the level of consistency between datasets, assessed using the PGoF test (Section 5.3.3). The use of the PGoF test was motivated by the well-known problems when fitting to MiniBooNE data without bin correlations. The same problem motivated the parameter rescaling method (Section 5.3.6), which has been used to ensure the errors produced by the fit cover the difference between all of the different datasets. The final results of the fit and inputs to analyses are given in Section 5.4. These are the best fit parameter values, scaled parameter errors, and a correlation matrix between the parameters which have been assigned errors. Parameters which should be fixed are also mentioned, with their recommended values.

The results from the fit show that no models which are currently available in NEUT describe all of the CCQE data adequately. In particular, there is a significant difference between MiniBooNE and MINERνA data which forces the model parameters away from theoretical expectations. Although the M_{A} value obtained from the fit to the RFG+RPA+MEC model is an improvement on past fits of the RFG model to MiniBooNE data alone, it is inconsistent with that obtained in global fits to light target bubble chamber data or high energy heavy target data [183]. There also seems to be a shape problem with the MEC model, which leads to the suppression of the MEC cross section when MEC normalisation is allowed to vary in the fit (at the best fit point MEC is suppressed to 27% of the Nieves nominal value). This suppression is driven by MINERνA, which completely removes the MEC component of the model when MiniBooNE is not included in the fit (see the individual fit results given in Appendix C). The SF+MEC model shows the same disagreement, and MEC is completely removed at the best fit point found in this work (Section 5.3.2). As would be expected, the SF model by itself requires an inflated M_{A} value to model the data. Including an RPA calculation appropriate for the SF model is likely to change this conclusion significantly, and this work will be revisited when such a calculation is available.

Moving away from the RFG model for CCQE interactions is an ambitious step for a neutrino experiment as it is a departure from the standard which has been used for decades [202]. The new models on the market are not perfect, and their implementation into NEUT and other neutrino interaction generators will always have technical foibles. However, further theoretical development of these models requires the engagement of the experimental community, and so using them in our simulations is essential to move the field onwards. It is also clear that the current approach of inflating M_{A} is inadequate,

and something better must be done in order to make precision measurements of neutrino oscillation parameters.

The fitting framework developed for this analysis is extensible and the general method for producing cross section errors developed in this work will be used with new CCQE models and datasets in future, and with new cross section channels entirely, to continue to contrain systematic errors for T2K oscillation and cross section analyses. The results from the CCQE fits presented here will also help inform the future model development required to fit the data. It is clear that alternative MEC models and fundamental parameters in the MEC model should be investigated, to see whether the disagreement with the MEC shape is telling us something meaningful about the Nieves model. It is also probable that the current RPA model is too inflexible, and this is partially responsible for the disagreement between MiniBooNE and MINERνA data. Both of these problems may relate to the fact that for several years, the only data available for theorists to use for building models against was from the MiniBooNE neutrino dataset. Converging on a new CCQE model which adequately describes all current and future data is likely to require several iterations between experimentalists and model builders. Confronting all the available models with a variety of data, as has been done in this analysis, and including these models in full MC simulations, as will be done in T2K with the output from this analysis, is an important step in this cycle from the experimental side.

Chapter 6

Implementation of the Effective Spectral Function model in NEUT

This chapter describes the implementation of the *Effective Spectral Function* (ESF) model into NEUT, and makes the first comparisons of the model with neutrino-nucleus scattering data. The ESF is a model for Charged-Current Quasi-Elastic (CCQE) and Neutral-Current Elastic (NCEL) neutrino-nucleus scattering which agrees with electron scattering data by construction. Agreement with the longitudinal response of electron scattering for all nuclear targets is guaranteed by ensuring that the outgoing lepton kinematics of the ESF match the predictions of the superscaling model described in Section 6.1, which is itself a parametrisation of a wealth of electron scattering data. Agreement with the transverse response of electron scattering data is found using the Transverse Enhancement Model described in Section 6.2, which parametrises the observed discrepancy between the longitudinal and transverse responses found in electron scattering data. The ESF model is described in detail in Section 6.3; details of the implementation in NEUT and validation plots are given in Section 6.4; the model is compared with the available neutrino-nucleus data in Section 6.6; and finally, some concluding remarks are made in Section 6.7.

6.1 The ψ' superscaling model

Electron-nucleus scattering data can be separated into longitudinal ($R_L(\omega, \vec{q})$) and transverse ($R_T(\omega, \vec{q})$) responses, which depend on the energy transfer, ω, and the three momentum transfer, $\vec{q}$. Longitudinal and transverse refer to the polarisation of the virtual

photon in the interaction; the former is associated with electric charge, and the latter with magnetisation [215]. The Rosenbluth separation [286] is a method for separating the responses from electron-nucleus scattering data by exploiting the relationship

$$\frac{d\sigma}{d\Omega dE'} = \frac{\alpha^2 \cos^2(\theta_e/2)}{2E \sin^2(\theta_e/2)} \left[\left(\frac{Q^2}{|\vec{q}|^2} \right)^2 R_L(\omega, \vec{q}) + \left\{ \left(\frac{Q^2}{2|\vec{q}|^2} \right) + \tan^2 \left(\frac{\theta_e}{2} \right) \right\} R_T(\omega, \vec{q}) \right], \tag{6.1}$$

where Ω is the solid angle, α is the fine structure constant, θ_e is the angle the electron was scattered through, Q^2 is the four-momentum transfer squared and E and E' are the energies of the initial and final state electron respectively. By taking a range of measurements where ω and $\vec{q}$ are fixed, and varying θ_e, it is possible to extract $R_L(\omega, \vec{q})$ and $R_T(\omega, \vec{q})$.

Reduced responses f_L and f_T are obtained by dividing the responses R_L and R_T by the expected cross section if all nuclear effects are neglected,

$$Z\sigma_{ep}(q) + N\sigma_{en}(q), \tag{6.2}$$

where Z and N are the atomic number and number of neutrons, and $\sigma_{ep}(q)$ and $\sigma_{en}(q)$ are the elastic scattering cross sections on single protons and neutrons respectively, and q is the four-momentum transfer. Note that $Q^2 = -q^2$: the use of Q^2 to denote four-momentum transfer squared and q for four-momentum transfer is a convention widely used in the literature.

It has been found that an appropriately constructed function can describe the electron scattering longitudinal reduced response on all nuclear targets, for all values of q. The latter is referred to as *scaling of the first kind*, and the former as *scaling of the second kind*. A function which exhibits both types of scaling is said to *superscale*. One such superscaling variable ψ' is a function of q and energy transfer ω:

$$\psi' = \frac{1}{\sqrt{\xi_F}} \frac{\lambda' - \tau'}{\sqrt{(1+\lambda')\tau' + \kappa\sqrt{\tau'(1+\tau')}}}, \tag{6.3}$$

which uses the dimensionless variables

$$\xi_F = \sqrt{1 + \frac{p_{\mathrm{F}}^2}{M_n^2}} - 1, \qquad \lambda' = \frac{\omega - E_{\mathrm{shift}}}{2M_n},$$
$$\kappa = \frac{|\vec{q}|}{2M_n}, \qquad \tau' = \kappa^2 - \lambda'^2,$$

where p_{F} is the Fermi momentum, E_{shift} is a parameter which centres the peak of ψ' on zero, and M_n is the struck nucleon mass. Note that ψ' is not a unique superscaling variable, but it is the one most commonly used.

It can be seen from Figure 6.1 that longitudinal electron scattering data plotted as a function of ψ' on a variety of targets and for different values of q exhibits both types of scaling. However, the transverse response plotted as a function of ψ' does not scale with the four momentum transfer, and does not scale perfectly with the nuclear species. It should be noted that the RFG model also superscales [215], but it cannot account for the asymmetry of the longitudinal response (which is apparent from Figure 6.1a), and is therefore a poor fit to electron-nucleus scattering data.

The superscaling function is tuned to the longitudinal response measured in electron-nucleus scattering data on a variety of nuclear targets and q values [71], giving the tuned function

$$F(\psi') = \kappa_{\text{Pauli}} \times \frac{1.3429}{p_{\text{F}} \left[1 + 1.7119^2 \left(\psi' + 0.19525\right)^2\right] \left(1 + \exp\left\{-1.69\psi'\right\}\right)}, \tag{6.4}$$

where the Pauli blocking factor, κ_{Pauli}, is given by [71]

$$\kappa_{\text{Pauli}} = \begin{cases} \dfrac{3|\vec{q}|}{4p_{\text{F}}} \left[1 - \dfrac{1}{12}\left(\dfrac{|\vec{q}|}{p_{\text{F}}}\right)^2\right] & \text{if } |\vec{q}| < 2p_{\text{F}} \\ 1 & \text{if } |\vec{q}| \geq 2p_{\text{F}}. \end{cases} \tag{6.5}$$

Note that the Fermi momentum p_{F}, which describes the expected broadening of the quasielastic peak due to Fermi motion of bound nucleons, and E_{shift}, which ensures the peak of $F(\psi')$ is centred on $\psi' = 0$, are also tuned to electron-nucleus scattering data and vary with the nuclear target as shown in Table 6.1. Together, p_{F} and E_{shift} ensure scaling of the second kind.

A	p_{F} (GeV)	E_{shift} (GeV)
3	0.115	0.001
$4 \leq A \leq 7$	0.190	0.017
$8 \leq A \leq 16$	0.228	0.0165
$17 \leq A \leq 25$	0.230	0.023
$26 \leq A \leq 38$	0.236	0.018
$39 \leq A \leq 55$	0.241	0.028
$56 \leq A \leq 60$	0.241	0.023
$A \geq 61$	0.245	0.018

TABLE 6.1: Values of the Fermi momentum, p_{F}, and the energy shift, E_{shift} parameters for nuclei with atomic number A. This table is reproduced from Table 1 of Reference [79].

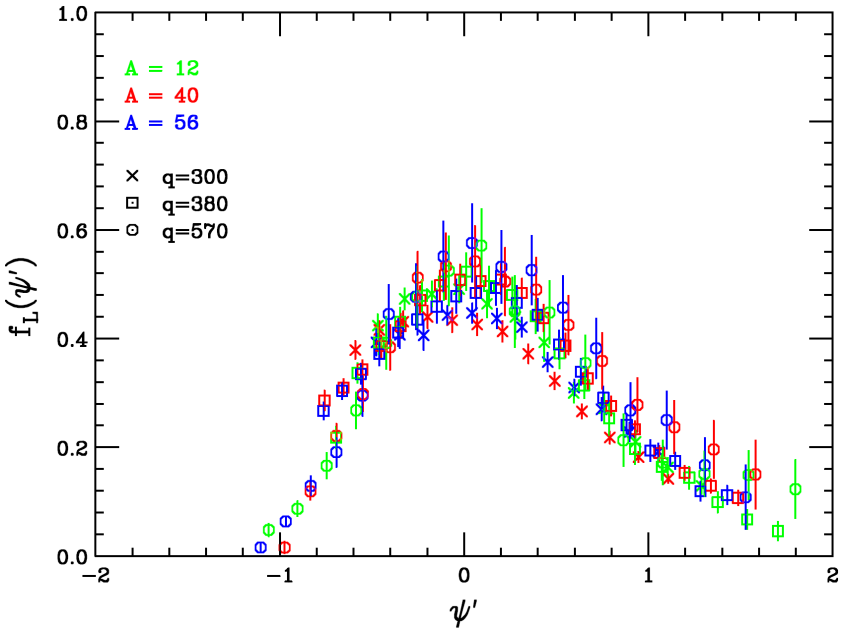

(A) Longitudinal response

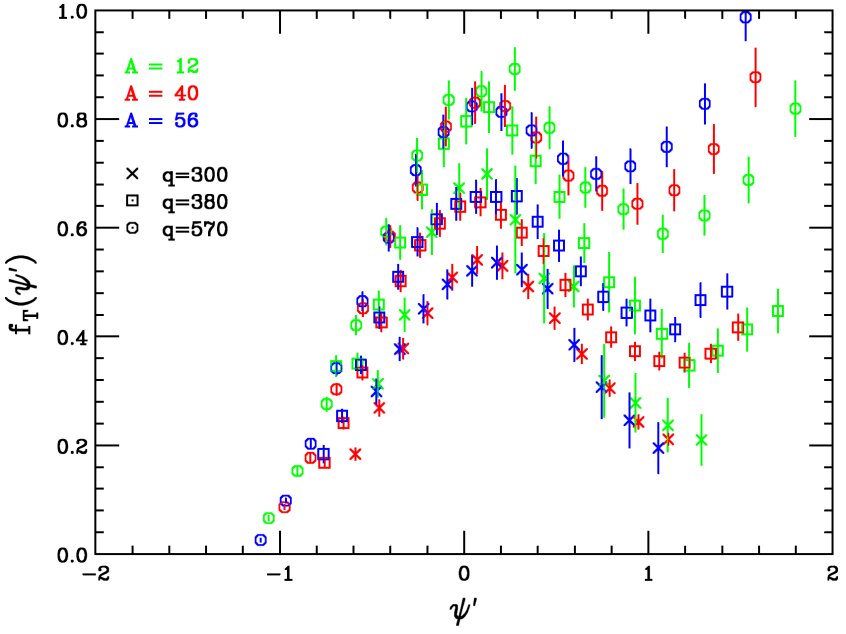

(B) Transverse response

FIGURE 6.1: Electron-nucleus scattering data separated into longitudinal and transverse responses, plotted as a function of ψ'. Data from ^{12}C (green), ^{40}Ar (red) and ^{56}Fe (blue) are shown for three different values of four-momentum transfer, q, 300 MeV (crosses), 380 MeV (squares) and 570 MeV (circles). These figures have been modified from Figures 10 and 11 of Reference [67], which were produced using data described in Reference [68].

6.2 The Transverse Enhancement Model

It has already been remarked that the transverse response in electron scattering data on nuclear targets does not scale with the four momentum transfer as is observed for the longitudinal response. A simple model to parametrise this discrepancy is the Transverse Enhancement Model (TEM) [69]. In the TEM, the ratio of the transverse to the longitudinal response is parametrised as a function of Q^2

$$R_{\mathrm{TEM}} = 1 + AQ^2 \exp\left(\frac{-Q^2}{B}\right), \tag{6.6}$$

R_{TEM} is tuned to electron scattering data on a carbon target as shown in Figure 6.2. The best fit values obtained in the original fit and shown in Figure 6.2 are $A = 6.0 \pm 0.7$ GeV^{-2} and $B = 0.34 \pm 0.01$ GeV^2 [69]. An update to the JUPITER data [71] used in the TEM fit gave the best fit values $A = 5.194$ GeV^{-2} and $B = 0.276$ GeV^2, which are quoted without errors in Reference [71]. Note that Figure 6.2 shows the fit parameters with errors from the original fit in Reference [69].

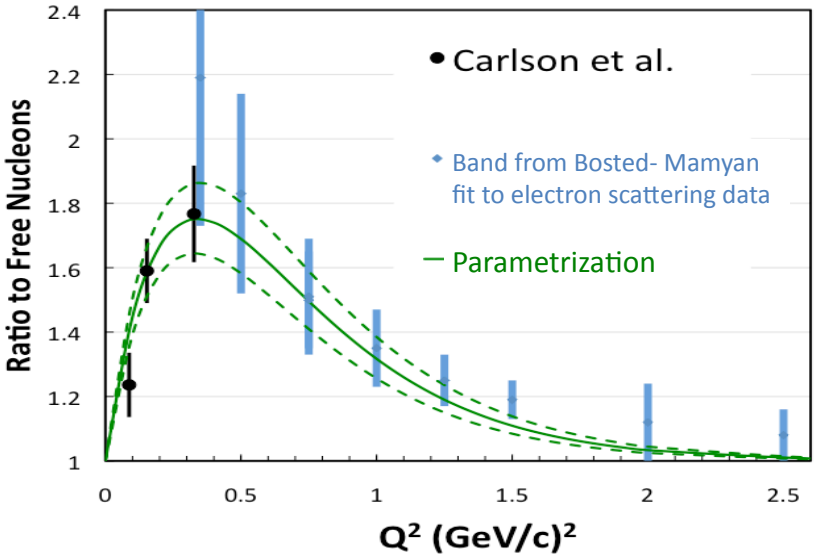

FIGURE 6.2: The ratio of the transverse to the longitudinal response from electron scattering on a carbon targets as a function of Q^2, reproduced from Figure 3 of Reference [69]. The black points at low Q^2 are taken from Carlson *et al.* [70], the error bands are taken from the JUPITER collaboration [71]. Dashed lines denote the upper and lower error bands from the fit.

The form of the TEM fit function given in Equation 6.6 can be used to parametrise the excess as an enhancement to the magnetic form factors

$$G_{M_n}^{nuclear}(Q^2) = G_{M_n}(Q^2) \times \sqrt{1 + AQ^2 \exp\left(\frac{-Q^2}{B}\right)},$$
$$G_{M_p}^{nuclear}(Q^2) = G_{M_p}(Q^2) \times \sqrt{1 + AQ^2 \exp\left(\frac{-Q^2}{B}\right)}, \tag{6.7}$$

where the magnetic form factors for protons and neutrons are $G_{M_p}(Q^2)$ and $G_{M_n}(Q^2)$ respectively[1]. It should be stressed that the TEM is a model of multinucleon effects which contribute to the transverse response of electron-nucleus scattering. It is not a measurement of an enhancement of the magnetic form factor; this parametrisation is simply a convenient way to include the observed enhancement in electron and neutrino scattering cross section formulae. For example, the magnetic form factors from Equation 6.7 can be trivially included in the Charged-Current Quasi-Elastic (CCQE) neutrino-nucleon cross section formula given in Section 2.2.1.

By construction, using the ψ' superscaling model with the TEM guarantees agreement with both the longitudinal and transverse responses of electron scattering data on all nuclear targets with $A \geq 3$. Note that the transverse response does not scale perfectly with the nuclear target, as can be seen in Figure 6.1b, so this agreement is only guaranteed for carbon. However, the disagreement is expected to be small for other targets, so the TEM is an approximation of the transverse enhancement expected for targets heavier than carbon even though it was only tuned to carbon data [69, 71][2].

An important limitation of the TEM worth bearing in mind is that it only models multinucleon interactions which contribute to the vector part of neutrino-nucleus interactions. Any modifications to the axial part of the cross section, or the axial-vector interference terms are not modelled. A discussion of the importance of these contributions can be found in Reference [215].

6.3 The Effective Spectral Function formalism

In Section 2.4, the Spectral Function (SF) of Benhar *et al.* [51, 176, 287] was introduced, which is a sophisticated description of the initial state nucleon distribution within a nucleus, in terms of the magnitude of the nucleon three-momentum, $|\vec{k}|$, and the removal energy, E_R, required to liberate the bound nucleon. Although the Benhar SF is an

[1] See Section 2.2.1 for a general discussion on the vector form factors.

[2] Of course, nuclear target dependent values for the parameters A and B could be obtained through fits to electron scattering data on other targets.

advance on the Relativistic Fermi Gas (RFG) model, it does not describe the outgoing lepton kinematic distributions of electron scattering data well [71]. This suggests that there are nuclear effects which affect the outgoing lepton kinematics, which are not currently understood.

The Effective Spectral Function (ESF) [71, 80] is based conceptually on the Benhar SF, but agrees with electron scattering data by construction without requiring a complete understanding of the physics behind the observed distribution. It models the outgoing lepton kinematic distribution observed in electron scattering by changing the initial state distribution of nucleons within the nucleus. The ψ' superscaling model described in Section 6.1 is used as a convenient parametrisation of the global electron scattering dataset[3]. By sweeping all of the possible FSI effects under the initial state nucleon rug, reasonable agreement can be found with electron scattering data without a full understanding of all of the FSI effects, and in a framework (SF) which is already available in many MC generators.

There is no superscaling prediction available for electron scattering on a deuterium target, but this is included in the ESF [71, 80] using the same formalism by ensuring agreement with an alternative theoretical prediction [288] which agrees with electron-deuterium scattering data.

6.3.1 ESF kinematics

Two different processes are modelled by the ESF as shown in Figure 6.3, where the particle naming conventions used in this chapter are defined. As for the Benhar SF, there is a mean field component, referred to as 1p1h (one particle, one hole), and a 2p2h (two particles, two holes) contribution due to short range correlations between nucleons in the initial state. The off-shell energy of the initial state nucleon for the 1p1h and 2p2h processes is expressed

$$E_i^{\text{off}}(1p1h) = M_A - \sqrt{V(Q^2)\vec{p}_i^{\,2} + (M^*_{A-1})^2}, \tag{6.8}$$

$$E_i^{\text{off}}(2p2h) = M_D - 2\Delta - \sqrt{V(Q^2)\vec{p}_i^{\,2} + M_s^2}, \tag{6.9}$$

where $M^*_{A-1} = M_A - M_i + \Delta$ is the mass of the $A-1$ nuclear remnant, M_A is the mass of the nucleus, M_D is the mass of the deuteron, M_i is the mass of the initial state nucleon, M_s is the mass of a spectator nucleon and Δ is the average binding energy. $V(Q^2)$ is a low Q^2 modification designed to produce better agreement with the superscaling model

[3] The fit to electron scattering data has already been done to tune the superscaling prediction so does not need to be done by the ESF model authors.

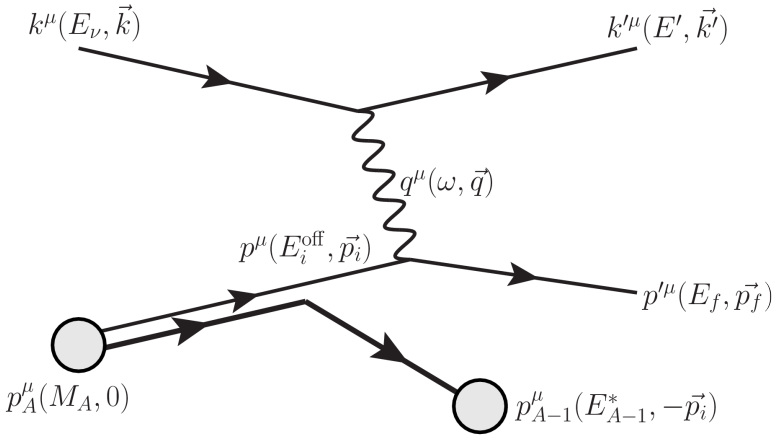

(A) 1p1h process

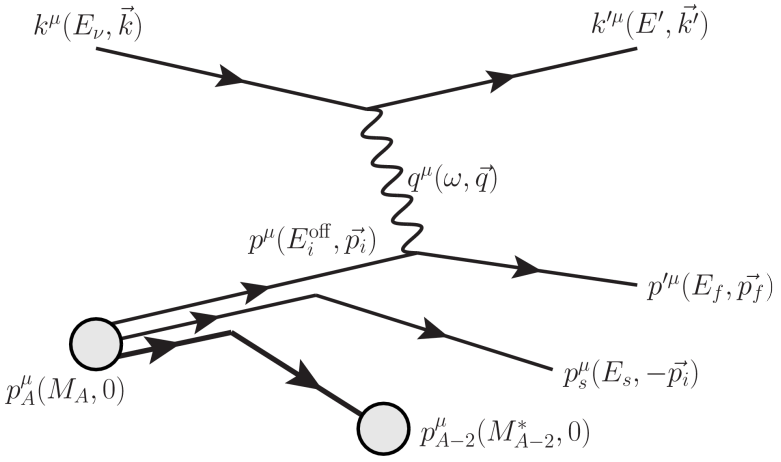

(B) 2p2h process

FIGURE 6.3: Feynman diagrams for the 1p1h and 2p2h processes included in the ESF model. The four-vector naming convention is as follows: the incoming neutrino, k^μ; the outgoing lepton, k'^μ; the initial state nucleon, p^μ; the final state nucleon, p'^μ; and the spectator nucleon, p_s^μ. Note that the final and spectator nucleons are on mass shell, and that the final state nuclear remnants are on mass shell, but in an excited state.

for $Q^2 \leq 0.3$ GeV^2:

$$V(Q^2) = 1 - \exp(xQ^2), \tag{6.10}$$

where x is a dimensionless variable to be tuned to data [71].

The removal energy E_R is the energy required to put the initial state nucleon on mass shell. In the Benhar SF, E_R is a continuous variable; in the ESF, E_R can only take two values for each value of $|\vec{p_i}|$, which correspond to the 1p1h and 2p2h interactions. The probability for the 1p1h (2p2h) process to occur is f_{1p1h} ($f_{2p2h} = 1 - f_{1p1h}$), which is assumed to be independent of the initial state nucleon momentum for simplicity in the ESF model. Note that for deuterium, $f_{2p2h} = 1$, as there are only two nucleons.

For both processes, the four momentum of the final state nucleon can be expressed

$$P_f^2 = (P_i + q)^2 = P_i^2 + 2P_i \cdot q - Q^2, \tag{6.11}$$

therefore

$$M_f^2 = (M_i^{\text{off}})^2 + 2E_\nu\omega - 2|\vec{q}|p_z - Q^2, \tag{6.12}$$

where p_z is the component of the initial nucleon momentum $\vec{p}_i$ which is parallel to $\vec{q}$, and the off-shell mass of the initial state nucleon is given by

$$M_i^{\text{off}} = \sqrt{(E_i^{\text{off}})^2 - V(Q^2)k^2} \tag{6.13}$$

where E_i^{off} is given by Equation 6.8 (Equation 6.9) for 1p1h (2p2h) interactions.

Finally, this leads to an expression for the energy transfer, ω, which depends on the off-shell energy of the nucleon, and which expresses energy conservation for the ESF model

$$\omega = E_\nu - E'_k = \frac{Q^2 + M_f^2 - (M_i^{\text{off}})^2 + 2|\vec{q}|p_z}{E_i^{\text{off}}}. \tag{6.14}$$

Pauli blocking is applied as for the superscaling function (Equation 6.5, using the p_{F} values from Table 6.1), and applies in the same way for neutral and charged current neutrino scattering and electron scattering for all nuclei heavier than deuterium. Deuterium is a special case: there is no Pauli blocking for electron scattering or neutral current neutrino scattering, only for charged current neutrino scattering where the final state has two of the same nucleons, and the Pauli blocking factor is expressed [71]

$$\kappa_{\text{Pauli}}^{\text{deuterium}} = 1 - \epsilon_1 \exp\left[\epsilon_2 (Q^2)^{\epsilon_3}\right], \tag{6.15}$$

where $\epsilon_1 = 0.59$, $\epsilon_2 = -17.2$ and $\epsilon_3 = 0.75$.

6.3.2 Initial state nucleon momentum distributions

The initial state nucleon momentum distribution used for the ESF is taken from the NOMAD parametrisation of the one dimensional distribution of Benhar's SF [71], and can be expressed in terms of 8 dimensionless parameters, b_s, b_p, α, β, c_0, c_1, c_2 and c_3:

$$P(|\vec{p}_i|) = \begin{cases} \dfrac{\pi}{4c_0}\dfrac{1}{N}\left(a_s + a_p + a_t\right) y^2 & \text{if } |\vec{p}_i| \leq 0.65 \text{ GeV} \\ 0 & \text{otherwise,} \end{cases} \tag{6.16}$$

where N is a normalisation factor to ensure that the integral of $0 \leq P(|\vec{p}_i|) \leq 0.65$ GeV is equal to 1, $c_0 = 0.197$ for all nuclear targets, and

$$y = \frac{|\vec{p}_i|}{c_0}, \qquad a_s = c_1 \exp\left[-(b_s y)^2\right],$$
$$a_p = c_2 (b_p y)^2 \exp\left[-(b_p y)^2\right], \qquad a_t = c_3 y^\beta \exp\left[-\alpha(y-2)\right]. \tag{6.17}$$

The ESF is tuned to the superscaling function separately for each nuclear target by floating the parameters Δ, f_{1p1h}, b_s, b_p, α, β, c_1, c_2 and c_3 [71,80], to fit the superscaling prediction in the variable

$$\Delta\omega = \omega - \frac{Q^2}{2M_f}, \tag{6.18}$$

for Q^2 values of 0.3 GeV^2, 0.5 GeV^2 and 0.7 GeV^2.

The results from the ESF fit to the superscaling function are reproduced in Table 6.2. The initial state nucleon momentum distributions obtained are plotted for a number of nuclei in Figure 6.4. As previously mentioned, the ESF prediction for deuterium is treated slightly differently, and is tuned to a theoretical prediction [288] which agrees with electron-deuterium scattering data.

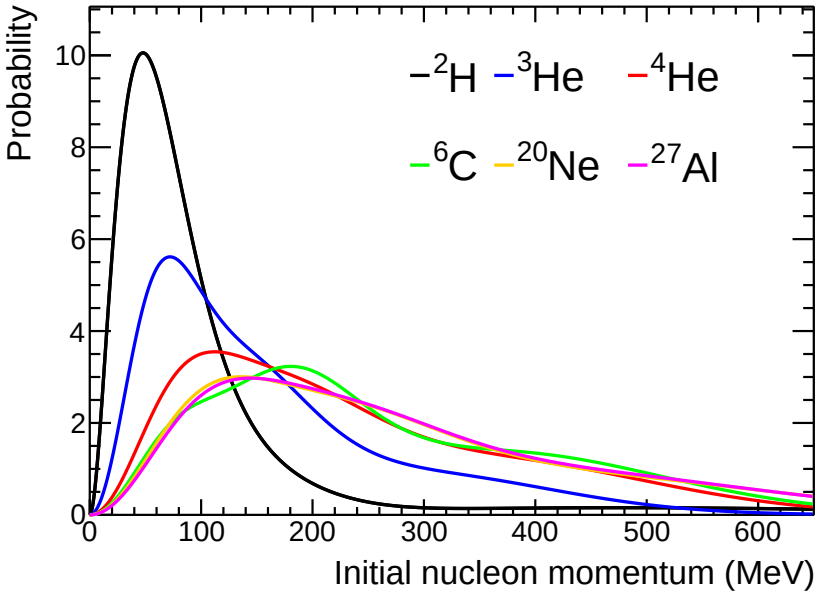

FIGURE 6.4: Initial state nucleon momentum distributions for a variety of nuclear targets. Targets heavier than ^{27}Al have very similar distributions so have not been shown on this plot.

The superscaling function depends on p_F and E_{shift}, which are given for eight A ranges as shown in Table 6.1. The ESF initial state nucleon distribution is tuned to match the superscaling function in each of these A ranges, and the results are valid for any nucleus with an atomic number in the specified A range. The deuterium theoretical prediction

is tuned to separately. The ESF can therefore be applied to any nucleus by using the appropriate input distribution from Table 6.2.

Additionally, the low Q^2 correction factor $V(Q^2)$ given in Equation 6.10 is tuned to superscaling data with $Q^2 \leq 0.3$ GeV^2 as described previously, giving a value of $x = 12.04$ [71] (applicable to all targets). This factor is worth remarking upon further because it is omitted from the NEUT implementation described in Section 6.4 ($V(Q^2) \to 1$). The low Q^2 correction was included to improve agreement between the superscaling prediction and the ESF for $Q^2 < 0.3$ GeV^2, where small discrepancies were observed. However, it should be stressed that the superscaling function is not tuned to electron scattering data below $Q^2 = 0.3$ GeV^2.

6.3.3 Including the TEM in the ESF prediction

By construction, the ESF is designed to produce good agreement with the superscaling prediction, which in turn guarantees good agreement with the longitudinal response of electron scattering data for $Q^2 \geq 0.3$ GeV^2. In order to ensure good agreement with the transverse response of electron scattering data, it is necessary to include the TEM. This is easily done by modifying the magnetic form factors as described in Section 6.2. As the transverse enhancement modelled by the TEM is caused by additional 2p2h processes, it is necessary to modify the fraction of 1p1h and 2p2h events

$$f_{1p1h}^{\mathrm{TEM}} = \frac{f_{1p1h}}{1.18}, \qquad f_{2p2h}^{\mathrm{TEM}} = \frac{f_{2p2h} + 0.18}{1.18}, \tag{6.19}$$

where the factor of 18% is the average enhancement to the total cross section due to the TEM.

Parameter	$A=2$	$A=3$	$4\leq A\leq 7$	$8\leq A\leq 16$	$17\leq A\leq 25$	$26\leq A\leq 38$	$39\leq A\leq 55$	$56\leq A\leq 60$	$A\geq 61$
Δ (MeV)	0.13	5.3	14.0	12.5	16.6	12.5	20.6	15.1	18.8
f_{1p1h}	0	0.312	0.791	0.808	0.765	0.774	0.809	0.822	0.896
b_s	0.41	3.06	2.14	2.12	1.82	1.73	1.67	1.79	1.52
b_p	1.756	0.902	0.775	0.737	0.610	0.621	0.615	0.597	0.585
α	8.29	10.93	9.73	12.94	6.81	7.20	8.54	7.10	11.24
β	3.6×10^{-3}	6.03	7.57	10.62	6.08	6.73	8.62	6.26	13.33
c_1	0.187	199.6	183.4	197.0	25.9	21.0	200.0	18.37	174.4
c_2	6.24	1.92	5.53	9.94	0.59	0.59	6.25	0.51	5.29
c_3	2.08×10^{-4}	5.26×10^{-5}	5.90×10^{-6}	4.36×10^{-5}	2.21×10^{-7}	1.22×10^{-7}	2.69×10^{-7}	1.41×10^{-7}	9.28×10^{-5}
N	10.3	6.1	18.9	29.6	4.5	4.1	40.1	3.6	38.0

TABLE 6.2: The fit parameters obtained for various nuclear targets when the parameters of the ESF were fitted to the superscaling prediction [71,80].

6.4 Details of the NEUT implementation

The NEUT implementation of the ESF closely follows the existing implementation of the Benhar SF model, which is described in Reference [274], and reuses as much of the existing code as possible within the somewhat restrictive NEUT framework. The basic event generation algorithm is as follows:

1. Select a neutrino based on precalculated $\sigma(E_\nu)$ tables.
2. Randomly select the initial state nucleon momentum from the ESF momentum distribution $P(|\vec{p}_i|)$.
3. Use a randomly generated number to determine whether to use 1p1h or 2p2h event kinematics.
4. Calculate centre-of-mass (COM) energy $E_{\mathrm{COM}} = E_i^{\mathrm{off}} + E_\nu$, using the off-shell energy of Equation 6.8 or 6.9 for 1p1h and 2p2h events respectively[4] (go to step 2 if below threshold).
5. Create outgoing lepton and nucleon in a random direction (in COM frame).
6. Boost back to lab frame.
7. Apply Pauli blocking ($\vec{q}$-dependent probability, if rejected, go to step 2).
8. Calculate the cross section for this event using Equation 6.20.
9. Draw against the maximum differential cross section at this E_ν to decide whether to accept the event (if rejected, go back to step 2).

The cross section as a function of neutrino energy is calculated using the equation

$$\frac{d\sigma}{dE_\nu} = \sum_{n=1}^{2} f_{npnh} \int d^3p \int d^3k' \delta \left(\omega - \frac{Q^2 + 2|\vec{q}|k_z + M_f^2 - (M_i^{\mathrm{off}})^2}{2E_i^{\mathrm{off}}} \right) \times L_{\mu\nu} H^{\mu\nu} \frac{G_{\mathrm{F}}^2 \cos^2 \vartheta_C}{8\pi^2 E_\nu E' E_f E_i^{\mathrm{on}}} P(|\vec{p}_i|), \tag{6.20}$$

where the delta function expresses the energy conservation given by Equation 6.14, G_{F} is the Fermi constant, ϑ_C is the Cabibbo angle, f_n denotes the f_{1p1h} or f_{2p2h} probability, $E_i^{\mathrm{on}} = \sqrt{|\vec{p}_i|^2 + M_i^2}$ is the on-shell mass of the initial state nucleon and $L_{\mu\nu}H^{\mu\nu}$ is the contraction of the leptonic and hadronic tensors, which is derived in Appendix D.

The $\sigma(E_\nu)$ tables and maximum differential cross section tables are produced using the same basic algorithm and cross section formula, except that 1 million events are

[4] Note that the factor $V(Q^2) \to 1$ for all Q^2 in this implementation.

generated for true E_ν values in 50 MeV increments, and a differential cross section is calculated based on the kinematics of the event according to Equation 6.20. The maximum differential cross section for the 1 million throws is recorded, and the total cross section is obtained by averaging the differential cross sections calculated for each of the throws (this amounts to numerical integration of the integrals in Equation 6.20). For efficiency, the events are generated in the neutrino-nucleus COM frame (energy and momentum conservation is easier), so the cross section formula used in NEUT is a slight modification to Equation 6.20, including a Jacobian to convert the integral over the outgoing lepton momentum into the COM frame. Details of the Jacobian are available in Reference [274], but this is a technical aspect of the existing SF implementation in NEUT, and does not change the physics of the ESF simulation.

The spectator nucleon in 2p2h events is treated as having three-momentum equal and opposite to the momentum of the struck nucleon, and is entered into the NEUT particle stack, so it is passed to the usual NEUT FSI routines and propagated out of the nucleus. If the TEM is also specified, the modified f_{1p1h}^{TEM} and f_{2p2h}^{TEM} probabilities are used to determine which set of event kinematics to use, and the electromagnetic form factors are modified (for details, see Appendix D).

The ESF has been implemented in NEUT for the following 12 targets: ^{2}H, ^{3}He, ^{4}He, $\mathbf{^{12}C}$, $\mathbf{^{16}O}$, ^{20}Ne, ^{27}Al, $\mathbf{^{40}Ar}$, $\mathbf{^{56}Fe}$, $\mathbf{^{63}Cu}$, $\mathbf{^{64}Zn}$ and $\mathbf{^{208}Pb}$. The isotopes in bold are present in one of the T2K detectors, and all T2K targets are available, so a consistent simulation is possible for future T2K analyses[5]. In principle the ESF should generalise readily to all nuclear targets, but unfortunately, due to fundamental design limitations in NEUT, the total cross section tables must be calculated separately for each nuclear target which makes adding new targets to any model non-trivial if the total cross section cannot be calculated analytically, as in this case[6]. Although some of the targets for which the ESF is implemented in NEUT have the same parameters in Tables 6.1 and 6.2, their different masses mean that the total cross section will be different, and separate tables had to be calculated for each.

Figures 6.5 and 6.6 show the total cross section as a function of neutrino energy calculated by NEUT. Figure 6.5 shows the ν_μ CCQE cross section on a variety of nuclear targets as predicted by the ESF model, and Figure 6.6 shows the CCQE cross section on carbon for all neutrino species.

[5]The Benhar SF is only implemented for ^{12}C, ^{16}O and ^{56}Fe, so is not available for all T2K targets.

[6]This limitation is a quirk of NEUT's long history, the ESF can be implemented for all nuclear targets in other generators fairly easily, as indeed it has been in GENIE [71].

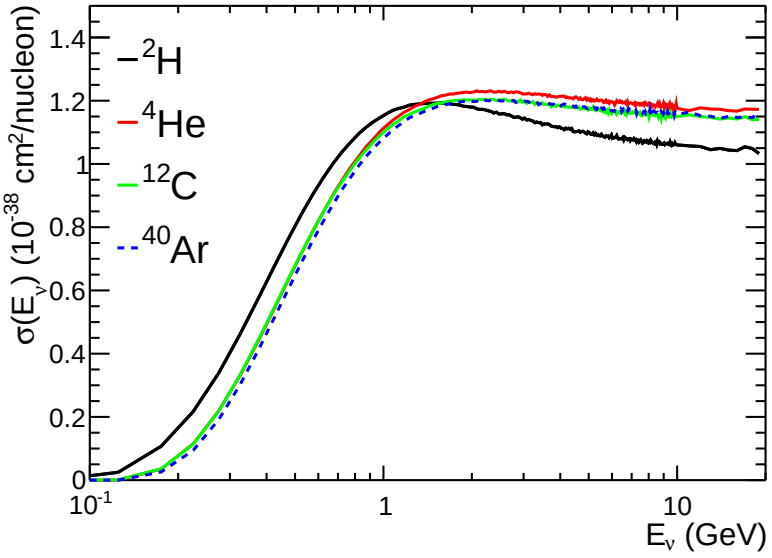

(A) ν_μ ESF

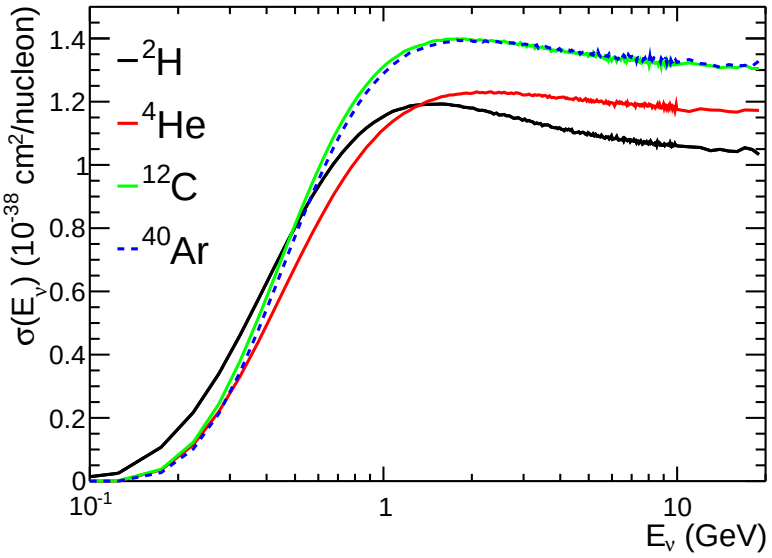

(B) ν_μ ESF + TEM

FIGURE 6.5: The total muon neutrino CCQE cross section prediction for the ESF model with and without TEM for a variety of nuclear targets as predicted by NEUT. Note that the TEM is only applied to ^{12}C and heavier elements.

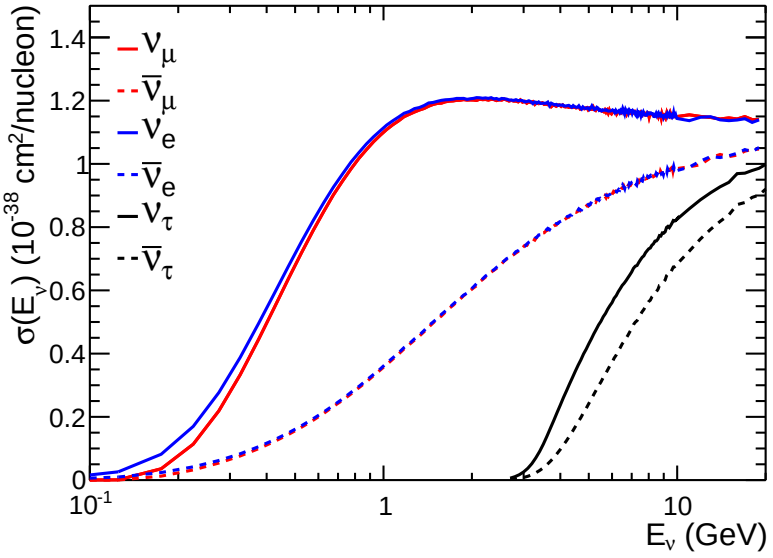

(A) ν – ^{12}C ESF

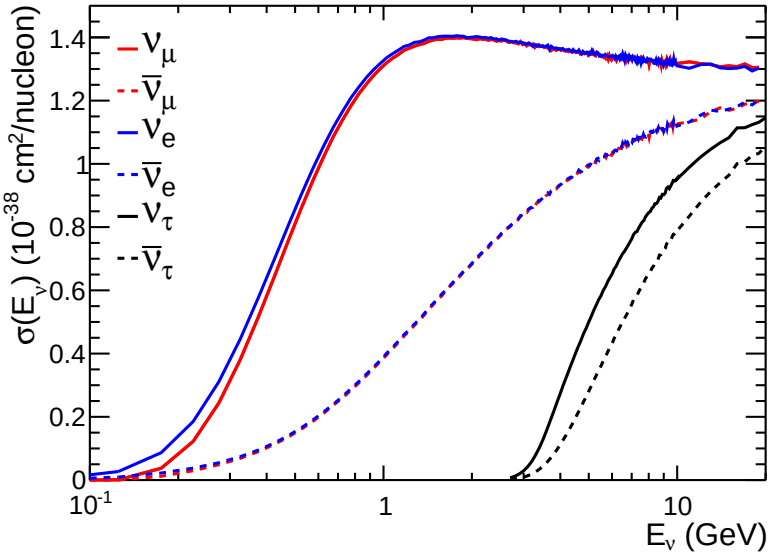

(B) ν – ^{12}C ESF + TEM

FIGURE 6.6: The total CCQE cross section predictions on ^{12}C for all neutrino flavours for the ESF model with and without the TEM, as predicted by NEUT.

6.5 Validation of the implementation

The ESF is tuned to the superscaling prediction using the variable $\Delta\omega$ (Equation 6.18), so this variable provides the most direct validation of the NEUT implementation. Figure 6.7 compares the output of NEUT, the superscaling prediction and the ESF prediction[7] as a function of $\Delta\omega$ for $E_\nu = 10$ GeV, $Q^2 = 0.5$ GeV^2, for a variety of nuclear targets. Figure 6.8 compares the output of NEUT and the superscaling prediction for carbon at various Q^2 values and fixed $E_\nu = 10$ GeV. The SF and RFG predictions from NEUT are also shown for comparison. Note that NEUT cannot generate events at fixed Q^2 values, so the NEUT plots were produced using events generated in a range of ± 0.05 GeV^2 around the target Q^2 value.

Figures 6.7 and 6.8 show that the broad features of the ESF model are consistent between the superscaling prediction and the NEUT output in terms of the variable $\Delta\omega$. It should be noted that although the ESF is only fitted to superscaling data at $Q^2 = 0.3$, 0.5 and 0.7 GeV^2, good agreement between the two, and the NEUT implementation of the ESF prediction, is found up to significantly higher Q^2 values, as shown for carbon in Figure 6.8. This agreement was also remarked upon for the ESF prediction in Reference [71]. Similar agreement was also found for all other nuclear targets, but the plots are not included here. Despite the omission of the factor $V(Q^2)$, which modifies the ESF prediction at low Q^2, agreement between the superscaling prediction and the NEUT implementation of the ESF is also reasonable for $Q^2 = 0.1$ GeV^2, as shown for carbon in Figure 6.8a. It should again be noted that the superscaling function is only tuned to data for $Q^2 \geq 0.3$ GeV^2, so agreement with the superscaling prediction at $Q^2 = 0.1$ GeV^2 does not necessarily ensure good agreement with electron scattering data at the same Q^2 value.

Figure 6.9 compares the initial state nucleon momentum distributions for various models on a variety of nuclear targets. The input momentum distributions for the ESF (as shown in Figure 6.4) are also included for comparison; the differences between the input and output distributions are expected and due to Pauli blocking. The difference between the SF and ESF distributions highlights the distortion of the SF required to model the electron-nucleus scattering data.

[7] The ESF predictions are shown in Reference [71], and were provided by the authors.

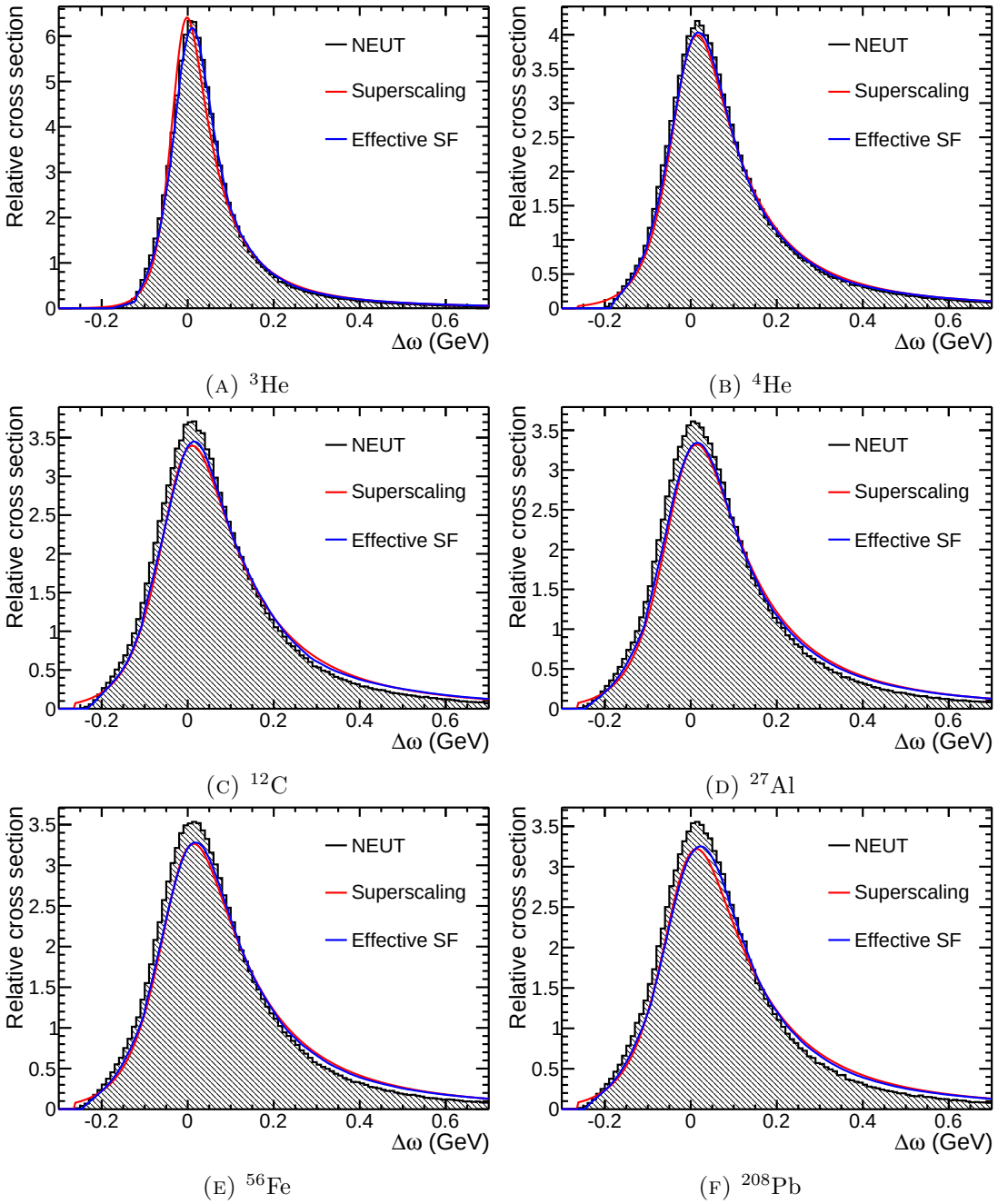

(A) ^{3}He (B) ^{4}He

(C) ^{12}C (D) ^{27}Al

(E) ^{56}Fe (F) ^{208}Pb

FIGURE 6.7: Comparisons of the $\Delta\omega$ distributions of the NEUT implementation of the ESF model with the superscaling prediction and the ESF fit function on a variety of nuclear targets at $E_\nu = 10$ GeV, $Q^2 = 0.5$ GeV^2.

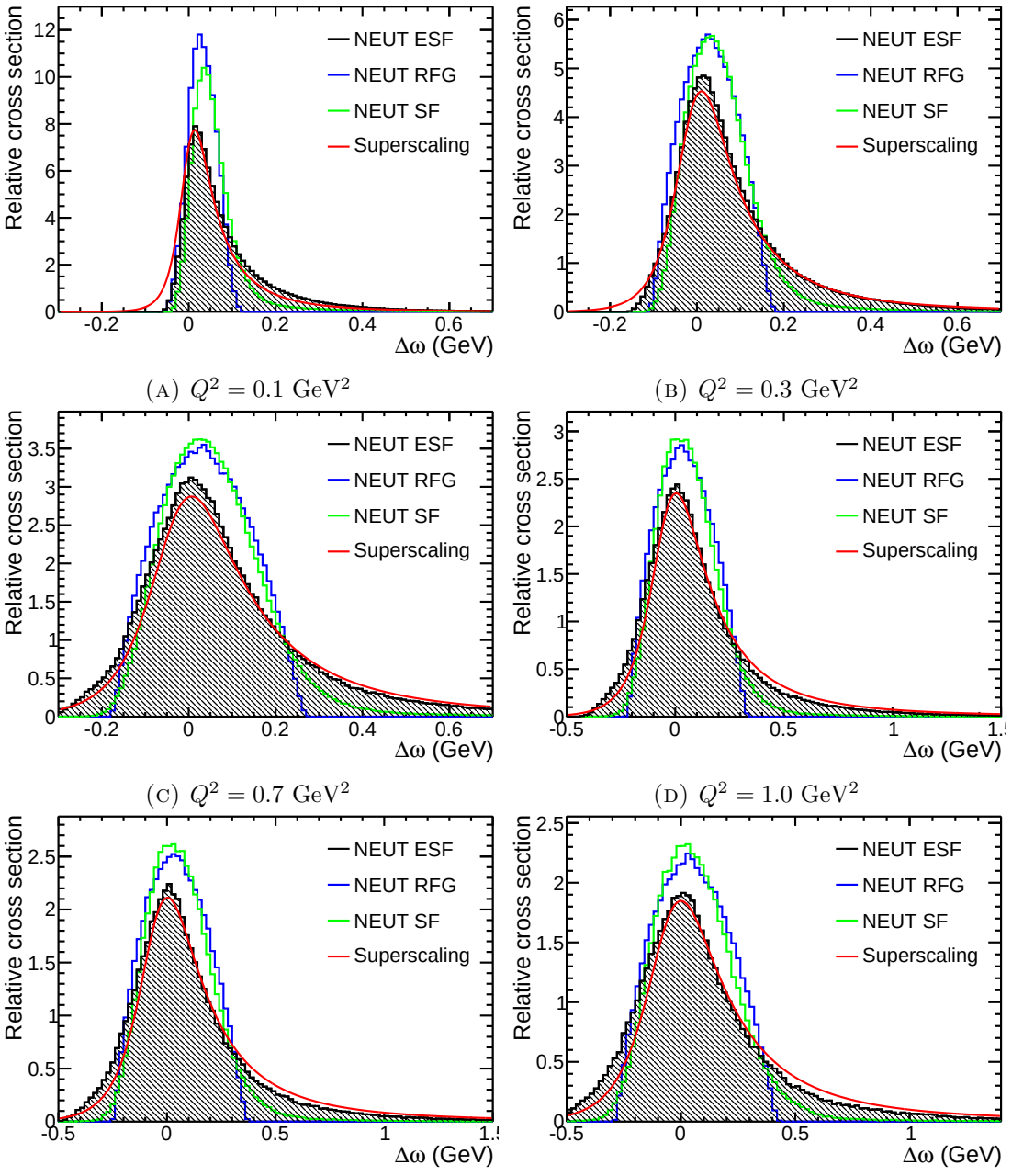

(A) $Q^2 = 0.1$ GeV^2 (B) $Q^2 = 0.3$ GeV^2

(C) $Q^2 = 0.7$ GeV^2 (D) $Q^2 = 1.0$ GeV^2

(E) $Q^2 = 1.2$ GeV^2 (F) $Q^2 = 1.5$ GeV^2

FIGURE 6.8: Comparisons of the $\Delta\omega$ distributions of the NEUT implementation of the ESF model with the superscaling prediction on carbon at $E_\nu = 10$ GeV and a variety of Q^2 values. The SF and RFG model predictions from NEUT are also shown for comparison.

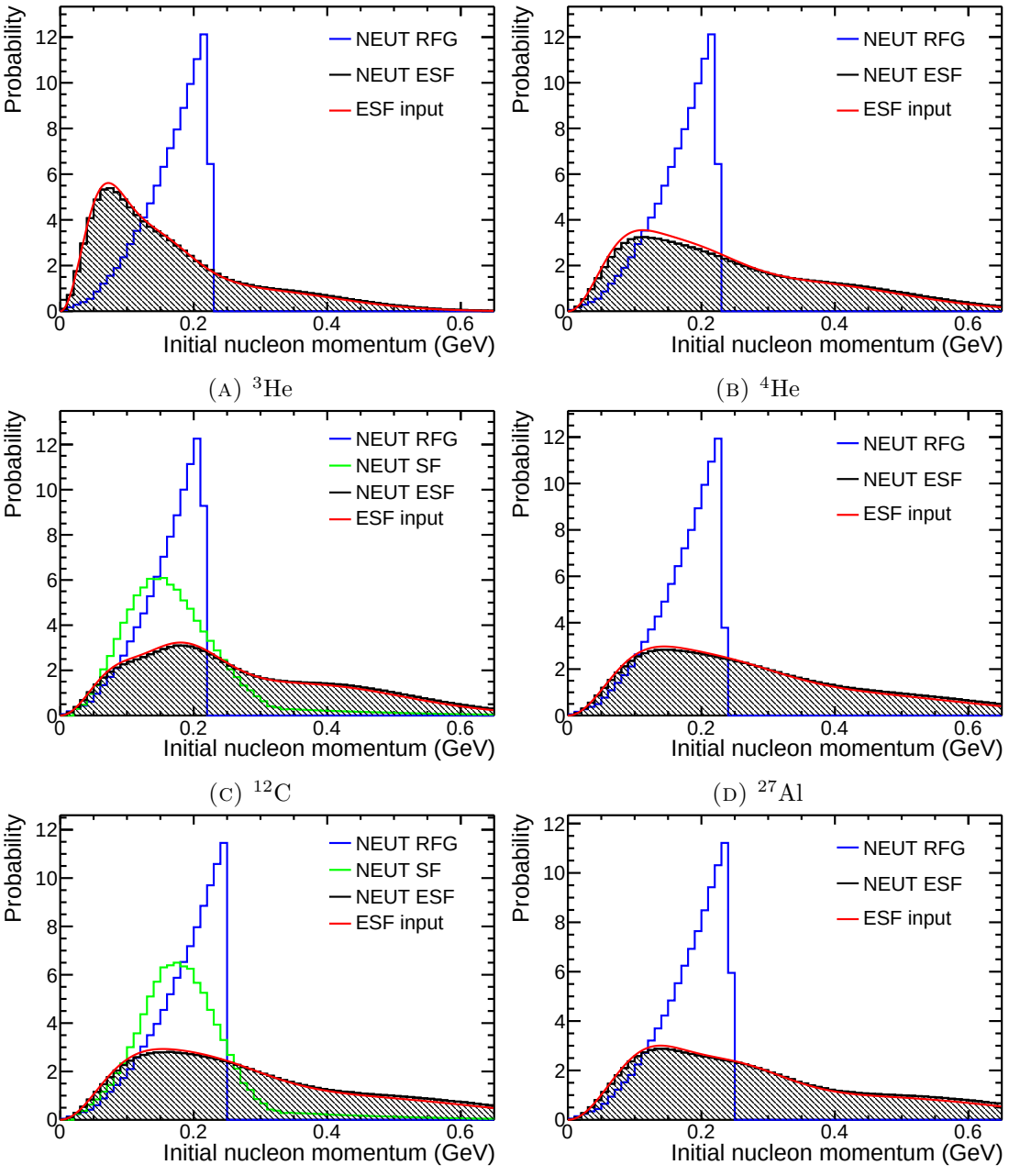

(A) ^{3}He (B) ^{4}He

(C) ^{12}C (D) ^{27}Al

(E) ^{56}Fe (F) ^{208}Pb

FIGURE 6.9: The initial state nucleon momentum distribution from NEUT is compared for the RFG, SF and ESF models for a variety of nuclear targets. The input ESF distribution is also shown for comparison with the NEUT output (the difference is expected and due to Pauli blocking).

6.6 Comparison with neutrino-nucleus data

A framework for fitting published datasets to cross section models was introduced in Chapter 5, and the same framework is used here to compare the ESF model with the MiniBooNE and MINERνA CCQE datasets (which were described in Section 5.2.1). The method for producing a NEUT prediction for each dataset is described in Section 5.2.2, and as in Chapter 5, MINUIT was used to minimise the χ^2 statistic given by Equation 5.3. Comparisons of the nominal model predictions for these datasets are shown in Section 6.6.1, fit results to each dataset individually are given in Section 6.6.2.

6.6.1 Nominal ESF model comparisons with neutrino-nucleus CCQE data

In Figure 6.10, the nominal ESF+TEM prediction from NEUT and MiniBooNE double-differential data are plotted on top of each other to highlight the fact that the NEUT prediction occupies more phase space than the data for both the neutrino and antineutrino samples. This is a commonly observed feature of fits to MiniBooNE double-differential data, and may simply be because the cross section is very low in these regions. In some fits to MiniBooNE double-differential data [195], *ad hoc* attempts are made to assign errors to the region of phase space outside the MiniBooNE datasets to constrain the model comparisons with the lack of a MiniBooNE measurement. In the fits described in Chapter 5, and in this chapter, this issue is largely neglected because there are no reliable methods for estimating the uncertainties in this region, although they are likely to be large and not a significant constraint in most fits. This neglect can be justified because the good agreement at the fringes of phase space occupied by the MiniBooNE data suggests that there are no serious issues with the model predictions in this region.

Comparing the ESF model to MiniBooNE double-differential neutrino mode data initially proved problematic. The agreement between the data and the ESF prediction looked reasonable by eye, but the χ^2 values obtained were surprisingly poor. By plotting the χ^2 contribution from each bin of the MiniBooNE datasets as shown in Figure 6.11, regions of disagreement are highlighted in a way that may not be obvious when comparing distributions by eye. The z-axis is capped at 15 units of χ^2, but the single bin of Figure 6.11a which is at this limit actually contributes $\sim$90 units of χ^2: the ESF+TEM prediction from NEUT considerably exceeds the MiniBooNE data in this bin. This is obviously a concern because it may indicate that the additional phase space occupied in the MC prediction is significant. However, because only one bin was badly affected, and it was found to exert undue influence over the fits performed in Section 6.6.2, this

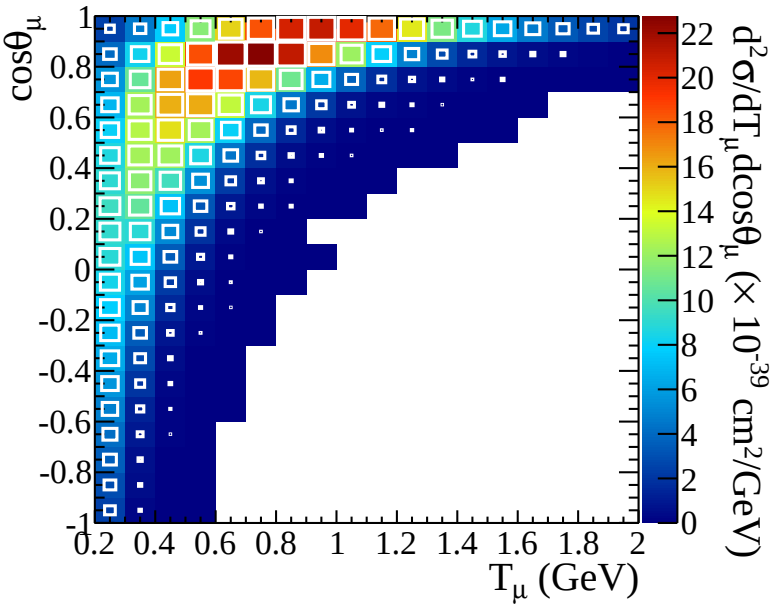

(A) Neutrino

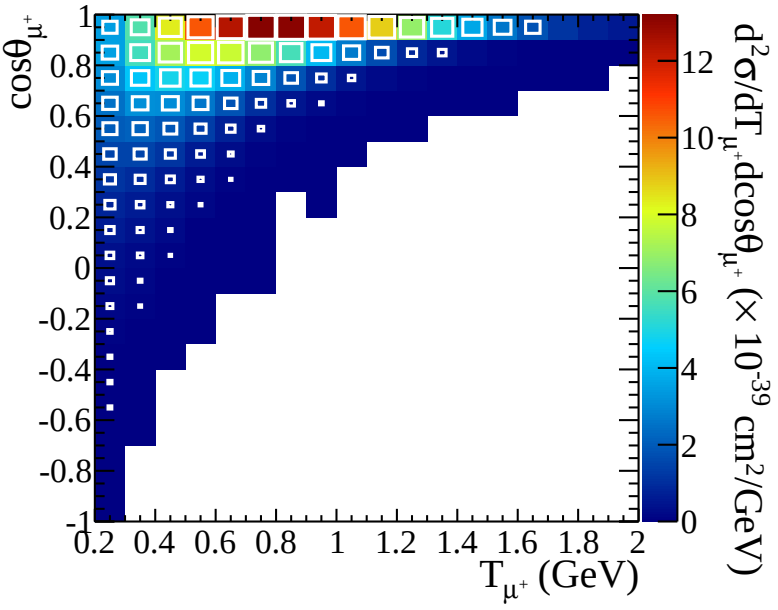

(B) Antineutrino

FIGURE 6.10: Comparisons of the nominal ESF+TEM model predictions from NEUT, and the MiniBooNE neutrino and antineutrino double-differential datasets. The MC prediction is shown in colour, and the MiniBooNE data is overlaid as white boxes, where the size of the box denotes the cross section in each bin. There are no bins with data but no NEUT prediction.

bin has been excluded from all χ^2 values calculated for the MiniBooNE neutrino double-differential dataset. Note that other bins in a similar region of phase space contribute significant χ^2 values, but these bins were included in the χ^2 calculation because they did not seem to exert such a strong pull on the normalisation.

The region with significant χ^2 contributions is also the region where the cross section is

lowest, and where MiniBooNE will have recorded the fewest events. In this region the statistical error is large, which could push the unfolded distributions downwards and add to the χ^2 contribution. However, it seems likely that these large χ^2 contibutions are due to the model, not the data. The same large χ^2 contributions were not observed for the RFG and SF nuclear models used in Chapter 5, and taking a ratio of the predicted ESF cross section over either of these models shows that the ESF prediction is much larger in this fringe of phase space (and the trend continues for the region of phase space where the MC makes a prediction but there is no data).

The nominal ESF and ESF+TEM model predictions are compared with MINERνA, MiniBooNE single-differential and MiniBooNE double-differential data in Figures 6.12, 6.13 and 6.14 respectively. As was remarked in Chapter 5, it is necessary to fit the MiniBooNE normalisation parameters $\lambda_{\nu}^{\mathrm{MB}}$ and $\lambda_{\bar{\nu}}^{\mathrm{MB}}$ to produce a meaningful χ^2 value for the MiniBooNE datasets. The best fit values for the normalisation parameters are given in Table 6.3. The MiniBooNE double-differential comparisons are also shown without the MiniBooNE scaling factors applied in Figure 6.15, which are easier to interpret by eye. As in Chapter 5, for ease of presentation, the double-differential distributions in this chapter have all been rebinned into 8 $\cos\theta_{\mu}$ slices of varying size, where merged bins have been averaged, and their errors combined in quadrature. All fits used the original 20 $\cos\theta_{\mu}$ bins from the MiniBooNE data releases.

Fit type		$\lambda_{\nu}^{\mathrm{MB}}$	$\lambda_{\bar{\nu}}^{\mathrm{MB}}$
MB ν 1D	ESF	0.656±0.006	–
	ESF+TEM	0.804±0.008	–
MB $\bar{\nu}$ 1D	ESF	–	0.780±0.011
	ESF+TEM	–	0.803±0.011
MB ν 2D	ESF	0.713±0.011	–
	ESF+TEM	0.827±0.012	–
MB $\bar{\nu}$ 2D	ESF	–	0.797±0.015
	ESF+TEM	–	0.833±0.015

TABLE 6.3: Table of best fit MiniBooNE normalisation parameter values for the nominal ESF and ESF+TEM model comparisons shown in Figures 6.13 and 6.14.

As is expected, the TEM is required to obtain reasonable agreement with data: considerably more tension is seen for all datasets when only the ESF is used. The ESF+TEM model appears to agree well with MINERνA data, as can be seen in Figure 6.12, though it should be noted that MINERνA also reported good (and indeed, slightly better) agreement with the RFG+TEM model in References [278, 279]. The disagreement seen for both MiniBooNE single-differential datasets in Figure 6.13 is consistent with that seen for other models (see Section 5.2.4); the deficit at high Q^2 suggests that a higher axial

mass value is required to fit these datasets. It is also clear from both the MiniBooNE single and double-differential data that the nominal ESF and ESF+TEM models significantly overestimate the MiniBooNE data at low Q^2. The same disagreement is not seen for the MINERνA data.

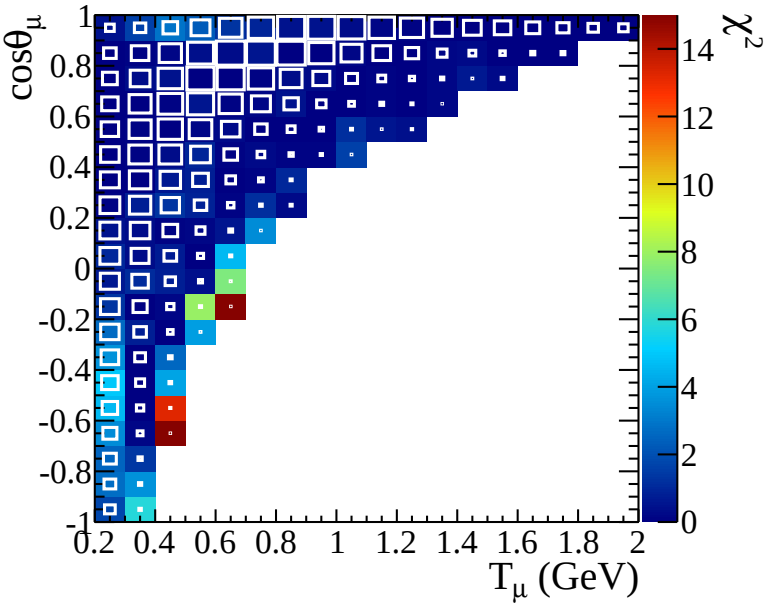

(A) Neutrino

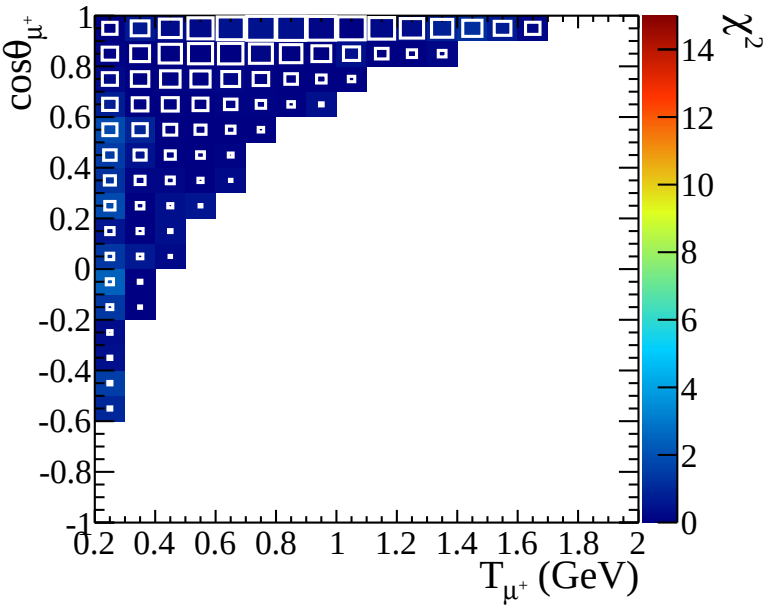

(B) Antineutrino

FIGURE 6.11: The χ^2 contributions from each bin in the MiniBooNE neutrino and antineutrino double-differential datasets for the nominal ESF+TEM model. The MiniBooNE normalisation parameters were allowed to vary to obtain a meaningful nominal χ^2 value. Note that the z-axis is capped at 15 units of χ^2, and the single bin at the limit contributes 90 units of χ^2, and is omitted from the fits. The published MiniBooNE data is overlaid as white boxes, where the size of the box denotes the cross section in each bin.

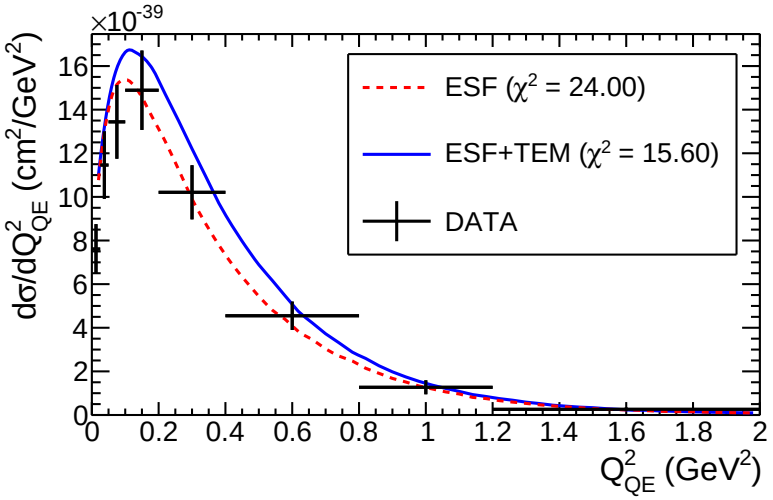

(A) Neutrino

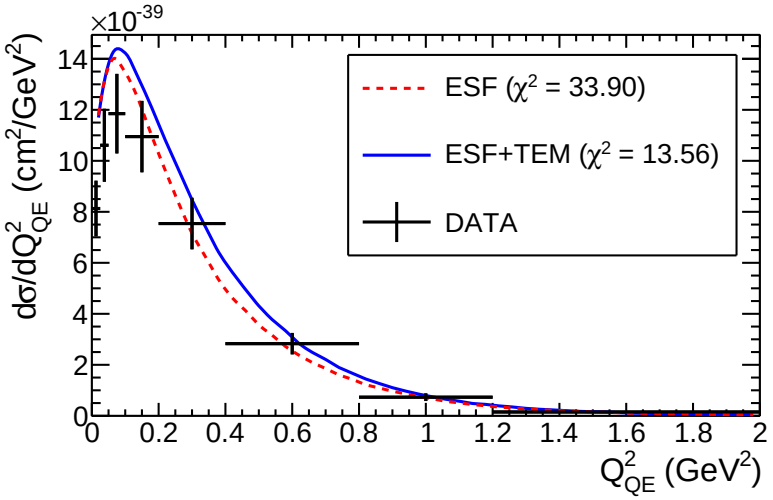

(B) Antineutrino

FIGURE 6.12: Nominal ESF and ESF+TEM predictions for the MINERνA $\theta_\mu \leq 20°$ datasets with $M_A = 1.01\,\text{GeV}$.

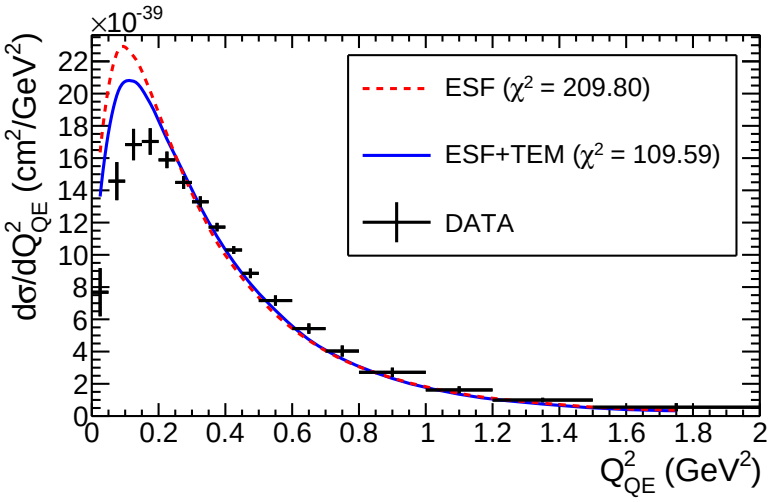

(A) Neutrino

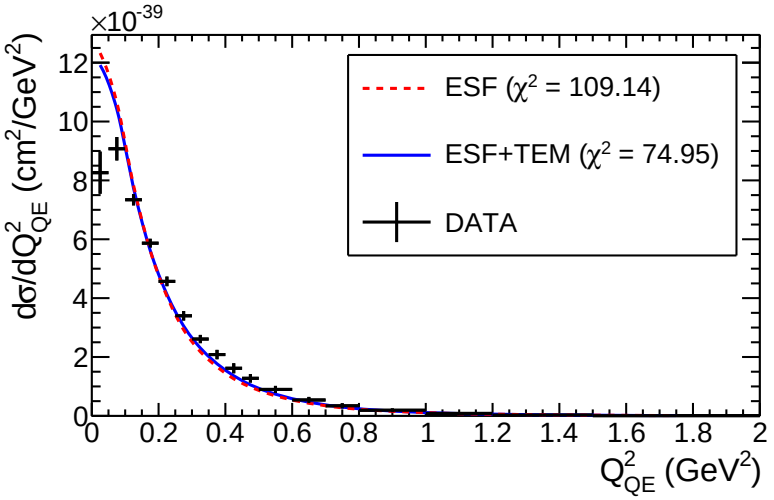

(B) Antineutrino

FIGURE 6.13: Nominal ESF and ESF+TEM predictions for the MiniBooNE single-differential datasets with $M_A = 1.01\,\text{GeV}$. The relevant MiniBooNE normalisation parameter has been allowed to vary to minimise the χ^2 value.

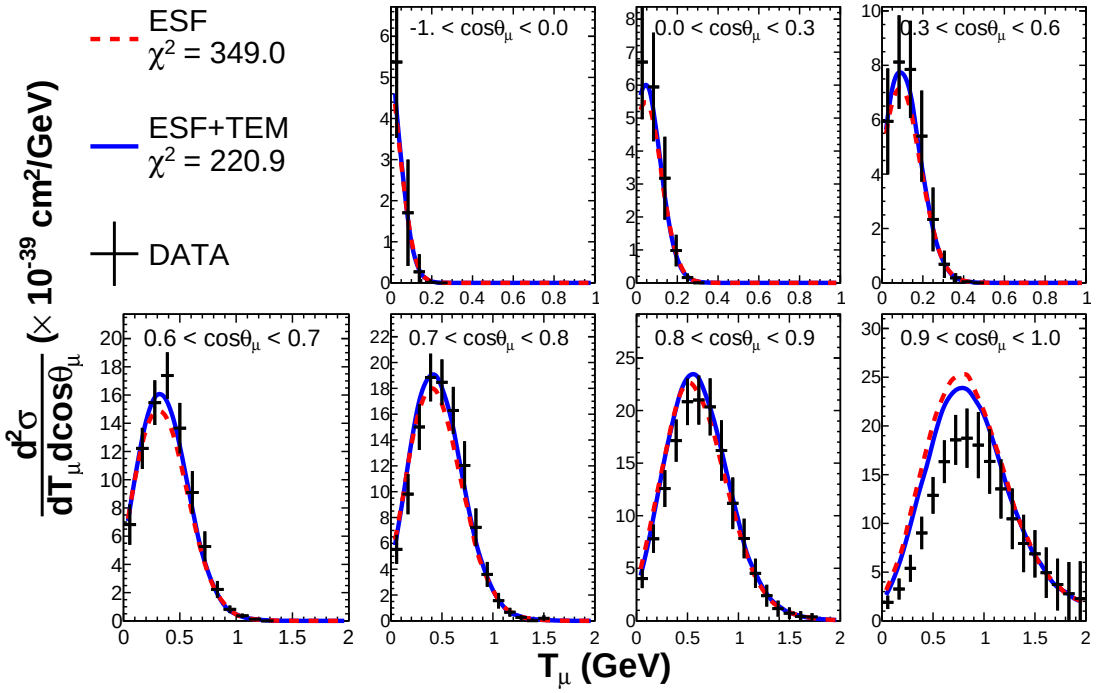

(A) Neutrino

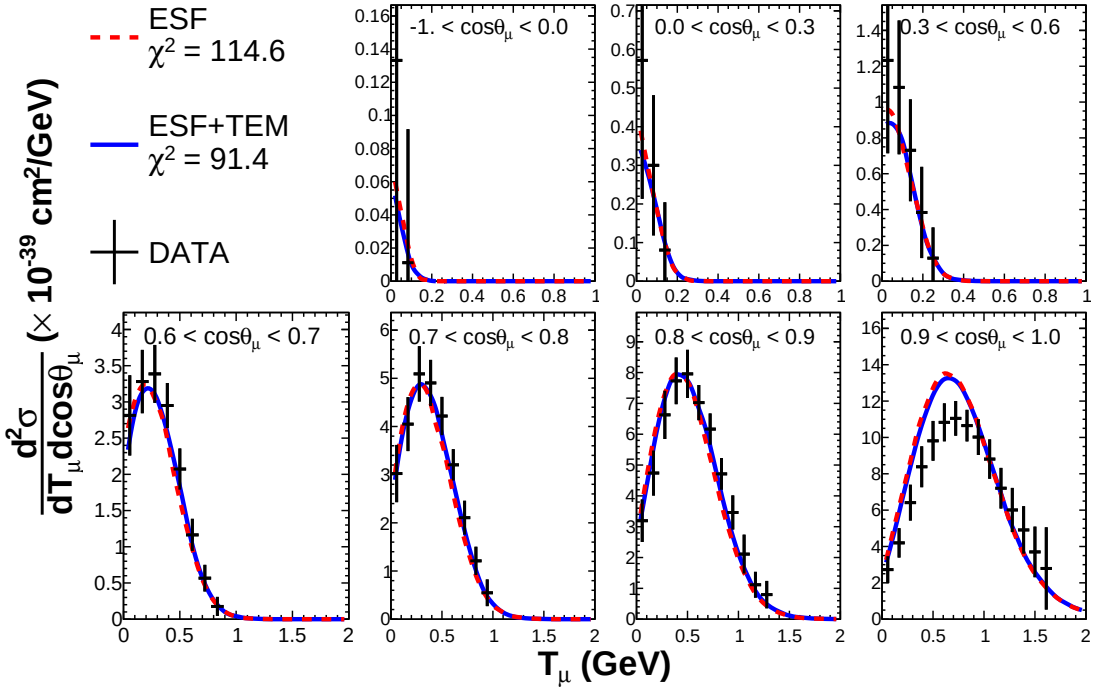

(B) Antineutrino

FIGURE 6.14: Nominal ESF and ESF+TEM model predictions for the MiniBooNE double-differential datasets with $M_A = 1.01$ GeV. The relevant MiniBooNE normalisation parameter has been allowed to vary to minimise the χ^2 value.

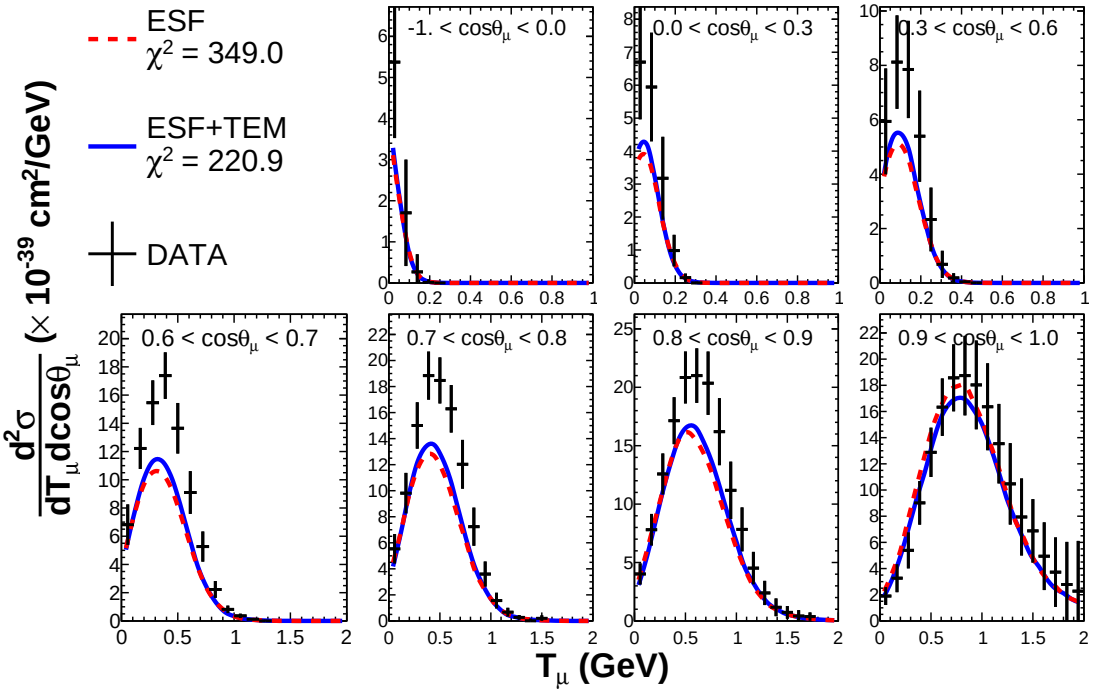

(A) Neutrino

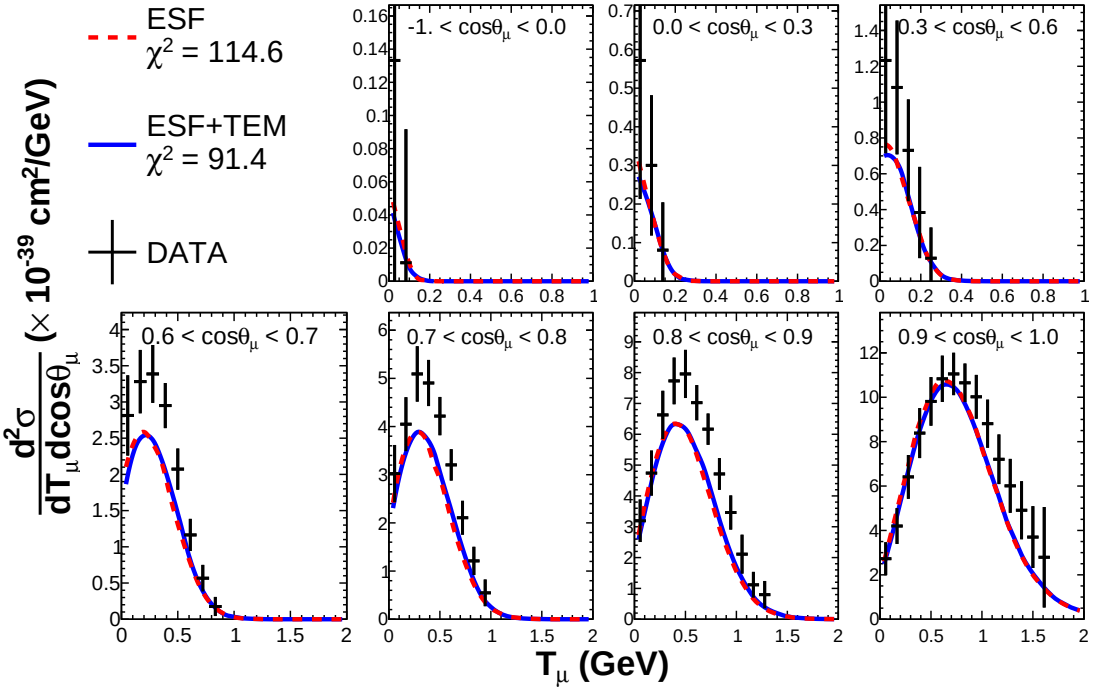

(B) Antineutrino

FIGURE 6.15: Nominal ESF and ESF+TEM model predictions for the MiniBooNE double-differential datasets with $M_A = 1.01\,\text{GeV}$. The relevant MiniBooNE normalisation parameter has been allowed to vary to minimise the χ^2 value, but the scaling factor has not been applied in this figure.

6.6.2 ESF fits to neutrino-nucleus CCQE data

There are two parameters in the ESF+TEM model which can easily be adjusted: the axial mass, M_{A}, and the Fermi momentum, p_{F}. The effect of changing these two parameters is shown for the MINERνA neutrino dataset in Figure 6.16. The axial mass enters into the hadronic tensor, so can be reweighted using existing NEUT reweighting code by recalculating the $L_{\mu\nu}H^{\mu\nu}$ term of Equation 6.20 with a modified M_{A} value (see Appendix D for details on the calculation of the $L_{\mu\nu}H^{\mu\nu}$ term). The Fermi momentum is a convenient parameter to modify the Pauli blocking function Equation 6.5 and therefore gives some flexibility at low Q^2. The motivation for this is mostly pragmatic: the superscaling function is not tuned to electron scattering data for $Q^2 \leq 0.3$ GeV^2, so some additional flexibility is desirable[8]. However, this treatment of the Fermi momentum is not consistent with the ESF model: p_{F} also features in the ψ' superscaling function (see Equation 6.3), and thus an increase in p_{F} would further smear the $\Delta\omega$ peak for all Q^2 values (and affect a broad range of Q^2 values). The p_{F} parameter used in the reweighting is simply a convenient way to parametrise changes to the Pauli blocking, and is not an easy to interpret physical parameter.

The best fit χ^2 and parameter values for fits of the ESF+TEM model to each of the six datasets individually are collected in Table 6.4. In each fit, the parameters M_{A} and p_{F} are allowed to vary, as well as any relevant MiniBooNE normalisation parameter. The best fit distributions are shown, and compared with the nominal ESF+TEM model predictions, for the MINERνA $\theta_\mu \leq 20^\circ$ neutrino and antineutrino datasets in Figure 6.17, the MiniBooNE single-differential neutrino and antineutrino datasets in Figure 6.18 and the MiniBooNE double-differential neutrino and antineutrino datasets in Figure 6.19. Additionally, the MiniBooNE double-differential datasets are shown without the MiniBooNE normalisation factors applied in Figure 6.20, which is easier to interpret by eye. The nominal distributions shown in Section 6.6.1 are reproduced in Figured 6.17, 6.18, 6.19 and 6.20 for comparison with the best fit distributions.

It is clear from Table 6.4 that all of the datasets required substantially enhanced Pauli blocking to obtain a good fit, although the effect is more pronounced for MiniBooNE than MINERνA. It is not clear how significant an enhancement is reasonable because the parameter p_{F} used in the fits is an effective parameter. However, as the low Q^2 region is not tuned to electron scattering data, the strong enhancement may indicate a deficiency with the model. It is particularly clear from Figure 6.20 that the nominal

[8] It should also be noted that the ESF implementation does not agree with the superscaling prediction for $Q^2 \leq 0.3$ GeV^2 as the factor $V(Q^2)$ has been omitted from Equations 6.8, 6.9 and 6.13 in the NEUT implementation of the model, so some disagreement at low Q^2 may be expected.

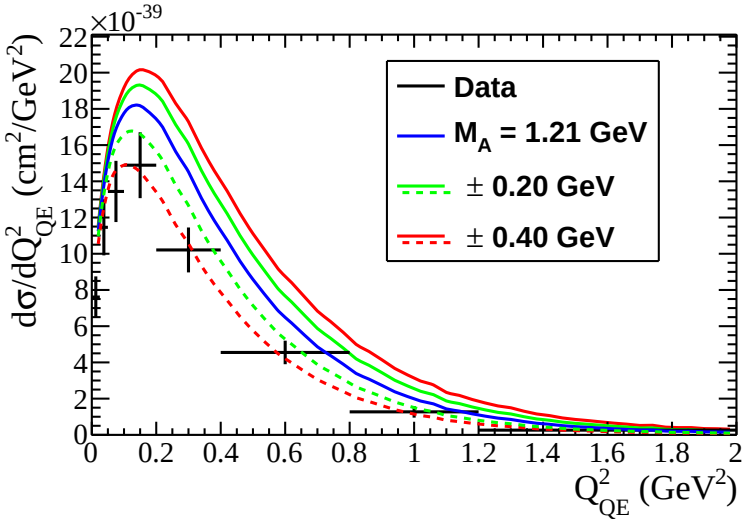

(A) M_A variations

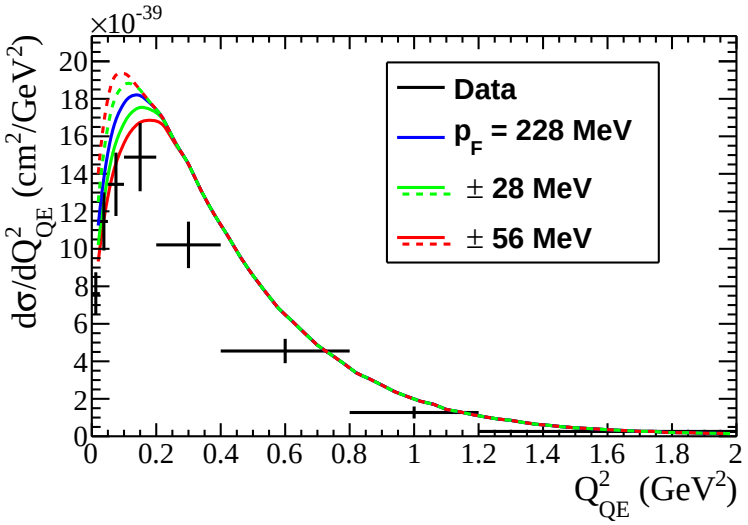

(B) p_F variations

FIGURE 6.16: Variations in the two variable parameters in the ESF+TEM fits, M_A and p_F for the MINERνA neutrino dataset. The nominal values for M_A and p_F are the NEUT default and the value obtained in fits to electron-nucleus scattering data on carbon respectively.

ESF+TEM prediction for MiniBooNE at low Q^2 (the most forward bins) is significantly above the data, so a substantial modification to the Pauli blocking is understandable.

It is also clear from Table 6.4 that the ESF+TEM model cannot reconcile the values of M_A preferred by MINERνA and MiniBooNE. Although the fits to MINERνA data are consistent with the value obtained by global fits to bubble chamber and pion electroproduction data (M_A ~1 GeV), the same is true for the RFG+TEM model [278, 279]. MiniBooNE favours an inflated, effective, axial mass M_A^{eff}, as was seen in Chapter 5 for fits using very different models, and discussed more generally in Section 2.3. Unfortunately, the ESF+TEM model does not seem to be an easy solution to the large axial

Fit type	χ^2/DOF	M_A (GeV)	p_F (MeV)	λ^{MB}
MiniBooNE ν 1D	2.9/15	1.29±0.09	315±26	0.973±0.064
MiniBooNE $\bar{\nu}$ 1D	9.4/15	1.34±0.13	281±21	0.903±0.058
MiniBooNE ν 2D	122.6/135	0.99±0.03	365 (at limit)	0.753±0.027
MiniBooNE $\bar{\nu}$ 2D	30.6/76	1.23±0.16	306±42	0.893±0.090
MINERνA ν	14.6/6	0.85±0.08	251±16	—
MINERνA $\bar{\nu}$	7.9/6	0.97±0.09	270±24	—

TABLE 6.4: χ^2_{min} and parameter values obtained at the best fit point for individual fits to each of six CCQE datasets. The errors shown come from MINUIT.

mass problem, despite the enforced agreement with electron scattering data.

The reasonable agreement obtained in the fit to the MiniBooNE single-differential neutrino sample, and the poor agreement obtained by the fit to the MiniBooNE double-differential neutrino sample, suggests that the ESF+TEM model has a problem modelling high angle events. Note that the single high angle bin which was found to dominate the χ^2 for the nominal model comparisons is not included in these results. However, it is clear from Table 6.4 that the high angle bins are dominating the fit, dragging down M_A, and increasing p_F dramatically to compensate. The regions at the fringes of the occupied phase space for the MiniBooNE double-differential distributions are at the highest values of Q^2 measured by the MiniBooNE single-differential distributions or higher (as can be seen in Section 5.2.5). It is clear from Figure 6.18 that there is no significant disagreement with the MiniBooNE Q^2 distribution, but at the best fit point, the χ^2 for the MiniBooNE double-differential neutrino mode sample is still dominated by the backwards going, high Q^2 bins as shown in Figure 6.21 (despite the extreme parameter variations required). Indeed, the situation has worsened relative to the sample plot for the nominal prediction (which is shown again in Figure 6.21 for comparison) because the increase in the axial mass has increased the cross section at high Q^2. Although good agreement was found between the ESF prediction from NEUT and the superscaling prediction up to $Q^2 = 1.5$ GeV^2 as shown in Figure 6.8, the ESF was only fit to a limited range of Q^2 values ($Q^2 = 0.3$, 0.5 and 0.7 GeV^2), so the disagreement at high angle may indicate a breakdown in the ESF at high Q^2. That said, the ESF model introduces a large high momentum tail to the initial nucleon momentum distribution, so a significant enhancement in the high Q^2, high ω region is a feature of the model, and may simply not fit the data well.

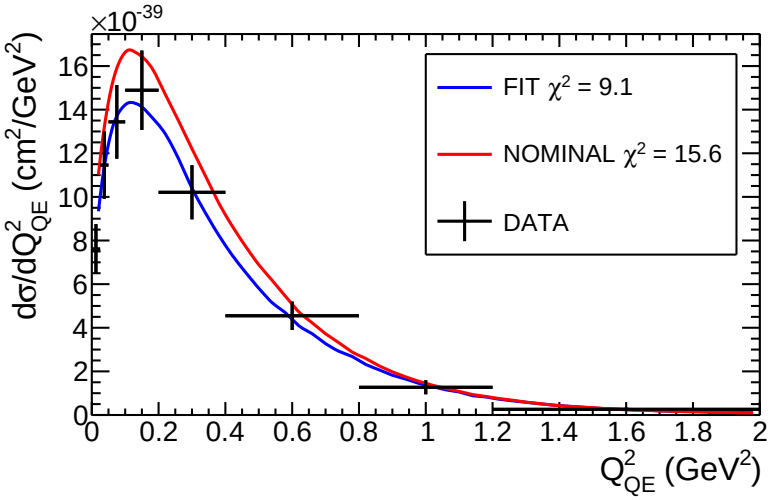

(A) Neutrino

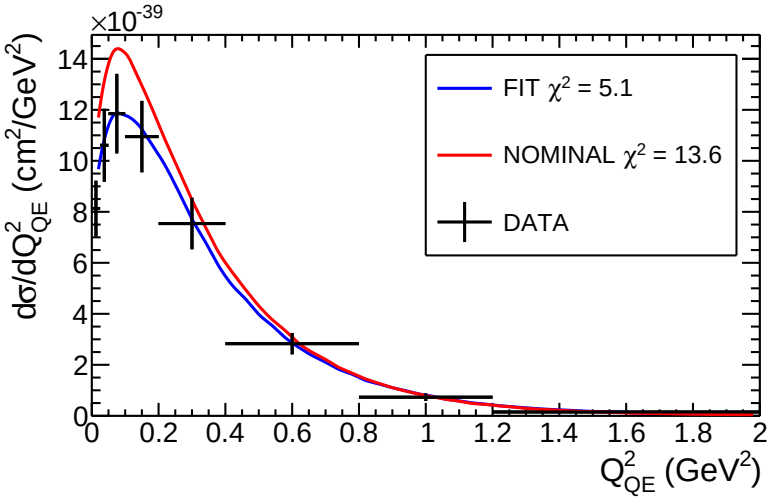

(B) Antineutrino

FIGURE 6.17: Nominal and best fit distributions for the MINERνA $\theta_\mu \leq 20°$ datasets. The best fit parameter values are given in Table 6.4.

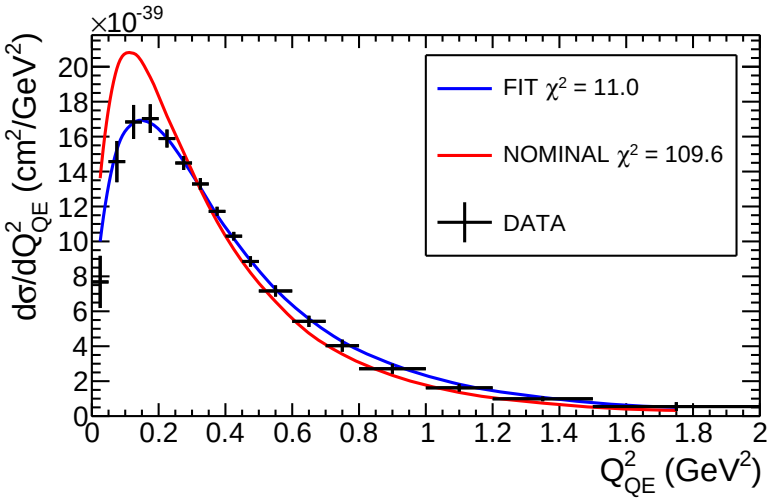

(A) Neutrino

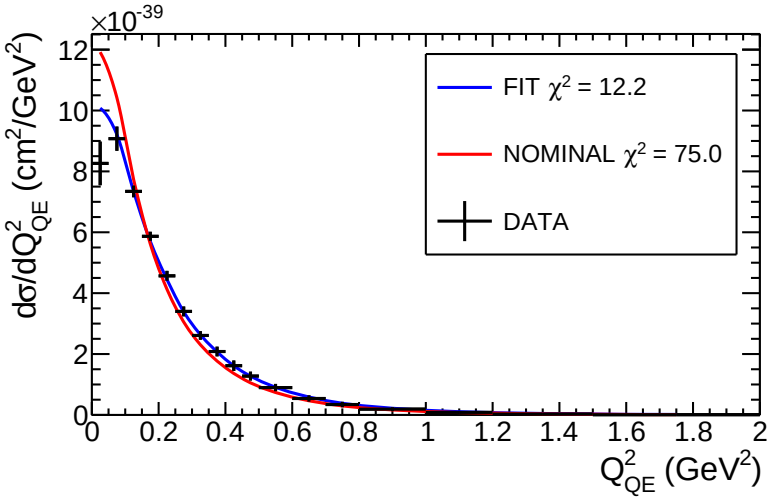

(B) Antineutrino

FIGURE 6.18: Nominal and best fit distributions for the MiniBooNE single-differential datasets. The best fit parameter values are given in Table 6.4. Note that the relevant MiniBooNE normalisation parameter is allowed to vary for the nominal prediction, the best fit value for which is given in Table 6.3.

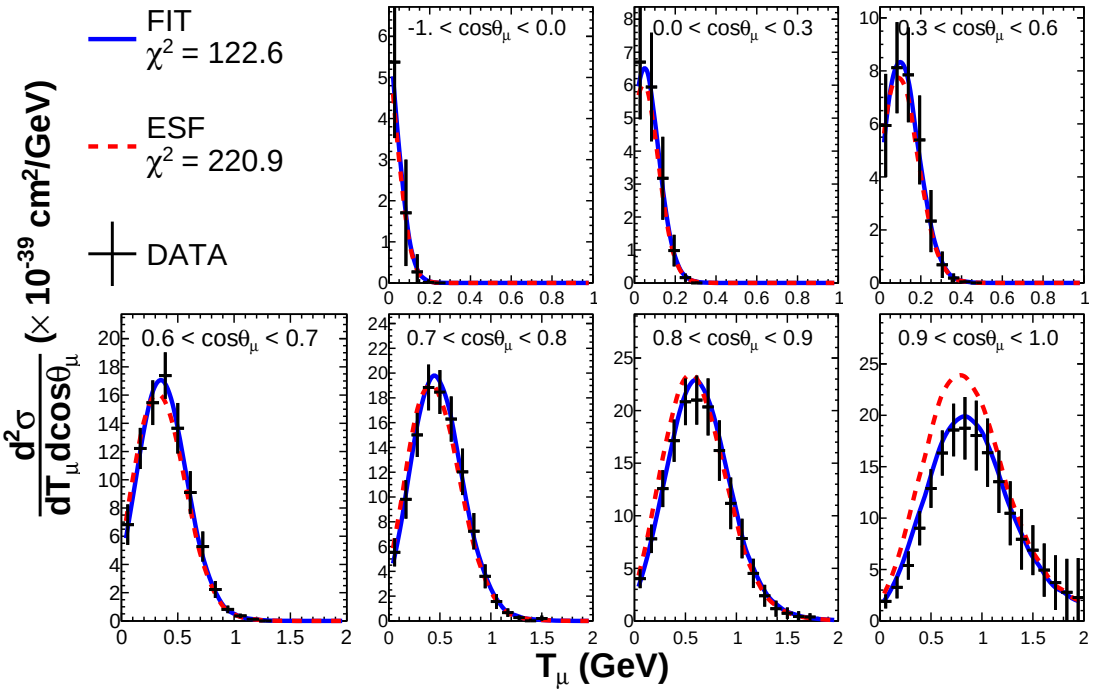

(A) Neutrino

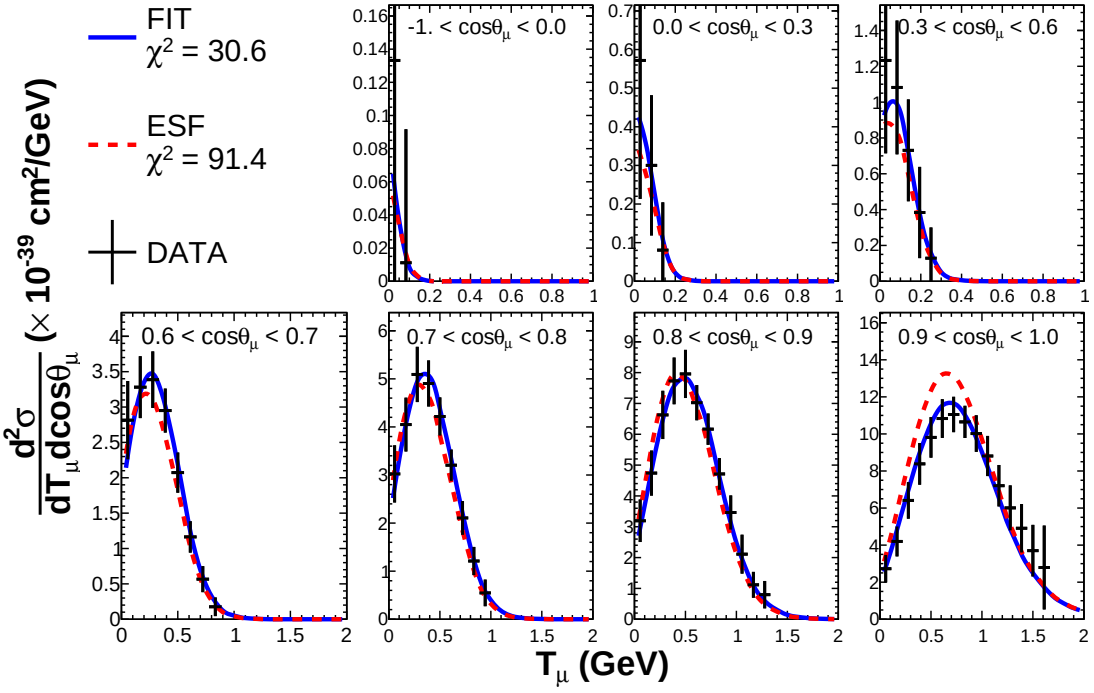

(B) Antineutrino

FIGURE 6.19: Nominal and best fit distributions for the MiniBooNE double-differential datasets. The best fit parameter values are given in Table 6.4. Note that the relevant MiniBooNE normalisation parameter is allowed to vary for the nominal prediction, the best fit value for which is given in Table 6.3.

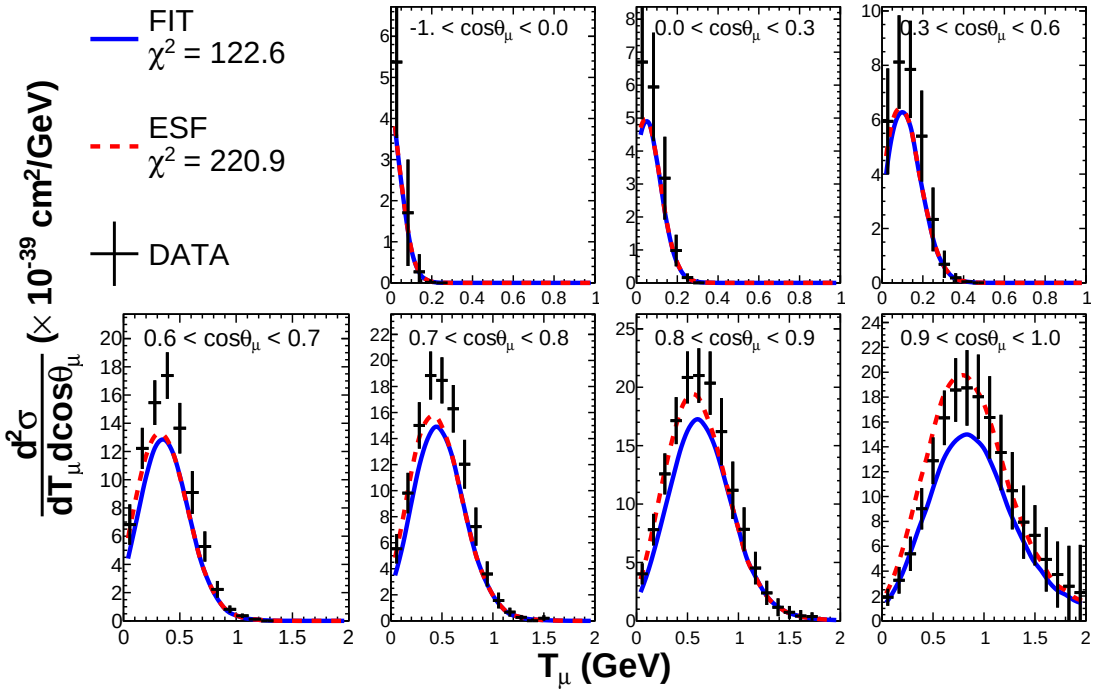

(A) Neutrino

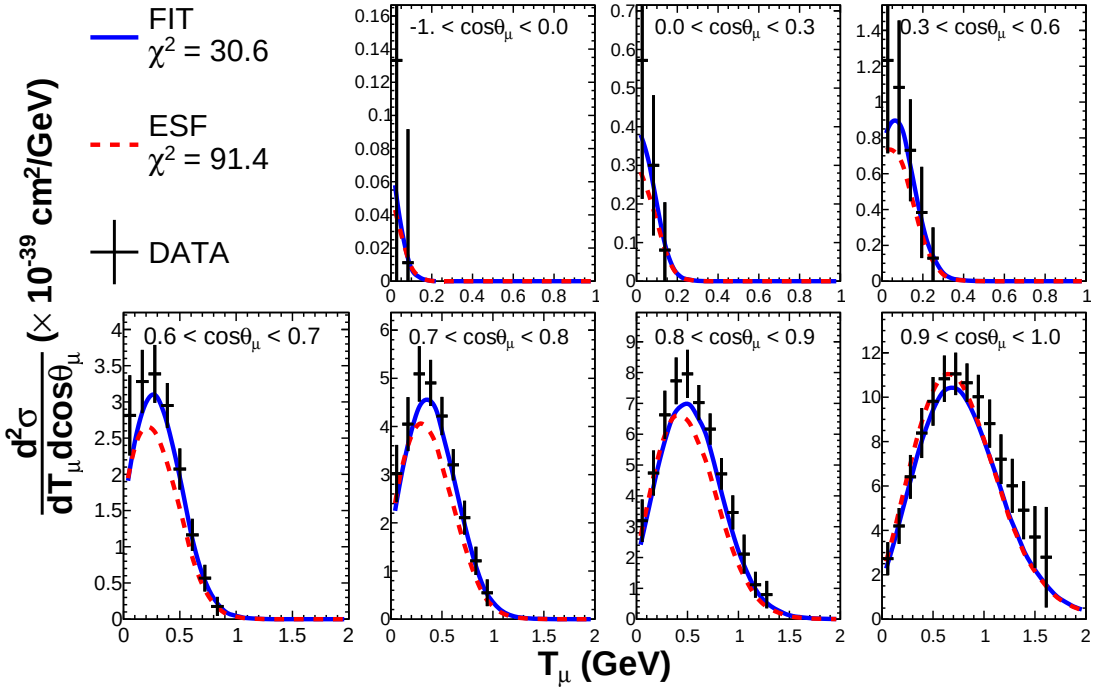

(B) Antineutrino

FIGURE 6.20: Nominal and best fit distributions for the MiniBooNE double-differential datasets shown without the MiniBooNE normalisation factors applied. The best fit parameter values are given in Table 6.4.

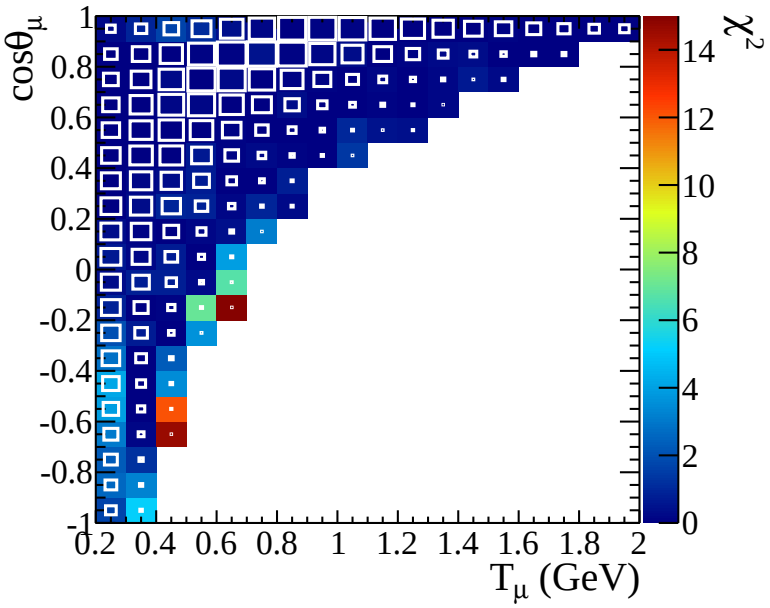

(A) Fitted

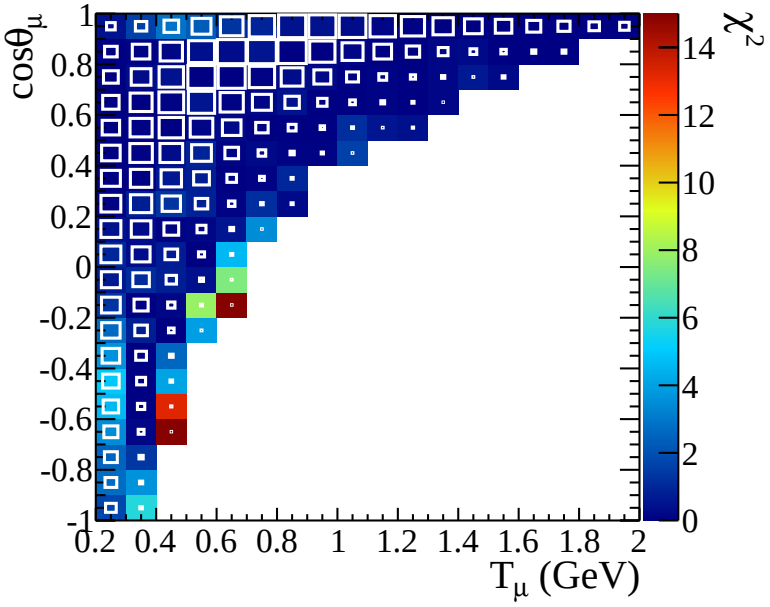

(B) Nominal

FIGURE 6.21: The χ^2 contributions from each bin in the MiniBooNE neutrino distribution with the best fit parameter values given in Table 6.4, and for the nominal prediction (reproduced from Figure 6.11). The z-axis is capped at 15 units of χ^2. Note that the bin $0.6 \leq T_\mu \leq 07$ GeV, $-0.2 \leq \cos\theta_\mu \leq -0.1$ is not included in the fits because the contribution is $\sim$90 units of χ^2. The published MiniBooNE data is overlaid as white boxes, where the size of the box denotes the cross section in each bin.

6.7 Summary

The Effective Spectral Function has been implemented in NEUT for a variety of targets and is ready to be used in T2K analyses. Crucially, and unlike many new theoretical models, it is consistently available for, and has been implemented for, all T2K target materials (^{12}C, ^{16}O, ^{56}Fe, ^{63}Cu, ^{64}Zn and ^{208}Pb). The Transverse Enhancement Model has also been implemented as an option for targets heavier than carbon (for which the TEM is valid). The NEUT implementation has been validated and shows good agreement with the theoretical ESF predictions [71, 80], and the ψ' superscaling model on which the ESF is tuned.

The combination of the ESF+TEM models is designed to ensure agreement with electron-nucleus scattering data by construction. The results presented in Section 6.6 are the first time that the ESF+TEM model has been compared with neutrino-nucleus scattering data. Reasonable agreement was found with the single-differential CCQE cross section results from both MiniBooNE and MINERνA for neutrino and antineutrino datasets, but MINERνA and MiniBooNE do not favour the same axial mass value. Significant issues were found with the MiniBooNE neutrino double-differential dataset, where it seems that the ESF cannot model the high angle events very well. This may be because the ESF is not tuned to high Q^2 electron scattering data, and the high angle region in which there is a discrepancy is at much higher Q^2 values than the ESF was tuned with. However, this may also be an unavoidable feature of the model, which adds a lot of strength to the high Q^2, high ω bins in the high angle region, and which does not appear to fit the available data well.

Fits to the global dataset were not performed, but the ESF+TEM model is now ready to be used as a candidate CCQE model for T2K, and will be included in the next generation NIWG fitting procedure using the framework described in Chapter 5.

Chapter 7

T2K oscillation analysis structure

This chapter provides a very broad overview of the structure of T2K oscillation analyses, with the aim of motivating the CCQE fits to external data described in Chapter 5, which are an important input to these analyses. There are three primary T2K oscillation analyses: VaLOR (**Va**lencia, **L**ancaster, **O**xford and **R**utherford Laboratory), p-theta (named after the binning used), and MaCh3 (**Ma**rkov **Ch**ain Monte Carlo **3**-neutrino flavour fit). ValOR and p-theta are frequentist analyses, and MaCh3 is bayesian. These fitting groups are independent, but should get very similar results, which provides an important final validation for any T2K oscillation analyses before publication. All of the T2K oscillation analyses use the ND280 off-axis detector (described in Section 3.1.2.2) to constrain the flux and cross section systematics which are used to generate the nominal unoscillated prediction at Super-Kamiokande (described in Section 3.1.3), and errors on these (nuisance) parameters in the oscillation fit. The VaLOR and p-theta oscillation groups used constraints provided by the BANFF (**B**eam **A**nd **N**D280 **F**lux extrapolation task **F**orce) group, whereas MaCh3 perform simultaneous near and far detector oscillation fits, but the near detector samples and treatment are very similar to that used by the BANFF group, which is described here.

Section 7.1 gives a general discussion of the importance of near detectors in constraining flux and cross section errors for oscillation analyses. The Neutrino Interactions Working Group (NIWG) cross section inputs for the 2015 BANFF fit are described Section 7.2. In Section 7.3 the BANFF fit is described. In Section 7.4 a brief summary of the BANFF output is given. Additionally, Section 7.5 describes a rescaling procedure for the CCQE priors which was used to ensure that the CCQE fit results would not unduly bias the BANFF fit.

7.1 Flux and cross section systematics and neutrino oscillation analyses

The event rate prediction at the far detector of a neutrino oscillation experiment as a function of p_μ, θ_μ is given by[1]

$$R(p_\mu, \theta_\mu) = \Phi(E_\nu) \times \sigma(E_\nu, p_\mu, \theta_\mu) \times \epsilon(p_\mu, \theta_\mu) \times P(\nu_A \rightarrow \nu_B), \tag{7.1}$$

where p_μ and θ_μ are the muon momentum and muon angle with respect to the incoming neutrino beam, E_ν is the neutrino energy, $R(p_\mu, \theta_\mu)$ is the event rate in each p_μ, θ_μ bin, Φ is the incoming neutrino flux, σ is the cross section, ϵ is the detector efficiency and $P(\nu_A \rightarrow \nu_B)$ denotes the oscillation probability for the channel of interest in the analysis.

It is clear from Equation 7.1 that the sensitivity of any neutrino oscillation experiment will be limited by the understanding of detector systematics, the neutrino cross section and the unoscillated neutrino flux. The detector systematics must be estimated using control samples or other techniques, and are nuisance parameters in the oscillation fits. The cross section and unoscillated neutrino flux uncertainties can be constrained by a near detector, where the measured event rate is given by

$$R(p_\mu, \theta_\mu) = \Phi(E_\nu) \times \sigma(E_\nu, p_\mu, \theta_\mu) \times \epsilon'(p_\mu, \theta_\mu), \tag{7.2}$$

where there is no oscillation probability, and the detector systematics have been denoted ϵ', as they are unlikely to be identical for the near and far detectors (although they may be very similar if both detectors have a similar design). Constraining the flux and cross section using a near detector greatly increases the power experiment to constrain the oscillation parameters.

7.2 Cross section inputs for the near detector fit

The NIWG are responsible for providing central values and uncertainties for the cross section parameters which are used in the oscillation analyses. These parameters are used as prior constraints in the BANFF fits to near detector data[2].

The 22 cross section parameters for the 2015 oscillation analyses are motivated and described in Reference [269], and all but 6 FSI parameter are summarised in Table 7.1.

[1] Of the three main T2K oscillation analyses, one uses p-theta (p_μ, θ_μ) binned events at SK, and two use E_{rec} bins calculated using p_μ and θ_μ according to Equation 5.1.

[2] These parameters are also used by analyses who perform cross section analyses at the near detector, and who cannot use the BANFF contraints without circularity (as the BANFF uses the same data in their fits).

Note that some of the parameters are treated independently for carbon and oxygen. This is to give the BANFF fit more freedom, and is not necessarily physically motivated.

- The 7 CCQE parameters are $M_{\mathrm{A}}^{\mathrm{QE}}$, p_{F} ^{12}C, E_b ^{12}C, MEC ^{12}C, p_{F} ^{16}O, E_b ^{16}O, MEC ^{16}O. E_b ^{12}C and E_b ^{16}O are based on electron scattering measurements [168], the others are constrained by the CCQE fits presented in Chapter 5. The ^{12}C/^{16}O difference for p_{F} is also based on electron scattering data (as the CCQE external data fits only use hydrocarbon targets). The error on the MEC normalisation parameter for ^{16}O is increased simply because there are no data constraints, and the MEC normalisation for ^{12}C was strongly suppressed in the CCQE external data fits.

- The 3 single pion production parameters C_5^A, $M_{\mathrm{A}}^{\mathrm{RES}}$ and the isospin $\frac{1}{2}$ non-resonant background are described in Reference [289], and come from a fit to single pion production data on deuterium and hydrogen. The NEUT model for resonant pion production uses the Rein-Sehgal model [170] with updated form factors [290]. The resonant axial mass is similar to the axial mass for CCQE, and the C_5^A parameter is the normalisation of the axial form factor for resonant pion production[3]. The isospin $\frac{1}{2}$ non-resonant background is a prediction of the Rein-Sehgal model, and the parameter scales their prediction.

- The ν_e/ν_μ ratio is motivated by studies based on Reference [291], which looked at how the different lepton masses affect many parts of the CCQE cross section.

- The CC-Other shape uncertainty affects charged-current multi-pion production, DIS and non-pion resonant production of γ, K or η. This uncertainty is known to ∼10% at 4 GeV [17], but there is no other information so a larger error is desirable at lower energies (the T2K flux is very small at 4 GeV). The functional form $\sigma_{\text{CC-Other}} = 0.4/E_\nu$ provides the desired behaviour. Note that the threshold for these interactions is ∼0.6 GeV so the ratio does not blow up at low E_ν.

- The remaining cross section uncertainties shown in Table 7.1 are simply scaling factors, based on the disagreement between the NEUT predictions and the sparse data that exists for these channels.

- Additionally, there are 6 Final State Interaction (FSI) parameters which affect various parts of the intranuclear cascade model used in NEUT [166, 174] (briefly described in Section 2.1.3). These parameters are split into low ($p_\pi \leq 500$ MeV) and high ($p_\pi > 500$ MeV) energy regions, which correspond approximately to the threshold for multi-pion production where different FSI models are used. The FSI

[3] The reanalysis of bubble chamber data described in Reference [40] reduced the error on C_5^A from ±0.25 to ±0.12 with no change to the central value.

parameters are tuned to a large body of pion-nucleus scattering data described in Reference [174]. The parameters are pion production, pion absorption, inelastic production at low and high energy, and charge exchange at low and high energy. For further details, see Reference [174].

	Parameter	NIWG recommendation
CCQE	$M_{\mathrm{A}}^{\mathrm{QE}}$ (GeV)	1.15 ± 0.07
	p_{F} ^{12}C (MeV)	223 ± 12
	E_b ^{12}C (MeV)	25 ± 9
	MEC ^{12}C (%)	27 ± 29
	p_{F} ^{16}O (MeV)	225 ± 12
	E_b ^{16}O (MeV)	27 ± 9
	MEC ^{16}O (%)	27 ± 104
1π	C_5^A	1.01 ± 0.12
	$M_{\mathrm{A}}^{\mathrm{RES}}$ (GeV)	0.95 ± 0.15
	$I = \frac{1}{2}$ background	1.3 ± 0.2
	ν_e/ν_μ	1.0 ± 0.02
	CC other shape	0.0 ± 0.4
	CC Coh ^{12}C	1.0 ± 1.0
	CC Coh ^{16}O	1.0 ± 1.0
	NC Coh	1.0 ± 0.3
	NC Other	1.0 ± 0.3

TABLE 7.1: Summary of the cross section errors from the NIWG group which are used as inputs to the T2K oscillation analyses.

Note that the CCQE priors used as inputs in the BANFF fit underwent a second rescaling procedure, described in Section 7.5, which was designed to ensure that the results of the CCQE fits did not unduly bias the ND280 fit. The motivation was some concern over the strong MEC suppression observed in the CCQE fits. The concern was that if similar suppression was not present in the ND280 data, and was caused by biases in the MINERνA and MiniBooNE cross section analyses, then the strong suppression of this parameter would become an issue in the BANFF fit. The second scaling procedure accounts for the slight difference in the CCQE parameter errors shown in Table 7.1 and Chapter 5, but the difference is small (<5%), so this discussion is only included for completeness.

The NIWG nominal cross section values are shown for a variety of charged current channels in Figure 7.1. The error bands shown are the 1σ error bands including all of the errors shown in Table 7.1, but do not include the FSI errors. Note that these generator level predictions cannot be directly compared with the BANFF samples as each sample contains a mixture of channels (due to FSI effects).

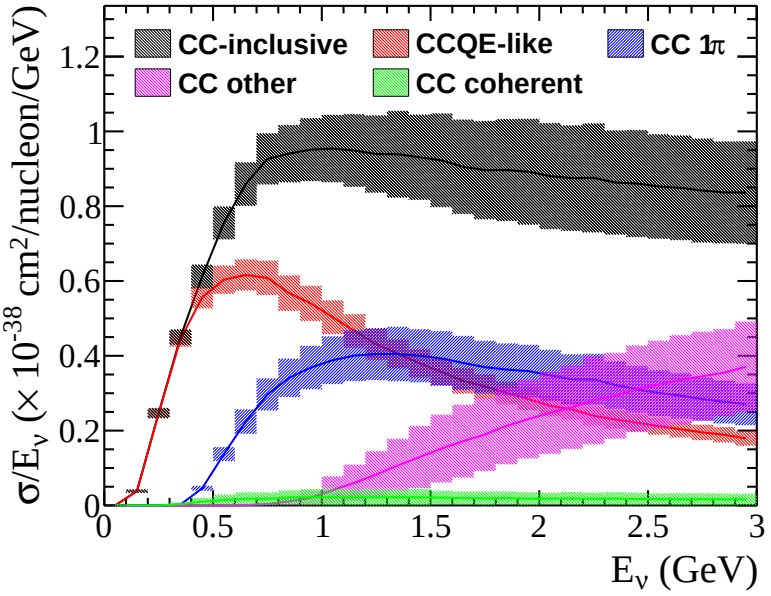

(A) $\nu_\mu - {}^{12}\mathrm{C}$

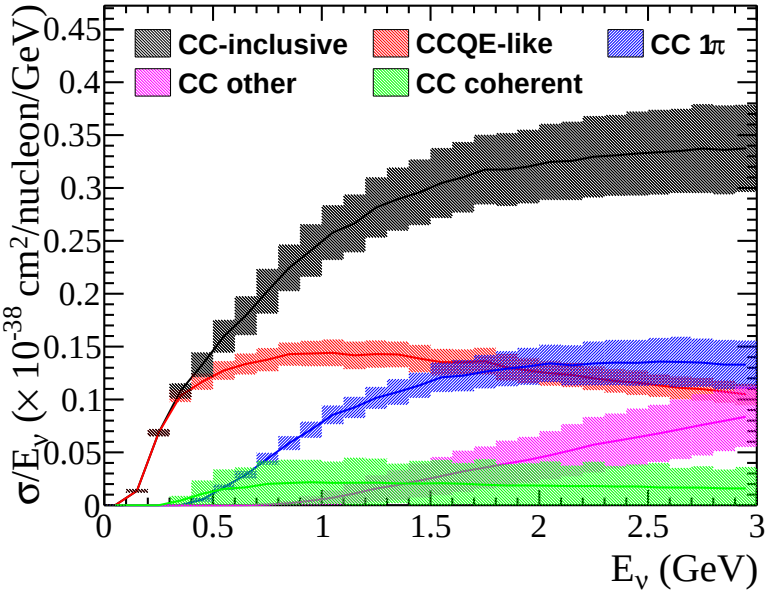

(B) $\bar{\nu}_\mu - {}^{12}\mathrm{C}$

FIGURE 7.1: The nominal NIWG 2015 cross section model for all charged current channels, shown with 1σ error bands for both $\nu_\mu - {}^{12}\mathrm{C}$ and $\bar{\nu}_\mu - {}^{12}\mathrm{C}$ interactions.

7.3 T2K near detector fit

The **B**eam **A**nd **N**D280 **F**lux extrapolation task **F**orce (BANFF) fit uses a variety of samples at the ND280 off-axis detector to constrain the flux and cross section errors. By using multiple samples, with different interaction modes and therefore different cross

sections, it is possible to break degeneracies between the flux and cross section systematics[4]. The BANFF fit described here will be used in the 2015 neutrino and antineutrino oscillation analyses, and uses the results of the CCQE fit results described Chapter 5. The BANFF fit strategy described [72] is similar to that used in previous oscillation analyses [73, 123, 124, 127, 128], although the beam and cross section inputs are updated and different samples are used.

As well as the NIWG cross section inputs described in Section 7.2, the BANFF fit includes prior estimates of the flux uncertainty, correlations and the nominal flux prediction from the beam group [57, 292]. The flux inputs are given as a function of E_ν for both positive and negative horn focusing (neutrino or antineutrino mode), for ν_μ, $\bar{\nu}_\mu$, ν_e and $\bar{\nu}_e$, for both the ND280 off-axis detector and SK. This gives a total of 100 highly correlated flux bins, with a ∼10% uncertainty on each bin.

The ten $p_\mu, \cos\theta_\mu$ binned ND280 samples included in the 2015 BANFF fit [72, 293, 294] are:

- ν_μ CC-inclusive (ν mode)
- ν_μ CC-0π (ν mode)
- ν_μ CC-1π (ν mode)
- ν_μ CC-Other (ν mode)
- $\bar{\nu}_\mu$ CC-inclusive ($\bar{\nu}$ mode)
- $\bar{\nu}_\mu$ CC 1-Track ($\bar{\nu}$ mode)
- $\bar{\nu}_\mu$ CC N-Tracks ($\bar{\nu}$ mode)
- ν_μ CC-inclusive ($\bar{\nu}$ mode)
- ν_μ CC 1-Track ($\bar{\nu}$ mode)
- ν_μ CC N-Tracks ($\bar{\nu}$ mode)

The six antineutrino mode samples are currently statistics limited, so have not been broken down into same final state topologies as the much higher statistics neutrino mode samples. All of these samples use interactions in FGD1 (see Section 3.1.2.2), which a predominantly hydrocarbon target. In future, additional FGD2 samples will

[4] For a simple example, consider a fully correlated normalised parameter affecting the flux, and a fully correlated normalisation parameter affecting the cross section. It is easy to see how adding additional samples would break the degeneracy when only the convolution of the flux and cross section (the event rate) is measured.

be included, which contains passive water layers. Because ND280 and SK are made of different target materials, the extrapolation from the near to far detector relies on a good understanding of the cross section model.

Each bin of the samples has a detector efficiency correction, which is necessary to make a comparison between data and MC. Detector efficiencies are calculated using control samples, and have associated uncertainties. Additional detector uncertainties come from sources such as distortions in the magnetic field, background from outside the fiducial volume of FGD1 and event pile-up. The detector systematics are calculated in References [293, 294] for the 2015 BANFF fit.

The ν_μ CC samples in neutrino mode are shown in Figure 7.2. The three topologies CC-0π, CC-1π and CC-Other have different dependencies on the cross section parameters. CC-0π has an enhanced CCQE component, CC-1π has an enhanced single pion production component, and CC-Other has enhanced DIS and multi-pion production components, but it is important to stress that the all interaction modes feature in all samples to some extent due to FSI and other effects.

The test statistic minimised in the BANFF fit is a binned likelihood, where $\Delta\chi^2_{\text{ND280}}$ is minus twice the logarithm of the likelihood [72]

$$\begin{aligned}\Delta\chi^2_{\text{ND280}} = \quad & 2\sum_i^{N_s} N_i^p(\vec{b},\vec{x},\vec{d}) - N_i^d + N_i^d ln[N_i^d/N_i^p(\vec{b},\vec{x},\vec{d})] \\ & + \left[\sum_i^{N_b}\sum_j^{N_b} \Delta b_i (V_b^{-1})_{i,j} \Delta b_j\right] \rightarrow \text{Flux priors} \\ & + \left[\sum_i^{N_x}\sum_j^{N_x} \Delta x_i (V_x^{-1})_{i,j} \Delta x_j\right] \rightarrow \text{NIWG priors} \\ & + \left[\sum_i^{N_s}\sum_j^{N_s} \Delta d_i (V_d^{-1})_{i,j} \Delta d_j\right] \rightarrow \text{Det. syst.,} \end{aligned} \tag{7.3}$$

where N_i^d is the number of events in the ith $p_\mu - \cos\theta_\mu-$ sample bin (of a total of N_s bins in all of the samples). N_i^p is the predicted number of events in the ith bin, which depends on the flux, $\vec{b}$, cross section, $\vec{x}$, and detector, $\vec{d}$, systematic parameters. The systematic parameters have prior probability distributions described above, which are treated as multivariate Gaussians which are described by the covariance matrices (with dimension) V_b (N_b), V_x (N_x) and V_d (N_s) for the flux, cross section and detector parameters respectively. Note that the number of detector systematics is equal to the total number of bins included in the sample. The deviations of the systematic parameters

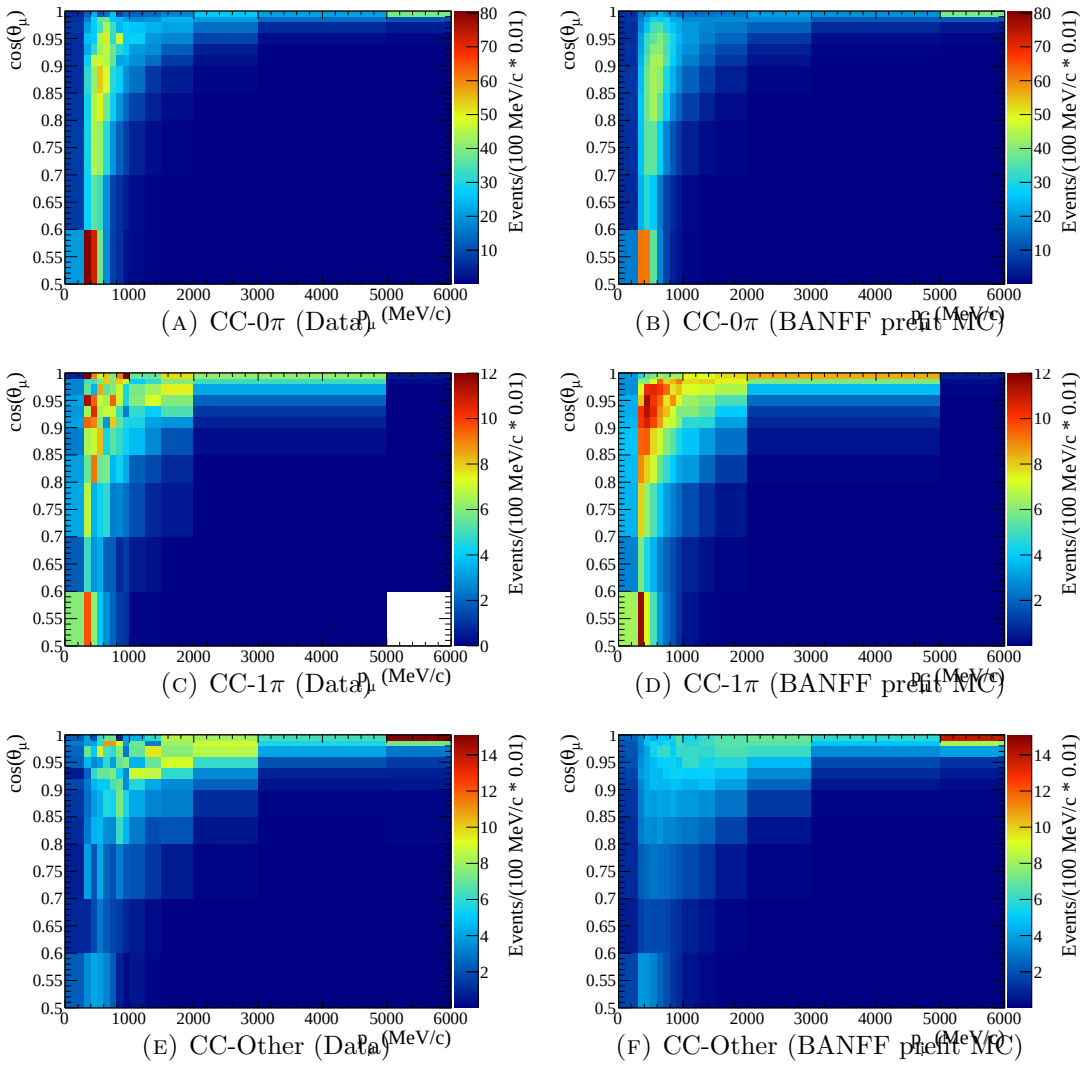

(A) CC-0π (Data) (B) CC-0π (BANFF prefit MC)

(C) CC-1π (Data) (D) CC-1π (BANFF prefit MC)

(E) CC-Other (Data) (F) CC-Other (BANFF prefit MC)

FIGURE 7.2: Comparison of the ND280 data and BANFF prefit NEUT MC for the three ν_μ final state topologies from the neutrino mode data. The highest p_μ bin extends to 30 GeV, and the lowest $\cos\theta_\mu$ bin extends to -1, but have been truncated for ease of presentation. These plots are reproduced from Figure 1 of Reference [72].

away from the central values provided to the BANFF are Δb, Δx and Δd for the flux, cross section and detector parameters respectively.

7.4 Output from the BANFF fit

The outputs of the BANFF fit are central values for all the flux, cross section and detector systematic parameters, and a covariance matrix describing their relationship. The detector systematics are not a useful output from the fit because the ND280 off-axis detector and SK have very different detector systematics because they have very different detector designs, so the interesting output of the BANFF fit is a covariance matrix describing the flux and cross section parameters and their central values[5]. This covariance matrix is then provided to the oscillation analysis groups, who fit for neutrino oscillation parameters using Equation 7.1, where the other inputs are the detector systematics for SK, and the measured SK event rate. In oscillation fits, all parameters except the event rate and oscillation probability are nuisance parameters, so the size of the 1σ error on the predicted SK event rate from the input flux and cross section covariance is an important limiting factor in the fit.

Figure 7.3 shows the effect of the BANFF 2013 prediction on the total error envelopes for the reconstructed energy distributions for the ν_μ and ν_e charged-current candidate event predictions at SK, using estimates of the oscillation parameters [73]. The total error band is shown with and without the BANFF ND280 constraint applied. It is clear that using the BANFF fit results greatly increases the power of the oscillation fit. Figure 7.4 shows the effect of the BANFF 2015 prediction on the total error envelopes for the reconstructed energy distributions for the $\bar{\nu}_\mu$ charged-current candidate event predictions at SK [74]. The oscillated and unoscillated spectra are both shown, with nominal oscillation parameters taken from Reference [73]. Again, the power of the BANFF fit to reduce the errors is clear, and the advantage of using ND280 data to update the prior central values for the upcoming $\bar{\nu}_\mu \rightarrow \bar{\nu}_\mu$ is obvious.

[5] Although the pulls on the detector systematic parameters are checked for unusually strong pulls to validate the BANFF fit results.

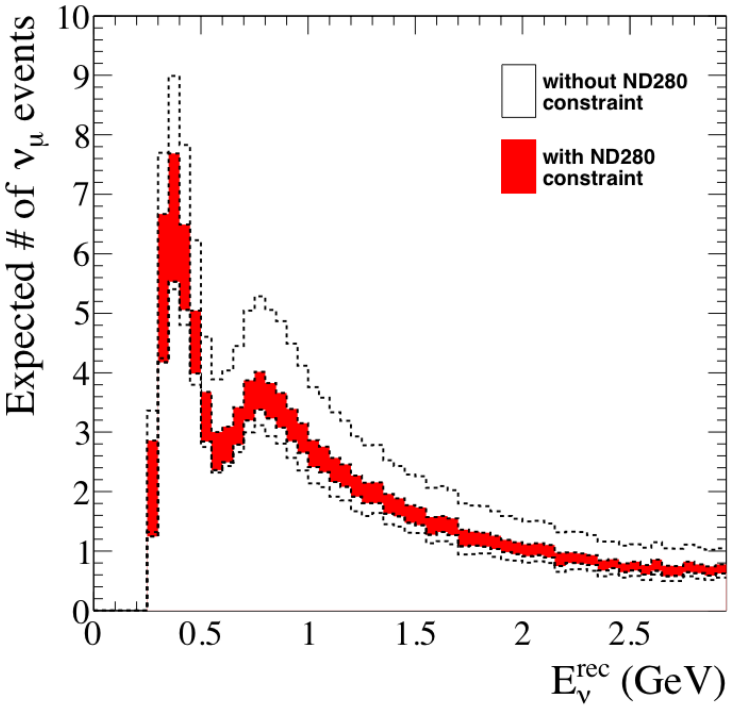

(A) ν_μ SK prediction

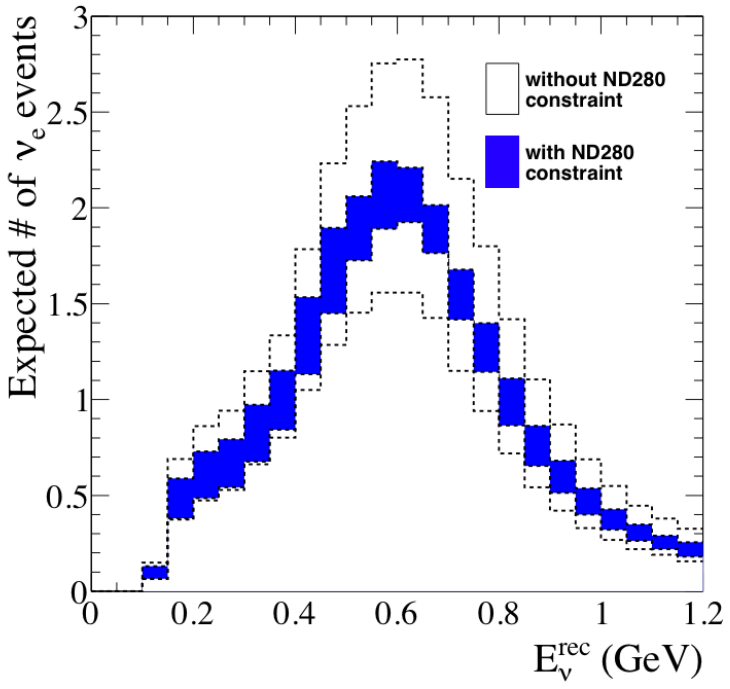

(B) ν_e SK prediction

FIGURE 7.3: Total error envelopes for the event rate prediction at SK with and without the ND280 (BANFF) constraint, shown for ν_μ and ν_e candidate events as a function of the reconstructed neutrino energy (Equation 5.1). This plot is reproduced from Figure 26 of Reference [73].

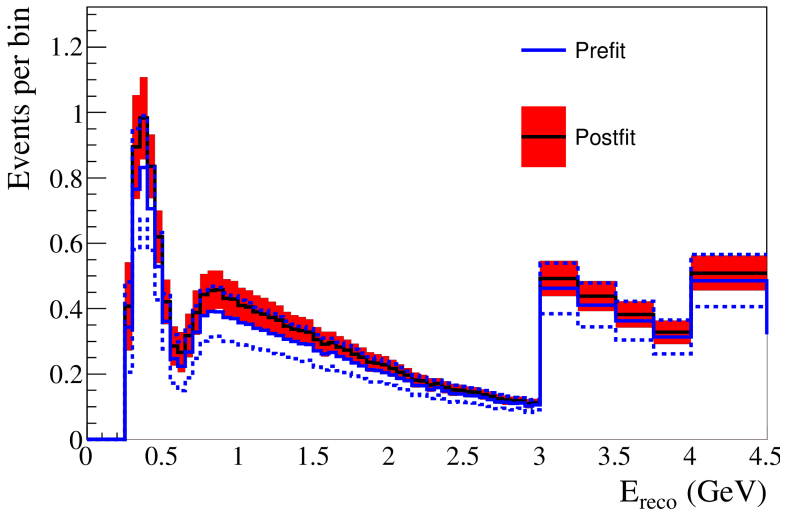

(A) Oscillated

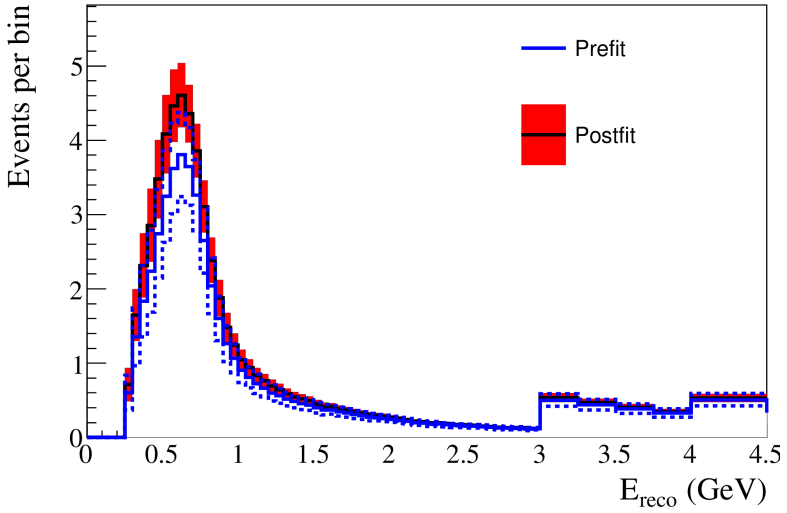

(B) Unoscillated

FIGURE 7.4: Total error envelopes for the event rate prediction at SK with and without the ND280 (BANFF) constraint, shown for the $\bar{\nu}u_\mu$ candidate event sample as a function of the reconstructed neutrino energy (Equation 5.1) with and without oscillations. This plot is reproduced Reference [74].

7.5 Turning the CCQE fit results into priors for oscillation analyses

The CCQE external data fit results described in Chapter 5 were used to select the RFG+RPA+MEC model for the CCQE-like cross section model, and were used to constrain the parameters M_A, MEC normalisation and p_F. The best fit values and parameter errors for the constrained parameters are reproduced in Table 7.2, and the correlation matrix between them is reproduced in Figure 7.5. Because of deficiencies in the datasets

used in the CCQE fits[6], Gaussian statistics are no longer reliable, and the value of $\Delta\chi^2 = 1$ used for estimating parameter errors by MINUIT cannot be relied upon. Following the general procedure used by groups fitting parton density distributions [283] who have to deal with similar deficiencies in the experimental data, the value of $\Delta\chi^2$ used to define the 1σ parameter errors is increased. Although no general procedures for inflating the errors are given in Reference [283], the test statistic for the Parameter Goodness of Fit (PGoF) test [281] used to assess the goodness of fit in the CCQE external data fits provides an approximation for the level of disagreement between all datasets.

Fit type	χ^2/DOF	M_A (GeV)	MEC (%)	p_F (MeV)
Unscaled	97.84/228	1.15±0.03	27±12	223±5
Scaled		1.15±0.06	27±27	223±11

TABLE 7.2: Errors for the CCQE parameters are reproduced from Section 5.4. The unscaled errors are given for reference, but the scaled errors should be used in analyses.

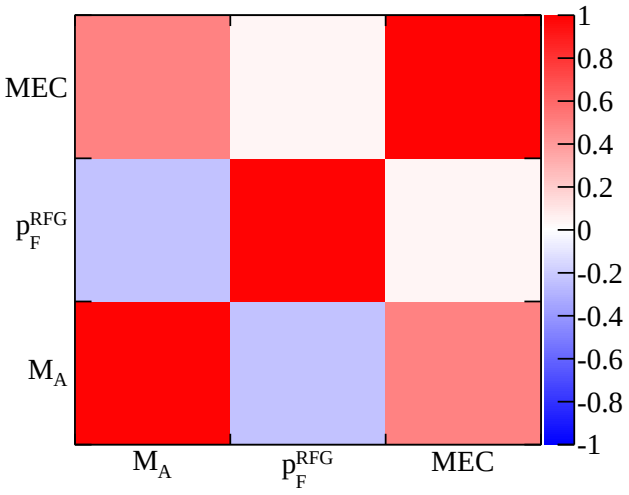

FIGURE 7.5: Correlation matrix for the CCQE parameters for the RFG+RPA+MEC model.

Because the best fit CCQE parameters obtained from the CCQE external data fits were contrary to expectation (in particular, the MEC component was highly suppressed as can be seen in Table 7.2), there was a concern that the parameter errors provided might not be large enough, and would bias the BANFF fit. A second PGoF rescaling procedure was defined through a discussion between the NIWG/OA/BANFF groups with the aim of ensuring that the external data fits would not bias the BANFF fit if the BANFF and external data disagreed very strongly. The rescaling procedure essentially deweights the

[6]In particular, no correlation matrices were provided for use with the MiniBooNE datasets used in the CCQE external data fits.

CCQE priors provided by the NIWG group by increasing the parameter errors. The method closely follows the PGoF procedure described in Section 5.3.3, where the χ^2_{PGoF} test statistic is used to scale the parameter errors. The χ^2_{PGoF} statistic is produced by comparing fits to ND280 data, external data, and ND280+external data

$$\bar{\chi}^2(\vec{\mathbf{x}}) = \chi^2_{\text{ND280+external, min}}(\vec{\mathbf{x}}) - \chi^2_{\text{ND280, min}}(\vec{\mathbf{x}}) - \chi^2_{\text{external, min}}(\vec{\mathbf{x}}), \tag{7.4}$$

where $\vec{\mathbf{x}}$ are the parameters varied in the fit (M_{A}, MEC normalisation and p_{F}). Note that the fits to ND280 data are performed with no CCQE prior errors included. ND280 data was included in the external data fits using the output covariance matrix for the three CCQE parameters M_{A}, MEC normalisation and p_{F} from the BANFF fit, where all other parameters were marginalised over. At each iteration of the external data fit with ND280 data included, the $\Delta\chi^2$ was calculated from the BANFF covariance matrix, and added to the total in the fit. Note that in this procedure, the ND280 data only contributes $\Delta\chi^2$, the χ^2_{min} contribution from the ND280 data is not included but this is not important for the PGoF test.

The aim of the PGoF is to test the compatibility of the different datasets in the framework of the model. Put simply, it tests whether the best fit parameter values for fits to subsets of the data pulls the fit parameters far from the best fit values found when fitting to all of the data. The PGoF gives a value for the incompatibility between the datasets: how much the χ^2 increases between the best fit points of each experiment, and the best fit point for the combined dataset. The PGoF value can therefore be used as a measure of how much the errors have to be inflated by to cover the difference between the best fit parameter values from the combined fit and the best fit values of individual datasets, this is shown explicitly in Equation 7.5

$$\Delta\chi^2 = \sqrt{\chi^2_{\text{PGoF}}/\text{DOF}_{\text{PGoF}}}. \tag{7.5}$$

Note that this PGoF rescaling procedure does not modify the correlations between parameters, it simply rescales the error on each parameter. An important caveat to keep in mind with this procedure is that the PGoF test still assumes that the subsamples of the data follow a χ^2 distribution, which is not the case for the MiniBooNE datasets used in the external data fits as no bin to bin correlations have been provided. However, the PGoF test has still proven to be a useful tool for identifying sources of tension in the external data fits (see Section 5.3.4). The error inflation procedure is also necessary because the MiniBooNE data lacks correlations, so the PGoF is likely to be an imperfect estimate of the scaling required. As has already been noted, the parton density distribution fitters who inflate errors in this way offered no general procedure for inflating the

errors correctly, so we followed a similarly pragmatic approach and used the only tool at our disposal. Refinements of the error inflation procedure can be expected in future.

By applying the PGoF procedure to a fit to ND280 and external data, the aim is to ensure that the prior errors cover both the external fit results, and ND280 data at 1σ. The PGoF rescaling procedure was tested with five fake data sets provided by the BANFF as described in Section 7.5.1, and results using a fit to real ND280 data are given in Section 7.5.2.

7.5.1 Fake data studies of the reinflation procedure

The CCQE error reinflation procedure was tested with five separate fake data fit results from the BANFF group. The fake data sets are listed below, and the BANFF fit values are given in Table 7.3.

1. NIWG 2014 central values,
2. Nominal NEUT prediction for non-relativistic RFG+RPA+MEC (with NIWG 2014 p_{F} value),
3. Throw of the NIWG 2014 parameters with errors as in Section 5.4,
4. SF+MEC fake dataset generated with NEUT,
5. GENIE nominal prediction.

Fake data set	M_{A} (GeV)	p_{F} (MeV)	MEC (% Nieves)
1	1.16	223	27
2	1.21	223	100
3	1.18	211	41
4	1.16	200	77
5	1.01	200	94

TABLE 7.3: BANFF best fit parameters for the five fake data sets used to test the CCQE error re-inflation procedure.

For each of the fake data sets, fits were performed to various subsets of the data, and various χ^2_{PGoF} statistics were calculated in order to investigate where the tensions lie between the ND280 preferred parameter values, and the parameter values preferred by the various datasets included in the external data fits. The formulae for calculating the various PGoF statistics are given explicitly in Table 7.4 for reference, and are given for the five fake datasets in Tables 7.5, 7.6, 7.7, 7.8 and 7.9 in the order given above.

	χ^2_{PGoF}
External	$\chi^2_{\text{external}} - \chi^2_{\text{MB}\,\nu} - \chi^2_{\text{MB}\,\bar{\nu}} - \chi^2_{\text{MN}\,\nu+\bar{\nu}}$
MINERνA vs MiniBooNE	$\chi^2_{\text{MB+MIN}} - \chi^2_{\text{MB}\,\nu+\text{MB}\,\bar{\nu}} - \chi^2_{\text{MN}\,\nu+\bar{\nu}}$
MINERνA vs BANFF	$\chi^2_{\text{MN+BANFF}} - \chi^2_{\text{MN}\,\nu+\bar{\nu}} - \chi^2_{\text{BANFF}}$
MiniBooNE vs BANFF	$\chi^2_{\text{MB+BANFF}} - \chi^2_{\text{MB}\,\nu+\text{MB}\,\bar{\nu}} - \chi^2_{\text{BANFF}}$
BANFF vs external	$\chi^2_{\text{MB+MIN+BANFF}} - \chi^2_{\text{external}} - \chi^2_{\text{BANFF}}$
MIN vs MB vs BANFF	$\chi^2_{\text{MB+MIN+BANFF}} - \chi^2_{\text{MB}\,\nu+\text{MB}\,\bar{\nu}} - \chi^2_{\text{MN}\,\nu+\bar{\nu}} - \chi^2_{\text{BANFF}}$
All	$\chi^2_{\text{MB+MIN+BANFF}} - \chi^2_{\text{MB}\,\nu} - \chi^2_{\text{MB}\,\bar{\nu}} - \chi^2_{\text{MN}\,\nu+\bar{\nu}} - \chi^2_{\text{BANFF}}$

TABLE 7.4: Explicit formulae for calculating the χ^2_{PGoF} test statistics for each of the subsets of the data investigated. Each χ^2 value listed in this table denotes the χ^2 at the minimum.

The PGoF scaling procedure defined in Section 5.3.3 scales the parameter errors according to the 'MINERνA vs MiniBooNE' row of the PGoF tables with the intention of approximately scaling the errors such that they cover all MiniBooNE and MINERνA datasets at 1σ. It should be noted that this is in some sense averaged over all of the datasets: some datasets will be covered at less than 1σ, and some will not be covered at 1σ. Similarly, the appropriate statistic for the PGoF *rescaling* procedure discussed here is the 'MINERνA vs MiniBooNE vs BANFF' row of the PGoF tables, which should scale the parameter errors such that the external and ND280 data are covered at 1σ.

As expected, the PGoF *rescaling* procedure has no effect when the NIWG prior central values are used to generate ND280 fake data, as can be seen from Table 7.5, and has little effect when a throw of the NIWG priors using the errors provided in Section 5.4 was used, as can be seen in Table 7.7. Unsurprisingly, the rescaling values for fake data sets 4 and 5, where completely different models were used to generate the fake data produce relatively large rescaling values as can be seen from Tables 7.8 and 7.9 which confirms the expected behaviour if the ND280 data strongly disagrees with all of the external data. Fake data set 3 (show in Table 7.7) is very similar to the NIWG priors except for the MEC parameter, which is set at the nominal Nieves model (100% Nieves), and the effect of the rescaling procedure is minimal. This can be understood because M_{A} and p_{F} both agree well with the best fit from the external data fits, so the disagreement in the MEC parameter is diluted by the agreement with the other two parameters. Also, it can be seen from Table 7.7 that the disagreement between the BANFF fake data and the external data is due to a strong disagreement between the BANFF fake data and MINERνA. As this is so similar to the disagreement between MINERνA and MiniBooNE, which drove the PGoF error inflation in Section 5.3.6, the error is not significantly increased by this reinflation procedure.

	χ^2_{min}	χ^2_{PGoF}/DOF	PGoF (%)
External	97.8	17.9/6	0.66
MINERνA vs MiniBooNE	97.8	15.9/3	0.12
MINERνA vs BANFF	30.4	7.0/3	7.19
MiniBooNE vs BANFF	59.5	0.9/3	82.54
BANFF vs external	97.9	0.1/3	99.18
MIN vs MB vs BANFF	97.9	16.0/6	1.38
All	97.9	18.0/9	3.52

TABLE 7.5: PGoF tests for fake data set 1. Explicit formulae for the PGoF statistics are given in Table 7.4.

	χ^2_{min}	χ^2_{PGoF}/DOF	PGoF (%)
External	97.8	17.9/6	0.66
MINERνA vs MiniBooNE	97.8	15.9/3	0.12
MINERνA vs BANFF	37.0	13.6/3	0.35
MiniBooNE vs BANFF	60.6	2.0/3	57.24
BANFF vs external	103.1	5.3/3	15.11
MIN vs MB vs BANFF	103.1	21.2/6	0.17
All	103.1	23.2/9	0.58

TABLE 7.6: PGoF tests for fake data set 2. Explicit formulae for the PGoF statistics are given in Table 7.4.

	χ^2_{min}	χ^2_{PGoF}/DOF	PGoF (%)
External	97.8	17.9/6	0.66
MINERνA vs MiniBooNE	97.8	15.9/3	0.12
MINERνA vs BANFF	30.9	7.5/3	5.76
MiniBooNE vs BANFF	59.7	1.1/3	77.71
BANFF vs external	98.7	0.9/3	82.54
MIN vs MB vs BANFF	98.7	16.8/6	1.00
All	98.7	18.8/9	2.69

TABLE 7.7: PGoF tests for fake data set 3. Explicit formulae for the PGoF statistics are given in Table 7.4.

	χ^2_{min}	χ^2_{PGoF}/DOF	PGoF (%)
External	97.8	17.9/6	0.66
MINERνA vs MiniBooNE	97.8	15.9/3	0.12
MINERνA vs BANFF	35.0	11.6/3	0.89
MiniBooNE vs BANFF	80.6	22.0/3	0.01
BANFF vs external	121.3	23.5/3	0
MIN vs MB vs BANFF	121.1	39.2/6	0
All	121.3	41.4/9	0

TABLE 7.8: PGoF tests for fake data set 4. Explicit formulae for the PGoF statistics are given in Table 7.4.

	χ^2_{min}	χ^2_{PGoF}/DOF	PGoF (%)
External	97.8	17.9/6	0.66
MINERνA vs MiniBooNE	97.8	15.9/3	0.12
MINERνA vs BANFF	35.6	12.2/3	0.67
MiniBooNE vs BANFF	107.3	48.7/3	0
BANFF vs external	142.7	44.9/3	0
MIN vs MB vs BANFF	142.7	60.8/6	0
All	142.7	62.8/9	0

TABLE 7.9: PGoF tests for fake data set 5. Explicit formulae for the PGoF statistics are given in Table 7.4.

7.5.2 Error re-inflation with ND280 data

The CCQE fit results from Section 5.4 are reproduced in Table 7.10, along with best fit parameter values and MINUIT errors from fits to ND280 real data and subsamples of the external data used in the CCQE fits. As previously noted, the ND280 data only contributes $\Delta\chi^2$ to these fits and no DOF, so the χ^2/DOF column of Table 7.10 must be treated with extreme caution. It can be seen that the ND280 data agrees relatively well with MiniBooNE data, and disagrees strongly with MINERνA data. The problem parameter in the combined ND280 + external data fit is clearly MEC normalisation, which is unsurprising as MINERνA caused the suppression of this parameter in the external data fits.

Fit type	χ^2/DOF	M_A (GeV)	MEC (%)	p_F (MeV)	λ_ν^{MB}	$\lambda_{\bar{\nu}}^{MB}$
MB+MIN	97.84/228	1.15±0.03	27±12	223±5	0.79±0.03	0.78±0.03
MIN	23/13	0.96±0.06	1±30	213±7	N/A	N/A
MB	59/212	1.19±0.03	57±18	229±5	0.85±0.04	0.83±0.04
BANFF	N/A	1.24	156	230	N/A	N/A
MB+BANFF	69.33/212	1.22±0.02	95±17	228±6	0.91±0.03	0.89±0.03
MIN+BANFF	54.69/13	1.14±0.03	48±13	214±6	N/A	N/A
MB+MIN+BANFF	119.88/228	1.18±0.02	51±11	223±1	0.83±0.03	0.82±0.03

TABLE 7.10: Best fit results for fits to various combinations of the data used in the CCQE external data fits and fits to ND280 data. The fits without BANFF samples included are taken from Chapter 5 and Appendix C.

The PGoF table for fits to subsets of the ND280 + external CCQE data is given in Table 7.11. As already observed, this confirms that the majority of the tension is between MINERνA and the ND280 data, and this disagreement is comparable to the disagreement between MINERνA and MiniBooNE. In this respect, the fit to ND280 data most closely resembles fake data set 3 (shown in Table 7.7), where the disagreement is largely in the MEC normalisation parameter.

	χ^2_{min}	χ^2_{PGoF}/DOF	PGoF (%)
External	97.8	17.9/6	0.66
MINERνA vs MiniBooNE	97.8	15.9/3	0.12
MINERνA vs BANFF	54.7	31.3/3	0
MiniBooNE vs BANFF	69.3	10.7/3	1.35
BANFF vs external	119.9	22.1/3	0.01
MIN vs MB vs BANFF	119.9	38.0/6	0
All	119.9	40.0/9	0

TABLE 7.11: PGoF tests for real ND280 data. Explicit formulae for the PGoF statistics are given in Table 7.4.

The NIWG priors with three error definitions are collected in Table 7.12. The unscaled errors are taken directly from MINUIT, but are underestimated because of the lack of correlations provided for the MiniBooNE datasets. The *scaled* errors are reproduced from Section 5.4, where the errors were inflated with the intention of covering MiniBooNE and MINERνA data at 1σ using Equation 7.5 with the MINERνA vs MiniBooNE PGoF value of 15.9/3, leading to a scaling factor of $\sqrt{15.9/3} \approx 2.3$ which is applied to the errors from MINUIT. The *rescaled* errors were defined in this section, and aim to ensure that the BANFF real data, MINERνA and MiniBooNE are all covered at 1σ by using Equation 7.5 with the BANFF vs MINERνA vs MiniBooNE PGoF value of 38.0/6, leading to a scaling factor of $\sqrt{38.0/6} \approx 2.5$ which is applied to the errors from MINUIT. The *rescaled* errors are the NIWG recommendation for the CCQE priors which should be used in the BANFF fit.

Fit type	χ^2/DOF	M_{A} (GeV)	MEC (%)	p_{F} (MeV)	$\lambda_{\nu}^{\mathrm{MB}}$	$\lambda_{\bar{\nu}}^{\mathrm{MB}}$
Unscaled		1.15±0.03	27±12	223±5	0.79±0.03	0.78±0.03
Scaled	97.84/228	1.15±0.06	27±27	223±11	0.79±0.07	0.78±0.07
Rescaled (+BANFF)		1.15±0.07	27±29	223±12	0.79±0.08	0.78±0.07

TABLE 7.12: Final NIWG CCQE priors with *scaled* and *rescaled* parameter errors.

Chapter 8

Concluding remarks

This thesis focuses on the impact of Charged-Current Quasi-Elastic (CCQE), and the closely related Neutral-Current Elastic (NCEL) cross section modelling uncertainties on neutrino oscillation measurements. For years it was thought that the CCQE cross section was relatively uninteresting as the Relativistic Fermi Gas (RFG) model agreed well with data on deuterium and hydrogen in the few-GeV region as well as with higher energy data on heavier nuclear targets. However, recently, a number of experiments have measured the CCQE cross section in the few-GeV region and have found a significant enhancement to the CCQE cross section which does not agree with hydrogen and deuterium data. This has typically been modelled by experiments by inflating the single free parameter in the RFG model, the axial mass. This approach cannot consistently describe all of the experimental data, and is effectively patching the RFG model up in lieu of a proper understanding of the enhancement. The theoretical background and an overview of current experimental data was given in Chapter 2.

In Chapter 4, a 3+1 sterile neutrino analysis using published NCEL and CCQE datasets from MiniBooNE was presented. The focus was on the effect of the cross section uncertainty on the analysis, and how inflating the axial mass may lead to biased analyses for similar experiments. It was found that the axial mass and sterile neutrino parameters were correlated, and treating them as uncorrelated (as has been done in published MiniBooNE analyses) is not, in general, a safe approach. A fit to the NCEL dataset gave the first results in the $\Delta m^2 - \sin^2 2\vartheta_{\mu s}$ plane, and a combined fit to NCEL and CCQE data was performed, which helps break the degeneracy between some parameters in the NCEL only fit, and produced stronger results. It was found that the results of this analysis are inconsistent with other sterile neutrino limits on 3+1 models, which could be considered an interesting way to look for tension in global sterile neutrino fits, and is certainly an interesting cross-check to make. However, it seems more likely that

this tension is because the NCEL and CCQE cross sections are incorrectly modelled by the simple RFG model with an inflated axial mass, and brings into question the validity of sterile neutrino limits produced using inadequate cross section model assumptions.

Recently, there has been a lot of theoretical work developing sophisticated models of nuclear affects to account for the "large axial mass anomaly" (an overview was given in Section 2.4). The Neutrino Interactions Working Group (NIWG) of T2K have tried to include as many of these new models in NEUT, T2K's primary neutrino interaction generator, for use in future T2K analyses. Chapter 5 describes a fitting framework developed to constrain cross section model parameters with published datasets, and fits to the available CCQE data to constrain the SF+MEC and RFG+RPA+MEC cross section models. The RFG+RPA+MEC model was chosen as it most consistently fit all of the available data, although significant tensions were found in the fit suggesting more work is required to develop a cross section model which consistently describes all of the CCQE cross section data available. Despite the problems observed in the fit, this work is the first time that a consistent fit to all of the available CCQE datasets has been performed with these new models, and can help guide future model development. The RFG+RPA+MEC model, parameter values and errors will be used by future T2K analyses on the basis of this work, making T2K the first long baseline neutrino oscillation experiment to include these new models in their analyses in a consistent way, which is a significant step forwards in the field, of which this work is a very small part. The fitting framework developed for this work was designed to be easily extensible, so other datasets and models could be used in the CCQE external data fits, and so it could be used to constrain the cross section parameters for other interaction modes.

In Chapter 6 describes the implementation of the Effective Spectral Function (ESF) model into NEUT. The ESF is a cross section model for CCQE and NCEL interactions which, unlike other models used for neutrino-nucleus scattering, guarantees agreement with electron scattering data by construction. This agreement is achieved by modifying the initial state nucleon momentum distribution inside the nucleus; all of the nuclear effects which distort the outgoing lepton kinematics in electron scattering are effectively modelled by changing the description of the initial state of the nucleus. The model is implemented in NEUT for all targets used in T2K, and so offers a fully consistent cross section model which can be used in future iterations of the CCQE fit procedure. In this work, comparisons of the ESF model with neutrino-nucleus scattering data are made for the first time. It was found that the ESF agreed reasonably well with MINERνA and MiniBooNE single-differential data, although different axial mass values were required to fit the data, so it does not appear to be a quick solution to the large axial mass anomaly. There was significant tension with the high angle component of the MiniBooNE neutrino

mode double-differential data, which may indicate problems modelling high Q^2 events with this model.

Finally, in Chapter 7, the T2K oscillation analysis structure was described, with a particular focus on the importance of cross section model uncertainties, to give context to the preceeding analysis chapters. The CCQE fit results presented in Chapter 5 will be used for 2015 and future T2K oscillation analyses, and future updates to the cross section model will use the fitting framework developed for Chapter 5 (which has been extended to other interaction channels). Additionally, the ESF model implementation in NEUT described in Chapter 6 will be used as a candidate model for future iterations of the CCQE fit.

As neutrino oscillation physics moves towards high precision measurements of oscillation parameters, large cross section uncertainties on the signal interactions will rapidly become a limiting factor on the precision of currently running and future oscillation experiments, and grossly inadequate cross section models risk biasing results. Future iterations of the work in this thesis are essential to overcome the problems with CCQE and other signal interactions.

Appendix A

Three-momentum transfer in the Nieves model

In this appendix, the effect that changing the three-momentum cut-off, $|\vec{q}|$, used in the Nieves model has on the CCQE fits is discussed. An analysis is carried out where $|\vec{q}|$ is included as an additional free parameter using the procedures given in Chapter 5. In Section A.1, the results of the fit are given; Section A.2 gives the PGoF results including the $|\vec{q}|$ parameter; finally, the results are compared with the main fit results in Section A.3.

The range of the three-momentum transfer investigated is limited in the range $0.9 \leq |\vec{q}| \leq 1.2$ GeV. The upper limit is technical – the NEUT files generated for production 6 were generated with $|\vec{q}| = 1.2\,\text{GeV}$, and the reweighting implementation cannot reweight events in unoccupied regions of phase-space. The lower limit was placed because lower values would start cutting heavily into the Delta peak, as can be seen from Figure 2.11.

A.1 Fit results including the three-momentum transfer parameter

The best fit results for combined fits to all four datasets including the three-momentum transfer parameter, $|\vec{q}|$, are summarised in Table A.1, along with the main fit result from Section 5.3.2 for comparison. The fit strategy is the same as is described in Section 5.3.2 with an additional parameter.

The SF+MEC results are unaffected by the inclusion of the new parameter. This is not a complete surprise as the MEC component was completely suppressed in the standard

fit; the additional freedom introduced by the new parameter did not relieve this tension. Both RFG+RPA+MEC models show improved agreement when the $|\vec{q}|$ cut goes to the lower allowed limit in the fits. This is because the $|\vec{q}|$ parameter introduces an additional freedom between MiniBooNE and MINERνA, having a more sizeable effect on the latter, and alleviating some of the tension between data from the two experiments. The most significant effect of reducing this tension is an increase in the MEC normalisation of $\sim$10%, although M_{A} also increases slightly at the best fit point compared with the result with $|\vec{q}|$ fixed at 1.2 GeV. The relativistic RPA model is still favoured over the non-relativistic RPA model.

Fit type		χ^2/DOF	M_{A} (GeV)	MEC (%)	p_{F} (MeV)	$\lvert\vec{q}\rvert$ (GeV)
Free $\lvert\vec{q}\rvert$	Rel. RPA	93.90/228	1.17±0.03	38±13	224±5	0.9 (at limit)
	Non-rel. RPA	114.03/228	1.10±0.03	46±14	225±5	0.9 (at limit)
	SF+MEC	97.46/228	1.33±0.02	0 (at limit)	234±3	1.2 (at limit)
Fixed $\lvert\vec{q}\rvert$	Rel. RPA	97.84/228	1.15±0.03	27±12	223±5	1.2 (fixed)
	Non-rel. RPA	117.87/228	1.07±0.03	34±12	225±5	1.2 (fixed)
	SF+MEC	97.46/228	1.33±0.02	0 (at limit)	234±4	1.2 (fixed)

TABLE A.1: The best fit parameter values for fits to all datasets with the three-momentum transfer allowed to vary in the range $0.9 \leq |\vec{q}| \leq 1.2$ GeV are presented for each model. The results of the CCQE fits with fixed $|\vec{q}| = 1.2$ GeV are included for reference.

The best fit distributions for the SF+MEC and relativistic RFG+RPA+MEC models, with the best fit parameters with free $|\vec{q}|$ cut given in Table A.1, are shown for the MINERνA and MiniBooNE datasets used in the fit in Figures A.1 and A.2 respectively.

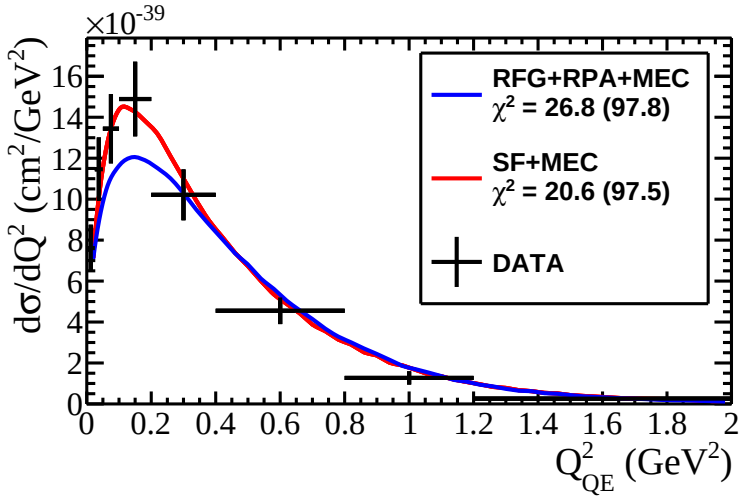

(A) Neutrino

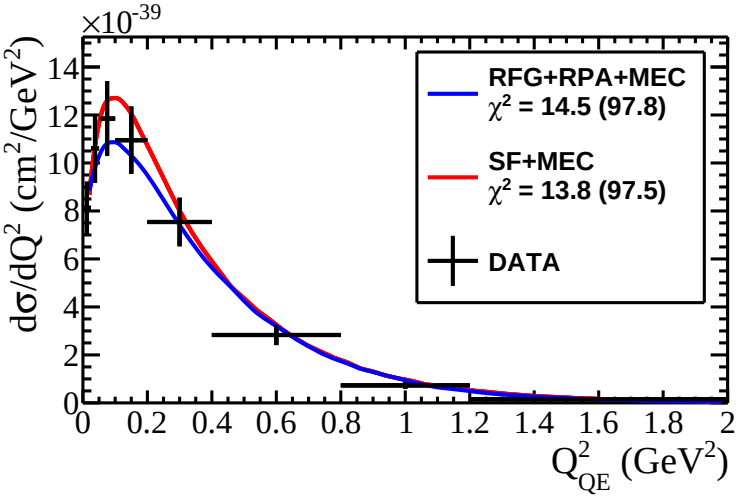

(B) Antineutrino

FIGURE A.1: Comparison of the best fit distribution from the fits to all datasets including the three-momentum transfer cut, detailed in Table A.1, with the MINERνA datasets used in the fit. The χ^2 values in the legend are the contribution from each dataset at the best fit point, and the total χ^2_{min} for the combined fit.

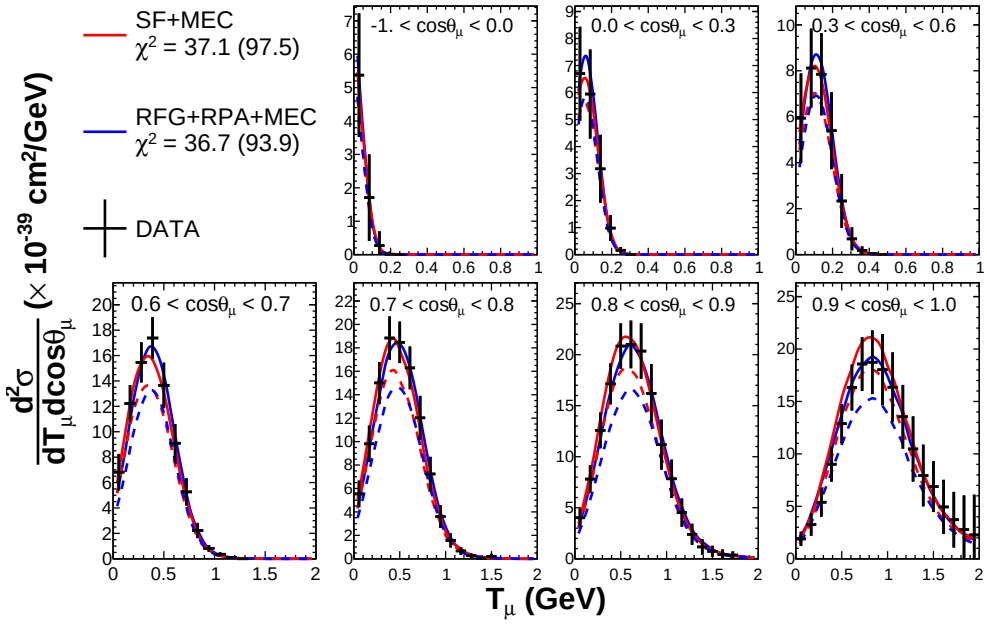

(A) Neutrino

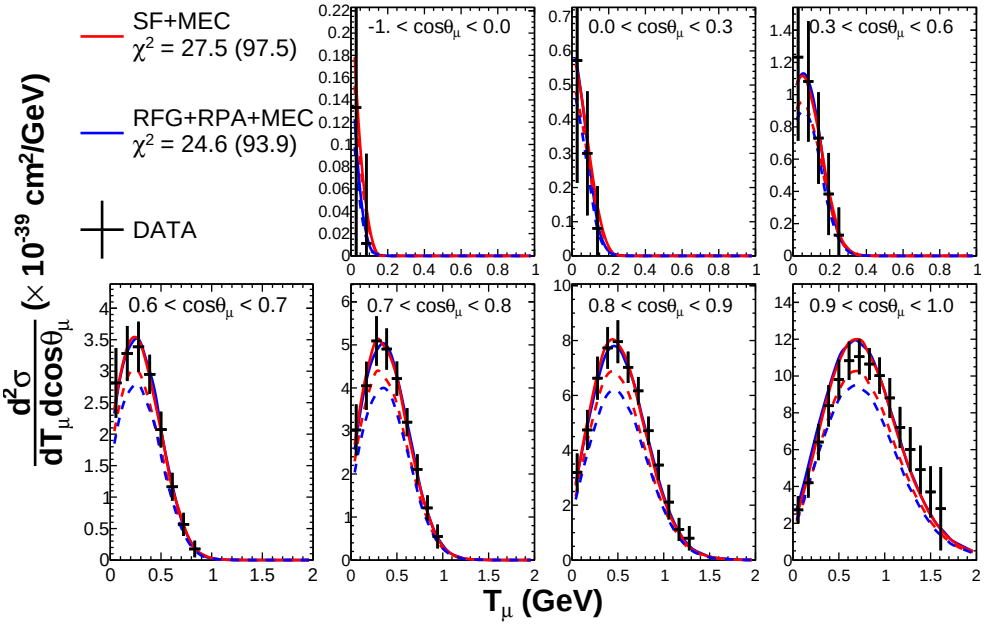

(B) Antineutrino

FIGURE A.2: Comparison of the best fit distribution from the fits to all datasets including the three-momentum transfer cut, detailed in Table A.1, with the MiniBooNE double-differential datasets used in the fit. The χ^2 values in the legend are the contribution from each dataset at the best fit point, and the total χ^2_{min} for the combined fit. Note that some of the $\cos\theta_\mu$ slices have been combined for presentational purposes. The solid lines include the MiniBooNE normalisation terms, the dashed lines do not, to highlight the large pulls on these parameters.

A.2 Parameter Goodness of Fit (PGoF) results with fixed $|\vec{q}| = 0.9$ GeV

The PGoF results shown in this section with $|\vec{q}| = 0.9$ GeV should be compared with the PGoF results using the nominal $|\vec{q}| = 1.2$ GeV in Section 5.3.4. Tables A.2, A.3 and A.4 should be compared with 5.7, 5.8 and 5.9 respectively. The PGoF test was defined and discussed in Section 5.3.3. Note that correlations between the MINERνA datasets are included for all fits where both are used, and are neglected when only one MINERνA dataset is included. This can lead to misleading PGoF results, and will lead to slightly better agreement for any tests involving an inconsistent use of correlations. In particular, this can lead to negative χ^2_{PGoF} values. However, the PGoF tests where this is an issue still indicate the approximate level of agreement between subsets of the data. It cannot mask strong disagreements, and cannot make good agreement look poor.

The PGoF tests in Section 5.3.4 were used to select between the RFG+RPA+MEC and SF+MEC models as candidates for the T2K default MC model. The $|\vec{q}| = 0.9$ GeV PGoF tests also show considerable tension between the datasets for the SF+MEC model, and considerably better agreement for both RPA models. This is expected, but it is an important consistency check to make.

Reducing the value of the three-momentum transfer cut in the fits improves the agreement for both RPA models relative to the nominal results shown in Section 5.3.4. In particular, it reduces the disagreement between MiniBooNE and MINERνA, although this is to be expected when a parameter is introduced which adds additional freedom between the two experiments. Again, the relativistic RPA model (Table A.3) is favoured over the non-relativistic RPA model (Table A.2), which supports the conclusion of the main analysis, that the relativistic RFG+RPA+MEC model should be used as the default T2K model.

Changing the value of the $|\vec{q}|$ cut does not greatly improve the SF+MEC model. MEC is still completely suppressed for most fits which combine more than a single dataset, so the differences between Tables A.4 and 5.9 are marginal.

	χ^2_{min}/DOF	SGoF (%)	χ^2_{PGoF}/DOF	PGoF (%)
All	114.0/228	100.00	21.9/6	0.13
MINERνA	29.7/13	0.53	2.0/3	57.35
MiniBooNE	65.7/212	100.00	3.2/3	36.43
ν	64.7/142	100.00	9.8/3	2.01
$\bar{\nu}$	44.6/83	99.98	9.3/3	2.51
MINERνA vs MiniBooNE	114.0/228	100.00	18.7/3	0.03
ν vs $\bar{\nu}$	114.0/228	100.00	4.7/3	19.54

TABLE A.2: Three-momentum transfer $|\vec{q}| = 0.9$ GeV PGoF results for various subsets of the data for the RFG+RPA+MEC model with the RPA shape parameter fixed at the non-relativistic limit.

	χ^2_{min}/DOF	SGoF (%)	χ^2_{PGoF}/DOF	PGoF (%)
All	93.9/228	100.00	14.3/6	2.69
MINERνA	22.8/13	4.41	2.0/3	57.48
MiniBooNE	58.6/212	100.00	1.8/3	62.50
ν	58.4/142	100.00	12.8/3	0.52
$\bar{\nu}$	37.2/83	100.00	5.1/3	16.38
MINERνA vs MiniBooNE	93.9/228	100.00	12.5/3	0.58
ν vs $\bar{\nu}$	93.9/228	100.00	-1.6/3	100.00

TABLE A.3: Three-momentum transfer $|\vec{q}| = 0.9$ GeV PGoF results for various subsets of the data for the RFG+RPA+MEC model with the RPA shape parameter fixed at the relativistic limit.

	χ^2_{min}/DOF	SGoF (%)	χ^2_{PGoF}/DOF	PGoF (%)
All	97.5/228	100.00	41.4/6	0.00
MINERνA	12.6/13	47.66	1.1/3	76.79
MiniBooNE	50.2/212	100.00	6.8/3	7.78
ν	54.8/142	100.00	25.1/3	0.00
$\bar{\nu}$	33.3/83	100.00	8.1/3	4.37
MINERνA vs MiniBooNE	97.5/228	100.00	34.6/3	0.00
ν vs $\bar{\nu}$	97.5/228	100.00	9.4/3	2.45

TABLE A.4: Three-momentum transfer $|\vec{q}| = 0.9$ GeV PGoF results for various subsets of the data for the SF+MEC model.

A.3 Comparison with main CCQE fit results

Table A.5 summarises the fit results for the relativistic RFG+RPA+MEC model where $|\vec{q}|$ is fixed at the nominal value of 1.2 GeV (the main fit results presented in Section 5.3.2), and the fit result from this section, where $|\vec{q}|$ favoured the lowest allowed fit

value of 0.9 GeV. The error inflation procedure described in Section 5.3.6 are applied to both datasets. The size of the errors is not significantly affected by allowing $|\vec{q}|$ to vary. Figure A.3 shows the correlation matrices obtained for both fits, which are extremely similar. Note that the rescaling procedure does not affect the parameter correlations.

	Fit type	χ^2/DOF	M_A (GeV)	MEC (%)	p_F (MeV)
$\|\vec{q}\| = 1.2$ GeV	Unscaled	97.84/228	1.15±0.03	27±12	223±5
	PGoF scaling		1.15±0.06	27±27	223±11
$\|\vec{q}\| = 0.9$ GeV	Unscaled	93.90/228	1.17±0.03	38±13	224±5
	PGoF scaling		1.17±0.06	38±26	224±10

TABLE A.5: The final errors for the CCQE parameters produced using the original fit with nominal $|\vec{q}| = 1.2$ GeV, compared with fit results from this appendix, where $|\vec{q}|$ was allowed to move to 0.9 GeV.

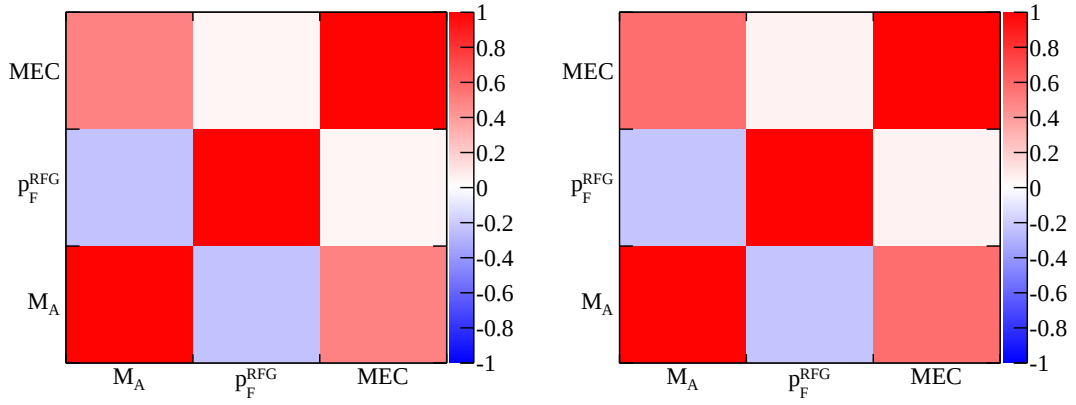

(A) $|\vec{q}| = 1.2$ GeV (B) $|\vec{q}| = 0.9$ GeV

FIGURE A.3: Correlation matrices for the CCQE parameters for the relativistic RFG+RPA+MEC model, for fits with $|\vec{q}| = 0.9$ GeV and $|\vec{q}| = 1.2$ GeV.

Appendix B

Shape-only CCQE fits

An important check of the CCQE fit results presented in Chapter 5 is to perform a shape-only fit to the MINERνA and MiniBooNE datasets and check that the best fit parameter values are not significantly different from the main CCQE fit results (which included normalisation). This is motivated by the suppression of the MiniBooNE normalisation seen in the main CCQE fit result (Section 5.3.2), and the decision to remove the CCQE normalisation parameter based on the lack of a significant pull on this parameter when included in the fits (Section 5.3.5). As well as checking that the best fit parameter values are not significantly altered by including normalisation uncertainties in the main CCQE fit, it is important to verify that the choice of the RFG+RPA+MEC model over the SF+MEC model is a robust decision, as this choice cannot be changed by T2K oscillation analyses.

The structure of this appendix closely follows that of Chapter 5: the shape-only χ^2 definition is given in Section B.1; the method for producing a shape-only covariance matrix for MINERνA dat is discussed in Section B.2; the combined fit results obtained by minimising the χ^2 are given in Section B.3; Section B.4 gives the PGoF results for the shape-only fits; finally, comparisons with the results from Chapter 5 are made in Section B.5.

B.1 Definition of the shape-only χ^2 statistic

The χ^2 statistic is given by:

$$\begin{aligned}\chi^2(\vec{\mathbf{x}}) = &\left[\sum_{k=0}^{N}\left(\frac{\nu_k^{DATA} - \lambda_\alpha \nu_k^{MC}(\vec{\mathbf{x}})}{\sigma_k}\right)^2\right] \rightarrow \text{MiniBooNE } \nu \\ &+ \left[\sum_{l=0}^{M}\left(\frac{\nu_l^{DATA} - \lambda_\beta \nu_l^{MC}(\vec{\mathbf{x}})}{\sigma_l}\right)^2\right] \rightarrow \text{MiniBooNE } \bar{\nu} \\ &+ \left[\sum_{i=0}^{16}\sum_{j=0}^{16}\left(\nu_i^{DATA} - \lambda_\gamma \nu_i^{MC}(\vec{\mathbf{x}})\right) V_{ij}^{-1} \left(\nu_j^{DATA} - \lambda_\gamma \nu_j^{MC}(\vec{\mathbf{x}})\right)\right] \rightarrow \text{MINER}\nu\text{A}\end{aligned} \tag{B.1}$$

where $\vec{\mathbf{x}}$ are the model parameters floated in the fit, V_{ij} is the shape-only extracted from the covariance matrix provided by MINERνA and λ_α, λ_β and λ_γ are parameters which scale the total integrated cross section of the Monte Carle prediction to match the total integrated cross section of the data for the MiniBooNE neutrino, MiniBooNE antineutrino and MINERνA samples respectively. Details on how the shape-only matrix is produced are given in Section B.2.

B.2 Producing the MINERνA shape-only covariance matrix

The method for extracting a shape-only covariance matrix from a covariance matrix which includes the normalisation uncertainty is taken from [78, 295]. The general covariance matrix M_{ij} is separated into three components as shown in Equation B.2, the components of which are defined in Equation B.3:

$$M_{ij} = M_{ij}^{shape} + M_{ij}^{mixed} + M_{ij}^{norm}, \tag{B.2}$$

where

$$
\begin{aligned}
M_{ij}^{shape} &= M_{ij} - \frac{N_j}{N_T}\sum_{k=1}^{n} M_{ik} - \frac{N_i}{N_T}\sum_{k=1}^{n} M_{kj} + \frac{N_i N_j}{N_T^2}\sum_{kl} M_{kl}, \\
M_{ij}^{mixed} &= \frac{N_j}{N_T}\sum_{k=1}^{n} M_{ik} + \frac{N_i}{N_T}\sum_{k=1}^{n} M_{kj} - 2\frac{N_i N_j}{N_T^2}\sum_{kl} M_{kl}, \\
M_{ij}^{norm} &= \frac{N_i N_j}{N_T^2}\sum_{kl} M_{kl}, \\
N_T &= \sum_i N_i,
\end{aligned}
\tag{B.3}
$$

where N_i denotes the entry in the ith bin, and there are n bins included in the covariance matrix.

Using this method it is possible to extract the matrix M_{ij}^{shape} from the full covariance matrix provided by MINERνA for the restricted phase-space $\theta_\mu \leq 20°$ sample, including cross-correlations between the neutrino and antineutrino samples. The original and extracted matrices are shown in Figure B.1. Shape-only matrices were provided by MINERνA for the full phase-space neutrino and antineutrino samples without correlations in their published CCQE papers [278, 279], but not for the matrices with cross-correlations given in subsequent data releases.

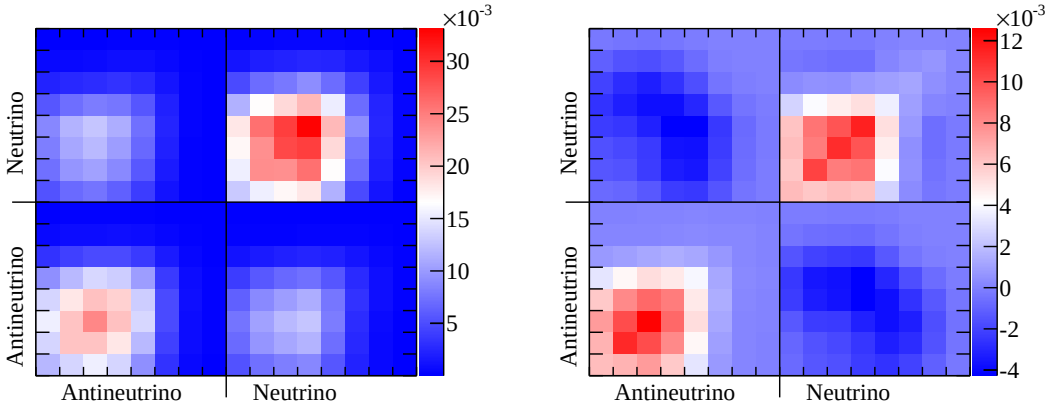

(A) Original matrix (B) Shape-only matrix

FIGURE B.1: Comparison of the matrix M_{ij} provided by MINERνA for the $\theta_\mu \leq 20°$ datasets including cross-correlations and the shape-only matrix M_{ij}^{shape} extracted from M_{ij} for the shape-only fit.

It was found that the extracted shape-only matrix had a determinant close to zero, so standard matrix inversion routines in ROOT fail. The reason for this is essentially rounding error due to the summation of many matrix elements in Equation B.3 to obtain elements of M_{ij}^{shape}, all of which are only available to a certain precision in the MINERνA

data release. The data release provides a correlation matrix to 3 decimal places, and bin errors given to 3 decimal places. Singular Value Decomposition (SVD) was used to invert M_{ij}^{shape}, but the rounding issue means that $M_{shape} \times M_{shape}^{-1} \neq I$, so we stress that there is a problem with the matrix inversion. This is shown in Figure B.2, where the inverted matrix, M_{shape}^{-1}, and $M_{shape} \times M_{shape}^{-1}$ are shown. It is clear that the latter is not an identity matrix; however, it was found that the χ^2 statistic behaved sensibly, so this imperfect matrix inversion was considered acceptable for the purposes of the cross-check described in this appendix. The problems are most noticeable in the highest Q^2_{QE} bins for both neutrino and antineutrino samples; note that the rounding error on the bin errors provided for these bins are ~5%[1].

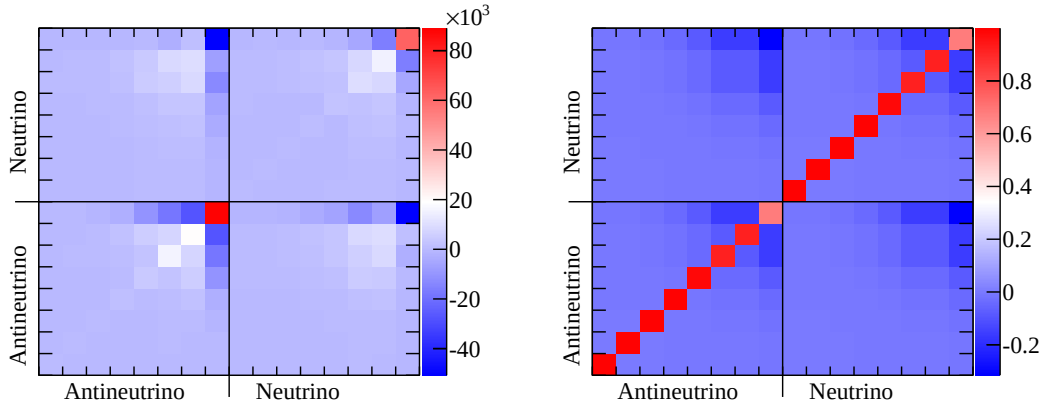

(A) M_{shape}^{-1} obtained through SVD

(B) $M_{shape} \times M_{shape}^{-1}$ (SVD)

FIGURE B.2: The attempt to invert the shape-only matrix using Singular Value Decomposition (SVD), and the multiplication of the shape-only matrix by the inversion attempt.

B.3 Shape-only fit results

The best fit results for the shape-only fits to all four datasets are summarised in Table B.1, along with the results found in Section 5.3.2 for comparison with the fits which include the normalisation uncertainties. The most important comparison is between the SF+MEC and RFG+RPA+MEC models for both fit strategies. It is clear that the shape-only fits to the SF+MEC model have a significantly higher χ^2 at the best fit point than either of the RFG+RPA+MEC models, as was the case with the fits including normalisation. This is explored further with the shape-only Parameter Goodness of Fit tests in Section B.4, but the fact that the $p_{\mathrm{F}}^{\mathrm{SF}}$ parameter is at a limit is indicative of the same tensions which affected the SF+MEC fit including normalisation.

[1] This issue, and a method for solving it, is discussed further in Reference [260].

The best fit parameter values for the RFG+RPA+MEC models are similar for the shape-only fit and the original fit, which is certainly reassuring. Small differences between the parameters would be expected simply due to the problems found inverting the MINERνA shape-only covariance matrix, so there do not appear to be any causes for concern here. The results found by the shape-only fits are covered by the final errors shown in Section 5.4 after the error inflation procedure. As in the main fits, the relativistic RPA model is favoured over the non-relativistic RPA model.

The best fit distributions are compared with data for MINERνA in Figure B.3, and for MiniBooNE in Figure B.4. In the legends of these figures, each line is given two χ^2 values, the contribution from that dataset to the χ^2_{min} in the combined shape-only fit, and the total χ^2_{min} in parentheses. Note that the relativistic RPA model is shown for comparison because this is the best fit model for fits with and without normalisation. Note also that in Figure B.3, the contributions from MINERνA are calculated for the individual datasets, ignoring cross-correlations, and making these numbers slightly misleading. Explicitly, $\chi^2_{\text{MIN total}} \neq \chi^2_{\text{MIN }\nu} + \chi^2_{\text{MIN }\bar{\nu}}$ due to cross-correlations, so the values shown in the figure must be treated with caution.

Fit type		χ^2/DOF	M_A (GeV)	MEC (%)	p_F (MeV)
Shape-only	Rel. RPA	75.39/228	1.15±0.03	41±17	224±5
	Non-rel. RPA	84.20/228	1.13±0.04	80±23	224±5
	SF+MEC	71.38/228	1.33±0.02	14±15	233±8
Including normalisation	Rel. RPA	97.84/228	1.15±0.03	27±12	223±5
	Non-rel. RPA	117.87/228	1.07±0.03	34±12	225±5
	SF+MEC	97.46/228	1.33±0.02	0 (at limit)	234±4

TABLE B.1: The best fit parameter values for the shape-only fits to all datasets are presented for each model. The results of the CCQE fits including normalisation are also shown for comparison.

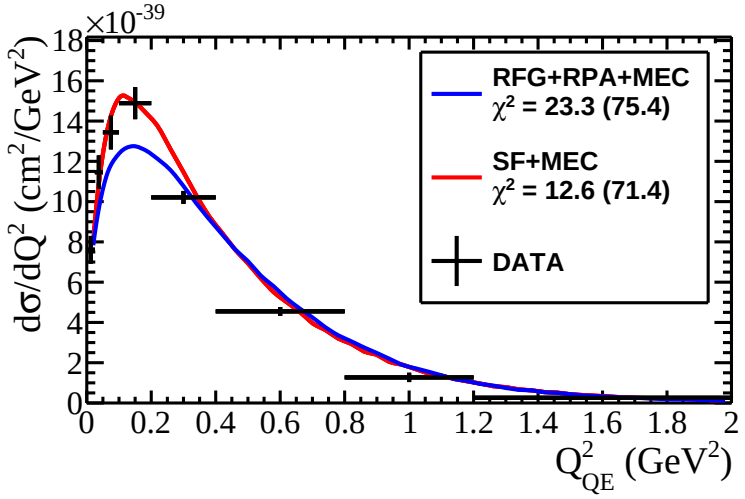

(A) Neutrino

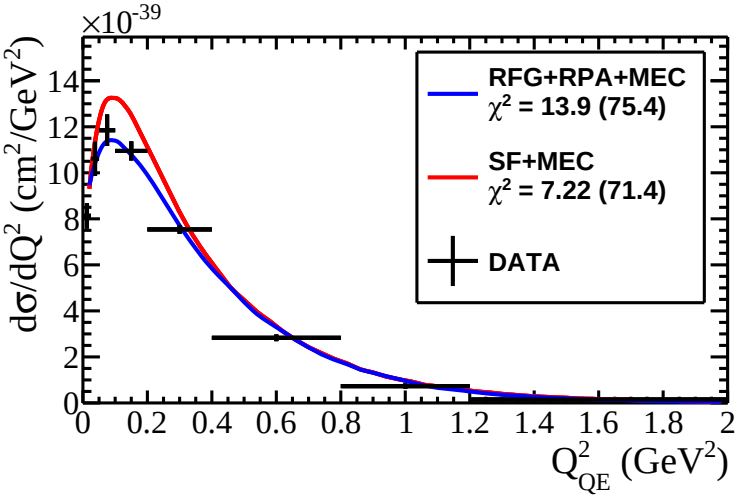

(B) Antineutrino

FIGURE B.3: Comparison of the best fit from the shape-only fits to all datasets detailed in Table B.1 with the MINERνA datasets used in the fit. The χ^2 values in the legend are the contribution from each dataset at the best fit point, and the total χ^2_{min} for the combined fit. Note that the integrated MC is scaled to match the integrated data in the shape-only fit.

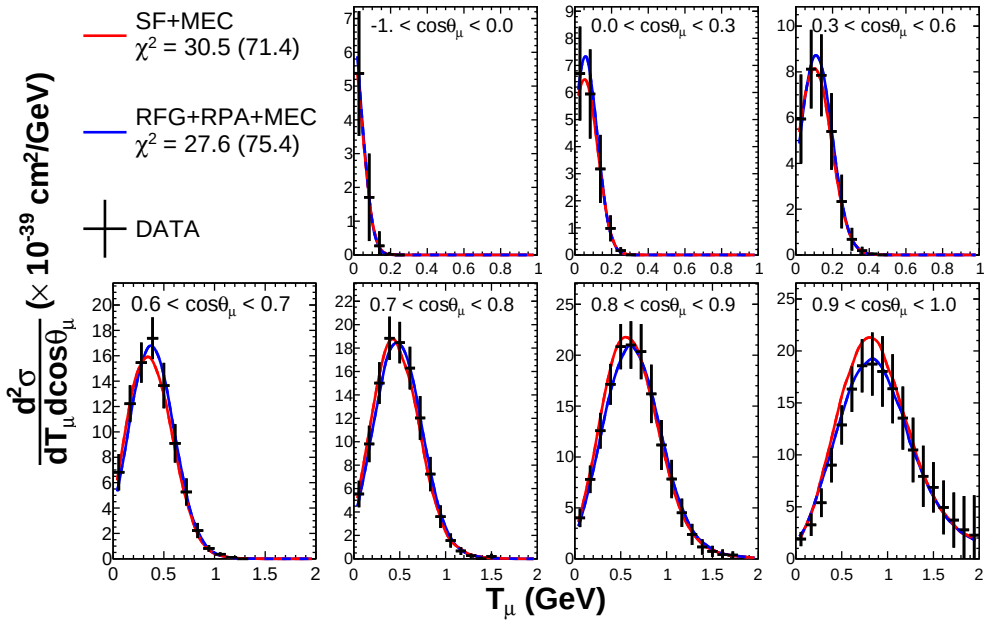

(A) Neutrino

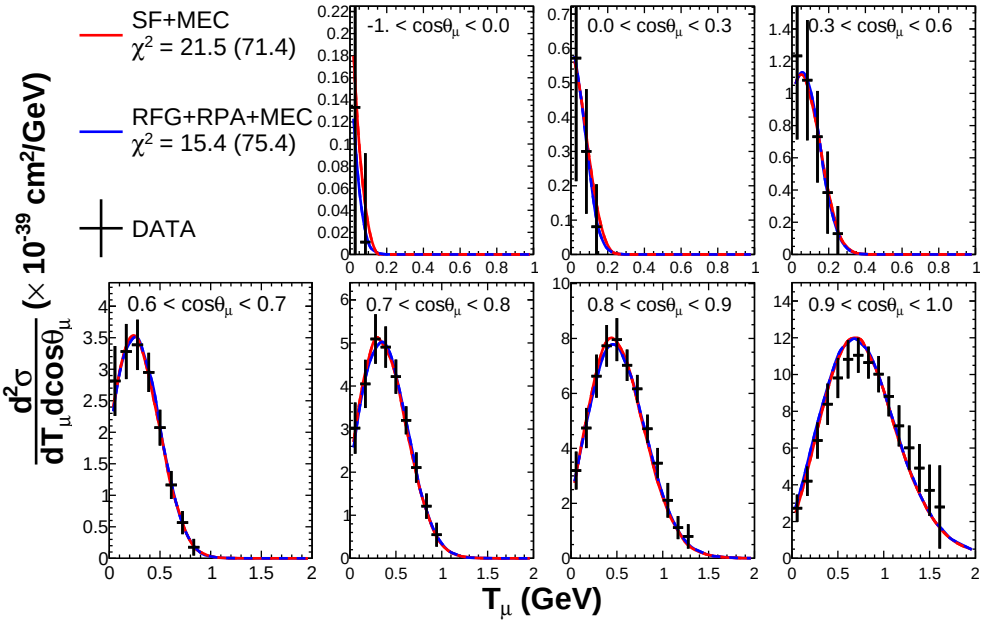

(B) Antineutrino

FIGURE B.4: Comparison of the best fit from the shape-only fits to all datasets detailed in Table B.1 with the MiniBooNE double-differential datasets used in the fit. The χ^2 values in the legend are the contribution from each dataset at the best fit point, and the total χ^2_{min} for the combined fit. Note that some of the $\cos\theta_\mu$ slices have been combined for presentational purposes. The integrated MC is scaled to match the integrated data in the shape-only fit.

B.4 Shape-only Parameter Goodness of Fit (PGoF) results

The shape-only PGoF results shown in this section should be compared with the PGoF results using the full error information in Section 5.3.4. Tables B.2, B.3 and B.4 should be compared with Tables 5.7, 5.8 and 5.9 respectively. The PGoF test was defined and discussed in Section 5.3.3. Note that correlations between the MINERνA datasets are included for all fits where both are used, and are neglected when only one MINERνA dataset is included. This can lead to misleading PGoF results, and will lead to slightly better agreement for any tests involving an inconsistent use of correlations. In particular, this can lead to negative χ^2_{PGoF} values. However, the PGoF tests where this is an issue still indicate the approximate level of agreement between subsets of the data. It cannot mask strong disagreements, and cannot make good agreement look poor.

The PGoF tests were used to select between the SF+MEC and RFG+RPA+MEC models as candidates for the T2K default MC model. The shape-only PGoF tests show considerable tension between the datasets for the SF+MEC model, and considerably better agreement for both RPA models. This is a key result of the shape-only fits because it verifies the choice of default model, which cannot be corrected by the ND280 fit if it is contradicted by ND280 data.

Both RFG+RPA+MEC models show similar trends, though the tension decreases slightly in the shape-only fits. As is the case for fits including normalisation, the tension for fits using the relativistic RPA model (Table B.3) seems to be less than in fits using the non-relativistic RPA model (Table B.2). The majority of the tension in both fits comes from MINERνA–MiniBooNE differences rather than neutrino–antineutrino differences. This supports the conclusion that we do not need to use different cross section parameters for neutrino and antineutrino interactions. Note that the greater tension in the main fit results caused the errors to be inflated in the final NIWG inputs to T2K oscillation analyses (Section 5.4), so the errors produced with the original fits will be more conservative than errors produced using shape-only fits.

	χ^2_{min}/DOF	SGoF (%)	χ^2_{PGoF}/DOF	PGoF (%)
All	84.2/228	100.00	9.0/6	17.34
MINERνA	32.0/13	0.24	3.9/3	26.90
MiniBooNE	44.8/212	100.00	1.5/3	67.66
ν	50.5/142	100.00	7.2/3	6.71
$\bar{\nu}$	30.7/83	100.00	2.7/3	43.29
MINERνA vs MiniBooNE	84.2/228	100.00	7.5/3	5.81
ν vs $\bar{\nu}$	84.2/228	100.00	3.0/3	38.62

TABLE B.2: Shape-only PGoF results for various subsets of the data for the RFG+RPA+MEC model with the RPA shape parameter fixed at the non-relativistic limit.

	χ^2_{min}/DOF	SGoF (%)	χ^2_{PGoF}/DOF	PGoF (%)
All	75.4/228	100.00	10.8/6	9.48
MINERνA	27.5/13	1.05	6.0/3	11.28
MiniBooNE	41.2/212	100.00	4.1/3	24.60
ν	49.0/142	100.00	14.6/3	0.22
$\bar{\nu}$	27.6/83	100.00	3.4/3	33.85
MINERνA vs MiniBooNE	75.4/228	100.00	6.7/3	8.39
ν vs $\bar{\nu}$	75.4/228	100.00	-1.2/3	100.00

TABLE B.3: Shape-only PGoF results for various subsets of the data for the RFG+RPA+MEC model with the RPA shape parameter fixed at the relativistic limit.

	χ^2_{min}/DOF	SGoF (%)	χ^2_{PGoF}/DOF	PGoF (%)
All	71.4/228	100.00	26.1/6	0.02
MINERνA	8.8/13	79.06	1.4/3	71.23
MiniBooNE	38.9/212	100.00	2.4/3	49.02
ν	37.5/142	100.00	10.1/3	1.74
$\bar{\nu}$	19.9/83	100.00	3.3/3	34.12
MINERνA vs MiniBooNE	71.4/228	100.00	23.7/3	0.00
ν vs $\bar{\nu}$	71.4/228	100.00	14.0/3	0.29

TABLE B.4: Shape-only PGoF results for various subsets of the data for the SF+MEC model.

B.5 Comparison with main CCQE fit results

Figure B.5 compares the correlation matrices produced by the shape-only and full CCQE fits using the relativistic RFG+RPA+MEC model. The best fit parameter values and errors for both fits are shown in Table B.5. Although there are slight differences, most

notably with the MEC normalisation parameter, the scaled errors from the fit with normalisation included more than cover these differences.

The shape-only fit supports the selection of a RFG+RPA+MEC model over the SF+MEC model. Additionally, the similarity of the best fit parameter values indicates that there are no significant biases resulting arising from the normalisation errors in the original fit. The errors produced by the fit including normalisation errors are more conservative than the errors from the shape-only fit, and cover the difference between the two fit strategies.

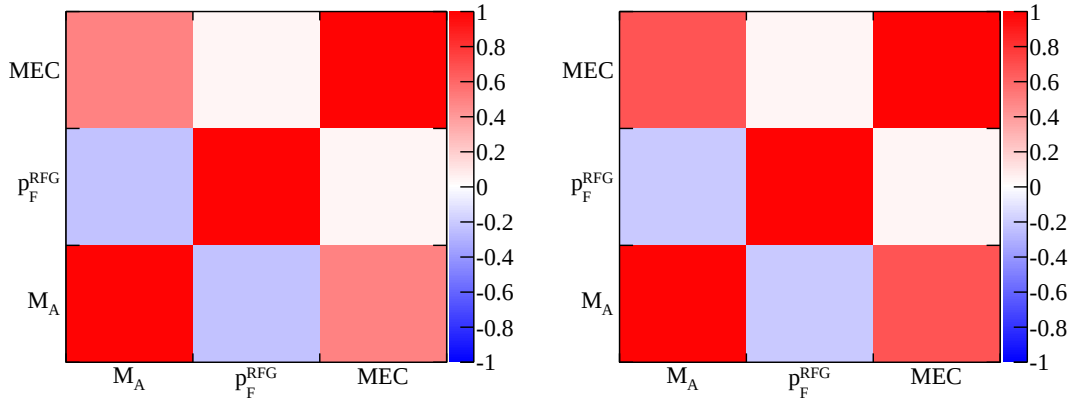

(A) Including normalisation (B) Shape-only

FIGURE B.5: Correlation matrices for the CCQE parameters for the non-relativistic RFG+RPA+MEC model, for the fit including normalisation uncertainties and the shape-only fit.

	Fit type	χ^2/DOF	M_A (GeV)	MEC (%)	p_F (MeV)
Including normalisation	Unscaled	97.84/228	1.15±0.03	27±12	223±5
	PGoF scaling		1.15±0.06	27±27	223±11
Shape-only	Unscaled	75.39/228	1.15±0.03	41±17	224±5

TABLE B.5: The final errors for the CCQE parameters produced using the original fit to the relativistic RFG+RPA+MEC model, compared with the shape-only fit results.

Appendix C

Additional CCQE fit results

This appendix gives additional CCQE fit results which inform or supplement the main fit results presented in Chapter 5. Fits to subsamples of the data are shown in Section C.1. These results are used to calculate the Parameter Goodness of Fit statistic shown in Section 5.3.4. Fits using various subsets of the parameters used in the main fits are presented in Section C.2. These results are not used to inform the main CCQE results, but give additional information about the importance of each parameter for each dataset, which may be of interest to the reader.

C.1 Fits to subsamples of the CCQE data

The combined fit results presented in Section 5.3.2 and reproduced in Table C.1 are for fits to all four datasets, MINERνA and MiniBooNE, neutrino and antineutrino. The Parameter Goodness of Fit (PGoF) test described in Section 5.3.3 involves fitting to all possible combinations of datasets, and comparing the best fit values for fits to subsamples of the data. Fits to various combinations of datasets were performed to produce the PGoF results presented in Section 5.3.4, the best fit χ^2 and parameter values for which are summarised in this appendix. Note that the MiniBooNE datasets used in all aspects of the CCQE fits were the double-differential datasets. For completeness, fits to the MiniBooNE single-differential cross section results are also shown in this appendix, but these were not used in any aspect of the fits used to produce the NIWG CCQE uncertainties, the main result of Chapter 5.

- Fit results for the individual datasets used in the CCQE fits are shown: MINERνA neutrino in Table C.2, MINERνA antineutrino in Table C.3, MiniBooNE neutrino in Table C.4 and MiniBooNE antineutrino in Table C.5.

Fit type	χ^2/DOF	M_A (GeV)	MEC (%)	p_F (MeV)	λ_ν^{MB}	$\lambda_{\bar{\nu}}^{MB}$
Rel. RPA	97.84/228	1.15±0.03	27±12	223±5	0.79±0.03	0.78±0.03
Non-rel. RPA	117.87/228	1.07±0.03	34±12	225±5	0.80±0.04	0.75±0.03
SF+MEC	97.46/228	1.33±0.02	0 (at limit)	234±4	0.81±0.02	0.86±0.02

TABLE C.1: Best fit χ^2 and parameter values for fits to all four datasets used in the CCQE fits. MINERνA and MiniBooNE (double-differential) neutrino and antineutrino datasets are included.

- Fit results for each neutrino species are shown: for the neutrino datasets (MINERνA and MiniBooNE) in Table C.6, and the antineutrino datasets (MINERνA and MiniBooNE) in table C.7.
- Fit results for each experiment are shown: for MINERνA (ν_μ and $\overline{\nu}_\mu$) in Table C.8, and for MiniBooNE (ν_μ and $\overline{\nu}_\mu$) in Table C.9.
- Fits to the MiniBooNE single-differential distributions are shown: for the neutrino dataset in Table C.10 and for the antineutrino dataset in Table C.11.

Care should be taken when interpreting these results. Individual datasets can tend toward strange combinations of parameter values because there is a lot of flexibility in the models used in the fits. In particular, fitting to individual MINERνA datasets can lead to strange results because there are relatively few datapoints to constrain a model with a number of free parameters.

There is a well documented problem which can occur when fitting strongly correlated datasets using a covariance matrix [296], which is known as Peelle's Pertinent Puzzle (PPP) [297], the hallmark of which is a best fit distribution below the data. Essentially, this phenomena arises because suppressing the prediction suppresses the relative size of the shape errors, and produces a better fit despite the penalty from the suppressed normalisation. There are some indications of PPP in the individual fits to MINERνA datasets which affects the best fit distributions in Figures C.1 and C.2, although the effect is not seen in the combined fit results including MiniBooNE. A method to remove this problem from the MINERνA dataset is presented in Reference [260], and this will be included in later iterations of the CCQE fits for T2K, but because of the lengthy internal review process, this update has not been included in the results shown in this work. The slight indications of a PPP effect are not a major concern for the CCQE fits presented in Chapter 5. Although it might reduce the χ^2 for, and slightly distort, the MINERνA only fit results, it appears to have no effect on the combined fit. The only effect will be a slight increase in the PGoF test statistics found in Section 5.3.4, and a slightly larger scaling factor applied to the errors from MINUIT to produce the CCQE inputs for T2K analyses (summarised in Section 5.4). Given the major known

issues with the MiniBooNE dataset, small PPP effects in the MINERνA-only fits can be considered a minor issue for the CCQE fits.

Fitting to different combinations of datasets changes the best fit distributions for each dataset. This is shown in Figures C.1 (MINERνA neutrino), C.2 (MINERνA antineutrino), C.3 (MiniBooNE neutrino) and C.4 (MiniBooNE antineutrino). For each dataset there are four distributions which correspond to: a fit to that dataset alone; a fit to both neutrino and antineutrino datasets from that experiment; a fit to the datasets from both experiments corresponding to that flavour; and a fit to all datasets.

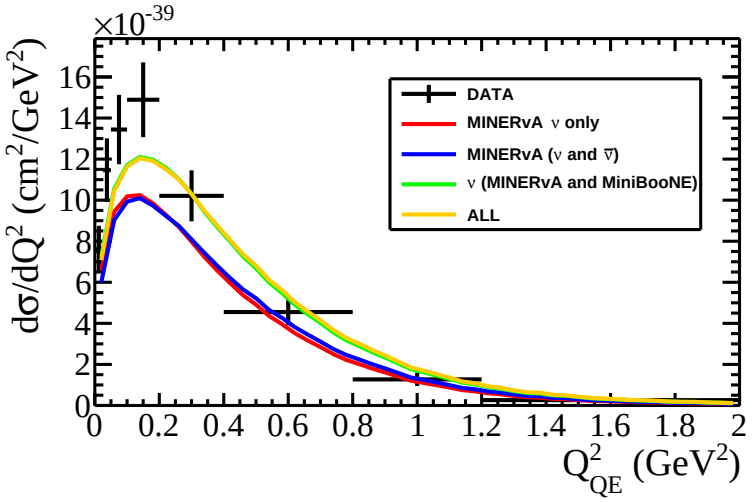

(A) MINERνA ν RFG+RPA+MEC

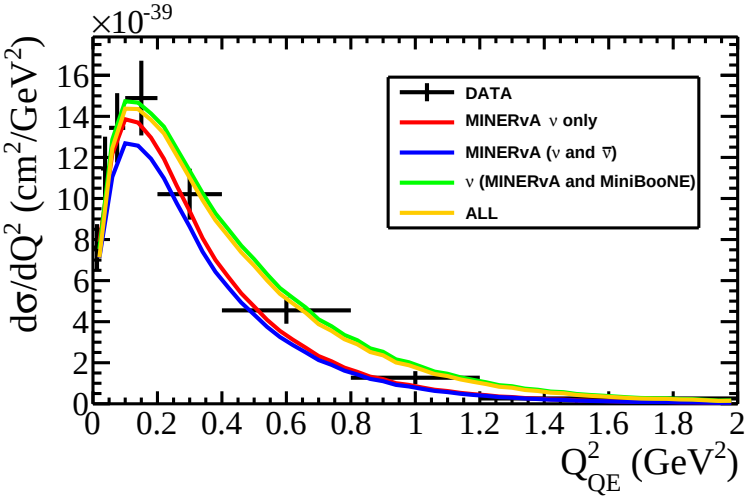

(B) MINERνA ν SF+MEC

FIGURE C.1: Best fit distributions for the MINERνA neutrino dataset which correspond to the best fit parameters found when fitting to different subsets of the data for both SF+MEC and non-relativistic RFG+RPA+MEC models. The parameter values and χ^2 values can be found in Table C.2 for the MINERνA ν-only fits, Table C.8 for the MINERνA ν and $\bar{\nu}$ fits, Table C.6 for the MINERνA and MiniBooNE ν fits, and Table C.1 for the fits to all datasets.

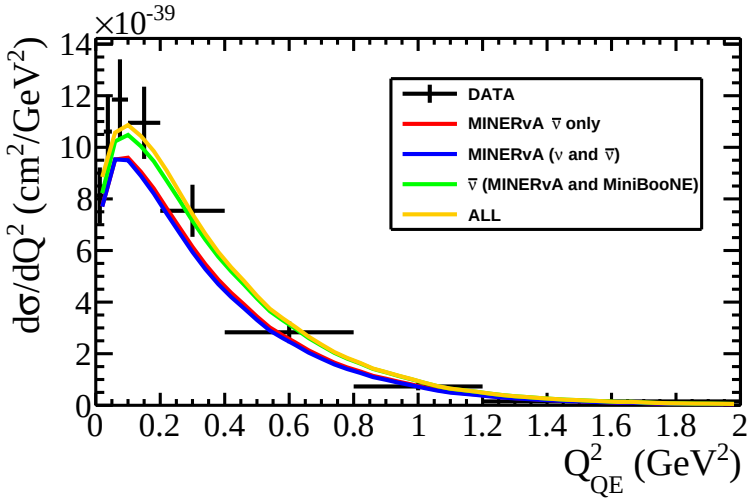

(A) MINERνA $\bar{\nu}$ RFG+RPA+MEC

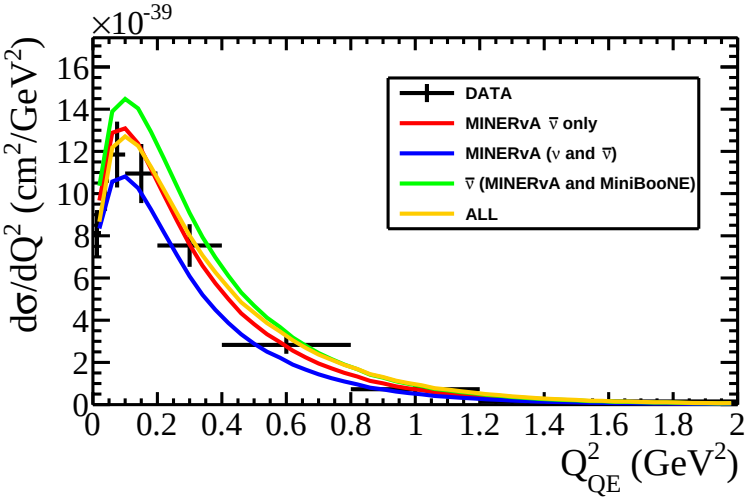

(B) MINERνA $\bar{\nu}$ SF+MEC

FIGURE C.2: Best fit distributions for the MINERνA neutrino dataset which correspond to the best fit parameters found when fitting to different subsets of the data for both SF+MEC and non-relativistic RFG+RPA+MEC models. The parameter values and χ^2 values can be found in Table C.3 for the MINERνA $\bar{\nu}$-only fits, Table C.8 for the MINERνA ν and $\bar{\nu}$ fits, Table C.7 for the MINERνA and MiniBooNE $\bar{\nu}$ fits, and Table C.1 for the fits to all datasets.

Fit type	χ^2/DOF	M_A (GeV)	MEC (%)	p_F (MeV)	λ_ν^{MB}	$\lambda_{\bar{\nu}}^{MB}$
SF	7/5	0.79±0.09	82±20	289±7	N/A	N/A
RPA (rel.)	14/5	0.87±0.09	20±20	223±21	N/A	N/A
RPA (non-rel.)	16/5	0.81±0.07	26±14	235±18	N/A	N/A

TABLE C.2: Best fit χ^2 and parameter values for fits to the MINERνA neutrino dataset.

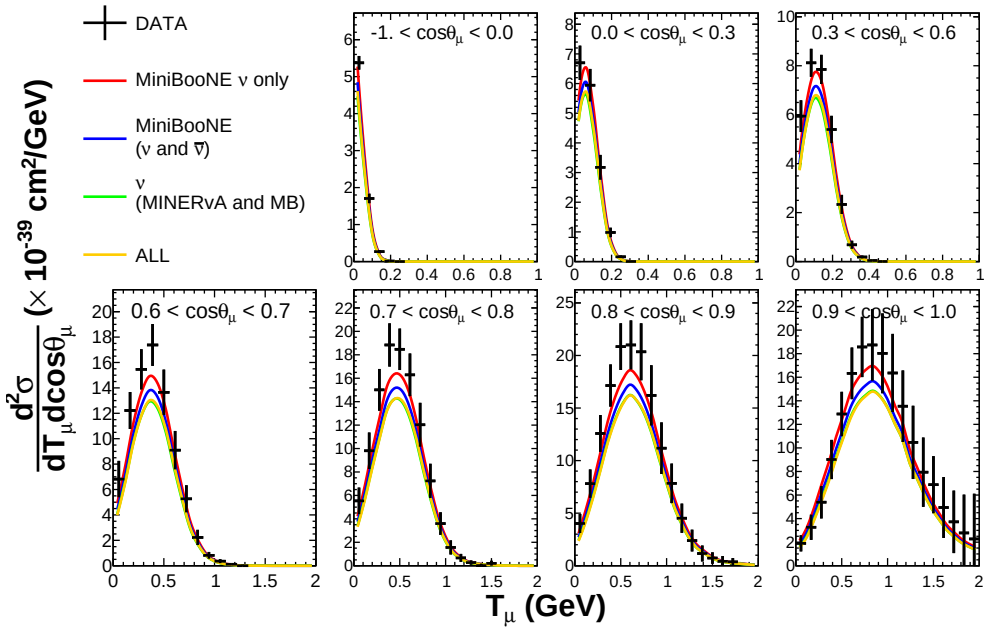

(A) MiniBooNE ν RFG+RPA+MEC

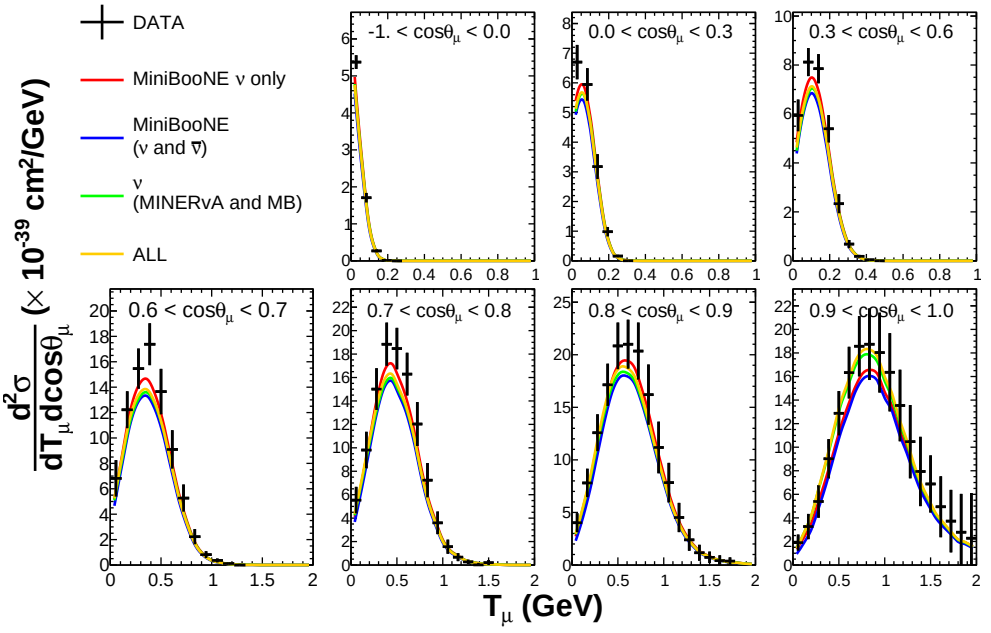

(B) MiniBooNE ν SF+MEC

FIGURE C.3: Best fit distributions for the MiniBooNE neutrino double-differential dataset which correspond to the best fit parameters found when fitting to different subsets of the data for both SF+MEC and non-relativistic RFG+RPA+MEC models. The parameter values and χ^2 values can be found in Table C.4 for the MiniBooNE ν-only fits, Table C.9 for the MiniBooNE ν and $\bar{\nu}$ fits, Table C.6 for the MINERνA and MiniBooNE ν fits, and Table C.1 for the fits to all datasets.

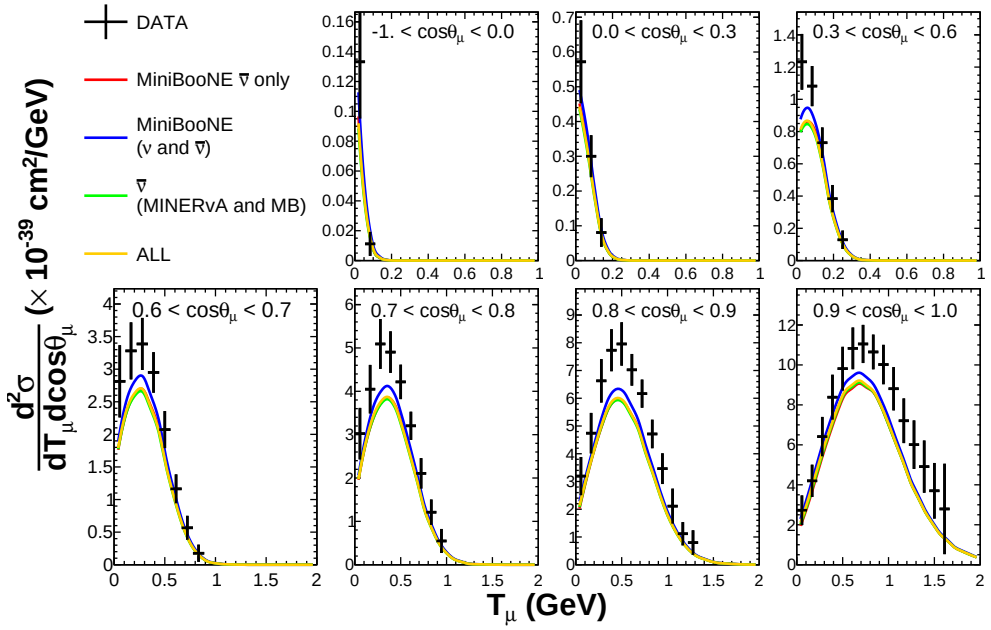

(A) MiniBooNE $\bar{\nu}$ RFG+RPA+MEC

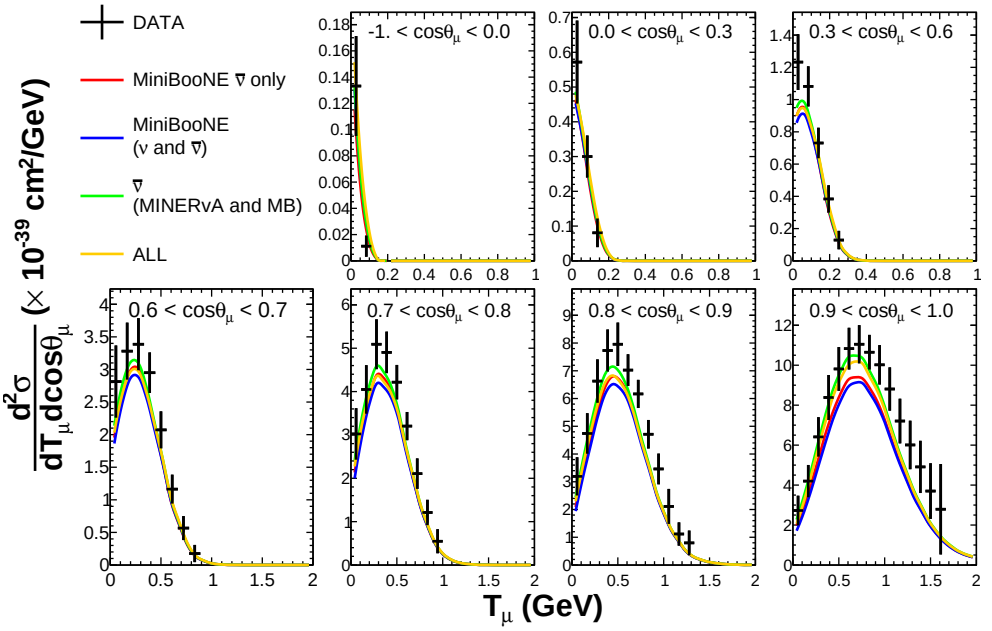

(B) MiniBooNE $\bar{\nu}$ SF+MEC

FIGURE C.4: Best fit distributions for the MiniBooNE antineutrino double-differential dataset which correspond to the best fit parameters found when fitting to different subsets of the data for both SF+MEC and non-relativistic RFG+RPA+MEC models. The parameter values and χ^2 values can be found in Table C.5 for the MiniBooNE $\bar{\nu}$-only fits, Table C.9 for the MiniBooNE ν and $\bar{\nu}$ fits, Table C.7 for the MINERνA and MiniBooNE $\bar{\nu}$ fits, and Table C.1 for the fits to all datasets.

Fit type	χ^2/DOF	M_A (GeV)	MEC (%)	p_F (MeV)	λ_ν^{MB}	$\lambda_{\bar{\nu}}^{MB}$
SF	4/5	1.13±0.10	31±12	237±9	N/A	N/A
RPA (rel.)	9/5	1.00±0.07	2±55	216±8	N/A	N/A
RPA (non-rel.)	13/5	0.96±0.06	0 (at limit)	217±2	N/A	N/A

TABLE C.3: Best fit χ^2 and parameter values for fits to the MINERνA antineutrino dataset.

Fit type	χ^2/DOF	M_A (GeV)	MEC (%)	p_F (MeV)	λ_ν^{MB}	$\lambda_{\bar{\nu}}^{MB}$
SF	22/134	1.40±0.06	56±49	298±35	88±6	N/A
RPA (rel.)	33/134	1.24±0.01	77±16	228±0	90±2	N/A
RPA (non-rel.)	40/134	1.12±0.05	80±28	233±0	88±7	N/A

TABLE C.4: Best fit χ^2 and parameter values for fits to the MiniBooNE neutrino double-differential dataset.

Fit type	χ^2/DOF	M_A (GeV)	MEC (%)	p_F (MeV)	λ_ν^{MB}	$\lambda_{\bar{\nu}}^{MB}$
SF	21/75	1.24±0.04	73±57	298±9	N/A	83±7
RPA (rel.)	24/75	1.18±0.03	0 (at limit)	215±11	N/A	78±3
RPA (non-rel.)	22/75	1.19±0.04	18±50	214±22	N/A	81±6

TABLE C.5: Best fit χ^2 and parameter values for fits to the MiniBooNE antineutrino double-differential dataset.

Fit type	χ^2/DOF	M_A (GeV)	MEC (%)	p_F (MeV)	λ_ν^{MB}	$\lambda_{\bar{\nu}}^{MB}$
SF	55/142	1.39±0.01	0 (at limit)	228±4	85±1	N/A
RPA (rel.)	63/142	1.12±0.04	34±15	229±7	76±5	N/A
RPA (non-rel.)	69/142	1.00±0.04	33±15	233±7	73±5	N/A

TABLE C.6: Best fit χ^2 and parameter values for fits to the MINERνA and MiniBooNE neutrino datasets.

Fit type	χ^2/DOF	M_A (GeV)	MEC (%)	p_F (MeV)	λ_ν^{MB}	$\lambda_{\bar{\nu}}^{MB}$
SF	34/83	1.27±0.03	70±27	256±11	N/A	88±3
RPA (rel.)	39/83	1.15±0.03	12±20	217±0	N/A	77±3
RPA (non-rel.)	46/83	1.12±0.07	12±34	221±0	N/A	75±8

TABLE C.7: Best fit χ^2 and parameter values for fits to the MINERνA and MiniBooNE antineutrino datasets.

Fit type	χ^2/DOF	M_A (GeV)	MEC (%)	p_F (MeV)	λ_ν^{MB}	$\lambda_{\bar{\nu}}^{MB}$
SF	13/13	0.73±0.08	76±17	298±10	N/A	N/A
RPA (rel.)	23/13	0.96±0.06	1±30	213±7	N/A	N/A
RPA (non-rel.)	30/13	0.91±0.05	1±84	216±6	N/A	N/A

TABLE C.8: Best fit χ^2 and parameter values for fits to the MINERνA neutrino and antineutrino datasets.

Fit type	χ^2/DOF	M_A (GeV)	MEC (%)	p_F (MeV)	λ_ν^{MB}	$\lambda_{\bar{\nu}}^{MB}$
SF	50/212	1.30±0.03	0 (at limit)	273±12	77±2	80±3
RPA (rel.)	59/212	1.19±0.03	57±18	229±0	85±4	83±4
RPA (non-rel.)	66/212	1.17±0.03	93±21	229±7	94±5	86±4

TABLE C.9: Best fit χ^2 and parameter values for fits to the MiniBooNE neutrino and antineutrino datasets.

Fit type	χ^2/DOF	M_A (GeV)	MEC (%)	p_F (MeV)	λ_ν^{MB}	$\lambda_{\bar{\nu}}^{MB}$
SF	4/14	1.55±0.08	126±27	334±25	99±5	N/A
RPA (rel.)	17/14	1.15±0.09	93±43	273±39	79±8	N/A
RPA (non-rel.)	21/14	1.04±0.08	101±10	286±41	75±6	N/A

TABLE C.10: Best fit χ^2 and parameter values for fits to the MiniBooNE neutrino single-differential dataset. Note that this dataset is not used in any of the CCQE fits used to produce the NIWG CCQE parametrisation, it is only included here for completeness.

Fit type	χ^2/DOF	M_A (GeV)	MEC (%)	p_F (MeV)	λ_ν^{MB}	$\lambda_{\bar{\nu}}^{MB}$
SF	4/14	1.29±0.07	105±74	296±29	N/A	87±7
RPA (rel.)	12/14	1.21±0.04	0 (at limit)	212±10	N/A	76±3
RPA (non-rel.)	12/14	1.20±0.04	0 (at limit)	211±8	N/A	76±3

TABLE C.11: Best fit χ^2 and parameter values for fits to the MiniBooNE antineutrino single-differential dataset. Note that this dataset is not used in any of the CCQE fits used to produce the NIWG CCQE parametrisation, it is only included here for completeness.

C.2 Limited parameter fits to individual CCQE datasets

A number of fit parameters are included in the CCQE fits presented in Chapter 5. It is interesting to look at the effect that releasing different combinations of parameters have on the best fit distributions, parameter values and χ^2 for individual datasets. The three parameters constrained by the CCQE fits MEC normalisation, p_{F} and M_{A} are added to the fit sequentially, and the best fit χ^2 and parameter values are shown: for the SF+MEC model in Tables C.12 (MINERνA ν), C.13 (MINERνA $\bar{\nu}$), C.14 (MiniBooNE single-differential ν), C.16 (MiniBooNE double-differential ν), C.15 (MiniBooNE single-differential $\bar{\nu}$) and C.17 (MiniBooNE double-differential $\bar{\nu}$); and for the relativistic RFG+RPA+MEC model in Tables C.18 (MINERνA ν), C.19 (MINERνA $\bar{\nu}$), C.20 (MiniBooNE single-differential ν), C.22 (MiniBooNE double-differential ν), C.21 (MiniBooNE single-differential $\bar{\nu}$) and C.23 (MiniBooNE double-differential $\bar{\nu}$). The best fit parameter distributions shown as a ratio of the MC prediction over the published data are shown for the SF+MEC model in Figure C.5 (C.6) for MINERνA (MiniBooNE), and for the relativistic RFG+RPA+MEC model in Figure C.7 (C.8) for MINERνA (MiniBooNE). Note that the MiniBooNE single-differential results are used for the ratio plots for ease of presentation and interpretation.

Fit type	χ^2/DOF	M_{A} (GeV)	MEC (%)	p_{F} (MeV)
All fixed	65.11/8	1.01 (fixed)	100 (fixed)	209 (fixed)
Free MEC	19.05/7	1.01 (fixed)	0 (at limit)	209 (fixed)
Free MEC+p_{F}	8.43/6	1.01 (fixed)	62±20	257±6
All free	7.33/5	0.79±0.09	82±20	289±7

TABLE C.12: Table of best fit parameter values for various combinations of free parameters for the MINERνA neutrino dataset and the SF+MEC model.

Fit type	χ^2/DOF	M_{A} (GeV)	MEC (%)	p_{F} (MeV)
All fixed	60.61/8	1.01 (fixed)	100 (fixed)	209 (fixed)
Free MEC	15.04/7	1.01 (fixed)	0 (at limit)	209 (fixed)
Free MEC+p_{F}	4.92/6	1.01 (fixed)	48±39	253±19
All free	4.27/5	1.13±0.10	31±12	237±9

TABLE C.13: Table of best fit parameter values for various combinations of free parameters for the MINERνA antineutrino dataset and the SF+MEC model.

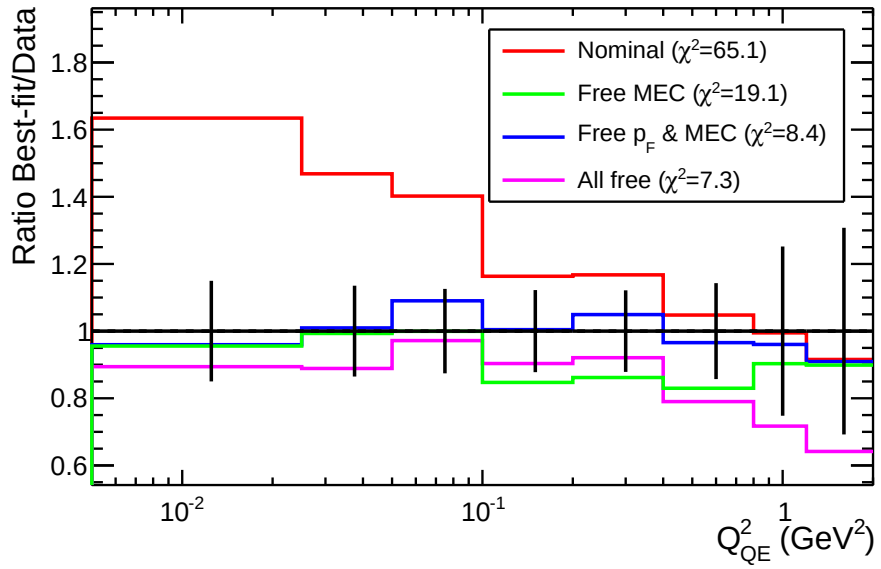

(A) MINERνA neutrino

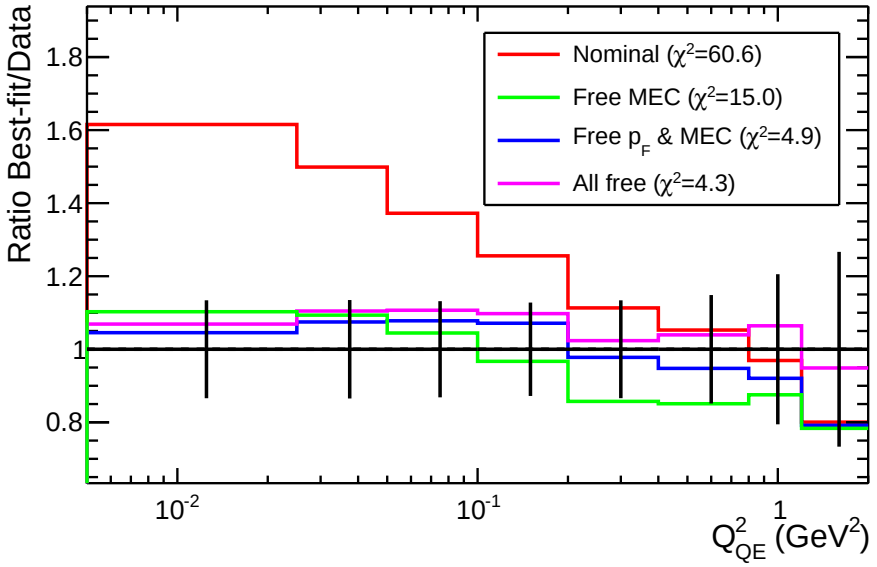

(B) MINERνA antineutrino

FIGURE C.5: Ratios of best fit distributions over data for the MINERνA neutrino and antineutrino datasets using the SF+MEC with various combinations of free parameters. The parameter values corresponding to these distributions can be found in Table C.12 (C.13) for the neutrino (antineutrino) dataset.

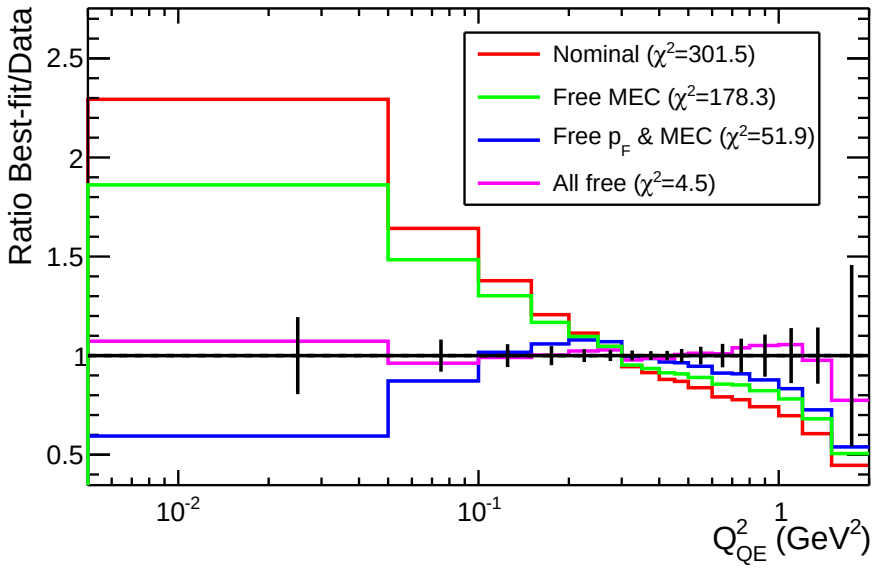

(A) MiniBooNE neutrino

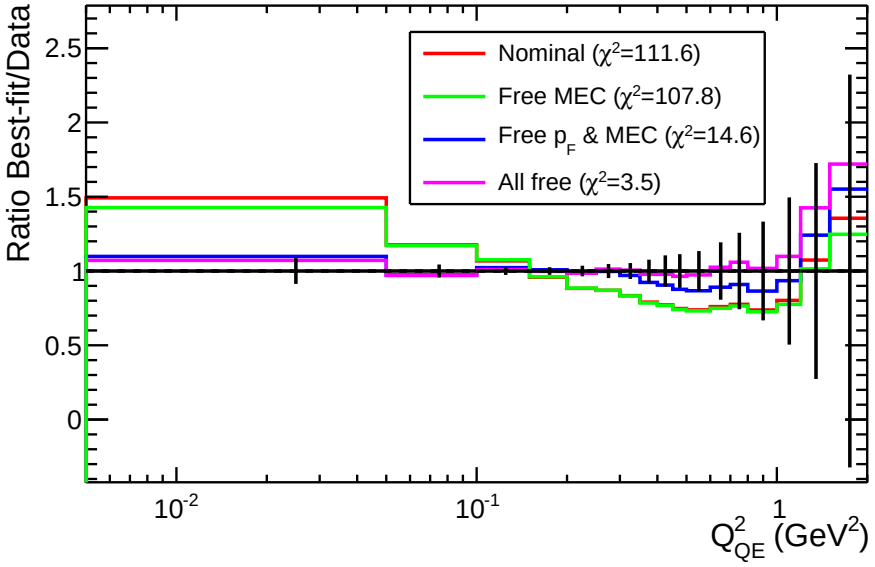

(B) MiniBooNE antineutrino

FIGURE C.6: Ratios of best fit distributions over data for the MiniBooNE neutrino and antineutrino single-differential datasets using the SF+MEC with various combinations of free parameters. The parameter values corresponding to these distributions can be found in Table C.14 (C.15) for the neutrino (antineutrino) dataset. Parameter values for the MiniBooNE neutrino and antineutrino double-differential distributions can be found in Table C.16 (C.17) for the neutrino (antineutrino) dataset.

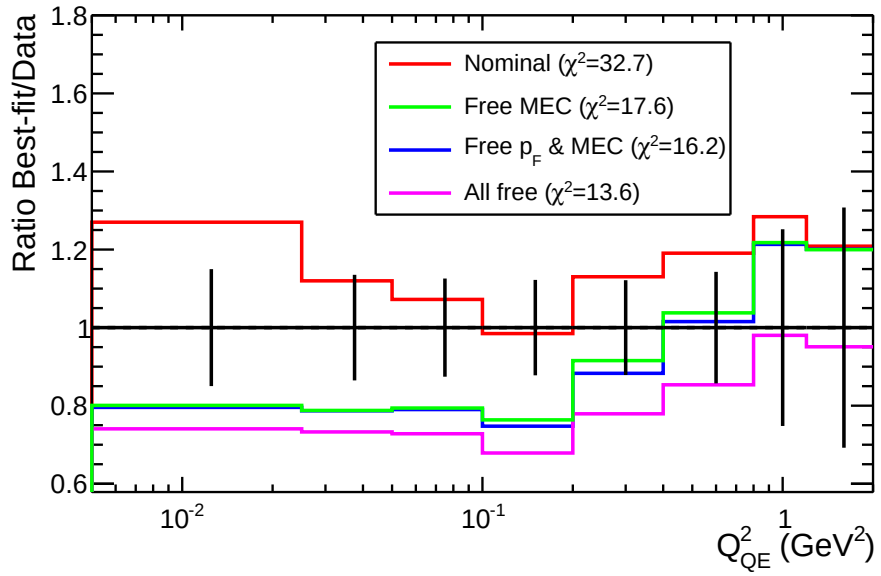

(A) MINERνA neutrino

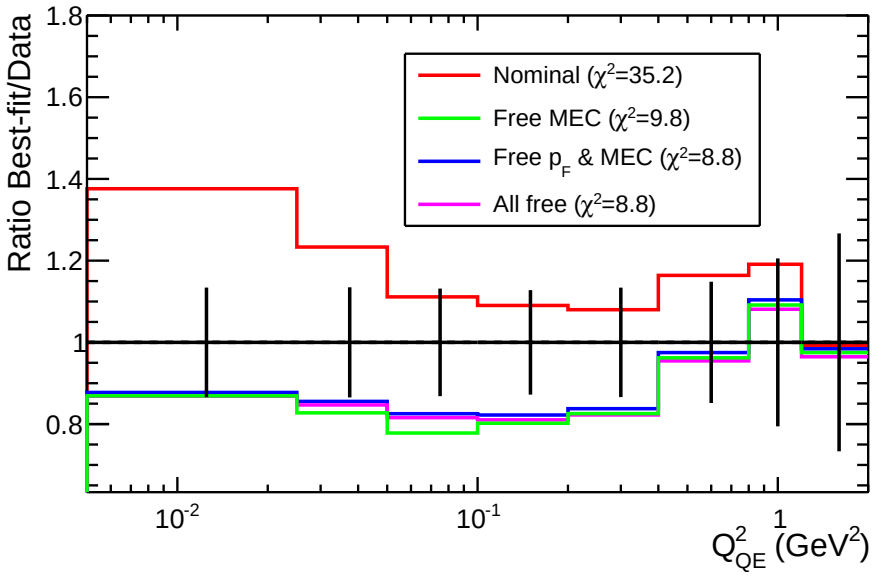

(B) MINERνA antineutrino

FIGURE C.7: Ratios of best fit distributions over data for the MINERνA neutrino and antineutrino datasets using the relativistic RFG+RPA+MEC with various combinations of free parameters. The parameter values corresponding to these distributions can be found in Table C.18 (C.19) for the neutrino (antineutrino) dataset.

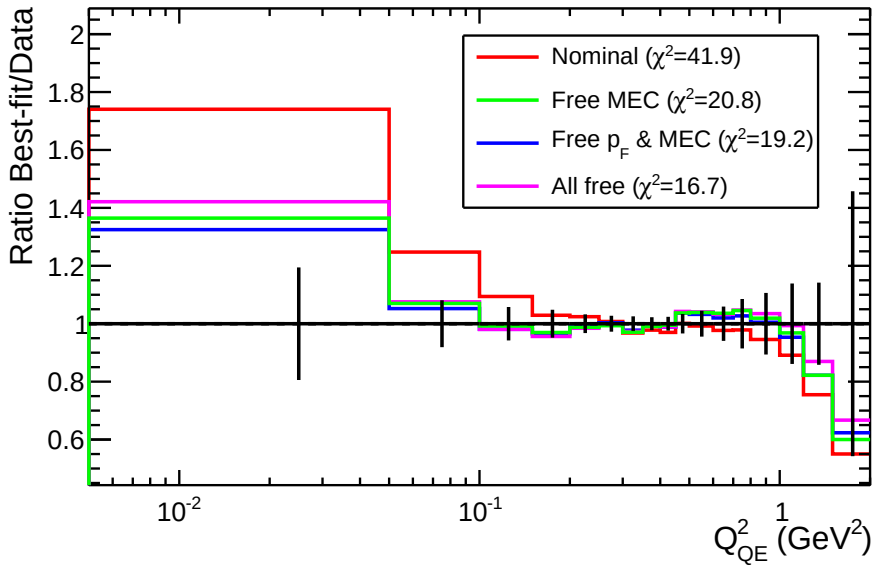

(A) MiniBooNE neutrino

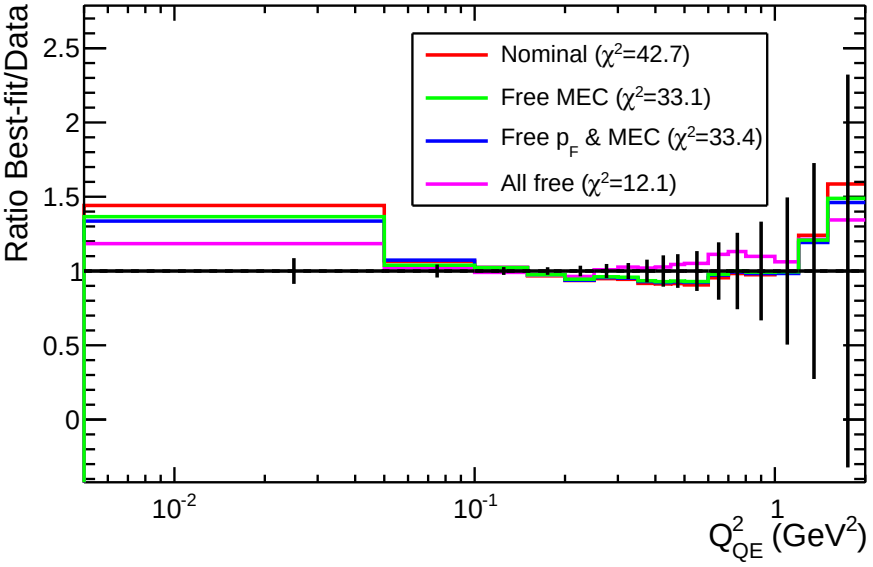

(B) MiniBooNE antineutrino

FIGURE C.8: Ratios of best fit distributions over data for the MiniBooNE neutrino and antineutrino single-differential datasets using the relativistic RFG+RPA+MEC with various combinations of free parameters. The parameter values corresponding to these distributions can be found in Table C.20 (C.21) for the neutrino (antineutrino) dataset. Parameter values for the MiniBooNE neutrino and antineutrino double-differential distributions can be found in Table C.22 (C.23) for the neutrino (antineutrino) dataset.

Fit type	χ^2/DOF	M_A (GeV)	MEC (%)	p_F (MeV)
All fixed	301.46/17	1.01 (fixed)	100 (fixed)	209 (fixed)
Free MEC	178.33/16	1.01 (fixed)	0 (at limit)	209 (fixed)
Free MEC+p_F	51.88/15	1.01 (fixed)	0±29	334 (at limit)
All free	4.48/14	1.55±0.08	126±27	334±25

TABLE C.14: Table of best fit parameter values for various combinations of free parameters for the MiniBooNE neutrino single-differential dataset and the SF+MEC model.

Fit type	χ^2/DOF	M_A (GeV)	MEC (%)	p_F (MeV)
All fixed	111.55/17	1.01 (fixed)	100 (fixed)	209 (fixed)
Free MEC	107.83/16	1.01 (fixed)	0 (at limit)	209 (fixed)
Free MEC+p_F	14.64/15	1.01 (fixed)	59±48	334 (at limit)
All free	3.51/14	1.29±0.07	105±74	296±29

TABLE C.15: Table of best fit parameter values for various combinations of free parameters for the MiniBooNE antineutrino single-differential dataset and the SF+MEC model.

Fit type	χ^2/DOF	M_A (GeV)	MEC (%)	p_F (MeV)
All fixed	457.76/137	1.01 (fixed)	100 (fixed)	209 (fixed)
Free MEC	264.65/136	1.01 (fixed)	0 (at limit)	209 (fixed)
Free MEC+p_F	91.78/135	1.01 (fixed)	0 (at limit)	334 (at limit)
All free	22.37/134	1.40±0.06	56±49	298±35

TABLE C.16: Table of best fit parameter values for various combinations of free parameters for the MiniBooNE neutrino double-differential dataset and the SF+MEC model.

Fit type	χ^2/DOF	M_A (GeV)	MEC (%)	p_F (MeV)
All fixed	118.54/78	1.01 (fixed)	100 (fixed)	209 (fixed)
Free MEC	118.09/77	1.01 (fixed)	51±67	209 (fixed)
Free MEC+p_F	33.85/76	1.01 (fixed)	66±46	334 (at limit)
All free	21.34/75	1.24±0.04	73±57	298±9

TABLE C.17: Table of best fit parameter values for various combinations of free parameters for the MiniBooNE antineutrino double-differential dataset and the SF+MEC model.

Fit type	χ^2/DOF	M_A (GeV)	MEC (%)	p_F (MeV)
All fixed	32.69/8	1.01 (fixed)	100 (fixed)	217 (fixed)
Free MEC	17.64/7	1.01 (fixed)	30±18	217 (fixed)
Free MEC+p_F	16.23/6	1.01 (fixed)	19±20	212±11
All free	13.57/5	0.87±0.09	20±20	223±21

TABLE C.18: Table of best fit parameter values for various combinations of free parameters for the MINERνA neutrino dataset and the relativistic RFG+RPA+MEC model.

Fit type	χ^2/DOF	M_A (GeV)	MEC (%)	p_F (MeV)
All fixed	35.16/8	1.01 (fixed)	100 (fixed)	217 (fixed)
Free MEC	9.84/7	1.01 (fixed)	0 (at limit)	217 (fixed)
Free MEC+p_F	8.81/6	1.01 (fixed)	3±29	216±6
All free	8.76/5	1.00±0.07	2±55	216±8

TABLE C.19: Table of best fit parameter values for various combinations of free parameters for the MINERνA antineutrino dataset and the relativistic RFG+RPA+MEC model.

Fit type	χ^2/DOF	M_A (GeV)	MEC (%)	p_F (MeV)
All fixed	41.89/17	1.01 (fixed)	100 (fixed)	217 (fixed)
Free MEC	20.78/16	1.01 (fixed)	24±14	217 (fixed)
Free MEC+p_F	19.16/15	1.01 (fixed)	39±20	257±34
All free	16.71/14	1.15±0.09	93±43	273±39

TABLE C.20: Table of best fit parameter values for various combinations of free parameters for the MiniBooNE neutrino single-differential dataset and the relativistic RFG+RPA+MEC model.

Fit type	χ^2/DOF	M_A (GeV)	MEC (%)	p_F (MeV)
All fixed	42.66/17	1.01 (fixed)	100 (fixed)	217 (fixed)
Free MEC	33.13/16	1.01 (fixed)	0 (at limit)	217 (fixed)
Free MEC+p_F	33.44/15	1.01 (fixed)	0 (at limit)	217±0
All free	12.14/14	1.21±0.04	0 (at limit)	212±10

TABLE C.21: Table of best fit parameter values for various combinations of free parameters for the MiniBooNE antineutrino single-differential dataset and the relativistic RFG+RPA+MEC model.

Fit type	χ^2/DOF	M_A (GeV)	MEC (%)	p_F (MeV)
All fixed	114.81/137	1.01 (fixed)	100 (fixed)	217 (fixed)
Free MEC	49.50/136	1.01 (fixed)	0 (at limit)	217 (fixed)
Free MEC+p_F	46.56/135	1.01 (fixed)	3±13	240±9
All free	32.93/134	1.24±0.01	77±16	228±0

TABLE C.22: Table of best fit parameter values for various combinations of free parameters for the MiniBooNE neutrino double-differential dataset and the relativistic RFG+RPA+MEC model.

Fit type	χ^2/DOF	M_A (GeV)	MEC (%)	p_F (MeV)
All fixed	47.67/78	1.01 (fixed)	100 (fixed)	217 (fixed)
Free MEC	40.75/77	1.01 (fixed)	0 (at limit)	217 (fixed)
Free MEC+p_F	38.25/76	1.01 (fixed)	0 (at limit)	260±16
All free	23.67/75	1.18±0.03	0 (at limit)	215±11

TABLE C.23: Table of best fit parameter values for various combinations of free parameters for the MiniBooNE antineutrino double-differential dataset and the relativistic RFG+RPA+MEC model.

Appendix D

Leptonic and hadronic tensor contraction for the Effective Spectral Function model

This appendix closely follows Appendix E of Reference [274], where the same formalism is used for the tensor contraction in the Benhar SF model. The implementation of the Effective Spectral Function (ESF) model in NEUT reuses the implementation of this contraction described in Reference [274].

The leptonic, $L_{\mu\nu}$, and hadronic, $H_{\mu\nu}$, tensors are given by

$$L_{\mu\nu} = 2(k_\mu k'_\nu + k'_\mu k_\nu - k \cdot k' g_{\mu\nu} - i\epsilon_{\mu\nu\rho\sigma} k^\rho k'^\sigma), \tag{D.1}$$

$$H^{\mu\nu} = -g^{\mu\nu} M_i^2 H_1 + p^\mu p^\nu H_2 + \frac{i}{2}\epsilon^{\mu\nu\kappa\lambda} p_\kappa q_\lambda H_3 - q^\mu q^\nu H_4 + \frac{1}{2}(p^\mu q^\nu + q^\mu p^\nu) H_5, \tag{D.2}$$

where M_i is the mass of the struck nucleon, k, k', p and q are the four-vector of the incoming lepton, the outgoing lepton, the initial state nucleon and the four-momentum transfer respectively. ϵ is the antisymmetric tensor, and $\epsilon_{\nu\mu\rho\sigma}\epsilon^{\nu\mu\kappa\lambda} = \delta^\kappa_\rho \delta^\lambda_\sigma - \delta^\lambda_\rho \delta^\kappa_\sigma$. The

components of the hadronic tensor are given by

$$
\begin{aligned}
H_1 &= F_{\mathrm{A}}^2(1+\tau) + \tau(F_1+F_2)^2, \\
H_2 &= F_{\mathrm{A}}^2 + F_1^2 + \tau F_2^2, \\
H_3 &= 2F_{\mathrm{A}}(F_1+F_2), \\
H_4 &= \frac{1}{4}F_2^2(1-\tau) + \frac{1}{2}F_1F_2 + F_{\mathrm{A}}F_P - \tau F_P^2, \\
H_5 &= H_2.
\end{aligned}
$$

where $\tau = \frac{Q^2}{4M_i^2}$, and the form factors are given by Equations 2.19, 2.20 and 2.21.

The Benhar SF follows the de Forest method [298] for treating interactions involving particles which are initially off-shell, by making the replacement $q^\mu(\omega, \vec{q}) \rightarrow \tilde{q}^\mu(\tilde{\omega}, \vec{q})$ in the hadronic tensor, where the reduced energy transfer $\tilde{\omega} = E_{p'} - E_p = \omega - E_R$. The ESF does not make this modification.

The contraction $L_{\mu\nu}H^{\mu\nu}$ gives the expression

$$
\begin{aligned}
L_{\mu\nu}H^{\mu\nu} = &-2k\cdot k' M_i^2 H_1 \\
&+ \left[2(k\cdot p)(k'\cdot p) - (k\cdot k')(p\cdot p)\right] H_2 \\
&\pm \left[(k\cdot q)(k'\cdot p) - (k\cdot p)(k'\cdot q)\right] H_3 \\
&+ \left[(k\cdot k')(q\cdot q) - (k\cdot q)(k'\cdot q)\right] H_4 \\
&+ \left[(k\cdot p)(k'\cdot q) - (k'\cdot p)(k\cdot q) - (k\cdot k')(p\cdot q)\right] H_5
\end{aligned}
\tag{D.3}
$$

where the + (–) sign in the third term refers to neutrinos (antineutrinos).

Bibliography

[1] J. N. Bahcall, A. M. Serenelli, and S. Basu, *New solar opacities, abundances, helioseismology, and neutrino fluxes*, *The Astrophysical Journal* **621** (2005) 85–88.

[2] Particle Data Group, K. Olive et al., *Review of Particle Physics*, *Chin. Phys.* **C38** (2014) 090001.

[3] M. Hitoshi, *Oscillation Parameter Plot, 2014 PDG Update* 2014. Available at http://hitoshi.berkeley.edu/neutrino/.

[4] KARMEN Collaboration, B. Armbruster et al., *Upper limits for neutrino oscillations $\bar{\nu}_\mu \to \bar{\nu}_e$ from muon decay at rest*, *Phys. Rev.* **D65** (2002) 112001, arXiv:hep-ex/0203021 [hep-ex].

[5] M. Antonello, B. Baibussinov, P. Benetti, E. Calligarich, N. Canci, et al., *Experimental search for the "LSND anomaly" with the ICARUS detector in the CNGS neutrino beam*, *Eur. Phys. J.* **C73** (2013) 2345, arXiv:1209.0122 [hep-ex].

[6] MiniBooNE Collaboration, A. Aguilar-Arevalo et al., *Improved search for $\bar{\nu}_\mu \to \bar{\nu}_e$ oscillations in the MiniBooNE experiment*, *Phys. Rev. Lett.* **110** (2013) 161801, arXiv:1207.4809 [hep-ex].

[7] S. Barish, M. Derrick, T. Dombeck, L. Hyman, K. Jaeger, et al., *Study of neutrino interactions in hydrogen and deuterium: inelastic charged current reactions*, *Phys. Rev.* **D19** (1979) 2521.

[8] ArgoNeuT Collaboration, C. Anderson et al., *First measurements of inclusive muon neutrino charged current differential cross sections on argon*, *Phys. Rev. Lett.* **108** (2012) 161802, arXiv:1111.0103 [hep-ex].

[9] D. Colley, G. Jones, S. O'Neale, S. Sewell, G. Bertrand-Coremans, et al., *Cross sections for charged current neutrino and antineutrino interactions in the energy range 10 GeV to 50 GeV*, *Z. Phys.* **C2** (1979) 187.

[10] N. Baker, P. Connolly, S. Kahn, M. Murtagh, R. Palmer, et al., *Total cross sections for muon-neutrino N and muon-neutrino P charged current interactions in the 7-ft bubble chamber*, *Phys. Rev.* **D25** (1982) 617–623.

[11] W. G. Seligman, *A next-to-leading order QCD analysis of neutrino - iron structure functions at the Tevatron*. PhD thesis, 1997.

[12] J. Berge, A. Blondel, P. Bockmann, H. Burkhardt, F. Dydak, et al., *Total neutrino and antineutrino charged current cross section measurements in 100-GeV, 160-GeV and 200-GeV narrow band beams*, *Z. Phys.* **C35** (1987) 443.

[13] Gargamelle SPS, J. Morfin et al., *Total cross sections and nucleon structure functions in the Gargamelle SPS neutrino / antineutrino experiment*, *Phys. Lett.* **B104** (1981) 235.

[14] Gargamelle Neutrino Propane, Aachen-Brussels-CERN-Ecole Poly-Orsay-Padua, S. Ciampolillo et al., *Total cross section for neutrino charged current interactions at 3 GeV and 9 GeV*, *Phys. Lett.* **B84** (1979) 281.

[15] A. Asratian, A. Bugorsky, V. S. Epshtein, R. Fakhrutdinov, V. Gemanov, et al., *Charged current neutrino interactions below 30 GeV*, *Phys. Lett.* **B76** (1978) 239.

[16] V. Anikeev, S. Belikov, A. Borisov, N. Bozhko, S. Chernichenko, et al., *Total cross section measurements for muon-neutrino, anti-muon-neutrino interactions in 3 GeV − 30 GeV energy range with IHEP-JINR neutrino detector*, *Z. Phys.* **C70** (1996) 39–46.

[17] MINOS Collaboration, P. Adamson et al., *Neutrino and antineutrino inclusive charged-current cross section measurements with the MINOS near detector*, *Phys. Rev.* **D81** (2010) 072002, arXiv:0910.2201 [hep-ex].

[18] NOMAD Collaboration, Q. Wu et al., *A Precise measurement of the muon neutrino-nucleon inclusive charged current cross section off an isoscalar target in the energy range* $2.5 < E_\nu < 40$ *GeV by NOMAD*, *Phys. Lett.* **B660** (2008) 19–25, arXiv:0711.1183 [hep-ex].

[19] NuTeV Collaboration, M. Tzanov et al., *Precise measurement of neutrino and antineutrino differential cross sections*, *Phys. Rev.* **D74** (2006) 012008, arXiv:hep-ex/0509010 [hep-ex].

[20] SciBooNE Collaboration, Y. Nakajima et al., *Measurement of inclusive charged current interactions on carbon in a few-GeV neutrino beam*, *Phys. Rev.* **D83** (2011) 012005, arXiv:1011.2131 [hep-ex].

[21] SKAT Collaboration, D. Baranov, A. Bugorsky, A. Ivanilov, V. Kochetkov, V. Konyushko, et al., *Measurements of the $\nu_\mu N$ total cross section at 2-GeV - 30-GeV in SKAT neutrino experiment*, *Phys.Lett.* **B81** (1979) 255.

[22] T2K Collaboration, K. Abe et al., *Measurement of the inclusive ν_μ charged current cross section on carbon in the near detector of the T2K experiment*, *Phys. Rev.* **D87** (2013) 092003, arXiv:1302.4908 [hep-ex].

[23] S. Barish, J. Campbell, G. Charlton, Y. Cho, M. Derrick, et al., *Study of neutrino interactions in hydrogen and deuterium. 1. Description of the experiment and study of the reaction neutrino $\nu_\mu + d \to \mu^- + p + p_s$*, *Phys. Rev.* **D16** (1977) 3103.

[24] D. Allasia, C. Angelini, G. van Apeldoorn, A. Baldini, S. Barlag, et al., *Investigation of exclusive channels in neutrino / antineutrino deuteron charged current interactions*, *Nucl. Phys.* **B343** (1990) 285–309.

[25] N. Baker, A. Cnops, P. Connolly, S. Kahn, H. Kirk, et al., *Quasielastic neutrino scattering: a measurement of the weak nucleon axial vector form-factor*, *Phys. Rev.* **D23** (1981) 2499–2505.

[26] G. Fanourakis, L. Resvanis, G. Grammatikakis, P. Tsilimigras, A. Vayaki, et al., *Study of Low-energy antineutrino Interactions on Protons*, *Phys. Rev.* **D21** (1980) 562.

[27] T. Kitagaki, S. Tanaka, H. Yuta, K. Abe, K. Hasegawa, et al., *High-energy quasielastic $\nu_\mu + n \to \mu^- + p$ scattering in deuterium*, *Phys. Rev.* **D28** (1983) 436–442.

[28] S. Bonetti, G. Carnesecchi, D. Cavalli, P. Negri, A. Pullia, et al., *Study of quasielastic reactions of neutrino and antineutrino in Gargamelle*, *Nuovo Cim.* **A38** (1977) 260–270.

[29] N. Armenise, O. Erriquez, M. Fogli Muciaccia, S. Nuzzo, F. Ruggieri, et al., *Charged current elastic antineutrino interactions in propane*, *Nucl. Phys.* **B152** (1979) 365–375.

[30] LSND Collaboration, L. Auerbach et al., *Measurements of charged current reactions of muon neutrinos on ^{12}C*, *Phys. Rev.* **C66** (2002) 015501, arXiv:nucl-ex/0203011 [nucl-ex].

[31] S. Belikov, A. Bugorsky, V. S. Epshtein, N. Kalganov, L. Klimenko, et al., *Quasielastic neutrino and antineutrinos scattering: total cross sections, axial vector form-factor*, *Z. Phys.* **A320** (1985) 625.

[32] SKAT Collaboration, J. Brunner et al., *Quasielastic nucleon and hyperon production by neutrinos and antineutrinos with energies below 30 GeV*, *Z. Phys.* **C45** (1990) 551.

[33] V. Lyubushkin et al., *A study of quasi-elastic muon neutrino and antineutrino scattering in the NOMAD experiment*, *The European Physical Journal C* **63** (2009) 355–381.

[34] MiniBooNE Collaboration, A. Aguilar-Arevalo et al., *First measurement of the muon neutrino charged current quasielastic double-differential cross section*, *Phys. Rev.* **D81** (2010) 092005, arXiv:1002.2680 [hep-ex].

[35] MiniBooNE Collaboration, A. Aguilar-Arevalo et al., *First measurement of the muon antineutrino double-differential charged current quasi-elastic cross section*, *Phys. Rev.* **D88** (2013) 032001, arXiv:1301.7067 [hep-ex].

[36] G. Radecky, V. Barnes, D. Carmony, A. Garfinkel, M. Derrick, et al., *Study of single pion production by weak charged currents in low-energy neutrino d interactions*, *Phys. Rev.* **D25** (1982) 1161–1173.

[37] T. Kitagaki, H. Yuta, S. Tanaka, A. Yamaguchi, K. Abe, et al., *Charged current exclusive pion production in neutrino deuterium interactions*, *Phys. Rev.* **D34** (1986) 2554–2565.

[38] J. Bell, C. Coffin, R. Diamond, H. French, W. Louis, et al., *Cross section measurements for the reactions neutrino* $p \to \mu^- + \pi^+ + p$ *and neutrino* $p \to \mu^- + K^+ + p$ *at high-energies*, *Phys. Rev. Lett.* **41** (1978) 1008.

[39] Aachen-Birmingham-Bonn-CERN-London-Munich-Oxford Collaboration, P. Allen et al., *A study of single meson production in neutrino and antineutrino charged current interactions on protons*, *Nucl. Phys.* **B264** (1986) 221.

[40] C. Wilkinson, P. Rodrigues, S. Cartwright, L. Thompson, and K. McFarland, *Reanalysis of bubble chamber measurements of muon-neutrino induced single pion production*, *Phys. Rev.* **D90** (2014) 112017, arXiv:1411.4482 [hep-ex].

[41] D. Rein and L. M. Sehgal, *Coherent* π^0 *production in neutrino reactions*, *Nucl. Phys.* **B223** (1983) 29.

[42] D. Rein and L. Sehgal, *PCAC and the deficit of forward muons in* π^+ *production by neutrinos*, *Phys. Lett.* **B657** (2007) 207–209, arXiv:hep-ph/0606185 [hep-ph].

[43] MINERνA Collaboration, A. Higuera et al., *Measurement of coherent production of $\pi^{\pm}$ in neutrino and antineutrino beams on carbon from E_{ν} of 1.5 to 20 GeV*, *Phys. Rev. Lett.* **113** (2014) 261802, arXiv:1409.3835 [hep-ex].

[44] SciBooNE Collaboration, K. Hiraide et al., *Search for charged current coherent pion production on carbon in a few-GeV neutrino beam*, *Phys. Rev.* **D78** (2008) 112004, arXiv:0811.0369 [hep-ex].

[45] K2K Collaboration, M. Hasegawa et al., *Search for coherent charged pion production in neutrino-carbon interactions*, *Phys. Rev. Lett.* **95** (2005) 252301, arXiv:hep-ex/0506008 [hep-ex].

[46] ArgoNeuT Collaboration, R. Acciarri et al., *First measurement of neutrino and antineutrino coherent charged pion production on argon*, *Phys. Rev. Lett.* **113** (2014) 261801, arXiv:1408.0598 [hep-ex].

[47] SKAT Collaboration, H. Grabosch et al., *Coherent pion production in neutrino and antineutrino interactions on nuclei of heavy freon molecules*, *Z. Phys.* **C31** (1986) 203.

[48] BEBC WA59 Collaboration, P. Marage et al., *Coherent single pion production by antineutrino charged current interactions and test of PCAC*, *Z. Phys.* **C31** (1986) 191–197.

[49] BEBC WA59 Collaboration, P. Allport et al., *Coherent production of π^{+} mesons in neutrino - neon interactions*, *Z. Phys.* **C43** (1989) 523–526.

[50] CHARM-II Collaboration, P. Vilain et al., *Coherent single charged pion production by neutrinos*, *Phys. Lett.* **B313** (1993) 267–275.

[51] O. Benhar and A. Fabrocini, *Two nucleon spectral function in infinite nuclear matter*, *Phys. Rev.* **C62** (2000) 034304, arXiv:nucl-th/9909014 [nucl-th].

[52] P. Sinclair et al., *Implementation of a multi-nucleon interaction model into NEUT*, *T2K-TN-170* (2014).

[53] L. Alvarez-Ruso, Y. Hayato, and J. Nieves, *Progress and open questions in the physics of neutrino cross sections at intermediate energies*, *New J. Phys.* **16** (2014) 075015, arXiv:1403.2673 [hep-ph].

[54] R. Gran, J. Nieves, F. Sanchez, and M. Vicente Vacas, *Neutrino-nucleus quasi-elastic and 2p2h interactions up to 10 GeV*, *Phys. Rev.* **D88** (2013) 113007, arXiv:1307.8105 [hep-ph].

[55] T2K Collaboration, K. Abe et al., *The T2K experiment*, *Nuclear Instruments and Methods in Physics Research Section A: Accelerators, Spectrometers, Detectors and Associated Equipment* **659** (2011) 106–135.

[56] Y. Hayato et al., "Letter of intent: neutrino oscillation experiment at JHF." Available at http://neutrino.kek.jp/jhfnu/loi/loi.v2.030528.pdf, 2003.

[57] T2K Collaboration, K. Abe et al., *The T2K Neutrino Flux Prediction*, *Phys. Rev.* **D87** (2013) 012001, arXiv:1211.0469 [hep-ex].

[58] J. Perkin, "Private communication." 2014.

[59] MINERνA Collaboration, L. Aliaga et al., *Design, calibration, and performance of the MINERνA detector*, *Nucl. Instrum. Meth.* **A743** (2014) 130–159, arXiv:1305.5199 [physics.ins-det].

[60] MiniBooNE Collaboration, A. Aguilar-Arevalo et al., *The MiniBooNE Detector*, *Nucl. Instrum. Meth.* **A599** (2009) 28–46, arXiv:0806.4201 [hep-ex].

[61] SciBooNE Collaboration, MiniBooNE, K. Mahn et al., *Dual baseline search for muon neutrino disappearance at* $0.5\ \mathrm{eV}^2 < \Delta m^2 < 40\ \mathrm{eV}^2$, *Phys. Rev.* **D85** (2012) 032007, arXiv:1106.5685 [hep-ex].

[62] Super-Kamiokande Collaboration, A. Himmel, *Recent results from Super-Kamiokande*, *AIP Conf.Proc.* **1604** (2014) 345–352, arXiv:1310.6677 [hep-ex].

[63] Super-Kamiokande Collaboration, K. Abe et al., *Limits on sterile neutrino mixing using atmospheric neutrinos in Super-Kamiokande*, *Phys. Rev.* **D91** (2015) 052019, arXiv:1410.2008 [hep-ex].

[64] C. Giunti and M. Laveder, *Status of 3+1 neutrino mixing*, *Phys. Rev.* **D84** (2011) 093006, arXiv:1109.4033 [hep-ph].

[65] MINOS Collaboration, P. Adamson et al., *Active to sterile neutrino mixing limits from neutral-current interactions in MINOS*, *Phys. Rev. Lett.* **107** (2011) 011802, arXiv:1104.3922 [hep-ex].

[66] C. Ciofi degli Atti and S. Simula, *Realistic model of the nucleon spectral function in few and many nucleon systems*, *Phys. Rev.* **C53** (1996) 1689, arXiv:nucl-th/9507024 [nucl-th].

[67] T. Donnelly and I. Sick, *Superscaling of inclusive electron scattering from nuclei*, *Phys. Rev.* **C60** (1999) 065502, arXiv:nucl-th/9905060 [nucl-th].

[68] J. Jourdan, *Quasielastic response functions: The Coulomb sum revisited*, *Nucl. Phys.* **A603** (1996) 117–160.

[69] A. Bodek, H. S. Budd, and E. Christy, *Neutrino quasielastic scattering on nuclear targets*, *Eur. Phys. J. C* **71** (2011) 1726.

[70] J. Carlson, J. Jourdan, R. Schiavilla, and I. Sick, *Longitudinal and transverse quasielastic response functions of light nuclei*, *Phys. Rev.* **C65** (2002) 024002, arXiv:nucl-th/0106047 [nucl-th].

[71] A. Bodek, M. Christy, and B. Coopersmith, *Effective spectral function for quasielastic scattering on nuclei*, *Eur. Phys. J.* **C74** (2014) 3091, arXiv:1405.0583 [hep-ph].

[72] M. Hartz et al., *Constraining the flux and cross section models with data from the ND280 detector for the 2014/15 oscillation analysis*, *T2K-TN-220* (2015).

[73] T2K Collaboration, K. Abe et al., *Measurements of neutrino oscillation in appearance and disappearance channels by the T2K experiment with 6.6E20 protons on target*, *Phys. Rev. D* **91** (2015) 072010, arXiv:1502.01550 [hep-ex].

[74] C. Andreopoulos et al., *T2K* 2.315×10^{20}*-POT three-flavour muon antineutrino disappearance analysis*, *T2K-TN-243* (2015).

[75] F. Capozzi, L. Fogli, G. E. Lisi, A. Marrone, D. Montanino, and A. Palazzo, *Status of three-neutrino oscillation parameters, circa 2013*, *Phys. Rev. D* **89** (2014) 093018.

[76] D. Perevalov, *Neutrino-nucleus neutral current elastic interactions measurement in MiniBooNE*. PhD thesis, 2009.

[77] MiniBooNE Collaboration, A. Aguilar-Arevalo et al., *Measurement of the neutrino neutral-current elastic differential cross section on mineral il at* $E_\nu \sim 1$ *GeV*, *Phys. Rev.* **D82** (2010) 092005, arXiv:1007.4730 [hep-ex].

[78] T. Katori, *A Measurement of the muon neutrino charged current quasielastic interaction and a test of Lorentz violation with the MiniBooNE experiment*. PhD thesis, 2008.

[79] P. Bosted and V. Mamyan, *Empirical fit to electron-nucleus scattering*, arXiv:1203.2262 [nucl-th].

[80] A. Bodek, M. Christy, and B. Coopersmith, *Effective spectral function for quasielastic scattering on nuclei from deuterium to lead*, arXiv:1409.8545 [nucl-th].

[81] F. Close *Neutrino*. Oxford University Press. 2010.

[82] W. Pauli, "Pauli letter collection: letter to Lise Meitner." Typed copy available at https://cds.cern.ch/record/83282, December, 1930.

[83] B. Pontecorvo, "Chalk River Laboratory PD-205 report." 1946.

[84] R. Davis, *Attempt to detect the antineutrinos from a nuclear reactor by the* $^{37}\mathrm{Cl} + \bar{\nu} \to e^- + ^{37}\mathrm{Ar}$ *reaction*, *Phys. Rev.* **97** (1955) 766–769.

[85] F. Reines and C. L. Cowan, *Detection of the free neutrino*, *Phys. Rev.* **92** (1953) 830–831.

[86] F. Reines and C. L. Cowan, *The Neutrino*, *Nature* **178** (1956) 446–449.

[87] F. Reines and C. Cowan, *The Reines-Cowan experiments: detecting the poltergeist*, *Los Alamos Sci.* **25** (1997) 4–27.

[88] J. C. Street and E. C. Stevenson, *New evidence for the existence of a particle of mass intermediate between the proton and electron*, *Phys. Rev.* **52** (1937) 1003–1004.

[89] COMET Collaboration, Y. Cui et al., *Conceptual design report for experimental search for lepton flavor violating* $\mu^- \to e^-$ *conversion at sensitivity of* 10^{-16} *with a slow-extracted bunched proton beam (COMET)*.

[90] G. Danby et al., *Observation of high-energy neutrino reactions and the existence of two kinds of neutrinos*, *Phys. Rev. Lett.* **9** (1962) 36–44.

[91] M. L. Perl et al., *Evidence for anomalous lepton production in* e^+e^- *annihilation*, *Phys. Rev. Lett.* **35** (1975) 1489–1492.

[92] B. Adeva et al., *A determination of the properties of the neutral intermediate vector boson*, *Physics Letters B* **231** (1989) 509–518.

[93] D. DeCamp et al., *Determination of the number of light neutrino species*, *Physics Letters B* **231** (1989) 519–529.

[94] M. Akrawy et al., *Measurement of the* Z^0 *mass and width with the OPAL detector at LEP*, *Physics Letters B* **231** (1989) 530–538.

[95] P. Aarnio et al., *Measurement of the mass and width of the* Z^0*-particle from multi-hadronic final states produced in* e^+e^- *annhilations*, *Physics Letters B* **231** (1989) 539–547.

[96] G. S. Abrams et al., *Measurements of Z-boson resonance parameters in* e^+e^- *annihilation*, *Phys. Rev. Lett.* **63** (1989) 2173–2176.

[97] ALEPH Collaboration, DELPHI Collaboration, L3 Collaboration, OPAL Collaboration, SLD Collaboration, LEP Electroweak Working Group, SLD Electroweak Group, SLD Heavy Flavour Group, S. Schael et al., *Precision electroweak measurements on the Z resonance*, *Phys. Rept.* **427** (2006) 257–454, arXiv:hep-ex/0509008 [hep-ex].

[98] K. Kodama et al., *Observation of tau neutrino interactions*, *Physics Letters B* **504** (2001) 218–224.

[99] J. N. Bahcall, W. F. Huebner, S. H. Lubow, P. D. Parker, and R. K. Ulrich, *Standard solar models and the uncertainties in predicted capture rates of solar neutrinos*, *Rev. Mod. Phys.* **54** (1982) 767–799.

[100] R. Davis, D. S. Harmer, and K. C. Hoffman, *Search for neutrinos from the sun*, *Phys. Rev. Lett.* **20** (1968) 1205–1209.

[101] B. T. Cleveland et al., *Measurement of the solar electron neutrino flux with the Homestake chlorine detector*, *The Astrophysical Journal* **496** (1998) 505–526.

[102] J. N. Bahcall, M. H. Pinsonneault, and G. J. Wasserburg, *Solar models with helium and heavy-element diffusion*, *Rev. Mod. Phys.* **67** (1995) 781–808.

[103] Kamiokande Collaboration, K. S. Hirata et al., *Observation of ^8B solar neutrinos in the Kamiokande-II detector*, *Phys. Rev. Lett.* **63** (1989) 16.

[104] GALLEX collaboration, W. Hampel et al., *GALLEX solar neutrino observations: results for GALLEX IV*, *Physics Letters B* **447** (1999) 127–133.

[105] GNO Collaboration, M. Altmann et al., *Complete results for five years of GNO solar neutrino observations*, *Phys. Lett.* **B616** (2005) 174–190, arXiv:hep-ex/0504037 [hep-ex].

[106] SAGE Collaboration, J. N. Abdurashitov et al., *Measurement of the solar neutrino capture rate with gallium metal. III. Results for the 2002-2007 data-taking period*, *Phys. Rev. C* **80** (2009) 015807.

[107] B. Pontecorvo, *Mesonium and anti-mesonium*, *J. Exptl. Theoret. Phys.* **33** (1957) 549–551.

[108] K. Hirata et al., *Observation of a small atmospheric ν_μ/ν_e ratio in Kamiokande*, *Physics Letters B* **280** (1992) 146–152.

[109] D. Casper et al., *Measurement of atmospheric neutrino composition with the IMB-3 detector*, *Phys. Rev. Lett.* **66** (1991) 2561–2564.

[110] Y. Fukuda et al., *Atmospheric ν_μ/ν_e ratio in the multi-GeV energy range*, *Physics Letters B* **335** (1994) 237–245.

[111] Y. Fukuda et al., *Study of the atmospheric neutrino flux in the multi-GeV energy range*, *Physics Letters B* **436** (1998) 33–41.

[112] Super-Kamiokande Collaboration, Y. Fukuda et al., *Evidence for oscillation of atmospheric neutrinos*, *Phys. Rev. Lett.* **81** (1998) 1562–1567.

[113] SNO Collaboration, Q. R. Ahmad et al., *Direct evidence for neutrino flavor transformation from neutral-current interactions in the Sudbury Neutrino Observatory*, *Phys. Rev. Lett.* **89** (2002) 011301.

[114] SNO Collaboration, Q. R. Ahmad et al., *Measurement of the rate of $\nu_e + d \to p + p + e^-$ interactions produced by ^8B solar neutrinos at the Sudbury Neutrino Observatory*, *Phys. Rev. Lett.* **87** (2001) 071301, arXiv:nucl-ex/0106015.

[115] Super-Kamiokande Collaboration, S. Fukuda et al., *Determination of solar neutrino oscillation parameters using 1496 days of Super-Kamiokande-I data*, *Phys. Lett.* **B539** (2002) 179–187, arXiv:hep-ex/0205075.

[116] Z. Maki, M. Nakagawa, and S. Sakata, *Remarks on the unified model of elementary particles*, *Progress of Theoretical Physics* **28** (1962) 870–880.

[117] L. Wolfenstein, *Neutrino oscillations in matter*, *Phys. Rev.* **D17** (1978) 2369.

[118] S. P. Mikheev and A. Y. Smirnov, *Resonance enhancement of oscillations in matter and solar neutrino spectroscopy*, *Sov. J. Nucl. Phys.* **42** (1985) 913–917.

[119] Super-Kamiokande Collaboration, J. Cravens et al., *Solar neutrino measurements in Super-Kamiokande-II*, *Phys. Rev.* **D78** (2008) 032002, arXiv:0803.4312 [hep-ex].

[120] KamLAND Collaboration, S. Abe et al., *Precision measurement of neutrino oscillation parameters with KamLAND*, *Phys. Rev. Lett.* **100** (2008) 221803, arXiv:0801.4589 [hep-ex].

[121] SNO Collaboration, B. Aharmim et al., *An independent measurement of the total active ^8B solar neutrino flux using an array of ^3He proportional counters at the Sudbury Neutrino Observatory*, *Phys. Rev. Lett.* **101** (2008) 111301, arXiv:0806.0989 [nucl-ex].

[122] MINOS Collaboration, P. Adamson et al., *Combined analysis of ν_μ disappearance and $\nu_\mu \to \nu_e$ appearance in MINOS using accelerator and atmospheric neutrinos*, *Phys. Rev. Lett.* **112** (2014) 191801, arXiv:1403.0867 [hep-ex].

[123] T2K Collaboration, K. Abe et al., *Measurement of neutrino oscillation parameters from muon neutrino disappearance with an off-axis beam*, *Phys. Rev. Lett. 111,* **211803** (2013) 211803, arXiv:1308.0465 [hep-ex].

[124] T2K Collaboration, K. Abe et al., *Precise measurement of the neutrino mixing parameter ϑ_{23} from muon neutrino disappearance in an off-axis beam*, *Phys. Rev. Lett.* **112** (2014) 181801, arXiv:1403.1532 [hep-ex].

[125] Super-Kamiokande Collaboration, R. Wendell et al., *Atmospheric neutrino oscillation analysis with sub-leading effects in Super-Kamiokande I, II, and III*, *Phys. Rev.* **D81** (2010) 092004, arXiv:1002.3471 [hep-ex].

[126] F. P. An et al., *Observation of electron-antineutrino disappearance at Daya Bay*, *Phys. Rev. Lett.* **108** (2012) 171803.

[127] T2K Collaboration, K. Abe et al., *Indication of electron neutrino appearance from an accelerator-produced off-axis muon neutrino beam*, *Phys. Rev. Lett.* **107** (2011) 041801.

[128] T2K Collaboration, K. Abe et al., *Observation of electron neutrino appearance in a muon neutrino beam*, *Phys. Rev. Lett.* **112** (2014) 061802, arXiv:1311.4750 [hep-ex].

[129] RENO Collaboration, J. K. Ahn et al., *Observation of reactor electron antineutrinos disappearance in the RENO experiment*, *Phys. Rev. Lett.* **108** (2012) 191802.

[130] C. Giunti and M. Laveder, *Implications of 3+1 short-baseline neutrino oscillations*, *Phys. Lett.* **B706** (2011) 200–207, arXiv:1111.1069 [hep-ph].

[131] R. Mohapatra and G. Senjanovic, *Neutrino mass and spontaneous parity violation*, *Phys. Rev. Lett.* **44** (1980) 912.

[132] K. Abazajian, M. Acero, S. Agarwalla, A. Aguilar-Arevalo, C. Albright, et al., *Light sterile neutrinos: a white paper*, arXiv:1204.5379 [hep-ph].

[133] J. L. Feng, *Dark Matter Candidates from Particle Physics and Methods of Detection*, *Ann. Rev. Astron. Astrophys.* **48** (2010) 495, arXiv:1003.0904 [astro-ph.CO].

[134] E. Borriello, M. Paolillo, G. Miele, G. Longo, and R. Owen, *Constraints on sterile neutrino dark matter from XMM–Newton observation of M33*, *Mon. Not. Roy. Astron. Soc.* **425** (2012) 1628–1632, arXiv:1109.5943 [astro-ph.GA].

[135] D. A. Prokhorov and J. Silk, *Can the excess in the FeXXVI Ly gamma line from the Galactic Center provide evidence for 17 keV sterile neutrinos?*, *Astrophys. J.* **725** (2010) L131, arXiv:1001.0215 [astro-ph].

[136] N. Mirabal, *Swift observation of Segue 1: constraints on sterile neutrino parameters in the darkest galaxy*, *Mon. Not. Roy. Astron. Soc.* **409** (2010) 128, arXiv:1010.4706 [astro-ph].

[137] M. Loewenstein and A. Kusenko, *Dark Matter Search Using XMM-Newton Observations of Willman 1*, *Astrophys. J.* **751** (2012) 82, arXiv:1203.5229 [astro-ph].

[138] T. Tamura, R. Iizuka, Y. Maeda, K. Mitsuda, and N. Y. Yamasaki, *An X-ray Spectroscopic Search for Dark Matter in the Perseus Cluster with Suzaku*, *Publ. Astron. Soc. Jap.* **67** (2015) 23, arXiv:1412.1869 [astro-ph].

[139] K. C. Y. Ng, S. Horiuchi, J. M. Gaskins, M. Smith, and R. Preece, *Improved Limits on Sterile Neutrino Dark Matter using Full-Sky Fermi-GBM Data*, arXiv:1504.04027 [astro-ph.CO].

[140] C. Giunti and M. Laveder, *3+1 and 3+2 sterile neutrino fits*, *Phys. Rev.* **D84** (2011) 073008, arXiv:1107.1452 [hep-ph].

[141] LSND Collaboration, C. Athanassopoulos et al., *Evidence for neutrino oscillations from muon decay at rest*, *Phys. Rev.* **C54** (1996) 2685–2708, arXiv:nucl-ex/9605001 [nucl-ex].

[142] LSND Collaboration, A. Aguilar-Arevalo et al., *Evidence for neutrino oscillations from the observation of $\bar{\nu}_e$ appearance in a $\bar{\nu}_\mu$ beam*, *Phys. Rev.* **D64** (2001) 112007, arXiv:hep-ex/0104049 [hep-ex].

[143] MiniBooNE Collaboration, A. Aguilar-Arevalo et al., *Unexplained excess of electron-like events from a 1-GeV neutrino beam*, *Phys. Rev. Lett.* **102** (2009) 101802, arXiv:0812.2243 [hep-ex].

[144] MiniBooNE Collaboration, SciBooNE, G. Cheng et al., *Dual baseline search for muon antineutrino disappearance at* $0.1\ \mathrm{eV}^2 < \Delta m^2 < 100\ \mathrm{eV}^2$, *Phys. Rev.* **D86** (2012) 052009, arXiv:1208.0322 [hep-ex].

[145] GALLEX collaboration, F. Kaether, W. Hampel, G. Heusser, J. Kiko, and T. Kirsten, *Reanalysis of the GALLEX solar neutrino flux and source experiments*, *Phys. Lett.* **B685** (2010) 47–54, arXiv:1001.2731 [hep-ex].

[146] SAGE Collaboration, J. N. Abdurashitov et al., *Measurement of the response of the Russian-American gallium experiment to neutrinos from a ^{51}Cr source*, *Phys. Rev.* **C59** (1999) 2246–2263, arXiv:hep-ph/9803418.

[147] SAGE Collaboration, J. N. Abdurashitov et al., *Measurement of the response of a Ga solar neutrino experiment to neutrinos from an ^{37}Ar source*, *Phys. Rev.* **C73** (2006) 045805, arXiv:nucl-ex/0512041.

[148] C. Giunti and M. Laveder, *Statistical significance of the gallium anomaly*, *Phys. Rev.* **C83** (2011) 065504, arXiv:1006.3244 [hep-ph].

[149] G. Mention et al., *The reactor antineutrino anomaly*, *Phys. Rev.* **D83** (2011) 073006, arXiv:1101.2755 [hep-ex].

[150] T. A. Mueller, D. Lhuillier, M. Fallot, A. Letourneau, S. Cormon, M. Fechner, L. Giot, T. Lasserre, J. Martino, G. Mention, A. Porta, and F. Yermia, *Improved predictions of reactor antineutrino spectra*, *Phys. Rev. C* **83** (2011) 054615.

[151] A. Hayes, J. Friar, G. Garvey, G. Jungman, and G. Jonkmans, *Systematic uncertainties in the analysis of the reactor neutrino anomaly*, *Phys. Rev. Lett.* **112** (2014) 202501, arXiv:1309.4146 [nucl-th].

[152] J. Conrad, C. Ignarra, G. Karagiorgi, M. Shaevitz, and J. Spitz, *Sterile neutrino fits to short baseline neutrino oscillation measurements*, *Adv. High Energy Phys.* **2013** (2013) 163897, arXiv:1207.4765 [hep-ex].

[153] J. Kopp, P. A. N. Machado, M. Maltoni, and T. Schwetz, *Sterile neutrino oscillations: the global picture*, *JHEP* **1305** (2013) 050, arXiv:1303.3011 [hep-ph].

[154] MINOS Collaboration, P. Adamson et al., *Active to sterile neutrino mixing limits from neutral-current interactions in MINOS*, *Phys. Rev. Lett.* **107** (2011) 011802, arXiv:1104.3922 [hep-ex].

[155] A. Boyarsky, O. Ruchayskiy, and M. Shaposhnikov, *The role of sterile neutrinos in cosmology and astrophysics*, *Ann. Rev. Nucl. Part. Sci.* **59** (2009) 191–214, arXiv:0901.0011 [hep-ph].

[156] S. Riemer-Sørensen, D. Parkinson, and T. M. Davis, *What is half a neutrino? Reviewing cosmological constraints on neutrinos and dark radiation*, *Publ. Astron. Soc. Austral.* **30** (2013) 29, arXiv:1301.7102 [astro-ph.CO].

[157] Planck Collaboration, P. Ade et al., *Planck 2013 results. XVI. Cosmological parameters*, *Astron. Astrophys.* **571** (2014) A16, arXiv:1303.5076 [astro-ph.CO].

[158] S. Riemer-Sørensen, D. Parkinson, and T. M. Davis, *Combining Planck data with large scale structure information gives a strong neutrino mass constraint*, *Phys. Rev.* **D89** (2014) 103505, arXiv:1306.4153 [astro-ph.CO].

[159] E. Giusarma, R. de Putter, S. Ho, and O. Mena, *Constraints on neutrino masses from Planck and Galaxy Clustering data*, *Phys. Rev.* **D88** (2013) 063515, arXiv:1306.5544 [astro-ph.CO].

[160] M. Archidiacono, E. Giusarma, S. Hannestad, and O. Mena, *Cosmic dark radiation and neutrinos*, *Adv. High Energy Phys.* **2013** (2013) 191047, arXiv:1307.0637 [astro-ph.CO].

[161] J. Kristiansen and Ø. Elgarøy, *Reactor sterile neutrinos, dark energy and the age of the universe*, *Astron. Astrophys.* **532** (2011) A67, arXiv:1104.0704 [astro-ph].

[162] K. Abe, T. Abe, H. Aihara, Y. Fukuda, Y. Hayato, et al., *Letter of Intent: The Hyper-Kamiokande Experiment – Detector Design and Physics Potential*, arXiv:1109.3262 [hep-ex].

[163] IceCube-PINGU Collaboration, M. Aartsen et al., *Letter of intent: the precision IceCube next generation upgrade (PINGU)*, arXiv:1401.2046 [physics.ins-det].

[164] D. Ayres et al., *NOνA proposal to build a 30 kiloton off-axis detector to study neutrino oscillations in the Fermilab NuMI beamline*, (2005), Available at hep-ex/0503053v1.

[165] IceCube Collaboration, J. Ahrens et al., *IceCube - the next generation neutrino telescope at the South Pole*, *Nucl. Phys. Proc. Suppl.* **118** (2003) 388–395, arXiv:astro-ph/0209556 [astro-ph].

[166] Y. Hayato, *A Neutrino Interaction Simulation Program Library NEUT*, *Acta Physica Polonica B* **40** (2009) 2477.

[167] C. Andreopoulos, A. Bell, D. Bhattacharya, F. Cavanna, J. Dobson, et al., *The GENIE neutrino Monte Carlo generator*, *Nucl. Instrum. Meth.* **A614** (2010) 87–104, arXiv:0905.2517 [hep-ph].

[168] E. J. Moniz, I. Sick, R. R. Whitney, J. R. Ficenec, R. D. Kephart, and W. P. Trower, *Nuclear Fermi Momenta from Quasielastic Electron Scattering*, *Phys. Rev. Lett.* **26** (1971) 445–448.

[169] S. Boyd, S. Dytman, E. Hernández, J. Sobczyk, and R. Tacik, *Comparison of models of neutrino-nucleus interactions*, *AIP Conference Proceedings* **1189** (2009) 60–73.

[170] D. Rein and L. M. Sehgal, *Neutrino-excitation of baryon resonances and single pion production*, *Annals of Physics* **133** (1981) 79–153.

[171] O. Buss, T. Gaitanos, K. Gallmeister, H. van Hees, M. Kaskulov, et al., *Transport-theoretical description of nuclear reactions*, *Phys. Rept.* **512** (2012) 1–124, arXiv:1106.1344 [hep-ph].

[172] S. Dytman, *Final state interactions in neutrino-nucleus experiments*, *Acta Phys. Polon.* **B40** (2009) 2445–2460.

[173] R. D. Woods and D. S. Saxon, *Diffuse surface optical model for nucleon-nuclei scattering*, *Phys. Rev.* **95** (1954) 577–578.

[174] P. de Perio, *Joint three-flavour oscillation analysis of ν_μ disappearence and ν_e appearance in the T2K neutrino beam*. PhD thesis, University of Toronto, 2014.

[175] T. Golan, C. Juszczak, and J. T. Sobczyk, *Final state interactions effects in neutrino-nucleus interactions*, *Phys. Rev.* **C86** (2012) 015505, arXiv:1202.4197 [nucl-th].

[176] O. Benhar and D. Meloni, *Total neutrino and antineutrino nuclear cross sections around 1-GeV*, *Nucl. Phys.* **A789** (2007) 379–402, arXiv:hep-ph/0610403 [hep-ph].

[177] C. Llewellyn Smith, *Neutrino reactions at accelerator energies*, *Phys. Rept.* **3** (1972) 261–379.

[178] R. Smith and E. Moniz, *Neutrino reactions on nuclear targets*, *Nucl. Phys.* **B43** (1972) 605.

[179] J. Arrington and I. Sick, *Precise determination of low-Q nucleon electromagnetic form factors and their impact on parity-violating e-p elastic scattering*, *Phys. Rev.* **C76** (2007) 035201, arXiv:nucl-th/0612079 [nucl-th].

[180] H. S. Budd, A. Bodek, and J. Arrington, *Modeling quasielastic form-factors for electron and neutrino scattering*, arXiv:hep-ex/0308005 [hep-ex].

[181] E. B. Hughes, T. A. Griffy, M. R. Yearian, and R. Hofstadter, *Neutron form factors from inelastic electron-deuteron scattering*, *Phys. Rev.* **139** (1965) B458–B471.

[182] J. R. Dunning, K. W. Chen, A. A. Cone, G. Hartwig, N. F. Ramsey, J. K. Walker, and R. Wilson, *Quasi-elastic electron-deuteron scattering and neutron form factors*, *Phys. Rev.* **141** (1966) 1286–1297.

[183] R. Bradford, A. Bodek, H. Budd, and J. Arrington, *A new parameterization of the nucleon elastic form factors*, *Nuclear Physics B - Proceedings Supplements* **159** (2006) 127 – 132.

[184] J. Kelly, *Simple parametrization of nucleon form factors*, *Phys. Rev.* **C70** (2004) 068202.

[185] A. Bodek, S. Avvakumov, R. Bradford, and H. Budd, *Vector and axial nucleon form factors: a duality constrained parameterization*, *The European Physical Journal C* **53** 349–354.

[186] E. D. Commins and P. H. Bucksbaum *Weak interactions of leptons and quarks.* Cambridge University Press. 1983.

[187] R. Dharmapalan, *Antineutrino neutral current interactions in MiniBooNE.* PhD thesis, 2012.

[188] HAPPEX Collaboration, A. Acha et al., *Precision measurements of the nucleon strange form factors at* $Q^2 \sim 0.1$ GeV^2, *Phys. Rev. Lett.* **98** (2007) 032301, arXiv:nucl-ex/0609002 [nucl-ex].

[189] G. T. Garvey, W. C. Louis, and D. H. White, *Determination of proton strange form factors from* $\nu - p$ *elastic scattering*, *Phys. Rev. C* **48** (1993) 761–765.

[190] L. Ahrens, S. Aronson, P. Connolly, B. Gibbard, M. Murtagh, et al., *Measurement of neutrino - proton and antineutrino - proton elastic scattering*, *Phys. Rev.* **D35** (1987) 785.

[191] MiniBooNE Collaboration, A. Aguilar-Arevalo et al., *Measurement of the antineutrino neutral-current elastic differential cross section*, *Phys. Rev.* **D91** (2015) 012004, arXiv:1309.7257 [hep-ex].

[192] MINERνA Collaboration, B. Tice et al., *Measurement of ratios of* ν_μ *charged-current cross sections on C, Fe, and Pb to CH at neutrino energies 2-20 GeV*, *Phys. Rev. Lett.* **112** (2014) 231801, arXiv:1403.2103 [hep-ex].

[193] T2K Collaboration, K. Abe et al., *Measurement of the inclusive electron neutrino charged current cross section on carbon with the T2K near detector*, *Phys. Rev. Lett.* **113** (2014) 241803, arXiv:1407.7389 [hep-ex].

[194] T2K Collaboration, K. Abe et al., *Measurement of the electron neutrino charged-current interaction rate on water with the T2K ND280 π^0 detector*, arXiv:1503.08815 [hep-ex].

[195] C. Juszczak, J. T. Sobczyk, and J. Zmuda, *On extraction of value of axial mass from MiniBooNE neutrino quasi-elastic double differential cross section data*, *Phys. Rev.* **C82** (2010) 045502, arXiv:1007.2195 [nucl-th].

[196] A. M. Ankowski, *Consistent analysis of neutral- and charged-current neutrino scattering off carbon*, *Phys. Rev.* **C86** (2012) 024616, arXiv:1205.4804 [nucl-th].

[197] K2K, R. Gran et al., *Measurement of the quasi-elastic axial vector mass in neutrino-oxygen interactions*, *Phys. Rev.* **D74** (2006) 052002, arXiv:hep-ex/0603034 [hep-ex].

[198] MINOS Collaboration, M. Dorman, *Preliminary results for CCQE scattering with the MINOS near detector*, *AIP Conf. Proc.* **1189** (2009) 133–138.

[199] T2K Collaboration, K. Abe et al., *Measurement of the ν_μ CCQE cross section on carbon with the ND280 detector at T2K*, arXiv:1411.6264 [hep-ex].

[200] T2K Collaboration, K. Abe et al., *Measurement of the ν_μ charged current quasi-elastic cross section on carbon with the T2K on-axis neutrino beam*, arXiv:1503.07452 [hep-ex].

[201] MINERνA Collaboration, J. Wolcott, *Measurement of electron neutrino CCQE-like cross section in MINERνA*, arXiv:1501.05214 [hep-ex].

[202] J. A. Formaggio and G. P. Zeller, *From eV to EeV: neutrino cross sections across energy scales*, *Rev. Mod. Phys.* **84** (2012) 1307–1341.

[203] K. S. Kuzmin, V. V. Lyubushkin, and V. A. Naumov, *Axial masses in quasielastic neutrino scattering and single-pion neutrinoproduction on nucleons and nuclei*, *Acta Phys. Polon.* **B37** (2006) 2337–2348, arXiv:hep-ph/0606184 [hep-ph].

[204] SciBooNE Collaboration, Y. Kurimoto et al., *Measurement of inclusive neutral current neutral pion production on carbon in a few-GeV neutrino beam*, *Phys. Rev.* **D81** (2010) 033004, arXiv:0910.5768 [hep-ex].

[205] MiniBooNE Collaboration, A. Aguilar-Arevalo et al., *Measurement of neutrino-induced charged-current charged pion production cross sections on mineral oil at $E_\nu \sim 1$ GeV*, *Phys. Rev.* **D83** (2011) 052007, arXiv:1011.3572 [hep-ex].

[206] MiniBooNE Collaboration, A. Aguilar-Arevalo et al., *Measurement of ν_μ-induced charged-current neutral pion production cross sections on mineral oil at $E_\nu \in 0.5 - 2.0$ GeV*, *Phys. Rev.* **D83** (2011) 052009, arXiv:1010.3264 [hep-ex].

[207] MiniBooNE Collaboration, A. A. Aguilar-Arevalo et al., *Measurement of ν_μ and $\bar{\nu}_\mu$ induced neutral current single π^0 production cross sections on mineral oil at $E_\nu \sim \mathcal{O}$ (1 GeV)*, *Phys. Rev.* **D81** (2010) 013005, arXiv:0911.2063 [hep-ex].

[208] MINERνA Collaboration, B. Eberly et al., *Charged pion production in ν_μ interactions on hydrocarbon at $\langle E_\nu \rangle = 4.0$ GeV*, arXiv:1406.6415 [hep-ex].

[209] P. Rodrigues, *Comparing pion production models to MiniBooNE data*, arXiv:1402.4709 [hep-ex].

[210] J. T. Sobczyk and J. Żmuda, *Investigation of recent weak single-pion production data*, *Phys. Rev.* **C91** (2015) 045501, arXiv:1410.7788 [nucl-th].

[211] O. Lalakulich and U. Mosel, *Pion production in the MiniBooNE experiment*, *Phys. Rev.* **C87** (2013) 014602, arXiv:1210.4717 [nucl-th].

[212] K. M. Graczyk, D. Kielczewska, P. Przewlocki, and J. Sobczyk, *C_5^A axial form factor from bubble chamber experiments*, *Phys. Rev.* **D80** (2009) 093001, arXiv:0908.2175 [hep-ph].

[213] K. M. Graczyk, J. Żmuda, and J. T. Sobczyk, *Electroweak form factors of the $\Delta(1232)$ resonance*, *Phys. Rev.* **D90** (2014) 093001, arXiv:1407.5445 [hep-ph].

[214] D. I. Scully, *Neutrino induced coherent pion production*. PhD thesis.

[215] G. Garvey, D. Harris, H. Tanaka, R. Tayloe, and G. Zeller, *Recent Advances and Open Questions in Neutrino-induced Quasi-elastic Scattering and Single Photon Production*, arXiv:1412.4294 [hep-ex].

[216] A. M. Ankowski and J. T. Sobczyk, *Argon spectral function and neutrino interactions*, *Phys. Rev. C* **74** (2006) 054316.

[217] A. Butkevich, *Quasi-elastic neutrino charged-current scattering off C-12*, *Phys. Rev.* **C80** (2009) 014610, arXiv:0904.1472 [nucl-th].

[218] T. Golan, C. Juszczak, and J. T. Sobczyk, *Final state interactions effects in neutrino-nucleus interactions*, *Phys. Rev.* **C86** (2012) 015505, arXiv:1202.4197 [nucl-th].

[219] T. Leitner, O. Buss, L. Alvarez-Ruso, and U. Mosel, *Electron- and neutrino-nucleus scattering from the quasielastic to the resonance region*, *Phys. Rev. C* **79** (2009) 034601.

[220] C. Maieron, M. Martinez, J. Caballero, and J. Udias, *Nuclear model effects in charged current neutrino nucleus quasielastic scattering*, *Phys. Rev.* **C68** (2003) 048501, arXiv:nucl-th/0303075 [nucl-th].

[221] A. Meucci, C. Giusti, and F. D. Pacati, *Relativistic Green's function approach to charged current neutrino nucleus quasielastic scattering*, *Nucl. Phys.* **A739** (2004) 277–290, arXiv:nucl-th/0311081 [nucl-th].

[222] V. Pandey, N. Jachowicz, T. Van Cuyck, J. Ryckebusch, and M. Martini, *Low-energy excitations and quasielastic contribution to electron- and neutrino-nucleus scattering in the continuum random phase approximation*, arXiv:1412.4624 [nucl-th].

[223] J. Nieves, I. R. Simo, and M. J. V. Vacas, *Inclusive charged-current neutrino-nucleus reactions*, *Phys. Rev. C* **83** (2011) 045501.

[224] M. Martini, M. Ericson, G. Chanfray, and J. Marteau, *A unified approach for nucleon knock-out, coherent and incoherent pion production in neutrino interactions with nuclei*, *Phys. Rev.* **C80** (2009) 065501, arXiv:0910.2622 [nucl-th].

[225] E. Oset and L. Salcedo, *Delta self-energy in nuclear matter*, *Nuclear Physics A* **468** (1987) 631–652.

[226] J. Nieves, J. E. Amaro, and M. Valverde, *Inclusive quasielastic charged-current neutrino-nucleus reactions*, *Phys. Rev. C* **70** (2004) 055503.

[227] J. Nieves, I. Ruiz Simo, and M. Vicente Vacas, *The nucleon axial mass and the MiniBooNE quasielastic neutrino-nucleus scattering problem*, *Phys. Lett.* **B707** (2012) 72–75, arXiv:1106.5374 [hep-ph].

[228] M. Martini, M. Ericson, and G. Chanfray, *Neutrino quasielastic interaction and nuclear dynamics*, *Phys. Rev.* **C84** (2011) 055502, arXiv:1110.0221 [nucl-th].

[229] J. Nieves, I. Ruiz Simo, and M. Vicente Vacas, *Two particle-hole excitations in charged current quasielastic antineutrino-nucleus scattering*, *Phys. Lett.* **B721** (2013) 90–93, arXiv:1302.0703 [hep-ph].

[230] M. Martini and M. Ericson, *Quasielastic and multinucleon excitations in antineutrino-nucleus interactions*, *Phys. Rev.* **C87** (2013) 065501, arXiv:1303.7199 [nucl-th].

[231] S. Bhadra, M. Cadabeschi, P. de Perio, V. Galymov, M. Hartz, et al., *Optical transition radiation monitor for the T2K experiment*, *Nucl. Instrum. Meth.* **A703** (2013) 45–58, arXiv:1201.1922 [physics.ins-det].

[232] A. Ichikawa, *Design concept of the magnetic horn system for the T2K neutrino beam*, *Nuclear Instruments and Methods in Physics Research Section A: Accelerators, Spectrometers, Detectors and Associated Equipment* **690** (2012) 27–33.

[233] K. Matsuoka et al., *Design and performance of the muon monitor for the T2K neutrino oscillation experiment*, *Nuclear Instruments and Methods in Physics Research Section A: Accelerators, Spectrometers, Detectors and Associated Equipment* **624** (2010) 591 – 600.

[234] A. C. D. Beavis and I. Chiang, "Long baseline neutrino oscillation experiment at the AGS, BNL 52459." 1995.

[235] T2K Collaboration, K. Abe et al., *Measurements of the T2K neutrino beam properties using the INGRID on-axis near detector*, *Nucl. Instrum. Meth.* **A694** (2012) 211–223, arXiv:1111.3119 [physics].

[236] UA1 Collaboration, G. Arnison et al., *Experimental Observation of Isolated Large Transverse Energy Electrons with Associated Missing Energy at* $\sqrt{s} = 540$ *GeV*, *Phys. Lett.* **B122** (1983) 103–116.

[237] J. Altegoer et al., *The NOMAD experiment at the CERN SPS*, *Nuclear Instruments and Methods in Physics Research Section A: Accelerators, Spectrometers, Detectors and Associated Equipment* **404** (1998) 96–128.

[238] S. Aoki et al., *The T2K Side Muon Range Detector (SMRD)*, *Nuclear Instruments and Methods in Physics Research Section A: Accelerators, Spectrometers, Detectors and Associated Equipment* **698** (2013) 135–146.

[239] S. Assylbekov et al., *The T2K ND280 off-axis* π^0 *detector*, *Nuclear Instruments and Methods in Physics Research Section A: Accelerators, Spectrometers, Detectors and Associated Equipment* **686** (2012) 48–63.

[240] P. A. Amaudruz et al., *The T2K fine-grained detectors*, *Nuclear Instruments and Methods in Physics Research Section A: Accelerators, Spectrometers, Detectors and Associated Equipment* **696** (2012) 1–31.

[241] N. Abgrall et al., *Time projection chambers for the T2K near detectors*, *Nuclear Instruments and Methods in Physics Research Section A: Accelerators, Spectrometers, Detectors and Associated Equipment* **637** (2011) 25–46.

[242] T2K UK Collaboration, D. Allan et al., *The Electromagnetic Calorimeter for the T2K Near Detector ND280*, *JINST* **8** (2013) P10019, arXiv:1308.3445 [physics.ins-det].

[243] Y. Fukuda, T. Hayakawa, E. Ichihara, M. Ishitsuka, and Y. I. *et al.*, *The Super-Kamiokande detector*, *Nuclear Instruments and Methods in Physics Research Section A: Accelerators, Spectrometers, Detectors and Associated Equipment* **501** (2003) 418–462.

[244] Super-Kamiokande Collaboration, M. Shiozawa et al., *Search for proton decay via $p \to e^+ + \pi^0$ in a large water Cherenkov detector*, *Phys. Rev. Lett.* **81** (1998) 3319–3323, arXiv:hep-ex/9806014 [hep-ex].

[245] Super-Kamiokande Collaboration, Y. Hayato et al., *Search for proton decay through $p \to \bar{\nu} + K^+$ in a large water Cherenkov detector*, *Phys. Rev. Lett.* **83** (1999) 1529–1533, arXiv:hep-ex/9904020 [hep-ex].

[246] Super-Kamiokande Collaboration, H. Nishino et al., *Search for Proton Decay via $p \to e^+ + \pi^0$ and $p \to \mu^+ + \pi^0$ in a large water Cherenkov detector*, *Phys. Rev. Lett.* **102** (2009) 141801, arXiv:0903.0676 [hep-ex].

[247] Super-Kamiokande Collaboration, K. Abe et al., *A Search for nucleon decay via $n \to \bar{\nu}\pi^0$ and $p \to \bar{\nu}\pi^+$ in Super-Kamiokande*, *Phys. Rev. Lett.* **113** (2014) 121802, arXiv:1305.4391 [hep-ex].

[248] Super-Kamiokande Collaboration, T. Tanaka et al., *An indirect search for WIMPs in the sun using 3109.6 days of upward-going muons in Super-Kamiokande*, *Astrophys. J.* **742** (2011) 78, arXiv:1108.3384 [astro-ph.HE].

[249] Super-Kamiokande Collaboration, M. Malek et al., *Search for supernova relic neutrinos at Super-Kamiokande*, *Phys. Rev. Lett.* **90** (2003) 061101, arXiv:hep-ex/0209028 [hep-ex].

[250] Super-Kamiokande Collaboration, T. Tanaka et al., *An indirect search for WIMPs in the sun using 3109.6 days of upward-going muons in Super-Kamiokande*, *Astrophys. J.* **742** (2011) 78, arXiv:1108.3384 [astro-ph.HE].

[251] Super-Kamiokande Collaboration, K. Ueno et al., *Search for GUT monopoles at Super-Kamiokande*, *Astropart. Phys.* **36** (2012) 131–136, arXiv:1203.0940 [hep-ex].

[252] S. E. Kopp, *The NuMI neutrino beam at Fermilab*, arXiv:physics/0508001 [physics].

[253] MINOS Collaboration, D. Michael et al., *The magnetized steel and scintillator calorimeters of the MINOS experiment*, *Nucl. Instrum. Meth.* **A596** (2008) 190–228, arXiv:0805.3170 [physics.ins-det].

[254] MiniBooNE Collaboration, A. Aguilar-Arevalo et al., *The neutrino flux prediction at MiniBooNE*, *Phys. Rev.* **D79** (2009) 072002, arXiv:0806.1449 [hep-ex].

[255] MiniBooNE collaboration, B. C. Brown et al., *Study of scintillation, fluorescence and scattering in mineral oil for the MiniBooNE neutrino detector*, *IEEE Nucl. Sci. Symp. Conf. Rec.* **1** (2006) 652–656.

[256] C. Wilkinson, S. Cartwright, and L. Thompson, *Using MiniBooNE neutral current elastic cross section results to constrain 3+1 sterile neutrino models*, *JHEP* **1401** (2014) 064, arXiv:1309.1081 [hep-ph].

[257] C. Wilkinson, S. Cartwright, and L. Thompson, *Using MiniBooNE NCEL and CCQE cross section results to constrain 3+1 sterile neutrino models*, *J. Phys. Conf. Ser.* **598** (2015) 012035, arXiv:1412.0461 [hep-ph].

[258] J. Conrad and M. Shaevitz, *Limits on electron neutrino disappearance from the KARMEN and LSND ν_e $-^{12}C$ cross section data*, *Phys. Rev.* **D85** (2012) 013017, arXiv:1106.5552 [hep-ex].

[259] D. Casper, *The Nuance neutrino physics simulation, and the future*, *Nucl. Phys. Proc. Suppl.* **112** (2002) 161–170, arXiv:hep-ph/0208030 [hep-ph].

[260] P. Stowell, C. Wilkinson, and S. Cartwright, *Effect of cross section models on the validity of sterile neutrino mixing limits*, arXiv:1501.02142 [hep-ph].

[261] MiniBooNE Collaboration, A. A. Aguilar-Arevalo et al., *A Search for muon neutrino and antineutrino disappearance in MiniBooNE*, *Phys. Rev. Lett.* **103** (2009) 061802, arXiv:0903.2465 [hep-ex].

[262] A. Bodek and J. Ritchie, *Further studies of Fermi motion effects in lepton scattering from nuclear targets*, *Phys. Rev.* **D24** (1981) 1400.

[263] A. Butkevich, *Analysis of flux-integrated cross sections for quasi-elastic neutrino charged-current scattering off ^{12}C at MiniBooNE energies*, *Phys. Rev.* **C82** (2010) 055501, arXiv:1006.1595 [nucl-th].

[264] C. Giunti, *Sterile neutrino fits*, arXiv:1106.4479 [hep-ph].

[265] M. Maltoni and T. Schwetz, *Sterile neutrino oscillations after first MiniBooNE results*, *Phys. Rev.* **D76** (2007) 093005, arXiv:0705.0107 [hep-ph].

[266] F. James and M. Roos, *Minuit: A System for function minimization and analysis of the parameter errors and correlations*, *Comput. Phys. Commun.* **10** (1975) 343–367.

[267] R. Brun and F. Rademakers, *ROOT: An object oriented data analysis framework*, *Nucl. Instrum. Meth.* **A389** (1997) 81–86.

[268] MINOS Collaboration, P. Adamson et al., *Search for sterile neutrino mixing in the MINOS long baseline experiment*, *Phys. Rev.* **D81** (2010) 052004, arXiv:1001.0336 [hep-ex].

[269] A. Bercellie et al., *Cross section parameters for the 2014 oscillation analysis*, *T2K-TN-192* (2014).

[270] A. Bercellie et al., *Implementation of additional NIWG cross section parameterizations for 2014 analyses*, *T2K-TN-193* (2014).

[271] T2K Collaboration, C. Wilkinson, *NEUT development for T2K and relevance of updated 2p2h models*, arXiv:1505.07994 [hep-ex].

[272] P. de Perio et al., *Cross section parameters for 2012 oscillation analysis*, *T2K-TN-108* (2012).

[273] P. Sinclair, *Implementation of a multinucleon neutrino interaction simulation and comparison with T2K data*. PhD thesis, Imperial College London, 2014.

[274] A. Furmanski, *Implementing the spectral function nuclear model in NEUT, and parametrizing systematic uncertainties*, *T2K-TN-184* (2013).

[275] J. T. Sobczyk, *Multinucleon-ejection model for two-body-current neutrino interactions*, *Phys. Rev. C* **86** (2012) 015504.

[276] MINERνA Collaboration, T. Walton et al., *Measurement of muon plus proton final states in ν_μ interactions on hydrocarbon at $\langle E_\nu \rangle = 4.2$ GeV*, *Phys. Rev. D* (2014), arXiv:1409.4497 [hep-ex].

[277] A. Redij and C. Wilkinson, *Implementation of the Random Phase Approximation model in NEUT and NIWGReWeight*, *T2K-TN-207* (2014).

[278] MINERνA Collaboration, G. Fiorentini et al., *Measurement of muon neutrino quasi-elastic scattering on a hydrocarbon target at $E_\nu \sim 3.5$ GeV*, *Phys. Rev. Lett.* **111** (2013) 022502, arXiv:1305.2243 [hep-ex].

[279] MINERνA Collaboration, L. Fields et al., *Measurement of muon antineutrino quasi-elastic scattering on a hydrocarbon target at $E_\nu \sim 3.5$ GeV*, *Phys. Rev. Lett.* **111** (2013) 022501, arXiv:1305.2234 [hep-ex].

[280] G. Cowan, K. Cranmer, E. Gross, and O. Vitells, *Asymptotic formulae for likelihood-based tests of new physics*, *Eur. Phys. J.* **C71** (2011) 1554, arXiv:1007.1727 [physics.data-an].

[281] M. Maltoni and T. Schwetz, *Testing the statistical compatibility of independent data sets*, *Phys. Rev.* **D68** (2003) 033020, arXiv:hep-ph/0304176 [hep-ph].

[282] D. Karlen, *Supplement to T2K-TN-192: analytic study of the PGoF statistic with neglected correlation*, *T2K-TN-192* (2014).

[283] J. Pumplin, D. Stump, and W. Tung, *Multivariate fitting and the error matrix in global analysis of data*, *Phys. Rev.* **D65** (2001) 014011, arXiv:hep-ph/0008191 [hep-ph].

[284] D. Stump, J. Pumplin, R. Brock, D. Casey, J. Huston, et al., *Uncertainties of predictions from parton distribution functions. 1. The Lagrange multiplier method*, *Phys. Rev.* **D65** (2001) 014012, arXiv:hep-ph/0101051 [hep-ph].

[285] J. C. Collins and J. Pumplin, *Tests of goodness of fit to multiple data sets*, arXiv:hep-ph/0105207 [hep-ph].

[286] M. N. Rosenbluth, *High energy elastic scattering of electrons on protons*, *Phys. Rev.* **79** (1950) 615–619.

[287] O. Benhar, A. Fabrocini, S. Fantoni, and I. Sick, *Spectral function of finite nuclei and scattering of GeV electrons*, *Nucl. Phys.* **A579** (1994) 493–517.

[288] M. Christy, N. Kalantarians, J. Ethier, and W. Melnitchouk, *Extraction of the neutron F_2 and F_L structure functions from inclusive deuterium data (paper in preparation)*.

[289] P. Rodrigues et al., *Tuning the NEUT resonance model*, *T2K-TN-197* (2014).

[290] K. M. Graczyk and J. T. Sobczyk, *Form factors in the quark resonance model*, *Phys. Rev. D* **77** (2008) 053001.

[291] M. Day and K. S. McFarland, *Differences in quasi-elastic cross sections of muon and electron neutrinos*, *Phys. Rev.* **D86** (2012) 053003, arXiv:1206.6745 [hep-ph].

[292] M. Friend et al., *Flux prediction and uncertainty updates with NA61 2009 thin target data and negative focussing mode predictions*, *T2K-TN-217* (2015).

[293] P. Bartet et al., ν_μ *CC event selections in the ND280 tracker using Run 2+3+4 data*, *T2K-TN-212* (2015).

[294] P. Berardi et al., *CC* $\bar{\nu}_\mu$ *event selection in the ND280 tracker using Run 5c antineutrino beam data*, *T2K-TN-224* (2015).

[295] M. H. Shaevitz, *Separating components of error matrices*, *BooNE Technical Note 253* (2008).

[296] G. D'Agostini, *On the use of the covariance matrix to fit correlated data*, *Nucl. Instrum. and Methods A* **346** (1994) 306 – 311.

[297] R. Peelle, "Peelle's pertinent puzzle, informal oak ridge national laboratory memorandum." 1987.

[298] T. De Forest, *Off-shell electron nucleon cross sections. The impulse approximation*, *Nucl. Phys.* **A392** (1983) 232–248.